מכון ויצמן למדע
WEIZMANN INSTITUTE OF SCIENCE

Thesis for the degree
Doctor of Philosophy

עבודת גמר (תזה) לתואר
דוקטור לפילוסופיה

Submitted to the Scientific Council of the
Weizmann Institute of Science
Rehovot, Israel

מוגשת למועצה המדעית של
מכון ויצמן למדע
רחובות, ישראל

במתכונת "רגילה"
In a "Regular" Format

By
Deepali Sharma

מאת
דיפאלי שרמה

הווצרות המזונים ω ו ϕ בהתנגשויות p+p ו
d+Au בעזרת הגלאי PHENIX ב- RHIC

ω - and ϕ-meson production in p+p and d+Au collisions at RHIC energies, using the PHENIX Detector

Advisor: Itzhak Tserruya

מנחה: יצחק צרויה

May 2010

סיון תש"ע

Dedicated to my loving parents, for without them this would not have been possible. Its impossible to pen down what I owe them. Also to Anju and Nitu who are always there for their Di.

Acknowledgements

It has been a long journey and I wouldn't have possibly made it to the end without the support and encouragement of certain people. It is therefore my very desire and a great pleasure to write a few words of appreciation for them and express my heartfelt thanks.

First of all I would like to express my sincere gratitude towards my thesis advisor Prof. Itzhak Tserruya, for giving me an opportunity to work with him. He has been very patient, supportive and encouraging, especially during the first year of my Ph.D, when I was trying to learn the PHENIX software and electron analysis details, and for that I will always be appreciative. His guidance and constructive criticism at many stages of analysis over the years of my Ph.D. tenure proved extremely useful and shaped this thesis in a significantly improved quality. For all this and many other things, I shall always be indebted to him.

Sincere thanks to Prof. D.K. Srivastava, who advised me to come to Weizmann and work with Itzhak. Thank you very much for giving me this opportunity. Many thanks to Prof. L. K. Magotra and Prof. Anju Bhasin, who encouraged me to take this decision of coming to Weizmann.

I am sincerely thankful to late Prof. Zeev Fraenkel for his encouragement, valuable suggestions regarding the analysis during the group meetings, and help with writing reports and analysis notes.

Many sincere thanks to my Ph.D. thesis committee members, Prof. Ehud Duchovni and Prof. Amos Breskin, for their useful remarks and careful checks of my work at different steps during the Ph.D.

I would like to express my sincere thanks to Dr. Ilia Ravinovich for many useful HBD related discussions and helping me with the hardware during HBD construction. Thanks to Sasha Milov for very fruitful physics discussions, guidance, support and being so friendly and helpful. My thanks goes to Sasha Kozlov and Anand Dubey, who helped me with some of the programming skills during my learning period. Thanks to Maxim Naglis for

many good discussions and some good time we spent together in the office, working towards completion of our graduate studies. I am deeply thankful to Mihael Makek for being a wonderful friend, and the nice time we spent together, especially our frequent dinner outings.

I would like to extend my warm thanks to entire PHENIX collaboration, as the data contained in this thesis is due to a collaborative effort of all those people. In particular, I would like to thank Prof. Tom Hemmick and Prof. Craig Woody for many useful physics conversations. Thanks to Prof. Rich Seto for all those useful ϕ meetings. A big thanks to Jason Kamin for making some of my stays at BNL enjoyable. I spent some good time with him in the counting house when we were bertaning GEMs and he also taught me some php programming. Thanks to Bob Azmoun, Sky Rolnick and Zvi Citron for providing a good company and rides across the BNL.

I would like to acknowledge the support by the Israel Science Foundation, the MINERVA Foundation and the Nella and Leon Benoziyo Center of High Energy Physics Research. Many thanks to the people who are managing the pc-farm, especially to Pierre Choukroun who has been very cooperative and friendly, and to Helen Katz. With the efficient pc-farm available here, It was much easier and faster to work on the analysis. The secretaries of the Particle Physics department deserve a special thanks for their kind support and help, that made my studies here smoother and hassle free.

I want to say a very special thanks to my those friends, who have been a part of my life long before I chose this path of Ph.D. I can not thank enough Poonam Di and Namerta who have always supported and motivated me and have helped me sail through many tough times. They are always there no matter what, in my hour of need. Poonam di especially is the nicest person I have ever known. Thanks to Aarti, Sulakshna, Simple, Munejah, Saloni and Radhu di for those wonderful and memorable days we spent in the hostel and university campus. Those two years were the best years of my student life. A warm thanks to Venu, who made my stays in Calcutta enjoyable and fun filled.

I made some wonderful friends in Israel, who made my stay here pleasant and memorable. Thank you very much Saroj and Neel bhaiya. You both had been a great support while you were here and I always miss you very much. A big thanks to Nara Singh ji for many wonderful physics/spiritual conversations,

and being so caring and affectionate. Many thanks to Lisa, she has been an amazing flat-mate and a great friend.

Lastly, but most importantly, I want to express my deep respects and sincere thanks to the two most important persons in my life, my parents. It is only due to them that I have been able to achieve this important milestone of my life. I just can not put in words what they are to me. After my parents, it is my sister and brother, Anjali and Nitin, who always love and support unconditionally their di. They are the best siblings, one could possibly have. I love and miss all the stupid/nice chit chats and fights that we have, whenever we all are together at home. You two will always be very special for me.

Abstract

The work presented in this thesis comprises of two parts. The first part is focussed on the studies of ω- and ϕ-meson production via their e^+e^- decay channel in $p+p$ and $d+Au$ collisions at $\sqrt{s_{NN}}$ = 200 GeV using the PHENIX detector. Currently PHENIX is the only detector at Relativistic Heavy Ion Collider (RHIC), that is capable to measure vector mesons simultaneously via their leptonic and hadronic decay channels.

Low mass vector mesons are among the most informative probes to understand the strongly coupled Quark Gluon Plasma (QGP) created at RHIC in $Au+Au$ collisions. The suppression of low mass vector mesons at high transverse momentum, compared to expectations from scaled $p+p$ results reflects the properties of the strongly interacting matter formed. The mass and/or width of the vector mesons could be modified due to the restoration of chiral symmetry in the QGP. A systematic approach including measurements in $p+p$, $d+Au$, and $Au+Au$ collisions is essential to unveil these effects. The $p+p$ measurements are essential as they serve as a baseline for all other systems. The $d+Au$ measurements help to unveil possible initial state effects and understand cold nuclear matter effects.

The results presented in this thesis include the transverse momentum spectra, rapidity density $\frac{dN}{dy}$, mean transverse momentum $\langle p_T \rangle$ values and nuclear modification factor R_{dAu} studied as a function of centrality. The invariant p_T spectra extend down to $p_T = 0$, and up to 3.5 GeV/c in $p+p$ and 6.0 GeV/c in the $d+Au$ collisions. The coverage down to very low p_T allowed a detailed discussion of the methodology used to derive the rapidity density from the data. The results are compared to complementary measurements of the ω and ϕ via hadronic decay channels ($\omega \to \pi^+\pi^-\pi^0, \gamma\pi^0$, $\phi \to K^+K^-$). Good agreement is seen between the leptonic and hadronic channels in the region of overlap for both the ω and ϕ. The R_{dAu} of ϕ and ω is compared to π^0 and other charged hadron results. Results indicate that R_{dAu} of ϕ and ω is similar to that of the pions and show a very little or no Cronin enhancement. This

demonstrates that the high-p_T suppression of ω and ϕ observed in $Au+Au$ collisions is not an initial, but rather a final state effect of the hot and dense matter produced in these collisions.

The second part of the thesis describes the construction and commissioning of a Hadron Blind Detector (HBD), and first results showing the detector performance. The HBD is a novel windowless Čerenkov detector that has been built as an upgrade for the PHENIX detector and will significantly improve the capability of PHENIX to measure the low mass lepton pairs. Its primary aim is to recognize and reject the electron pairs originating from π^0 Dalitz decays and γ-conversions by exploiting their small opening angle in the field free region around the collision vertex, thereby considerably reducing the combinatorial background. The detector performed very well in Run9 $p+p$ and also in the ongoing $Au+Au$ run and gave the expected level of performance. Preliminary results indicate a clear separation between electrons and hadrons, a hadron rejection factor close to 50, excellent electron detection efficiency of the order of 90%, a yield of 20 photoelectrons per incident electron, and a good separation of single vs double electrons. With the HBD performing so well, we expect a qualitative and more precise measurement of low mass dileptons from the current $Au+Au$ run using the HBD.

Contents

List of Figures

List of Tables

Chapter 1

Introduction

1.1 Quarks, Gluons and Quantum Chromodynamics

The first subatomic particle to be identified was the electron, in 1898. Ten years later, Ernest Rutherford discovered that atoms have a very dense nucleus, which contains protons [1]. In 1932, James Chadwick discovered the neutron [2], another particle located within the nucleus. And so scientists thought they had found the smallest atomic building blocks. This changed in 1964 when Murray Gell-Mann [3] and George Zweig [4] independently proposed the quark model. The model was based on Gell-Mann's 1961 formulation of a particle classification system known as the *Eightfold Way* [5] or, technically SU(3) flavor symmetry. A similar scheme was also developed independently by Yuval Ne'eman [6] in the same year.

According to the quark model, the hadrons are not elementary particles, but are instead composed of combinations of quarks and antiquarks. The original model was comprised of three flavors of quarks - **up (u), down (d), strange (s)** - each with a spin (1/2), and with electric charge +2/3, -1/3 and -1/3, respectively. In addition, each quark carries a color charge of either *red, green or blue*. For every quark flavor, there is a corresponding type of antiparticle known as antiquark, with properties of equal magnitude but opposite sign. During the later years, three more quark flavors, **charm, bottom**, and **top** [7–11] were discovered and added to the quark model. Table 1.1 provides a list of all quarks and their physical properties.

In this model, the mesons consist of a quark and an anti-quark, $q\bar{q}$, and baryons (anti-baryons) are made of three quarks, qqq ($\bar{q}\bar{q}\bar{q}$). However since all the hadrons observed experimentally are neutral (colorless) in their color charge, the three quarks in the baryon must be combined in a colorless combination, *red-green-blue*, irrespective of the quark

Quarks				Leptons			
Name	Symbol	Charge(×e)	Rest mass (MeV/c^2)	Name	Symbol	Charge(×e)	Rest mass (MeV/c^2)
up	u	+2/3	1.5-3.3	e-neutrino	ν_e	0	<0.003
down	d	-1/3	3.5-6.0	electron	e	-1	0.511
strange	s	-1/3	104^{+26}_{-34}	μ-neutrino	ν_μ	0	<0.19
charm	c	+2/3	1270^{+70}_{-110}	muon	μ	-1	105.6
bottom	b	-1/3	4200^{+170}_{-70}	τ-neutrino	ν_τ	0	<18.2
top	t	+2/3	171200±2100	tau	τ	-1	1776.8

Table 1.1: Quarks and Leptons along with their physical properties [12].

flavors. The mesons on other hand must have a quark of particular color and an anti-quark of the anti-color of the quark.

Over the past few years, the framework of the quark model has been extended to include the leptons and the forces that govern matter, and this generalized version is known as the *Standard Model (SM)*. Within the framework of the SM, quarks and leptons are fermions, containing no underlying substructure, and the number of leptons is the same as the number of quark types. A list of the leptons along with their physical properties is given in Table 1.1.

Name	Relative strength	Range	Exchange particle
gravity	10^{-38}	∞	graviton
weak	10^{-13}	$< 10^{-18}$ m	Z^0, W^+, W^-
electromagnetic	10^{-2}	∞	photon
strong	1	∞	gluon

Table 1.2: Forces and their strength relative to the strong force.

The SM also accounts for the forces that govern the interactions between particles. These forces are the electromagnetic, the weak and the strong forces, each one conveyed by a distinct mediator or exchange particle. Table 1.2 lists each of the forces, their strength relative to the strong force, and the exchange particles. The electromagnetic force can be either attractive or repulsive and acts between electrically charged objects. The weak force is responsible for β-decay and radioactivity. The strong force describes the interaction of quarks and gluons in hadrons and binds quarks in hadrons, and nucleons within the nucleus. The gravitational force, which acts as an attractive force between two massive bodies, is yet to be incorporated into the Standard Model.

The properties of the strong force are described by the theory known as *Quantum Chromodynamics (QCD)*, analogous to *Quantum Electrodynamics (QED)* that is used to describe the properties of ordinary atomic matter. In the QCD framework, quarks interact by exchanging massless gauge fields, gluons. There are eight spin-1 gluons which carry color charge [13], unlike the photon in QED which is electrically neutral, and therefore interact both with quarks and gluons by exchanging other gluons. This phenomenon has profound consequences on the behavior of strongly interacting matter.

A phenomenological parameterization of the QCD potential between a quark-antiquark pair is:

$$V(r) = -\frac{A(r)}{r} + K \cdot r \tag{1.1}$$

where r is the distance between q and $\bar{q}$. The first term resembles the Coulomb potential, except for the dependence on distance of A. It is the second term, the linear rise of the potential with increasing distance, that gives origin to the unique properties of QCD. The coefficient A in Eq. 1.1 is proportional to the strong coupling constant α_s, also known as the "running" coupling constant, since its value depends on the momentum transfer scale Q considered. At small distances, or large momentum transfer, $\alpha_s \rightarrow 0$, implying weakening of the interaction. Hence for small distances, quarks and gluons are weakly coupled and this property is referred to as *asymptotic freedom*. Due to the small value of α_s, pQCD (perturbative QCD) calculations, similar to the ones performed for electroweak interactions, are possible and provide an excellent basis to the theory. On the other hand, when $r \rightarrow \infty$, *i.e.* at large distances or small momentum transfer, the second term of Eq. 1.1 dominates, making the effective coupling strong and resulting in the phenomenon of *quark confinement*. As a consequence of confinement, no isolated colored object has ever been observed experimentally.

1.2 Deconfinement and Phase Diagram

The study of nuclear matter at extreme conditions of temperature and/or density provides interesting possibilities for insight into the fundamental properties of QCD. It was suggested [14] that at very high densities, such as the ones that can be found in the core of neutron stars, quarks are so close together that it is no longer possible to assign them to a specific hadron, and the system can better be described as a "quark soup". Similarly at very high temperatures, large thermal momentum transfers allow for asymptotic freedom to set in, and quarks can move freely throughout volumes larger than that of a nucleon.

Perturbative QCD calculations work for very small distances between the quarks, but fail as the interaction strength grows at larger distances. For distance scales over $\sim 1 fm$, lattice QCD calculations can provide quantitative results. In this framework, Monte Carlo integration techniques are used to calculate expectation values of observables, using the QCD partition function $\mathcal{Z}$, which is a function of the volume, temperature and baryon chemical potential μ_B. Results from lattice QCD [15] point to the existence of a phase transition from nuclear matter to a deconfined phase of quarks and gluons, known as the quark-gluon plasma (QGP) [16]. Fig. 1.1 shows the lattice QCD results for the evolution of the energy density and pressure with temperature. At a critical temperature of $T_c \approx 170\ MeV$, both the energy density and pressure rise very quickly, as is characteristic in a phase transition. The critical temperature depends on the number of quark flavors used in the simulation. For 2-flavor QCD, the current estimate for the critical temperature is $T_C = 173 \pm 8$ MeV [17].

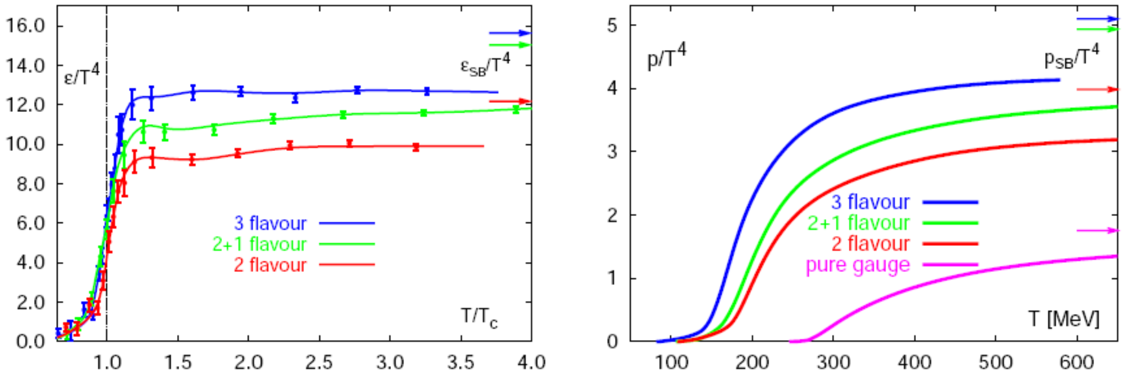

Figure 1.1: Lattice QCD results for the energy density as a function of T/T_c (left) and pressure as a function of temperature (right), both scaled by T^4. The different lines correspond to the number of quark flavors used in the simulation.

The order of the phase transition is still a matter of debate. Depending on the number of flavors used in the lattice calculations, and on the value of the quark masses for **u, d** and **s**, the phase transition may appear to be first order, a crossover, or even second order (for particular choices of the masses). A recent version of the phase diagram of QCD matter is shown in Fig. 1.2 [18, 19]. It describes, in a qualitative form, the different phases that nuclear matter can go through, as the temperature and density change. The vertical axis in the figure is the temperature, and the horizontal axis represents the baryon chemical potential, μ_B, which grows with the baryon density of the system. The most realistic models in terms of the quark masses ($m_u, m_d \neq 0$ and $m_s \gg m_u, m_d$) suggest that the line separating the hadron gas from the quark-gluon phase is a first-order phase transition, ending in a critical point. For lower value of μ_B, in the region between the critical point and the vertical axis, a crossover is expected to occur [20, 21]. Lattice calculations provide information on the order of the phase transition on or near the $\mu_B = 0$ axis. Away from this axis, what is known about the phase diagram comes from perturbation theory and models [22, 23].

Measurements made in two separate regimes of the phase diagram provide insight into the properties of the quark gluon plasma. Neutron stars are believed to exist in the low temperature and high baryochemical potential regime of the QCD phase diagram. The typical radius of a neutron star is of the order of 10 km, while its mass is comparable to the mass of the sun, which results in neutrons to overlap in its core. Advances in the study of high density baryonic matter can provide valuable input to the study of compact astrophysical objects.

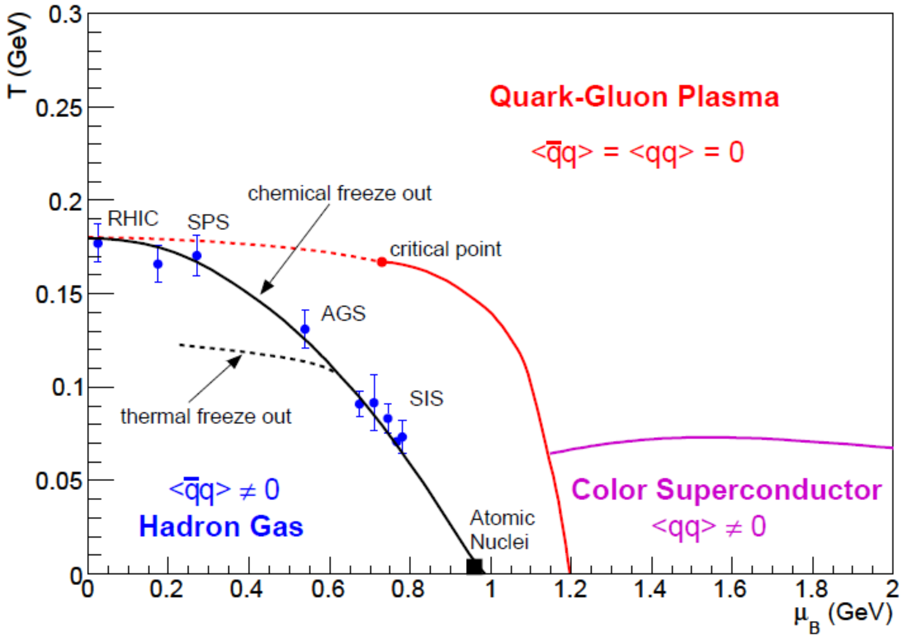

Figure 1.2: Schematic phase diagram of QCD matter as function of temperature T and baryonic chemical potential μ_B. The measured chemical freeze out points for SIS, AGS, SPS and RHIC energies are shown as points [19]. Phase co-existence lines are shown by the red and magenta full lines, and the dashed red line represents the cross-over. The black dashed and full line denote the thermal freeze out, and phenomenological condition of a chemical freeze-out respectively.

The other extreme of the QCD phase diagram *i.e.*, the region of vanishing baryochemical potential and high temperature resembles the conditions that existed in the early universe at $\sim 10^{-5}$ s after the Big Bang. The theory of the Big Bang postulates that at one time all matter and energy in the universe was compressed into a single point which subsequently exploded. Some of the energy released by the explosion was converted into matter that existed in the *quark-gluon plasma (QGP)* phase. As the system expanded, it cooled and condensed into a hadron gas. Since the time of the Big Bang, the universe has continued to expand and cool. Now the study of relativistic heavy-ion collisions provides a means of achieving in the laboratory the conditions that existed at the time of the Big Bang.

1.3 Chiral Symmetry Restoration (CSR)

In addition to the transition into a deconfined state of quarks and gluons, lattice QCD calculations also predict a phase transition into a chirally symmetric phase at high temperatures or densities, that presumably occurs at the same time as the deconfinement phase transition. An object or system has chirality if it differs from its mirror image. Such objects then come in two forms, left (L) and right (R), which are mirror images of each other. One can determine the chirality of a particle by taking the projection of its spin along its momentum direction[1].

For a particle with mass, both the right- and left-handed components must exist, since massive particles travel slower than the speed of light and a particle that appears left-handed in a particular reference frame will look right-handed from a reference frame moving faster than the particle. This implies that chirality is not conserved. In a massless world, chirality is conserved. This is a sufficient but not necessary condition.

The QCD Lagrangian can be expressed as:

$$\mathcal{L}_{QCD} = -\frac{1}{4}F^a_{\mu\nu}F^{\mu\nu}_a + i\sum_n \bar{\psi}_n\gamma^\mu \left[\partial_\mu + igA^a_\mu\frac{\lambda_a}{2}\right]\psi_n - \sum_n m_n\bar{\psi}_n\psi_n \tag{1.2}$$

where $F^a_{\mu\nu}$ are the gluon field tensors given by:

$$F^a_{\mu\nu} = \partial_\mu A^a_\nu - \partial_\nu A^a_\mu - g f_{abc}A^b_\mu A^c_\nu \tag{1.3}$$

λ_a are the eight Gell-Mann matrices, and f_{abc} are the structure constants of the SU(3) group formed by λ_a. g is $\sqrt{4\pi\alpha_s}$, where α_s is the strong coupling constant representing the strength of the interaction, ψ_n are the 4-component Dirac spinors associated with each quark field of 3 colors and n flavors and A^a_μ are the 8 gluon gauge fields.

The first term, $\frac{1}{4}F^a_{\mu\nu}F^{\mu\nu}_a$, of the Lagrangian corresponds to the free gluon field, the term, $ig\sum_n\bar{\psi}_n\gamma^\mu A^a_\mu\frac{\lambda_a}{2}\psi_n$, corresponds to the interaction of the quark field with the gluon field, and the last term $\sum_n m_n\bar{\psi}_n\psi_n$ corresponds to the free quarks of mass m_n. m_n represents the diagonal matrix of current quark masses, which are parameters of the Standard Model.

---

[1] This in fact is the definition of helicity. In the high energy limit, chirality $\approx$ helicity.

In an ideal massless world, the quark helicity or chirality is conserved, implying that the numbers of left-handed and right-handed quarks are conserved separately and therefore one needs two descriptions of QCD related by a mirror transformation or chirally symmetric to each other. In the real world where quarks have a finite mass, chiral symmetry is "explicitly" broken by the mass term ($m_n\bar{\psi}_n\psi_n$) in the Lagrangian (Eq. 1.2), and only the total number of quarks (left-handed + right-handed) is conserved. However, the u and d quark masses is so small that chiral symmetry is expected to be an approximate symmetry in the light quark sector of QCD. The chiral symmetry of QCD implies that all states have a chiral partner with opposite parity and equal mass. In reality, the chiral partners are split in mass. For instance, the chiral partner of the ρ meson ($J^P = 1^-$) with m =770 is a_1 ($J^P = 1^+$) with m =1250 MeV. For nucleons the splitting is even larger: the chiral partner of N $(1/2^+)$ with m = 940 MeV is N^* $(1/2^-)$ with m= 1535 MeV. The difference is too large to be explained by the small *current*[1] quark masses ($m_u \approx 4\,MeV$, $m_d \approx 7\,MeV$) and hence it is concluded that chiral symmetry is "spontaneously≡dynamically" broken, or conversely one can say that the *constituent*[2] quark mass is generated by the spontaneous breaking of chiral symmetry.

It is called "spontaneous" because there is no corresponding symmetry breaking term in the Lagrangian, as is the case for the mass term in the "explicit" symmetry breaking. The symmetry in this case is broken due to a non-vanishing ground state expectation value of the quark condensate $\langle\bar{q}q\rangle \neq 0$, implying that the ground state of QCD is unstable against the condensation of $\bar{q}q$ pairs. In other words, the vacuum is not empty, and the value of $\langle\bar{q}q\rangle \sim -(254MeV)^3$ can be loosely thought of as the density of these $\bar{q}q$ pairs. The phenomenon of spontaneous breaking of chiral symmetry according to the Goldstone theorem [24] results in the appearance of eight massless Goldstone bosons (π^+, π^-, π^0, K^+, K^-, K^0, η, η'), which turn to be light rather than massless due to the small current quark masses.

In the limit of high temperatures ($T > T_C$) or high baryon densities ($\rho > \rho_C$), numerical lattice QCD calculations predict that the quark condensate "melts", the constituent masses approach the current masses and chiral symmetry is approximately restored. The dynamics of breaking and partial restoration of chiral symmetry is of great interest in nuclear physics [25–27]. Unfortunately, the chiral condensate is not an observable and one needs suitable probes to explore the effects of chiral symmetry restoration (see Section 1.5).

---

[1] The current quark masses are generated by the spontaneous symmetry breaking of the Higgs field

[2] The constituent quark masses are generated by the spontaneous chiral symmetry breaking

1.4 Relativistic Heavy Ion Collisions

Colliding heavy ions at relativistic energies as a means to create a system of hot and dense nuclear matter in the laboratory, was first suggested in the early 1970s [28]. The almost simultaneous collisions of the nucleons in the two nuclei result in a large amount of energy deposited over a very short time interval, within a volume approximately equal to the size of the nucleus, which can create an energy density above that required for the phase transition ($\sim$ 1 GeV/fm^3).

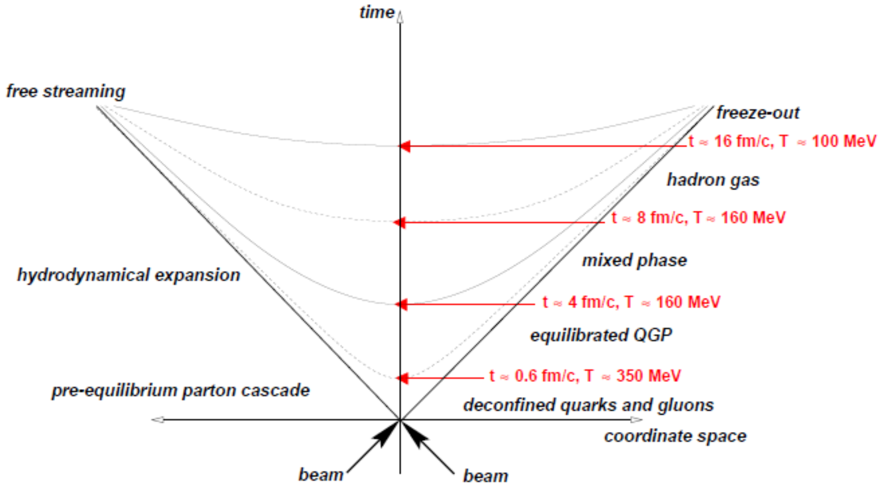

Figure 1.3: Space time evolution of the medium created in relativistic heavy ion collisions. The mixed phase would exist only if the transition is of first order [29].

In a relativistic heavy ion collision viewed in the center of mass system, the two nuclei approach each other not as symmetric spheres, but as thin, Lorentz contracted disks. Nucleons in the overlap region participate in the collision, and are referred to as “participants”. Those nucleons that are not involved in the collision continue to travel along the beam axis and are called “spectators”. Fig. 1.3 shows the evolution of the matter created in high-energy heavy-ion collisions in space-time, with the space coordinate along the beam direction z.

Immediately after impact, the collision system exists in a pre-equilibrium state. The participants deposit their original kinetic energy into the collision system and some of this energy is used for parton production. If the energy density achieved is sufficient, it is possible that a quark-gluon plasma is formed. Parton re-scattering can lead to thermal equilibrium during this stage. Once equilibrium is achieved, common thermodynamic quantities like temperature and pressure can be used to characterize the system and its evolution from this point onwards can be modeled by relativistic hydrodynamics.

The pressure created in the initial stage of the collision results in an expansion of the system formed. As it expands, the temperature drops, eventually crossing the transition temperature ($\approx 160-170$ MeV) and hadronization occurs wherein the partons get bound within hadrons. The system at this stage is composed of deconfined quarks and gluons, and hadrons. This mixed phase would exist only if the transition is of first order. Inelastic collisions between the newly formed hadrons continue to occur until the system cools to the chemical freeze-out point (≈ 100 MeV). This is when the relative yields of all particle species produced are fixed. Finally, elastic collisions between the hadrons cease at the thermal freeze-out point. At this point, the momentum distributions of all particles are frozen. After thermal freeze-out that the particles produced in the collision stream freely and can be measured by the detectors.

The hot and dense medium created in heavy-ion collisions is extremely short-lived ($\sim 5-10 fm/c$). One is therefore forced to use final-state observables and extrapolate backwards to characterize the properties of the system at early times. Many “signatures” of QGP formation and associated characteristics of the medium have been proposed (see for example [30, 31] for an overview). In the following sections, we discuss the observables that are most relevant to the work carried out in this thesis.

1.5 Low Mass Vector Mesons

Low mass vector mesons (ρ, ω, ϕ) are among the most interesting probes to understand several aspects of heavy-ion collisions, in particular chiral symmetry restoration. Theoretical studies [32–34] indicate in-medium modifications of their spectral properties (mass and/or width). These modifications can provide information about the behavior of the resonances close to the chiral restoration boundary. Since hadrons are formed in the mixed phase, or in the hot and dense hadron gas (HG) close to the phase boundary, their decay into dileptons can convey valuable information about their properties close to the onset of CSR [35]. The dileptons interact only electromagnetically and thus escape unaffected from the hot and dense matter, carrying clean information about the vector meson properties at the time of their production.

There are several theoretical approaches to the investigation of meson modification and its density dependence [33, 36]. Some of them predict a lowering of the in-medium mass of the vector mesons even at normal nuclear density ρ_0. For example Brown and Rho, using an effective QCD Lagrangian were the first to conjecture a linear decrease of the ρ-meson mass with the baryon density, giving a reduction of the ρ and ω masses by $\sim$ 20% at normal nuclear density [36]. Another model based on QCD sum rules, proposed by Hatsuda and Lee [33], predicts also a linear dependence of the masses on density, with a decrease in mass of $\sim$ 120-180 MeV/c^2 for the ρ and ω mesons, and $\sim$ 20-40 MeV/c^2 for the ϕ meson, at normal nuclear density. Other theoretical approaches predict only a broadening of the width; e.g. for ω, a broadening of the width up to 60 MeV/c^2 [37–39] has been predicted, whereas for the ϕ meson a factor between 5 or 6 [40, 41] and 10 [42] at normal nuclear density have been suggested. When the width of the ϕ meson broadens by a factor of 10, the lifetime of ϕ meson, $c\tau_\phi$, in a nucleus is reduced from 46 fm/c to 5 fm/c and the probability of in-medium decay increases, thereby increasing the probability to observe in-medium properties.

A more promising way to unveil these effects is provided by the simultaneous measurement, within the same apparatus, of the vector mesons through their leptonic and hadronic decay modes. The ϕ-meson measurement via its e^+e^- and K^+K^- decay channels, is particularly interesting. The ϕ mass is close to the two kaon threshold, $m_\phi - 2m_K \simeq$ 32 MeV. Therefore, even small changes in the spectral properties of the ϕ or K can have an impact on the branching ratio of the $\phi \to K^+K^-$ decay. For example, models predicting a drop of the ϕ mass lead to the suppression of the dominant decay channel to K^+K^- pairs [43, 44]. In this case, the relative branching ratios of the K^+K^- and e^+e^- decay channels should change dramatically, thus providing us a powerful tool to evidence in-medium effects. Several theoretical attempts taking into account the in-medium modifications (mass and broadening) of kaons and ϕ-mesons show an excess of the ϕ-meson yield from the dilepton channel versus the K^+K^- channel by a factor between 1.1 and 1.6 [43, 45].

1.5.1 Summary of Experimental Results from SPS and RHIC

The enhancement of low mass dileptons [46, 47], first observed by the CERES experiment, was one of the main discoveries of the CERN SPS heavy-ion program. This enhancement was quantitatively reproduced only by invoking the thermal radiation from a high density hadron gas ($\pi^+\pi^- \to \rho \to \gamma^* e^+e^-$) with in-medium modification of the ρ that could be linked to chiral symmetry restoration. Both the Brown-Rho [36] scaling and the Rapp-Wambach model [48] of in-medium broadening of the ρ were able to reproduce equally well the enhancement [49].

The CERES results motivated new experiments aiming at precise spectroscopic studies of the vector meson resonances ρ, ω and ϕ, in order to explore in-medium modifications of their spectral properties [50, 51]. Results from the NA60 [50] experiment, confirmed also by the upgraded CERES experiment [51], showed a significant increase of the width, with no significant mass shift of the ρ meson, favoring the broadening scenario.

The PHENIX experiment at RHIC has measured e^+e^- pair production in $Au+Au$ collisions at $\sqrt{s_{NN}}$ = 200 GeV and has reported also an enhancement of the dilepton yield of 4.7 ± 0.4 (stat.) ± 1.5 (syst.) ± 0.9 (model) in the mass region from 150 to 750 MeV/c^2, compared to the expectations from the known sources [52]. But the same models that successfully describe the SPS results are so far unable to explain the PHENIX results.

At SPS, the ϕ-meson has been studied via the K^+K^- decay channel by NA49 [53] and via the $\mu^+\mu^-$ decay channel by NA50 [54] in 158 AGeV $Pb+Pb$ collisions. Differences in the ϕ yield by factors of 2 to 4 were found between NA49 and NA50 in the common m_T range covered by the two experiments, leading to what is known as the SPS ϕ puzzle. A recent reanalysis of the NA50 data [55] shows a smaller difference, with the disagreement now at a factor of ~ 2. There is also significant disagreement in the inverse slope parameters derived from the two experiments. The differences are too large to be explained by the different rapidity coverage or the slightly different centrality selection of the two experiments.

CERES is the first experiment that measured simultaneously the ϕ meson through both the e^+e^- and K^+K^- decay channels within the same apparatus [47], in central 158 AGeV $Pb+Au$ collisions. Consistent results were found in the two channels within the large experimental uncertainties of the dilepton data. The K^+K^- yield was found in good agreement with the NA49 results whereas the e^+e^- data are compatible within 1-2 σ with the reanalyzed $\mu^+\mu^-$ data of NA50, or in other words the precision of the CERES e^+e^- data is insufficient to rule out the present level of difference between NA49 and NA50.

Additional insight on this issue is provided by the recent results from NA60 on ϕ production via muon and kaon decays in 158 AGeV $In+In$ collisions, but no coherent picture emerges yet from all SPS measurements. In NA60, the yields and inverse slopes from the two decay channels are in agreement within errors [56], *i.e.* the discrepancy seen in $Pb+Pb$ between the $\mu^+\mu^-$ (NA50) and K^+K^- (NA49) decay channels is not seen in $In+In$. The temperature parameters T measured by NA60 and NA49 are in agreement with each other and show an increase with centrality, whereas the NA50 results are consistent with a flat distribution [57]. On the other hand, the ϕ/ω ratio is in very good agreement with the NA50 results.

The study of low mass vector mesons under the much better conditions offered at RHIC (higher initial temperature, larger energy density, larger volume and longer lifetime of the system) promises to be very interesting. A prediction about the spectral functions of ρ, ω and ϕ at RHIC energies by R.Rapp [58, 59] is shown in Fig. 1.4. In this calculation the ρ and ω spectral functions show a strong broadening towards higher temperatures and densities. The ϕ seems to retain more of its resonance structure, although, at the highest

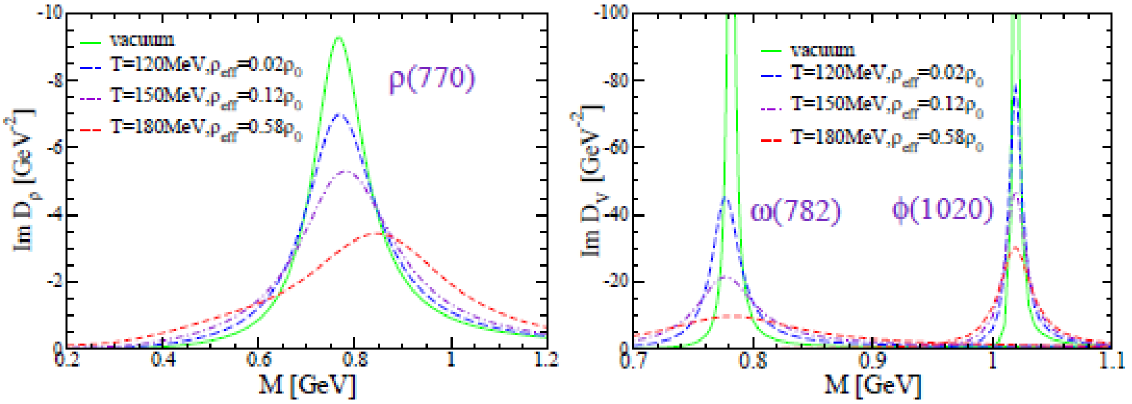

Figure 1.4: In-medium spectral function of the vector mesons for different temperatures and densities [58, 59].

temperature, the hadronic rescattering increases its vacuum width by over a factor of 7 to $\sim$ 32 MeV.

The PHENIX experiment at RHIC can measure ϕ via both its e^+e^- and K^+K^- decay channels. With its excellent mass resolution of the order of 1% at the ϕ mass, PHENIX should be able to perform spectroscopic studies of the ω- and ϕ-mesons, once the combinatorial background is reduced with the HBD upgrade. Both STAR [60] and PHENIX [61] have measured the ϕ-meson via its K^+K^- decay mode in $Au+Au$ collisions at $\sqrt{s_{NN}}$ = 200 GeV. The results revealed no significant change in the centroid and width values of the ϕ-meson from the PDG accepted values. Preliminary PHENIX results [62] of the rapidity density per pair of participants in $\sqrt{s_{NN}}$ = 200 GeV $Au+Au$ collisions may indicate a possible larger yield in the dilepton channel compared to the kaon one. However, within the large statistical and systematic uncertainties of the e^+e^- data, the two channels yield consistent results. A more definite statement will have to await for the improvement in data quality expected with the HBD upgrade of the PHENIX experiment.

1.6 The Nuclear Modification Factor

To quantify possible cold/hot nuclear medium effects in $p+A$ or $A+B$ collisions, we need a baseline expectation for the spectra for the case when no such effects are present. Given that hard parton scatterings have small cross-sections at RHIC energies, one can regard the nucleus as an incoherent superposition of partons ("point-like scaling"). The cross-section in $p+A$ or $A+B$ collisions, compared to $p+p$ collisions is then expected to be proportional to the relative number of possible point-like encounters, N_{coll}. In general, for a high-p_T particle produced in an $A+B$ collision with centrality f, one can define the *nuclear modification factor* as the ratio:

$$R_{AB}(p_T) = \frac{d^2N^{AB}/dp_T dy}{(\langle N_{coll}\rangle/d^2N^{pp})/dp_T dy} \tag{1.4}$$

where p_T is the transverse momentum, y is the rapidity, $\langle N_{coll}\rangle$ is the average number of inelastic binary nucleon-nucleon collisions for the given centrality class f, with an inelastic $p+p$ cross-section σ_{inel}^{pp} (See Section 2.2.6.1 for more details). $\langle N_{coll}\rangle$ can be calculated via a Glauber Monte Carlo calculation taking into account the experimental centrality selection, as described in detail in [78] for the PHENIX experiment. $d^2N^{AB}/dp_T dy$ and $d^2N^{pp}/dp_T dy$ correspond to the differential yield per event in $A+B$ and $p+p$ collisions, respectively. The differential yield is related to the differential cross-section $d^2\sigma^{pp}/dp_T dy$ and the total inelastic $p+p$ cross-section by:

$$\frac{d^2N^{pp}}{dp_T dy} = \frac{d^2\sigma^{pp}/dp_T dy}{\sigma_{inel}^{pp}} \tag{1.5}$$

In the absence of medium-induced effects, particle production in nucleus-nucleus collisions should scale with the number of binary collisions in the high-p_T region, resulting in $R_{AB} = 1$ at high-p_T. In the low p_T region, the yield is not expected to scale with N_{coll}, but with the number of participants, N_{part} and reflects the bulk properties of the system. This scaling can be modified when the initial parton distribution is changed in the nuclear environment or when the partons lose energy in the medium prior to fragmentation resulting in $R_{AB} < 1$.

Sometimes when reference $p+p$ data are not available, the ratio R_{CP} of central to peripheral yields, scaled by their respective binary nucleon-nucleon collisions, is also used as a measure of the nuclear modification of particle production:

$$R_{CP}(p_T) = \frac{N_{coll}^{peripheral} \times d^2N^{AB}/dp_T dy|_{central}}{N_{coll}^{central} \times d^2N^{AB}/dp_T dy|_{peripheral}} \tag{1.6}$$

One of the most intriguing observations from experiments at RHIC is the large suppression of high-p_T neutral pion and charged hadron yields in $Au+Au$ collisions with respect to $p+p$ results scaled by the number of binary nucleon-nucleon collisions [79–83]. This can be seen in Fig. 1.5 which shows the nuclear modification factors R_{AA} for inclusive charged hadrons and neutral pions in $Au+Au$ collisions at $\sqrt{s_{NN}} = 200$ GeV, as measured by PHENIX at various centralities [81, 82]. R_{AA} is below 1 for the most central collisions, a manifestation of suppressed hadron production in $Au+Au$, while as the collision centrality evolves to more peripheral collisions, R_{AA} approaches 1 as it should.

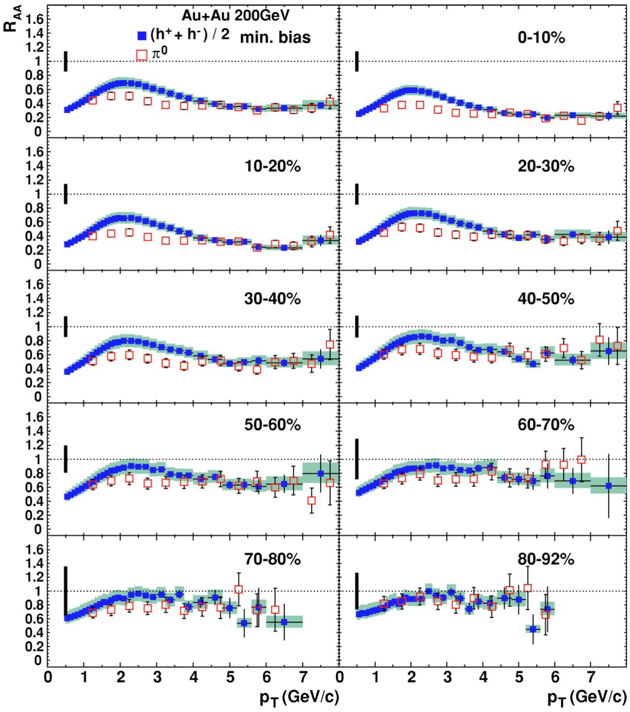

Figure 1.5: R_{AA} for $(h^{+}+h^{-})/2$ and π^{0} as a function of p_T for minimum bias and nine centrality classes in $Au+Au$ collisions at $\sqrt{s_{NN}}$ = 200 GeV. The error bars on the π^{0} data points include statistical and systematic errors on the $Au+Au$ data and $p+p$ reference. The error bars on $(h^{+}+h^{-})/2$ data points are statistical errors only. The shaded band on charged R_{AA} includes the remaining systematic errors on the charged $p+p$ reference summed in quadrature with the systematic errors from the $Au+Au$ data. The black bar on the left side of each panel shows the common normalization error [81–83].

A more detailed plot showing R_{AA} separately for mesons (ϕ, π^{0}, η, ω $K^{+}+K^{-}$), baryons ($p+\bar{p}$) and direct γ in central $Au+Au$ collisions at $\sqrt{s_{NN}}$ = 200 GeV, as measured by PHENIX [84–87], is shown in Fig. 1.6. For the central collisions, the protons show no suppression but rather are enhanced at $p_T > 1.5$ GeV/c, whereas all other mesons including ϕ and ω are suppressed. For $p_T > 5.0$ GeV, the suppression level of all mesons seems to fall to the same level.

This suppression, called *jet quenching* has been interpreted as energy loss of the energetic partons traversing the produced medium [88, 89]. If dense and hot partonic matter is formed during the initial stages of a heavy-ion collision the high energetic partons produced in hard scattering processes interact with this dense medium and lose energy via induced gluon radiation or collisional energy loss. This is a final state effect in the spatially extended medium created in $A+A$ collisions. One can not rule out initial-state effects that include nuclear modifications to the parton momentum distributions (structure functions), and soft scatterings of the incoming parton prior to its hard scattering. These effects should be present not only in $A+A$, but also in $p+A$, $d+A$.

Interpretations of $Au+Au$ collisions based on initial-state parton saturation effects [90] or final-state hadronic interactions [91] can also lead to a considerable suppression of the hadron production at high-p_T. It is therefore of paramount interest to determine experimentally the modification, if any, of the hadron yields due to initial-state nuclear effects

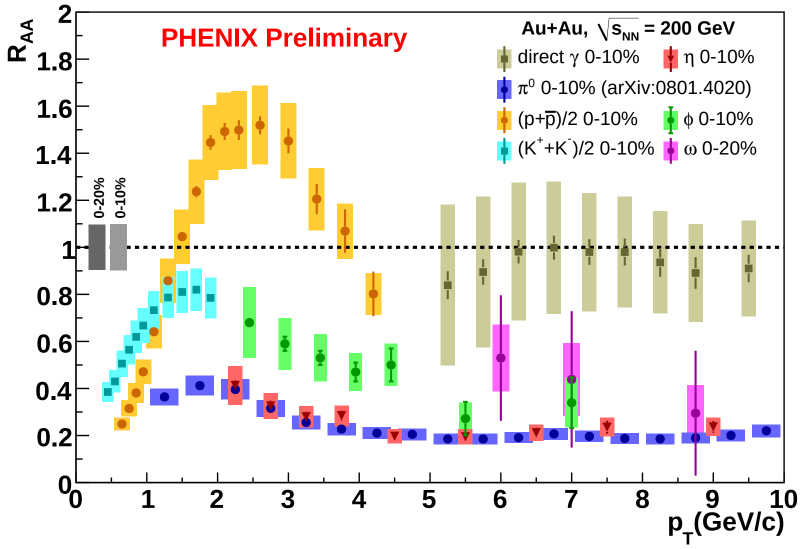

Figure 1.6: R_{AA} vs. p_T for ϕ, π^0, η, ω, $K^+ + K^-$, $p + \bar{p}$ and direct γ in central $Au+Au$ collisions. Values for ϕ are from Ref [84], $K^+ + K^-$ and $p + \bar{p}$ are from Ref. [85], π^0 are from Ref. [86], η, ω and direct γ are from Ref [87]. The uncertainty in the determination of $\langle N_{coll} \rangle$ is shown as a box on the left. The global uncertainty of $\sim$ 10% related to the $p + p$ reference normalization is not shown.

for a system in which a hot, dense medium is not produced in the final state. This is where $d + Au$ collisions play an important part to determine whether or not there are initial state effects that could affect the $Au+Au$ collisions and to disentangle them from the final state effects resulting from the hot and dense matter created.

1.7 Cold Nuclear Matter Effects

As already discussed in the previous section, a vital question for the interpretation of the $Au+Au$ results is whether the high-p_T suppression is due to final state or initial state effects already present in elementary hadronic collisions. In order to disentangle and quantitatively describe these effects, it is necessary to create experimental conditions in which one class of effects is present while the other is not. The $d + Au$ collisions provide one such example of a system where no hot, dense medium is formed in the final state. Since the initial state in $d + Au$ collisions is similar to that in $Au+Au$ collisions, and it is believed that the QGP does not exist in $d + Au$ collisions, the results from $d + Au$ collisions are crucial to interpret the information about jet quenching in $Au+Au$ collisions. Besides, the measurements of particle spectra in $d + Au$ and $p + p$ collisions provide the reference for $Au+Au$ collisions and also help to understand the “Cronin Effect” in $d + Au$ collisions.

Cronin effect It has been observed experimentally since the early 70's that, when comparing elementary $p+p$ collisions to $p+A$ collisions, the cross-section does not simply scale with the number of target nucleons in A. This was first shown by Cronin *et.al.* in 1974 [92] for a low energy fixed target experiment, using a proton beam on beryllium, titanium, and tungsten targets. They found that

$$E\frac{d^3\sigma^{pA}}{dp^3}(p_T) = E\frac{d^3\sigma^{pp}}{dp^3} \cdot A^{\alpha(p_T)} \tag{1.7}$$

with $\alpha > 1$ for transverse momenta larger than approximately 2 GeV/c as shown in Fig. 1.7. This is known as the "*Cronin effect*", a generic term for the experimentally observed broadening of the transverse momentum distributions at intermediate p_T in $p+A$ collisions as compared to $p+p$ collisions [89, 92–95]. The Cronin effect is generally attributed to multiple soft scattering of the incoming partons when propagating through the target nucleus [89, 95]. Since the particle production cross-section falls steeply towards high-p_T, these soft scatterings result in a smearing effect, that leads to an enhancement of particle production typically around 1.5-4 GeV/c compared to $p+p$ collisions.

The Cronin effect was observed and studied in detail in fixed target $p+A$ collisions up to 400 GeV [92–94]. The results indicate that α decreases with energy and strongly depends on the particle species. The Cronin effect was also observed at lower beam energy $A+A$ collisions at CER-ISR $\alpha+\alpha$ collisions at $\sqrt{s_{NN}}$ = 31 GeV [96] and CERN SPS $Pb+Pb$, $Pb+Au$ collisions at $\sqrt{s_{NN}}$ = 17 GeV [97].

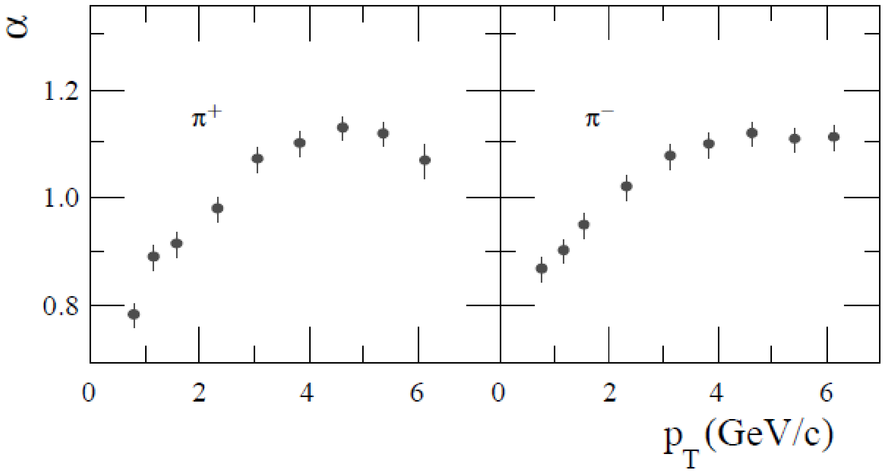

Figure 1.7: Dependence of the exponent α defined in Eq. 1.7 on the transverse momentum, representing the nuclear enhancement for charged pion production in proton collisions with a tungsten (W) target at incident proton energy of 300-GeV [92, 93].

At RHIC energies, studies are being carried out to quantify the Cronin effect. At these energies, multiple parton collisions are possible even in $p+p$ collisions [98]. This combined with the hardening of the spectra with increasing beam energy would reduce the Cronin effect [89, 95]. There are several models which give different predictions of the Cronin effect at 200 GeV. One of the models is the initial multiple parton scattering model [94, 100]. In this model, the transverse momentum of the parton inside the proton is broadened when the proton traverses the Au nucleus, due to the multiple scatterings between the proton and the nucleons inside the Au nucleus. The magnitude of the Cronin effect increases to a maximum value between 1 and 2 at $2.5 < p_T < 4.5$ GeV/c and then decreases with increasing p_T [89, 95]. The effect is predicted to be larger in central $d+Au$ collisions as compared to peripheral $d+Au$ collisions [101]. Another model is the gluon saturation model [90]. For sufficiently high beam energy, gluon saturation is expected to result in a relative suppression of the hadron yield at high-p_T, in both $p+A$ and $A+A$ collisions, resulting in a substantial decrease and finally in the disappearance of the Cronin effect [102]. Also at RHIC energies, a more detailed investigation about the Cronin effect dependence on the particle species in $d+Au$ collisions is needed.

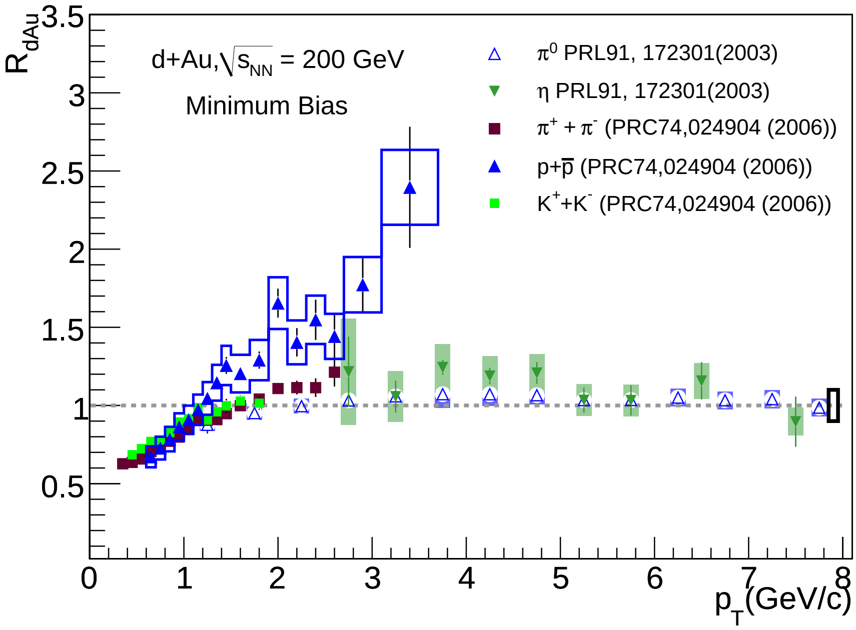

Figure 1.8: Nuclear modification factor R_{dAu} for pions, kaons, protons and eta meson in $d+Au$ collisions, as measured by PHENIX. The charged pions, kaons and protons results are from Ref. [85] and neutral pions and eta results are from are from Ref. [99].

Fig. 1.8 shows the nuclear modification factor R_{dAu} for charged pions, kaons and protons [85], plotted together with neutral pions and eta mesons [99], for the minimum bias $d+Au$ collisions. The data clearly indicate that there is no suppression of high-p_T particles in $d+Au$ collisions. We, however, observe a very small or no Cronin enhancement for all the mesons. The protons on the other hand show a considerably larger Cronin enhancement, indicating that baryons have different nuclear enhancement compared to mesons.

The observation of an enhancement of high-p_T hadron production in $d+Au$ collisions indicates that the suppression in central $Au+Au$ collisions is not an initial state effect. The data suggest, instead, that the hadron suppression at high-p_T in $Au+Au$ collisions is due to final state interactions in the dense and dissipative medium produced during the collisions.

1.7.1 Present Status of Results About Cold Nuclear Matter Effects on Vector Mesons

A few experiments have attempted to study the effects of cold nuclear matter on the vector meson spectral functions. These include KEK-PS E325, CLAS, CBELSA/TAPS and TAGX. However, the results reported so far from these experiments are controversial and insufficient for a consistent picture to emerge. The KEK experiment reported a significant excess of e^+e^- in the low-mass side of the ω and ϕ mesons [63–65] measured in 12 GeV $p+C$ and $p+Cu$ collisions. This was attributed to a decrease of the vector meson mass with the nuclear density ρ, with no in-medium broadening. A similar effect was originally reported by the CBELSA/TAPS experiment in the photoproduction of ω mesons identified through the $\pi^0\gamma$ decay channel, on Nb and LH$_2$ targets [66]. The data analysis was consistent with a dropping mass of 13%, in agreement with the expected predictions of Brown and Rho [27] and Hatsuda and Lee [33], and with the KEK results. However, subsequent transparency ratio measurements on C, Ca, Nb and Pb targets indicated a strong broadening of the ω meson of 130-150 MeV/c^2 [67], which prompted a reanalysis of the same data [68]. This reanalysis did not confirm the previous finding of mass shift, but on the contrary the results were found in better agreement with the scenario of ω broadening without mass shift.

The CLAS experiment searched for in-medium modifications of vector mesons in photo-induced reactions on various targets ^{2}H, C, Fe and Ti over on energy range of 0.6-3.8 GeV [69]. The CLAS results are inconsistent with the KEK results mentioned above. They rule out the dropping mass scenarios of Refs. [27, 33] and are consistent with other models that predict a broadening of the spectral shape without or with very small mass shift [70–72].

The TAGX collaboration measured the ρ meson, identified via its $\pi^+\pi^-$ decay channel, in photoproduction reactions on ^{2}H, ^{3}He and ^{12}C at E_γ = 0.6 -1.12 GeV [73–75]. The results show a mass decrease of the ρ in ^{3}He, of the order of 45-65 MeV/c^2[131], in contrast to the CLAS results previously mentioned. On the other hand, the ^{12}C data show mainly a broadening of the ρ, with no mass shift, that is reasonably reproduced by the many body effective Lagrangian approach of Rapp and Wambach [76] or the similar picture of Ref. [77].

1.8 Studies Done in This Thesis

The work carried out in this thesis can be divided into two parts. The first part describes the ω- and ϕ-meson production via their e^+e^- decay channel in $p+p$ and $d+Au$ collisions at $\sqrt{s_{NN}}$ = 200 GeV using the PHENIX detector at RHIC. As discussed in Section 1.5, low vector mesons are among the most valuable probes in high energy heavy-ion collisions and so their measurements in baseline $p+p$ and $d+Au$ collisions are equally crucial. The measurements in $p+p$ collisions accomplishes the first step of establishing the properties of these mesons in the elementary collision of two nucleons at RHIC energies. The $d+Au$ analysis allows then to study any effects arising from the wave function of the Au nucleus, such as the Cronin effect. The study of central and peripheral $d+Au$ collisions allows to measure the centrality dependence of various observables in cold nuclear matter. The $p+p$ and $d+Au$ results therefore serve as the final link for a comprehensive study of ω- and ϕ- meson production in $Au+Au$ collisions that will help to disentangle the cold and hot nuclear matter effects. More specifically, the work done in this thesis includes:

- Measurement of the transverse momentum spectra of ω and ϕ via their e^+e^- decay channel in $p+p$ and $d+Au$ collisions at $\sqrt{s_{NN}}$ = 200 GeV.
- Measurement of the ω and ϕ rapidity density $\frac{dN}{dy}$ and mean transverse momentum $\langle p_T \rangle$ in $p+p$, and for the minimum bias and centrality selected $d+Au$ collisions at $\sqrt{s_{NN}}$ = 200 GeV, without involving any model dependent extrapolations, and discussion of the methodology commonly used to extract $\frac{dN}{dy}$.
- Measurement of the nuclear modification factor R_{dAu}, in $d+Au$ collisions and its centrality dependence. A comparison to other charged hadrons results from PHENIX is also presented.
- Comparison of ω, $\phi \rightarrow e^+e^-$ results to some of their hadronic decay modes.

The second part of the thesis describes the work carried out by the author in the construction and commissioning of a Hadron Blind Detector that has been built as an upgrade to the PHENIX detector. PHENIX is presently the only experiment capable of measuring low-mass dileptons. As will be explained in Chapter 5, these measurements with the original configuration of PHENIX, suffer from a huge combinatorial background arising from unrecognized π^0 Dalitz decays and γ conversions, resulting in very large statistical and systematic uncertainties. To overcome this problem, we developed a Hadron Blind Detector, which is a novel Čerenkov detector that significantly improves the capability of the PHENIX detector to measure the low-mass electron pairs. The HBD recognizes and reject Dalitz decays and conversion pairs thereby improving the signal to background ratio significantly.

Chapter 2

Experimental Overview

In this chapter, I briefly describe the Relativistic Heavy Ion Collider (RHIC), the experimental facility dedicated to the study of heavy ion collisions at Brookhaven National Laboratory, and the PHENIX detector used to collect the data analyzed in this thesis, emphasizing the subsystems of the PHENIX detector which are relevant to this thesis.

2.1 RHIC

The Relativistic Heavy Ion Collider [103] is a versatile colliding type accelerator located at Brookhaven National Laboratory (BNL) in the United States. It is capable of accelerating a wide variety of nuclei up to 100 GeV per nucleon, and protons up to 250 GeV. RHIC started its operation in the year 2000. The designed luminosity is $2 \times 10^{26}\ cm^{-2}s^{-2}$ for Au ions and $2 \times 10^{32}\ cm^{-2}s^{-2}$ for proton. A layout of the RHIC accelerator complex is shown in Fig. 2.1.

The collider consists of two independent super-conducting concentric rings, 3.8 km in circumference, each one having an independent ion source, permitting the collision of unlike ion species. One is known as the *Blue Ring*, where the beam circulates clockwise and the other one as the *Yellow ring*, where the beam circulates counterclockwise. The ring shape is approximately circular, except for the six regions around the intersection points, where the beam trajectories are steered by magnets into straight lines to have them collide head-on.

2.1.1 Acceleration and Collisions

Fig. 2.1 shows the path of the gold beam through the accelerator complex, the Tandem - Van De Graaff, the Booster synchrotron, the AGS (Alternating Gradient Synchrotron) and finally RHIC. The proton beam has a slightly different path. It is first accelerated in the proton linear accelerator LINAC, before being injected into the AGS. The Au ions with a charge of -1 (Au^{-}) originate from a pulsed sputter ion source and are sent through the Tandem Van der Graaff accelerator, where they get accelerated in two stages through a 14 MV electrostatic potential. At the end of the first stage, the ions are stripped of 12 electrons by a thin carbon stripping foil. An additional 21 electrons are stripped at the exit of the Tandem where the ions have an energy of $\sim$1 MeV/nucleon. The resulting beam of Au^{+32} ions is then delivered to the Booster Synchrotron where more acceleration occurs, up to 95 MeV/nucleon. At the exit from the Booster another stripping foil removes 45 electrons, bringing the ions to a +77 charge state. This beam is then injected into the AGS, where it is accelerated to the RHIC injection energy of 10.8 GeV/nucleon and stored before delivery to the RHIC rings. The beam is directed towards the AGS-to-RHIC

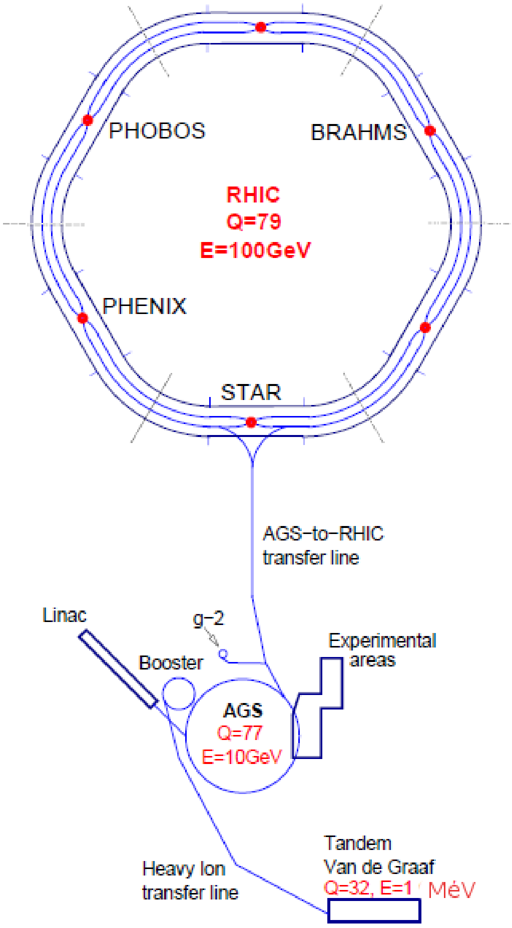

Figure 2.1: Overview of RHIC accelerator complex

transfer line where the remaining two electrons are removed before injection into RHIC.

After entering RHIC, the ions are accelerated to their final energy of 100 GeV/nucleon and after that they can be made to collide at the interaction points that are equipped with detectors. The beams are steered to maximize experimental collision rates, and stored for several hours while the experiments collect data. At the beginning of a store RHIC achieves typical collision rates of 10 kHz of minimum bias $Au+Au$ collisions.

2.1.2 The RHIC Experiments

At the time RHIC started running in the year 2000, there were four experiments; two small experiments BRAHMS [104] and PHOBOS [105], and two large experiments, PHENIX [106] and STAR [107], positioned at 2 o'clock, 10 o'clock, 8 o'clock and 6 o'clock on the RHIC rings respectively.

Since its commissioning in the year 1999, RHIC had 9 successful runs, colliding a variety of species, ranging from $p+p$, $d+Au$, $Cu+Cu$ and $Au+Au$ at various energies. The runs are several (18-25) weeks long each year. Run10, which is still ongoing is mainly devoted to $Au+Au$ collisions at $\sqrt{s_{NN}}$ =200, 62.4, 39 and 7 GeV. The collision species and energies for the various RHIC runs, along with the integrated luminosity recorded by PHENIX are given in Table 2.1. The analyses carried out in this thesis are based on the Run5 $p+p$ and Run8 $d+Au$ data sets. The delivered luminosity of RHIC and the recording capacity of PHENIX have consistently increased over the course of years *e.g.*, in year 2008, PHENIX accumulated 30 times more $d+Au$ data than in year 2003.

2.2 The PHENIX Detector

PHENIX[1] [106] is a sophisticated multi-system detector designed especially to measure direct probes, such as leptons, photons, muons and also hadrons. A schematic view of the PHENIX detector is shown in Fig. 2.2. The detector consists mainly of four spectrometers: two central arm spectrometers and two muon spectrometers. The analysis done in this thesis is based on electrons identified in the central arm spectrometers. More details about the muon spectrometers can be found in [108]. The Beam-Beam Counters (BBC) and Zero-Degree Calorimeters (ZDC) are used to define the minimum bias trigger, and provide centrality and vertex information.

---

[1] The acronym stands for *Pioneering High Energy Nuclear Interaction eXperiment* and named as such since it "rose from ashes"of four abandoned proposals for RHIC experiments; TALES, SPARC, OASIS and DIMUON.

Run	Year	Species	$\sqrt{s_{NN}}$ (GeV)	$\int Ldt$	$N_{Tot}(sampled)$
1	2000	$Au+Au$	130	1 μb^{-1}	10M
2	2001/2002	$Au+Au$	200	24 μb^{-1}	170M
		$p+p$	200	0.15 pb^{-1}	3.7G
3	2002/2003	$d+Au$	200	2.74 nb^{-1}	5.5G
		$p+p$	200	0.35 pb^{-1}	6.6G
4	2003/2004	$Au+Au$	200	241μb^{-1}	1.5G
		$Au+Au$	62.4	9 μb^{-1}	58M
5	2004/2005	$Cu+Cu$	200	3 nb^{-1}	8.6G
		$Cu+Cu$	62.4	0.19 pb^{-1}	0.4G
		$Cu+Cu$	22.5	2.7 μb^{-1}	9M
		$p+p$	200	3.8 pb^{-1}	85G
6	2006	$p+p$	200	10.7 pb^{-1}	230G
		$p+p$	62.4	0.1 pb^{-1}	28G
7	2007	$Au+Au$	200	0.813 nb^{-1}	5.1G
8	2008	$d+Au$	200	80 nb^{-1}	160G
		$p+p$	200	5.2 pb^{-1}	115G
9	2009	$p+p$	500	14 pb^{-1}	308G
		$p+p$	200	16 pb^{-1}	936G

Table 2.1: The 9 RHIC runs and the integrated luminosity delivered to the PHENIX experiment. N_{Tot} corresponds to the total number of sampled events.

The first detector in the central arms is the Drift Chamber (DC), that provides high resolution tracking of particles in r and ϕ outside the magnetic field. Just behind the DCs is the first layer of Pad Chambers (PC1). PC1 is followed by the Ring Imaging Čerenkov detector (RICH), which provides electron identification. In the west arm, the RICH is followed by two other layers of Pad Chambers (PC2 and PC3). The PCs provide 3-dimensional space point measurement of the particle track, which is crucial for the pattern recognition and to determine the track polar angle θ. The east arm has only one additional layer of PC3 and is also equipped with a Time Expansion Chamber (TEC), as an additional tracker and eID element, and a Time of Flight (TOF) detector for particle identification. The latter two subsystems are not used in the current analysis. The last detector in the central arms is the Electro-Magnetic Calorimeter (EMCal), which provides an energy measurement of photons and electrons. There are two types of calorimeters in PHENIX: the lead-scintillator (PbSc) and the lead-glass (PbGl). The central arms also contain a Central Magnet that provides an axial magnetic field, parallel to the beam around

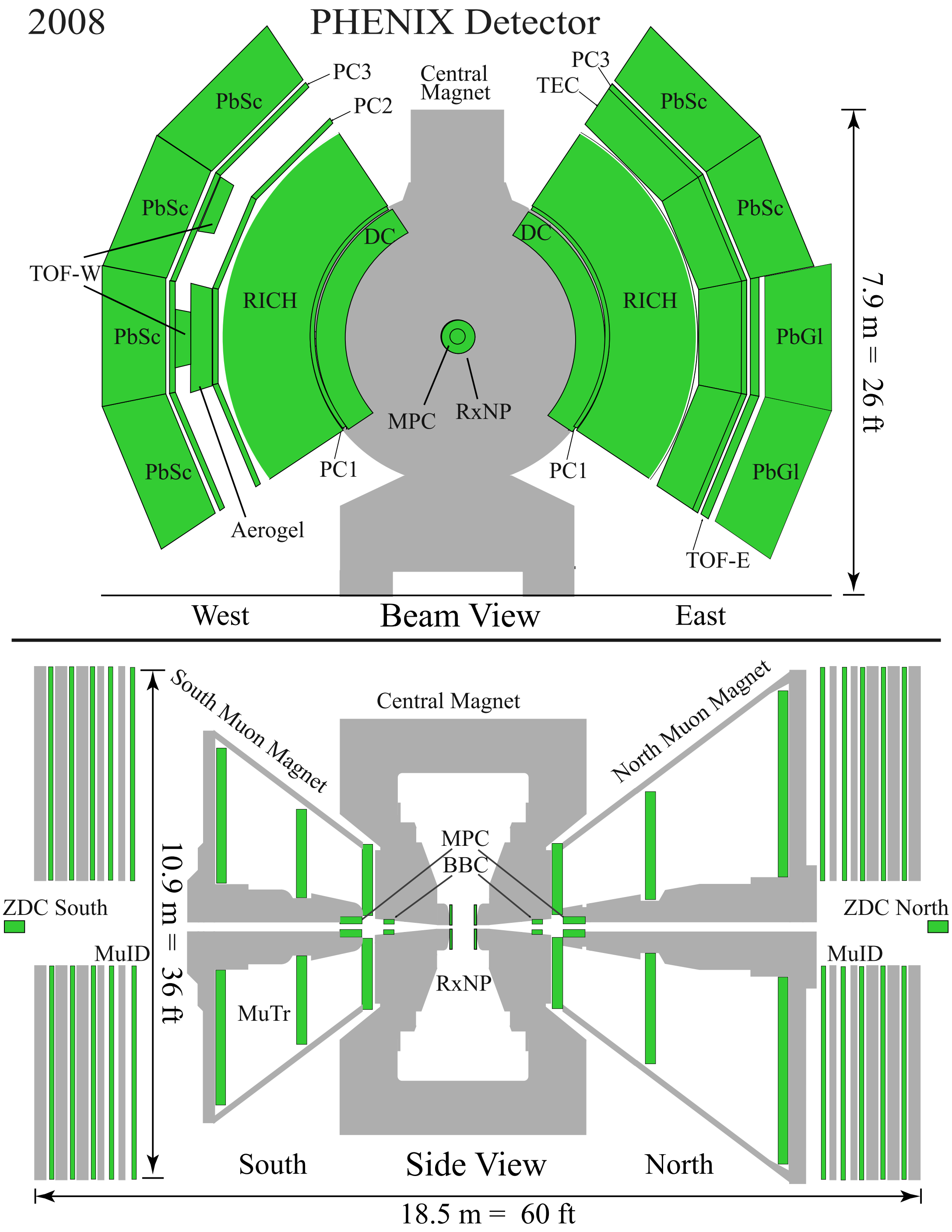

Figure 2.2: The PHENIX detector layout in the 2008 run. The upper panel shows the beam view where the two central arms and central magnet can be seen. The lower panel shows the side view where the two muon arms and the two muon magnets can be seen.

the interaction region. Underlying this high granularity, strong particle identification detector, is a Data-Acquisition System (DAQ) capable of sampling data at the highest rates delivered by RHIC. A summary of the various PHENIX central arm subsystems along with their purpose is presented in Table 2.2.

Subsystem	$\Delta\eta$	$\Delta\phi$	Specifications
Magnet: central	±0.35	360°	Upto 1.15T· m
Beam-beam counters (BBC)	± 3.1 to 3.9	360°	Start timing, fast vertex
Zero-degree Calorimeter (ZDC)	±2 mrad	360°	Minimum-bias trigger
Drift Chambers (DC)	±0.35	2×90°	Good momentum and mass resolution $\Delta m/m$ = 0.4% at m = 1GeV
Pad Chambers (PC)	±0.35	2×90°	Pattern recognition tracking in non-bend direction
TEC	±0.35	90°	Pattern recognition, dE/dx
Ring-Imaging $\hat{C}$erenkov Detector (RICH)	±0.35	2×90°	Electron identification
Time-of-flight (TOF)	±0.35	45°	hadron ID,$\sigma <$ 100 ps
PbSc EMCal	±0.35	90°+ 45°	Electron/Photon ID
PbGl EMCal	±0.35	45°	Good $e^{\pm}/\pi^{\pm}$ separation at $p >$ 1 GeV/c by EM shower and p <0.35 GeV/c by TOF. $K^{\pm}/\pi^{\pm}$ separation up to 2.4GeV/c by TOF

Table 2.2: Summary of the PHENIX central arm subsystems.

PHENIX Coordinate System and Acceptance The global coordinate system used in PHENIX is shown in Fig. 2.3. It is defined relative to the beam axis with the origin located at the center of the interaction region (IR). For both cartesian and cylindrical coordinate systems, the beam line defines the z axis with the positive direction pointing to the North. The y axis points upwards and the x axis points horizontally to the west arm, so that we have a right handed coordinate system. Cylindrical coordinates (θ, ϕ, z) are often used, where the polar angle θ is defined relative to the beam axis z, such that $\theta = 90^{\circ}$ is perpedicular to it and the azimuthal angle ϕ is 0 at the x axis (west).

Fig. 2.4 shows the PHENIX acceptance in terms of pseudo-rapidity η and ϕ. The muon arms cover the full azimuthal range at forward rapidity. Each one of the two central

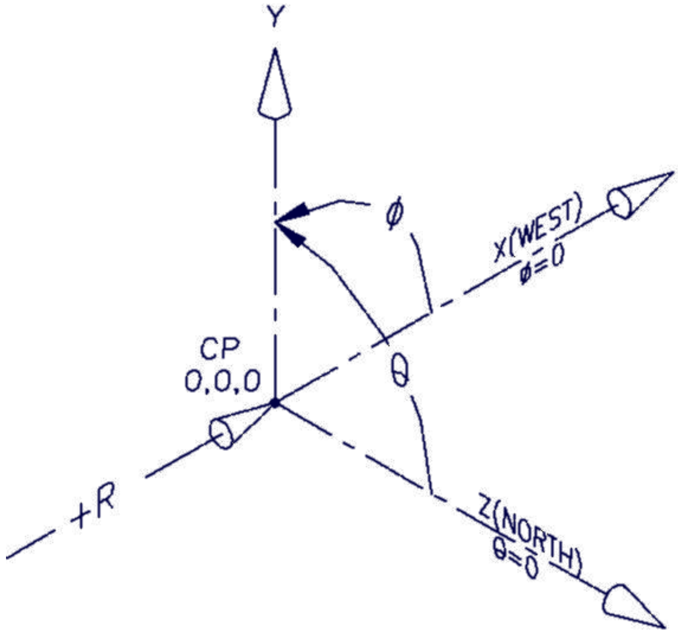

Figure 2.3: PHENIX global coordinate system.

arms covers the pseudo-rapidity range, $|\eta| < 0.35$ ($70^\circ < \theta < 110^\circ$), with 90° in ϕ, and are offset from each other by 67.5°.

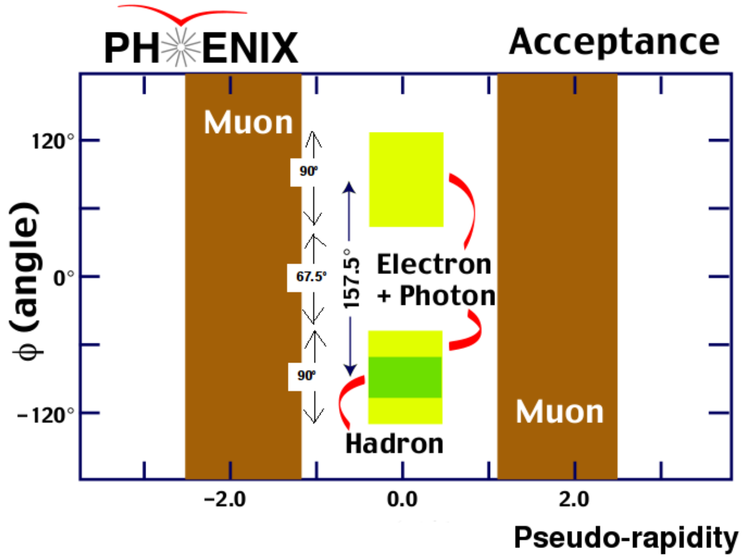

Figure 2.4: PHENIX acceptance for identified electrons, muons, photons and hadrons.

2.2.1 Trigger and Event Characterization Detectors

In PHENIX, the tasks to define the start time of a collision, provide the trigger for a collision and measure the vertex position along the beam axis are accomplished by two subsystems: the Beam Beam Counters and the Zero Degree Calorimeters.

2.2.1.1 Beam Beam Counters

The BBC [109, 110] consist of two sets (North and South) of Čerenkov arrays that measure relativistic charged particles in a narrow cone around the beam axis ($3.0 \leq |\eta| \leq 3.9$, 2π in ϕ). Each BBC counter is positioned around the beam axis at 1.44 m from the nominal $z = 0$ interaction point and has an inner radius of 5 cm and an outer radius of 30 cm. Each BBC counter is made up of 64 photomultiplier tubes equipped with quartz Čerenkov radiators in front. The BBC is designed to operate under various collision species (dynamic range 1-30 minimum ionizing particles), high radiation and large magnetic field (0.3T).

With an intrinsic time resolution of σ_t = 50 ps, the BBC provides a high precision measurement of the collision time and the vertex position. For each collision, the BBC measures the time of the collision with respect to the RHIC collider clock (synchronized with beam bunches). This time is referred to as the BBC $t - zero$ and is determined by taking the time difference between the North and South BBCs. Thus if t_N^{BBC} and t_S^{BBC} represent the average hit time over the individual PMTs of the North and South detector, then the vertex position in z (z_{vtx}^{BBC}) and the start time (t_0^{BBC}) of the collision are given by:

$$t_0^{BBC} = \frac{t_N^{BBC} + t_S^{BBC}}{2} - \frac{L}{c} \tag{2.1}$$

$$z_{vtx}^{BBC} = c \times \frac{t_N^{BBC} - t_S^{BBC}}{2} \tag{2.2}$$

where c is the speed of light and L is the distance to the BBC (1.44 m). The $z-$ vertex resolution of the BBC varies with the collision species. It is 1.2 cm for $p+p$ and 0.3 cm for central $Au+Au$ collisions due to the larger charge detected in the latter case, which yields a better time resolution.

A coincidence of the two BBCs and a vertex position along the beam axis within $|z| <$ 30 cm constitute the Minimum Bias Level-1 trigger requirement (see Section 2.2.6).

2.2.1.2 Zero Degree Calorimeter

The ZDCs [111, 112] are unique in the sense that they are common to all four RHIC experiments. The main purpose of the ZDC is to provide event characteristics such as collision centrality and vertex position, and monitor the beam luminosity. The ZDC measures the total energy of the forward neutrons unbound by Coulomb excitation or evaporated from unstable spectators, produced in the interaction between two colliding nuclei.

The ZDCs are sampling type hadron calorimeters which are located at 18 m from the interaction point, just behind beam bending magnets, such that charged particles will be deflected out of the acceptance before they can hit the ZDC. The total energy deposited by spectator neutrons is anti-correlated with the total charge deposited in the BBC and is used together with the BBC charge to determine the centrality of the collision. In $Au+Au$ collisions, the ZDC is an important part of the Minimum Bias trigger and of the centrality determination, but in $p+p$ and $d+Au$ collisions studied in this thesis, the ZDC is not used in the centrality determination due to the lack of spectator neutrons (see Section 2.2.7).

2.2.2 PHENIX Magnets

The PHENIX magnet system [113] comprises the Central Magnet (CM) and the North and South muon magnets (MMN and MMS). The CM is energized by two pairs of concentric coils (inner and outer) that provide an axially symmetric field parallel to the beam and around the beam axis. They cover the polar angle range of $70^\circ < \theta < 110^\circ$, that corresponds to a pseudo-rapidity range of $|\eta| < 0.35$.

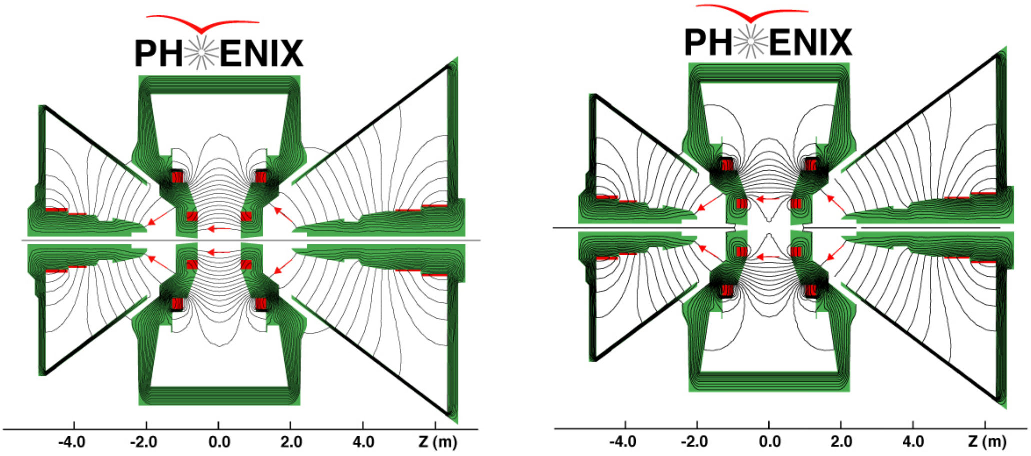

(a)

(b)

Figure 2.5: Magnetic field lines in the PHENIX detector, for the two central magnet coils operated in the $++$ (left) and $+-$ (right) mode.

Charged particles are bent in the plane perpendicular to the beam axis. The bending angles are accurately measured by the drift chambers (Section 2.2.3) and are used to

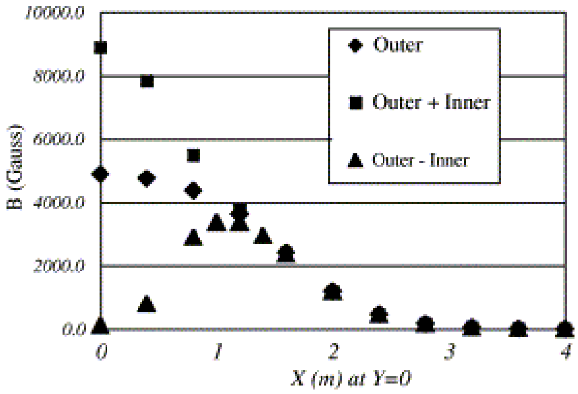

Figure 2.6: PHENIX magnetic field values

determine the particle momentum. The inner and outer coils can be run with the fields in adding (the "$++$" or "$--$" configuration) or bucking ("+-" configuration) mode. Fig. 2.5 shows the CM and MM field lines for the two field configurations. For the "$++(--)$" field configuration, both coils have their fields pointing to the negative (positive) z-axis. At the center close to the beam axis, the field lines uniformly point along the beam direction. However, the residual field at the DC distance of $\sim$ 2 m is highly non-uniform and has a significant r component at large z.

In the "$+-$" field configuration, the currents in the inner and outer coils go in opposite directions, resulting in an almost field free region up to a radial distance of $\approx 50-60$ cm around the interaction region. This zero-field region is essential for the Hadron Blind Detector (Section 5.2) operation. Fig. 2.6 shows the total strength of the CM as a function of R at $z=0$ for the "$++$", "$+$" and "$+-$" configurations. The field integrals at $z\sim 0$ are 1.04, 0.78 and 0.43 [Tm] in "$++$", "$+$" and "$+-$" configurations, respectively. For Run5 and the first half of Run8, the field configuration used was "$--$" and "$++$" respectively. In the second half of Run8, the field was switched to "$--$" configuration.

2.2.3 Charged Particle Tracking

There are two primary charged particle tracking subsystems in PHENIX; Drift Chambers and Pad Chambers. The DC along with PC1 form the inner tracking system, while PC2 and PC3 form the outer tracker.

2.2.3.1 The Drift Chambers

The PHENIX drift chamber [114] is a multiwire gaseous detector located at a radial distance of $2.02 < R < 2.48$ m. There is one chamber on each arm, and they are mirror copies of each other, each one subtending 90° in azimuth and 2 m along the z direction. The DC measures the trajectories of charged particles in the $r-\phi$ plane in order to determine their charge and transverse momentum p_T.

The active volume of the DC is filled with a mixture of 50% Argon and 50% Ethane. The mixture was chosen due to its good uniform drift velocity at an electric field of $E \sim 1$ kV/cm, high gain, and low diffusion coefficient. Each chamber volume is defined by a cylindrical titanium frame, divided into 20 identical keystones, each one covering 4.5° in ϕ. There are six types of wire modules in each keystone, called X1, U1, V1, X2, U2 and V2. The X1 and X2 wires are aligned parallel to the beam pipe to perform precise track measurements in the $r-\phi$ plane. The U and V stereo wires are oriented at $\approx \pm 6°$ angle relative to the X wires (see Fig. 2.7), and measure the z coordinate of the track. The magnitude of the stereo angle was chosen such that the z resolution would be comparable to that of the pad chambers. Each wire module contains, alternating in azimuth direction, four anode (sense) and four cathode planes. In addition to anode and cathode wires, each plane contains "gate" wires and "back" wires as shown in the left panel of Fig. 2.7. The latter shape the electrical field lines such that every sense wire is alternatively sensitive to

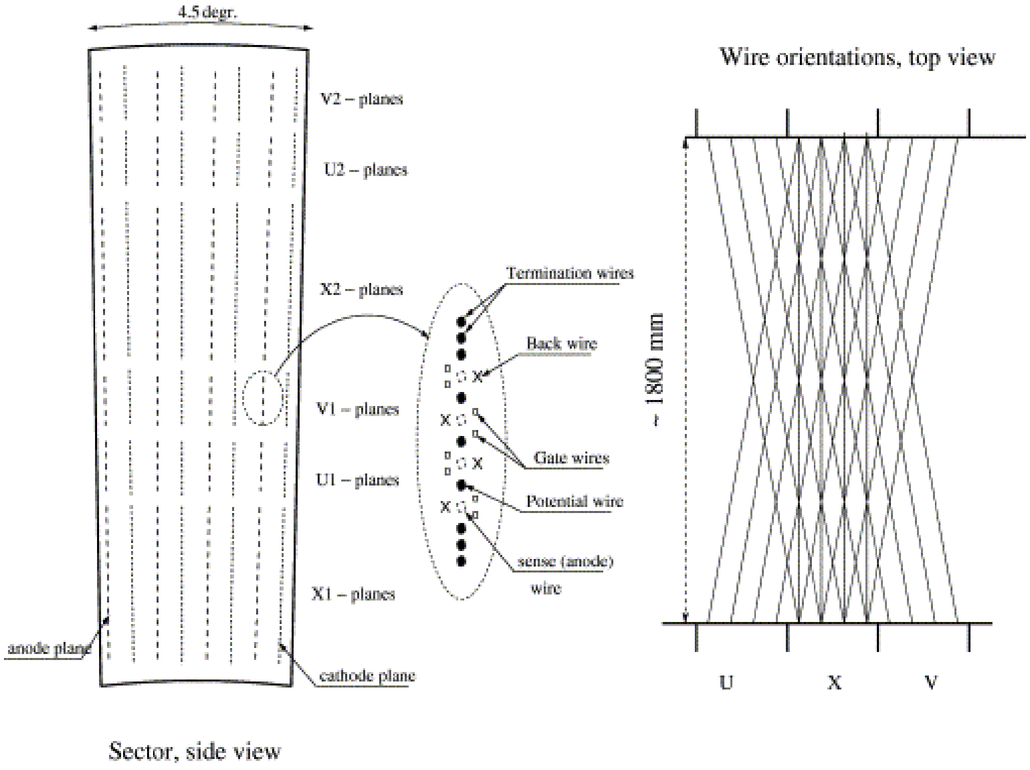

Figure 2.7: Left: Cut-away $r-\phi$ view of the wire layout within one keystone of the drift chamber. Right: The relative orientation of the U, V and X wire layers [115].

drift charges from only one side, therefore limiting the left-right ambiguity to a region of ±2 mm.

In order to allow for pattern recognition with up to 500 tracks, each sense wire is electrically insulated in the middle by a 100 μm thick kapton strip, effectively doubling the number of readout channels. In total the drift chamber contains 6500 wires and therefore 13000 readout channels.

2.2.3.2 The Pad Chambers

The PCs [116] consist of three layers of multiwire proportional chambers, with a cathode pad readout. They provide space points along the trajectory of charged particles to determine the polar angle θ, used to calculate the p_z component of the momentum vector.

PC1 is essential for the 3D momentum determination by providing the z-coordinate at the exit of the DC. The DC and PC1 information are combined to determine the straight line trajectories outside the magnetic field. PC2 and PC3 are needed to resolve ambiguities in the outer detectors where about 30% of the particles striking the EMCal are produced by either secondary interaction or decays outside the aperture of DC and PC1.

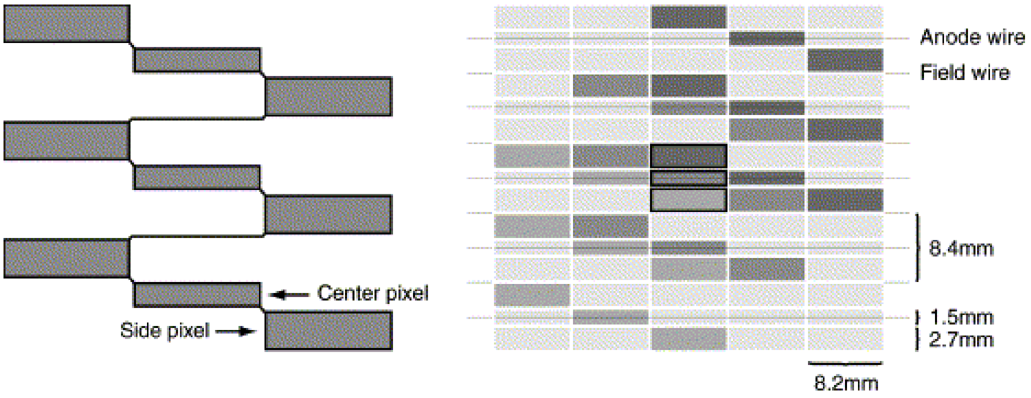

Figure 2.8: Left: The nine pixels forming one pad in the PC. Right: The interleaved pad design [115].

The first layer of pad chambers (PC1) is installed just behind the drift chambers, while the third layer (PC3) is situated right in front of the electromagnetic calorimeter. The second layer of pad chambers (PC2) is only present in the west arm following the RICH detector. Each PC contains a single layer of wires within a gas volume that is confined by two cathode planes located at ±6 mm from the wire plane. One cathode plane is solid copper, while the other one is segmented into a fine array of pixels as shown in Fig. 2.8. The basic unit is a pad formed by nine non-neighboring pixels connected together, which are read out by one common channel. One cell contains three adjacent pixels in the ϕ direction and an avalanche must be sensed by all three pixels to form a valid hit. The three pixels in a cell always belong to different, but neighboring channels and each cell corresponds to a unique channel triplet. This interleaved design scheme saves a factor of nine in readout channels while allowing a fine position resolution of 1.7 mm in the z direction in PC1.

2.2.3.3 Track Reconstruction

Fig. 2.9 sketches the path of a charged particle in the bending ($r - \phi$) plane (left) and in the $r - z$ plane, perpendicular to the bend plane (right). The coordinates measured with DC and PC1 and used to reconstruct the particle trajectory are defined as follows:

- ϕ: azimuthal angle of the intersection point of the track candidate with a "reference circle" located at a radius of 2.2 m, at the middle of the drift chamber.
- ϕ_0: track's azimuthal angle at the vertex.
- α: angle of the track candidate with respect to an infinite momentum (*i.e.* straight) track having the same intersection point with the reference circle in the $r - \phi$ plane. α is proportional to the inverse of the transverse momentum and its sign depends on the charge of the particle.
- zed: z coordinate of the track at the intersection point with the reference circle of the DC.
- β: inclination angle of the track with respect to the z-axis at the intersection point in the $r - z$ plane.
- δ: inclination of the track w.r.t. an infinite momentum track at the DC reference radius of 2.2 m in the $r - z$ plane.
- θ: polar angle of the infinite momentum track.
- θ_0: track's polar angle at the vertex.

The track finding algorithm assumes that all tracks in a given event originate at the vertex as determined by the BBC. The first stage of track finding utilizes a *combinatorial Hough transform* technique [117] in the $r - \phi$ plane. In this technique, the drift chamber hits in X1 and X2 are mapped pair-wise into a 2-dimensional space defined by the azimuthal angle ϕ and the track bending angle α. The basic assumption is that tracks are straight lines within the DC. In this case, all hit pairs of a given track will have the same ϕ and α, thus resulting in a local maximum in the mapped space. The reconstructed tracks are then associated with X1 and X2 hits. Only those tracks are considered as valid that have

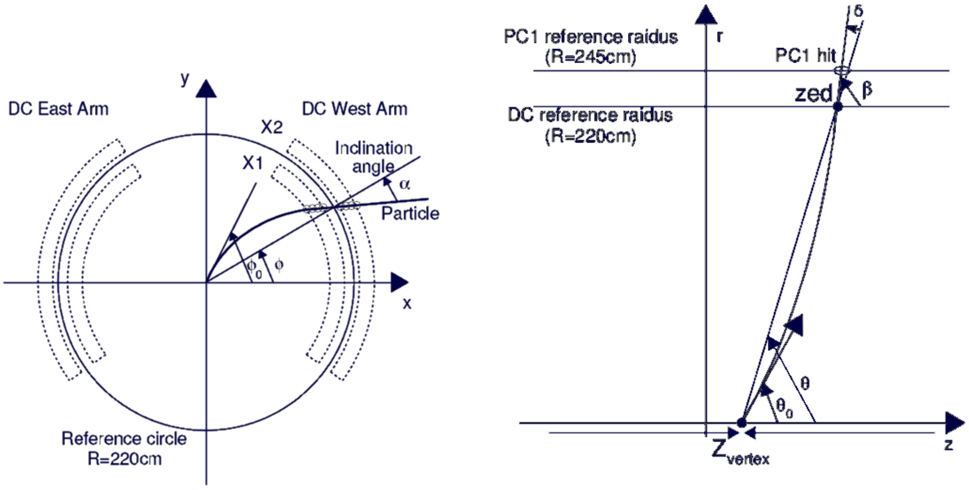

Figure 2.9: Left: Schematic view of a track in the DC $x - y$ $(r - \phi)$ plane. The X1 and X2 hits in the DC are shown as small circles. Right: Schematic view of a track in the DC $r - z$ plane. See text for the definition of the various angles.

at least 8 X1 and X2 hits associated to them. An iterative track fitting procedure is used to associate hits to tracks. The procedure assigns weights to hits in accordance with their deviation from the projected track guess. In the end, each hit is associated only to a single track. Once the track is reconstructed in the $r - \phi$ bend plane, the direction of the track is specified by ϕ and α.

Tracks are then reconstructed in the $r - z$ plane by combining the information of PC1 hits, UV wire hits and the collision vertex measured by the BBC. First the straight line track in the $r - \phi$ plane is extended to PC1. If there is an unambiguous PC1 hit association (within 2 cm distance between the track projection point and the PC1 hit position in the $r - \phi$ plane), the track vector in the non-bend plane is fixed by the PC1 hit z position and the z vertex measured by the BBCs. The intersection points at the UV wires of DC are calculated. If UV hits are within 5 cm from the track in the $r - z$ plane, the UV hits are associated [115].

Track Quality Each reconstructed track is assigned a *track quality* value, based on the hit information of the X and UV wires in the DC and the associated PC1 hit. This information is implemented in the data as a 6-bit variable called **track quality,** Q_{track} for each track and defined using the following binary pattern:

$$Q_{track} = A \times 2^0 + B \times 2^1 + C \times 2^2 + D \times 2^3 + E \times 2^4 + F \times 2^5 \qquad (2.3)$$

where A, B, C, D, E, F are quality bits defined as follows:

- A = 1 if the X1 plane is used.
- B = 1 if the X2 plane is used.
- C = 1 if there are hits in the UV plane.
- D = 1 if there are unique hits in the UV plane.
- E = 1 if there are hits in PC1.
- F = 1 if there are unique hits in PC1.

Otherwise the bits are set to 0. It is to be noted that A and B cannot be zero simultaneously due to the requirement of at least 8 hits in the X1, X2 planes for a real track as mentioned above. The resulting set of patterns is summarized in Table 2.3. The highest quality that a track can have is 63, *i.e.*, it is reconstructed based on hits in the X1 and X2 planes, with unique hit association in PC1 and UV. In the analysis, we used tracks with quality equal to 63 or 31 (*i.e.*, requiring hits in X1 and X2, a unique UV hit, and a unique or ambiguous PC1 hit) or 51 (*i.e.* demanding hits in X1 and X2, a unique PC1 hit, and no matching UV hit).

Comment	A	B	C	D	E	F	Quality, Q_{track}
$PC1^{found}_{unique}$ & UV^{found}_{unique}	1	0	1	1	1	1	61
	0	1	1	1	1	1	62
	1	1	1	1	1	1	63
$PC1^{found}_{unique}$ & no UV	1	0	0	0	1	1	49
	0	1	0	0	1	1	50
	1	1	0	0	1	1	51
$PC1^{found}_{ambiguous}$ & UV^{found}_{unique}	1	0	1	1	1	0	29
	0	1	1	1	1	0	30
	1	1	1	1	1	0	31
$PC1^{found}_{ambiguous}$ & UV^{found}	1	0	1	0	1	0	21
	0	1	1	0	1	0	22
	1	1	1	0	1	0	23
$PC1^{found}_{ambiguous}$ & no UV	1	0	0	0	1	0	17
	0	1	0	0	1	0	18
	1	1	0	0	1	0	19

Table 2.3: Summary of DC track quality

2.2.3.4 Momentum Determination

The deflection angle α is related to the magnetic field integral along the trajectory of a charged particle by:

$$\alpha \simeq \frac{K}{p_T} \tag{2.4}$$

and can therefore be used as a measurement of its transverse momentum p_T. However, the assumption that the field is zero at the DC is not a perfect one. For an accurate momentum measurement, one must use the full tracking model. Due to the complex PHENIX magnetic field, an analytic parameterization of the tracks is not possible. Therefore we use a non-linear grid interpolation technique [118] where the momentum of a charged particle is determined through a knowledge of the magnetic field and the intersection of its trajectory with a few planes of the tracking detectors. This grid provides the field integral $f(p,r,\theta_0,z)$ as a function of the total track momentum (p), the radius (r) from the beam axis, the theta angle (θ_0) of the track and the position z of the collision vertex. The grid is generated by propagating particles through the measured magnetic field map and numerically integrating f for each grid point.

The field integral $f(p,r,\theta_0,z)$ varies linearly with the ϕ angle at a given radius r, since this is just the momentum kick given by $\int Bdl$ *i.e.*,

$$\phi = \phi_0 + q\frac{f(p,r,\theta_0,z)}{p} \tag{2.5}$$

An iterative procedure is used to find the true momentum, starting with an initial estimate of the momentum obtained from the reconstructed angle α, and the measured polar angle θ from the PC1/DC match. For each hit associated to the track, the field integral $f(p,r,\theta_0,z)$ value is extracted from the grid. A fit in ϕ *vs* f is performed to extract the quantities ϕ_0 and q/p for every track and the extracted values are then fed back into the Eq. 2.5. The extracted p and ϕ_0 values converge usually in less than four iterations. A similar procedure is used in the $z - r$ plane to find the value of the θ_0 angle.

The momentum resolution for reconstructed charged particles with momentum above 200 MeV/c is

$$\frac{\sigma_p}{p} = 0.7\% \oplus 1\% p \text{ (GeV/c)} \tag{2.6}$$

where the first term is due to multiple scattering ($\sigma_{m.s}$) and the second is due to the intrinsic DC resolution (σ_{DC}).

2.2.4 Electron Identification

PHENIX is equipped with two primary detectors for electron identification: a ring imaging Čerenkov detector and an electromagnetic calorimeter.

2.2.4.1 Ring Imaging Čerenkov Detector

Each of the two central arms contains a RICH detector [119, 120], that serves as the primary device for electron identification in PHENIX. It is a threshold gas Čerenkov detector that provides an e/π rejection better than one part in 10^3 at momenta below 4.87 GeV/c. In addition to that, RICH is part of the PHENIX Level-1 electron trigger that enables to collect the rare electron and di-electron events in $p+p$ and $d+Au$ collisions.

Each RICH detector has a gas volume of 40 m^3, an entrance window with an area of 8.9 m^2, and an exit window with an area of 21.6 m^2. The radiator gas is CO_2, which has a refractive index n= 1.00410 at 20°C and 1 atm [121]. This corresponds to a threshold velocity β_t = $1/n$ = 0.99590168 and a γ - factor of γ_t=$1/\sqrt{1-\beta^2}$ = 34.932, resulting in a Čerenkov threshold of $p_T = m\gamma\beta$ = 18 MeV/c for electrons ($m_e = 0.511$ MeV/c^2) and 4.87 GeV/c for charged pions ($m_\pi = 139.57$ MeV/c^2). The RICH is used for pion identification above $p_T > 4.8$ GeV/c.

The Čerenkov light is focussed by two intersecting spherical mirrors with a total area of 20 m^2 onto two arrays of 1280 photo-multiplier tubes (PMT), located on either side of the entrance window. The PMTs are equipped with 2 inch diameter Winston cones and have magnetic shields that allow them to operate in a magnetic field of up to 0.01T. In total, the RICH detector has 5120 PMTs ($2arms \times 2sides \times 16\ in\ \theta \times 80\ in\ \phi$). An average of 10 photons per $\beta \approx 1$ particle are emitted under the angle $\theta_C(1/(n\beta) \approx 9$ mrad and get focussed to a ring on the PMT array with a diameter of about 11.8 cm.

2.2.4.2 Electromagnetic Calorimeter

The EMCal [122] in PHENIX is used to measure the spatial position and energy of electrons and photons. It is also used in the electron trigger and provides a trigger on rare events with high momentum photons. The PHENIX EMCal actually consists of two subsystems with different technologies. The first one is a sampling calorimeter with a shashlik design [123], consisting of 15552 lead-scintillator (PbSc) towers that cover 3/4 of the central arm acceptance. The other quarter is covered by a homogeneous detector of 9216 lead-glass (PbGl) Čerenkov calorimeters, which were previously used in the CERN experiment WA98 at the SPS.

Each PbSc tower has a cross-section of 5.25 cm × 5.25 cm and a length of 37.0 cm (18 X_0) and contains 66 sampling cells made of alternating tiles of Pb and scintillator. These cells are connected by penetrating optical fibers doped with wavelength shifters for light collection. The light is read out by phototubes (FEU115) at the back of the towers. Four optically isolated towers are mechanically grouped together into a single structural identity called a module. The modules are grouped together in 36, as an array of 12×12 towers called a supermodule (SM). Then 18 of these supermodules (in a 3×6 grid) are joined together to form a sector. There are 6 PbSc sectors, 4 in west and 2 in east arm. The energy resolution of the PbSc calorimeter obtained from tests using an electron beam is

$$\frac{\sigma_E}{E} = \frac{8.1\%}{\sqrt{E(\mathrm{GeV})}} \oplus 2.1\%^1 \tag{2.7}$$

and the measured position resolution is

$$\sigma_x(E) = \frac{5.9(\mathrm{mm})}{\sqrt{E(\mathrm{GeV})}} \oplus 1.4(\mathrm{mm}) \tag{2.8}$$

The PbSc calorimeter has an excellent time resolution of $\sim$ 100 ps for electromagnetic, and $\sim$ 270 ps for hadronic, showers independent of energy well above a threshold of about 10 MeV.

The PbGl is a Čerenkov calorimeter with 1.648 index of refraction. It consists of an array of thick optical glass towers embedded with 51% Pb-Oxide. Each PbGl tower has a cross-section of 4.0 cm × 4.0 cm and is 40 cm long (14.3 X_0). The towers are grouped in 6×4 to form modules, which in turn are grouped into 192 supermodules as an array of 16×12 towers. At the back of the towers, PMT's (FEU84) are used for readout. The energy resolution of the PbGl calorimeter as obtained from electron beam tests is

$$\frac{\sigma_E}{E} = \frac{5.9\%}{\sqrt{E(\mathrm{GeV})}} \oplus 0.76\% \tag{2.9}$$

and the measured position resolution is

$$\sigma_x(E) = \frac{8.4(\mathrm{mm})}{\sqrt{E(\mathrm{GeV})}} \oplus 0.2(\mathrm{mm}) \tag{2.10}$$

The intrinsic time resolution is better than 300 ps for electromagnetic showers above the minimum ionizing peak energy.

With a thickness of 18 X_0 in the PbSc and 14.3 X_0 in the PbGl, electrons and photons deposit their entire energy within the calorimeter as electromagnetic shower of subsequent Bremsstrahlung and e^+e^- pair creation. In contrast, hadrons loose energy primarily

---

[1] where $\oplus$ *is defined as* $\alpha \oplus \beta = \sqrt{\alpha^2 + \beta^2}$

through ionization and atomic excitations. The nuclear interaction length, λ_I of PbSc and PbGl is 0.5 and 1.05 respectively, and thus only few hadrons interact strongly and deposit a significant fraction of their energy. Thus by requiring the particle energy to match the measured momentum ($E/p \approx 1$), one can reduce significantly the hadronic background and extract a clean sample of electrons.

2.2.5 Data Acquisition System

PHENIX has implemented an advanced design of Data Acquisition System (DAQ) [124], that can handle the high interaction rates of approximately 500 kHz in $p+p$ collisions ($\sim$ 60 kbytes event size) and the large event sizes ($\sim$ 200 kbytes) of the high multiplicity $Au+Au$ events at an interaction rate of $\sim$ 10 kHz. With data archiving rates of over 400 MB/s and high level triggers (see Section 2.2.6.2), the DAQ is able to handle these high interaction rates and event sizes with the provision to accommodate future improvements in the luminosity. These high rates are achieved using a parallel, pipelined and buffered readout. That is, each component of the DAQ is required to be able to take data, process it, and send it out, with all these processes occurring in parallel. The PHENIX DAQ is nearly free of deadtime, until the input rate is higher than the maximum data-taking rate. The typical data recording rates of $p+p$ and $d+Au$ were 5 kHz and 7 kHz respectively, during Run5 and Run8. A block diagram of the data acquisition flow is shown in Fig. 2.10.

The data acquisition system employs the concept of granule and partition. A granule is the smallest unit, consisting of individual timing control and data collection for each subsystem. A partition is a combination of granules, that share the busy signals and accept signals. This configuration makes it possible to run the DAQ with the desired combination of detectors.

The overall control of the DAQ is provided by the Master Timing Module (MTM), the Granule Timing Module (GTM), and the Global Level-1 Trigger System (GL1). The MTM receives the 9.4 MHz RHIC clock and delivers it to the GTM and GL1. The GTM delivers the clock, the control commands (Mode Bits), and the event accept signal to the Front End Modules (FEMs) of each detector. The GTM is equipped with a fine tuning of the clock with $\sim$ 50 ps step, in order to compensate for the timing differences among the FEMs. The GL1 produces the first LVL1 trigger decision, combining LVL1 signals from various detector components.

The FEM of each detector converts the detector analog response into a digitized signal. The LVL1 trigger signals are simultaneously generated. The decision generation, whether an event should be taken or not, takes $\sim$ 30 bunch crossings. While the GL1 system is making the decision, the event data is stored in analog form in switched capacitor arrays

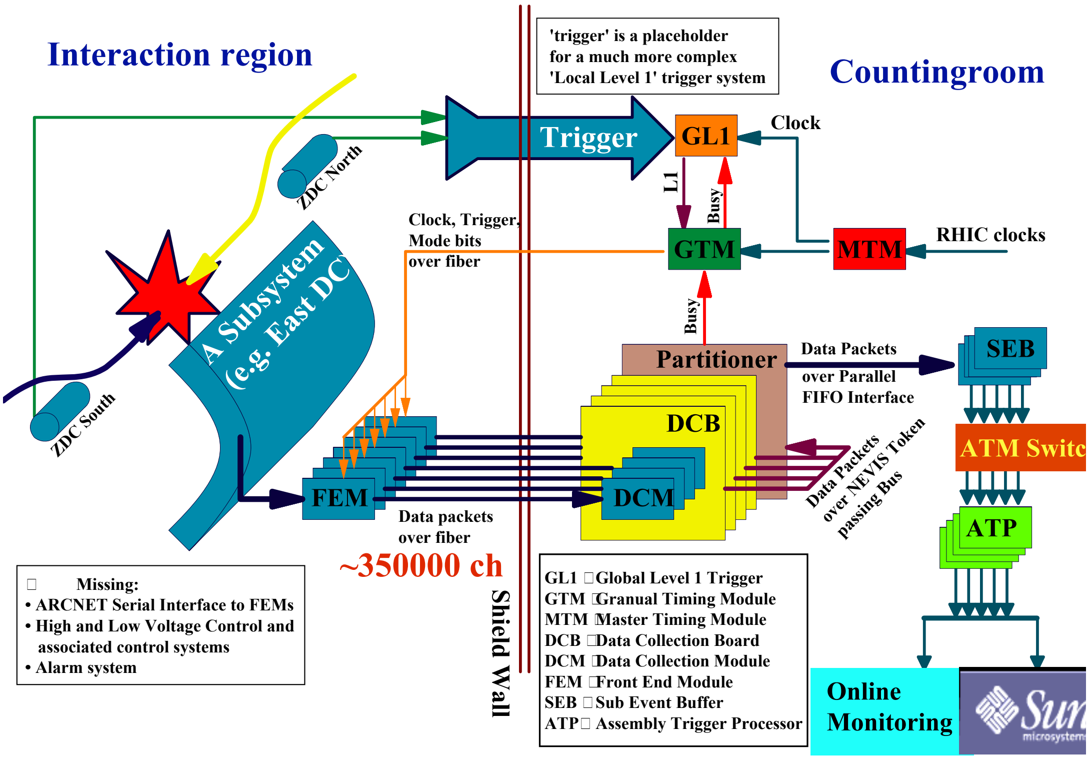

Figure 2.10: Schematics of the PHENIX DAQ

called Analog Memory Units (AMU). After receiving the accept signal, each FEM starts to digitize the data. The data collection from each FEM is performed by a Data Collection Module (DCM) connected to the FEM via an optical fiber cable. The DCMs provide data buffering, zero suppression, error checking and data formatting. The DCMs send the compressed data to the Event Builder (EvB).

The EvB consists of 39 Sub Event Buffers (SEBs), an Asynchronous Transfer Mode (ATM) switch and 52 Assembly Trigger Processors (ATPs). The SEBs are the front end of the EvB and communicate with each granule. The SEBs transfer the data from granule to the ATP via the ATM, where the event assembly is performed. The combined data are stored on disk with a maximum recording rate of 400 Mbytes/s and are used for online monitoring and for generation of the second level (LVL2) software trigger.

2.2.6 Event Trigger

The event rate is usually higher than the recording ability and so a triggering system is needed that can select potentially interesting events and provide sufficient rejection of uninteresting events to reduce the data rate to a level which can be handled by the PHENIX data acquisition system thus making best use of the available luminosity. PHENIX uses two levels of event triggering, referred to as Level 1 (LVL1) and Level 2 (LVL2). Only LVL1 trigger is discussed here since the current analysis uses only that.

The LVL1 trigger system consists of two components: Local Level-1 (LL1) and Global Level-1 (GL1). The LL1 communicates directly with the associated subsystem trigger detectors such as BBC, EMCal and RICH and processes the different trigger algorithms. The GL1 takes the LL1 information and generates a LVL1 *accept/reject* signal. When the LVL1 issues an *accept* decision, a “dead for X” beam crossings is imposed for trailing events, where X is some number of beam crossings. A second LVL1 accept cannot be issued during this period. The “Dead for X” has two important effects. First, it allows the tracking chambers to collect their signal completely, since some of them take more than one clock-tick to process the signal. Second, any “events” due to noise that may have durations of several clock ticks are avoided.

2.2.6.1 Minimum Bias Trigger

The *Minimum Bias* trigger in PHENIX is based on the response of the BBC and is referred to as BBCLL1. The collision vertex and the number of hits in the BBC photomultipliers are key variables for this trigger. For $p+p$ and $d+Au$ collisions, it requires a coincidence between the north and south sides of the BBC, with at least one hit on each side and accepts the events if the BBC vertex is within 38 cm of the nominal interaction vertex.

$$MB \equiv (BBC \geq 1) \cap (|z_{vertex}| < 38\ cm) \tag{2.11}$$

Eq. 2.11 clearly implies a dependence of the MB trigger on the event multiplicity, as a consequence of which the BBC accepts only part of the total cross-section. The BBC cross-section in $p+p$ collisions was determined via the Van Der Meer scan technique [125] and was found to be σ_{BBC}^{p+p} = 23.0 ± 2.2mb or 54.5 ±6% of the total inelastic $p+p$ cross-section at this center of mass energy (σ_{inel}^{p+p} = 42 ± 3 mb). For $d+Au$ collisions, our measured cross-section is σ_{BBC}^{d+Au} = 1.99 ± 0.10 b [126] using photodissocoation of the deuteron as a reference [127] and this corresponds to 88.5 ± 4% of the total $d+Au$ inelastic cross-section, σ_{inel}^{d+Au} = 2260 ± 100 mb.

It is obvious that events with a hard parton scattering are more likely to be registered because the track multipllicity in the BBC is higher for these events. On the other hand, soft partonic scattering or single- or double-diffractive scattering produce far fewer tracks in the BBC and are more likely to fail in generating a trigger. This means that of all the events that contain a hard scattering process, the fraction recorded will be higher than the "inclusive" BBC trigger cross section. This dependence of the trigger cross section upon the physics process is termed as "bias", and was determined using events with unbiased clock triggers[1] and containing charged hadrons in the central arm acceptance. Results showed that for these events, BBC fires on 79 ± 2 % (99 ± 2 %) of $p+p$ (minimum bias $d+Au$) events, independent of p_T and, as expected this fraction is higher than the inclusive BBC efficiency. For central $d+Au$ collisions, the event multiplicity is already high enough for the MB trigger not to be biased. Depending upon the centrality (see next Section 2.2.7), this fraction varies from 85% to 100% from peripheral to central $d+Au$ collisions.

To obtain the invariant yield of particles in $p+p$ and $d+Au$ collisions, we therefore correct the measured yield of particles for the fraction of events missed by the MB trigger and for the trigger bias. The correction factor is equal to 0.545/0.79 for $p+p$ and 0.88/0.99 for minimum bias $d+Au$ collisions.

2.2.6.2 EMCal RICH Trigger (ERT)

In order to increase the rate of events containing electrons, PHENIX uses a special Level-1 electronic trigger known as ERT (EMC-RICH) trigger. The acceptance covered by the EMCal and RICH detectors is divided into 16 trigger segments. Each segment consists of 9 (PbSc)/16 (PbGl) and 16 RICH trigger tiles. Each trigger tile consists of 144 EMCal towers (20 RICH phototubes).

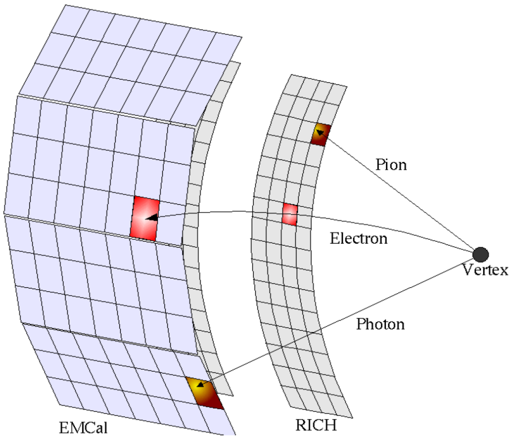

Figure 2.11: The principal scheme of the electron trigger.

The basic principle of the trigger is based on the online summing of the energy signals in a tile of 2×2 EMCal towers. If the sum exceeds a tunable threshold value, an ERTLL1_2x2 is issued and a hit in the corresponding RICH tile (4×5 PMT's) is required. The location of the RICH tile depends on the momentum of the trigger particle and is determined from a look-up table, assuming

---

[1] Clock trigger (or "Forced trigger") is a special trigger mechanism which forces a random event ($f_{Clock} = 1\ Hz$) to be stored at a certain bunch crossing as determined by RHIC, independent of Level 1 trigger decision.

that the trigger particle is an electron, *i.e.* its momentum is equal to the energy deposited within the 2×2 EMCal towers. After a spatial match between the EMC and RICH tiles is found, the trigger electronics issues the Local Level 1 (ERTLL1_E) trigger. The energy threshold of the ERT trigger can be adjusted by varying the threshold settings. For the $p+p$ run, E_{th} was set to 400 MeV, whereas in $d+Au$, E_{th} was set to 600 or 800 MeV. The efficiency of the ERT trigger is discussed in more details in Section 3.6.

2.2.7 Centrality Determination in $d+Au$

One of the parameters used to characterize a heavy-ion collision is the centrality, which is a measure of the *impact parameter (b) i.e.*, the distance between the centers of the two colliding nuclei, that determines the geometrical overlap between the nuclei. In general, the collision centrality can be defined from any experimental observable that is a monotonic function of the overlapping volume, which is then itself related to centrality, impact parameter, the number of participants and number of collisions.

For $d+Au$ collisions, PHENIX uses the charge measured in the BBC South, BBCS (*Au*- going side) as the observable for the centrality determination. We assume that the BBCS signal is proportional to the number of participating nucleons, N_{part}^{Au} in the *Au* nucleus and that the hits in the BBCS are uncorrelated to each other. The distribution of the mean number of participating nucleons N_{part}, as well as the mean number of binary collisions N_{coll} are determined using a Monte Carlo simulation of the Glauber model [128]. The Glauber model is based on a purely geometric picture of a heavy ion reaction. It assumes that the nucleons travel on straight-line trajectories and a collision between two nucleons takes place if their distance in the transverse plane is smaller than $\sqrt{\sigma_{NN}/\pi}$, where $\sigma_{NN} = 42$ mb, is the inelastic nucleon-nucleon cross-section at $\sqrt{s_{NN}} = 200$ GeV.

In these calculations, the deuteron nucleus is modeled using the wave function derived by Hulthen [129]

$$\phi_d(\mathbf{r}_{pn}) = \left(\frac{\alpha\beta(\alpha+\beta)}{2\pi(\alpha-\beta)^2}\right)^{\frac{1}{2}} \frac{(e^{-\alpha\mathbf{r}_{pn}} - e^{-\beta\mathbf{r}_{pn}})}{\mathbf{r}_{pn}}, \tag{2.12}$$

where $\alpha = 0.228\ fm^{-1}$; $\beta = 1.18\ fm^{-1}$; and $\mathbf{r}_{pn}$ refers to the separation between the proton and the neutron. The *Au* nucleus is modeled using a Woods-Saxon density distribution

$$\rho(r) = \frac{1}{1+e^{\left(\frac{r-c}{a}\right)}}, \tag{2.13}$$

where the diffuseness parameter a = 0.54 fm, c is the nuclear radius = $1.12A^{1/3}$ - $0.86A^{-1/3}$ = 6.40 fm.

	00%-20%	20%-40%	40%-60%	60-88%
$\langle N_{coll} \rangle$	15.1 ± 1.0	10.3 ± 0.7	6.6± 0.4	3.2 ± 0.2
$\langle N_{part} \rangle$	15.6 ± 0.9	11.1 ± 0.6	7.7± 0.4	4.2 ± 0.3
Trigger bias correction	0.94 ± 0.01	1.00 ± 0.006	1.03 ± 0.017	1.031 ± 0.055

Table 2.4: Mean number of binary collisions, participating nucleons from the *Au* nucleus, and trigger bias corrections for the $d+Au$ centrality bins.

Using the above parameters and taking into account the BBC efficiency, the response of the BBC can be simulated for different values of the impact parameter. The Glauber simulation results for N_{part} and N_{coll} corresponding to the centrality bins used in this analysis are summarized in the Table 2.4.

Fig. 2.12 shows the distribution of the normalized charge in BBCS and the classification into different centrality classes; 00%-20%, 20%-40%, 40%-60%, and 60-88%. The 88% upper limit comes from the fact discussed earlier, that BBCLL1 fires on 88% of the total inelastic $d+Au$ cross-section.

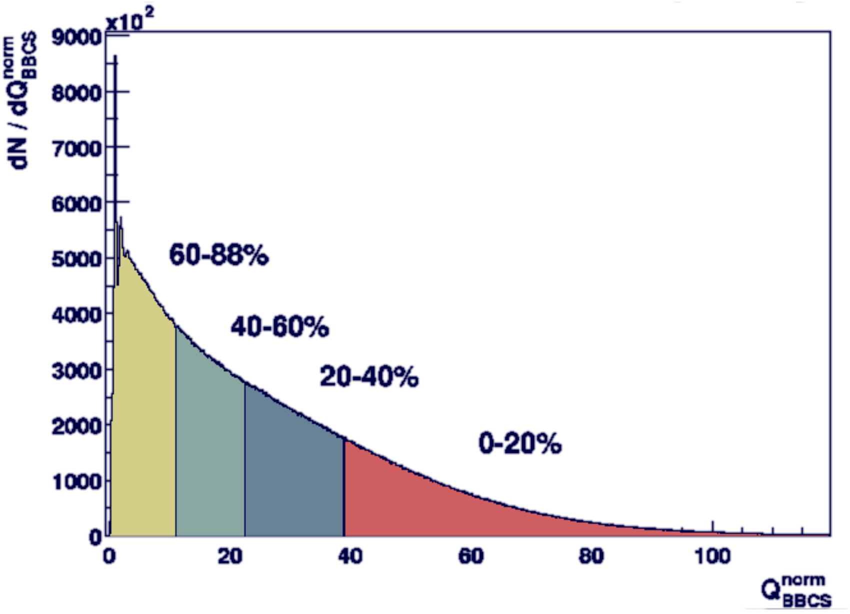

Figure 2.12: Distribution of the normalized charge in the BBC south (BBCS). The normalization is done such that the normalized charge corresponds to the number of hits.

However there are two effects that must be considered in $d+Au$ collisions. The first is the "*BBC trigger bias*" effect and as already discussed in Section 2.2.6.1, this effect is only important in the most peripheral $d+Au$ centrality bin. The second bias is an artifact of the way we categorize collisions into different centralities, using the BBCS distribution.

This second bias arises from the fact that events containing high-p_T hadrons from hard scatterings may have a larger multiplicity, and consequently they produce a larger signal in the BBCS. Such events would be considered more central compared to the ones without a hard scattering. This effect gives an opposite bias from the first trigger bias effect in the most peripheral bin as events can be shifted out of this bin but not into it. The corrections for both biases were studied using simulations and the Glauber model. The combined corrections for these effects range from 0% to 5% depending on the centrality category, and are summarized in the Table 2.4.

Chapter 3

Data Analysis

3.1 Analysis Overview

This chapter presents the details of the analysis performed in the present work for the measurement of ϕ- and ω-mesons, via their e^+e^- decay channel in $p+p$ and $d+Au$ collisions at $\sqrt{s_{NN}}$ = 200 GeV. The analysis is based on two data sets that correspond to two RHIC running periods - Run5 ($p+p$) and Run8 ($d+Au$) (see Table 2.1). The Run5 $p+p$ data was taken with a "$--$" field polarity and an ERT threshold, (E_{th}) of 400 MeV. The first half of the Run8 $d+Au$ data was taken with the "$++$" field configuration and E_{th} = 600 MeV, and the second half was taken with the "$--$" field configuration and E_{th} = 800 MeV. These two subsamples of Run8 were analyzed separately and the results were combined using a weighted average procedure described later in Section 3.10.

Both analysis follow mostly a similar procedure, so they are discussed in parallel, highlighting the differences where they exist.

In general, the analysis procedure can be divided into the following steps.

- Event selection that includes vertex determination and event trigger selection.
- Track selection and electron identification.
- Quality assurance studies.
- Single electron trigger efficiency determination.
- Pair analysis that involves estimating the background and signal extraction.
- Monte Carlo simulations to account for the acceptance, reconstruction and trigger effects.

The next sections describe in detail the steps highlighted above.

3.2 Data Sample and Event selection

This section presents an overview of the various data sets used in the analysis and the global event selection cuts.

Data Set Both $p+p$ and $d+Au$ analyses involve the use of two types of data samples: the first one is a *Minimum Bias* data set *i.e.* the events selected by requiring the minimum bias trigger (MB) condition only (Section 2.2.6), that serves as a reference sample. The second one is an *ERT* data set, that requires the ERT trigger to be fired (Section 2.2.6) in each event. Only events that are triggered in coincidence with the MB trigger (ERTLL1_E&BBCLL1) are considered in the analysis so that a cross-section for MB collisions can be extracted.

Due to the limited bandwidth of the data acquisition, usually only a fraction of all minimum bias events is recorded. This fraction is determined by a scale down factor, specified at the beginning of each run for each trigger and is subject to change depending on the beam conditions. These scale down factors are recorded in the database and need to be considered when determining the total luminosity recorded. The number of sampled minimum bias events corresponding to the ERT data set is calculated from the sample of minimum bias events as follows:

$$N_{MB}^{sampled} = \sum_{run} N_{MB}^{run} \cdot f_{scale\_down\_factor}^{run} \cdot N_{ERT}^{MB} / N_{MB}^{ERT} \tag{3.1}$$

where N_{MB}^{run} is the number of events recorded with the MB trigger in a particular run, with a scale down factor $f_{scale\_down\_factor}^{run}$. $N_{ERT}^{MB}/N_{MB}^{ERT}$ serves as a correction for those cases where during the data reconstruction, some file segment[1] of either the MB or ERT sample is lost. In such a case the number of ERT triggered events in the MB sample (N_{ERT}^{MB}) is not equal to the number of MB triggered events in the ERT sample (N_{MB}^{ERT}). This ratio is plotted as a function of run number for the $p+p$ analysis in Fig. 3.1(a) and as a 1D projection in Fig. 3.1(b). Runs that have a ratio > 2 or < 0.5 are rejected, while the other runs with a ratio not equal to one (5 runs), are corrected by this ratio. The total number of analyzed and sampled events is summarized in the Table 3.1.

Vertex Cut The collision vertex is determined by the BBC's on an event by event basis, as explained in Section 2.2.1.1. Due to the specific geometry of the PHENIX detector, events that have a collision vertex far from the center of the detector (z_{vtx} = 0 cm) have

---

[1] A Run is divided into segments of typically 100K events to keep the size of the output files low and allow parallel processing during the offline production

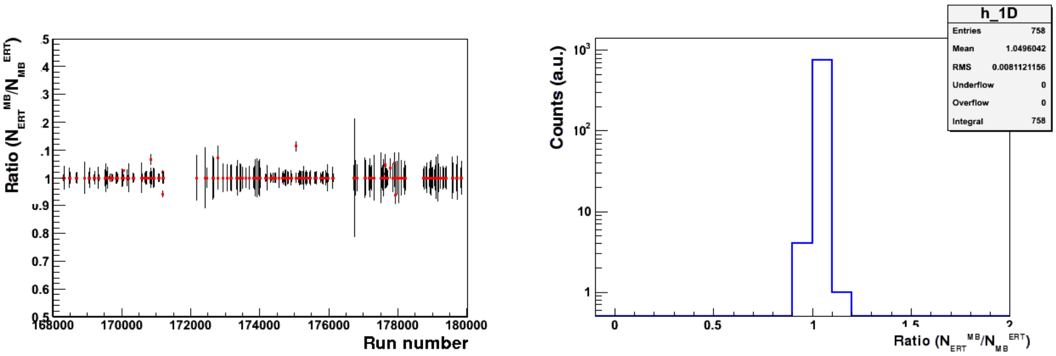

(a) $N^{MB}_{ERT}/N^{ERT}_{MB}$ as a function of run number

(b) $N^{MB}_{ERT}/N^{ERT}_{MB}$

Figure 3.1: Ratio of triggered events in the ERT and MB samples

Run	E^{ERT}_{th}	*analyzed ERT events*	*Sampled MB events*	*Field configuration*
$p+p$	400 MeV	261M	53.01B	$--$
$d+Au$	600 MeV	2.15B	52.6B	$++$
	800 MeV	1.48B	89.2B	$--$

Table 3.1: Analyzed ERT events and MB events in the various data samples.

a higher probability to interact with the material of the central magnet, thus creating an additional conversion electron background. The collision vertex distribution for $p+p$ collisions can be seen in Fig. 3.2 (left). One can see clearly that the vertex distribution is centered around z_{vtx} = 0 cm, and has a FWHM of $\approx$ 30 cm, but additional structures can be seen outside $-30 \leq z_{vtx} \leq 28$, when we require the event to have an electron (black line), as compared to the vertex distribution for all events (blue line). Fig. 3.2 (right) shows the number of e^+e^- per event as a function of the BBC vertex, that also shows the increase in the external conversion electrons at the edges.

Thus we apply an offline cut of $-30 \leq z_{vtx} \leq 28(30)$ cm for $p+p$ ($d+Au$) to avoid this additional conversion background.

3.3 Track Selection

Section 2.2.3.3 described in detail the track reconstruction using DC1 and PC1. This section describes the various track selection cuts using DC-PC1 and hit position information from the EMCal.

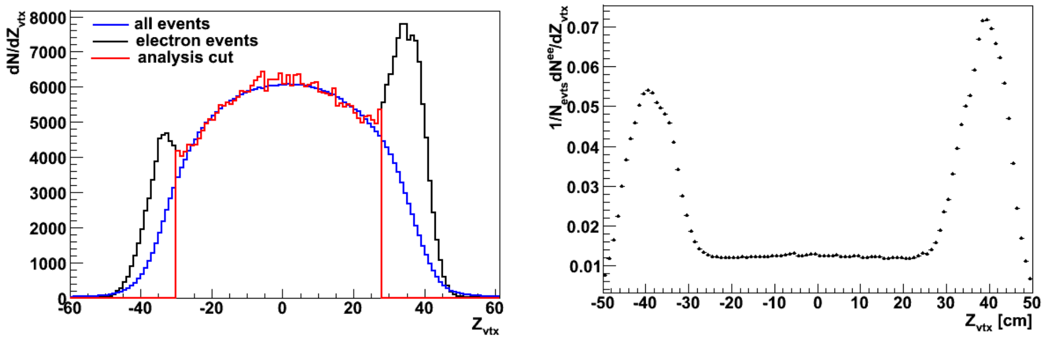

Figure 3.2: The left panel shows the vertex distribution for all events (blue), for events with at least one electron (black), and the offline vertex cut used (red). The right panel shows the number of $e^+ + e^-$ per ERT event as a function of vertex position for $p+p$ collisions.

3.3.1 Track Quality

In the $p+p$ analysis, we used all quality tracks[1] to preserve statistics, whereas for the $d+Au$, only tracks with quality equal to 63 or 31 or 51 were selected and these represent about 55% of the total number of tracks. The quality distributions for Run5 $p+p$ and Run8 $d+Au$ are shown in Fig. 3.3.

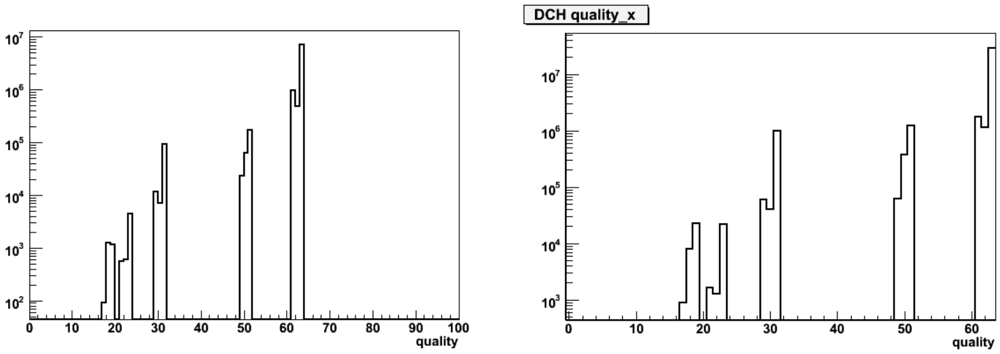

Figure 3.3: Track quality distributions in Run 5 (left) and Run 8 (right)

3.3.2 Track Matching to EMCal

The distance between the projection point of a reconstructed track to the surface of the EMCal and the closest hit position (the centroid of the electromagnetic shower[2]) is expressed by δ_ϕ in ϕ and δ_z in z- direction.

$$\delta_\phi = \phi_{projected} - \phi_{hit}; \qquad \delta_z = z_{projected} - z_{hit} \tag{3.2}$$

---

[1] refer Section 2.2.3.3 for track quality definition

[2] Details for the reconstruction of shower center with the EMCal can be seen in [115].

These variables are momentum dependent and, due to detector misalignment, not always centered at zero. They are more convenient to use, if expressed in terms of standard normal distributions, with mean at zero and sigma equal to one. These normalized variables, called as *emcsdphi_e* and *emcsdz_e*, are built in such a way so as not to have p_T, charge or EMCal sector dependence and thus provide an easier way to apply the cuts in units of sigma. The procedure to derive these variables is described below.

Derivation of *emcsdphi_e* In addition to momentum, sector and charge dependence, δ_ϕ also has a dependence on the z-position of the DC (zed). This is due to the existence of a z-dependent residual magnetic field after DC. Fig. 3.4 shows the δ_ϕ distribution as a function of zed for two momentum bins, ($0.3 \leq p_T < 0.32$ GeV/c (left)) and ($1.1 \leq p_T < 1.4$) GeV/c (right)), for electrons (top panels) and positrons (middle panels). A dependence of δ_ϕ on zed in opposite directions for electrons and positrons, which is more pronounced at low p_T, can be clearly seen. Below we describe the steps, to derive *emcsphi_e* for one given EMCal sector, which is then repeated for all the other EMCal sectors.

1. In the first step, we remove the zed dependence. For this, we accumulate 2-dimensional histograms of δ_ϕ and zed for various p_T bins, separately for electrons and positrons as shown in the top two panels of Fig. 3.4.
2. From these 2d histograms, the 1-dimensional δ_ϕ distributions are extracted for various zed bins, and are fitted with a Gaussian function to extract the centroid and sigma. An example of δ_ϕ distribution for one zed bin fitted to a Gaussian function is shown in Fig. 3.4-e.
3. We then fit the zed-dependent distributions of the extracted centroid and sigma for a given p_T bin using a polynome of 2^{nd} degree ($p_0(p_T) + p_1(p_T) \cdot zed + p_2(p_T) \cdot zed^2$). The black lines in the histograms in the top and middle panels of Fig. 3.4 show the fits to the centroids (represented by black points). An example of the fit to the sigmas is shown in the bottom right panel of Fig. 3.4.
4. The next step is to remove the p_T dependence. For this we fit the parameters p_0, p_1 and p_2 extracted in the previous step, to another function ($c_0 + c_1/p_T + c_2/p_T^2$). Examples of these fits are shown in Fig. 3.5, with the top panels showing the fits to the parameters describing the centroids, and the bottom panels showing the same for the sigmas.

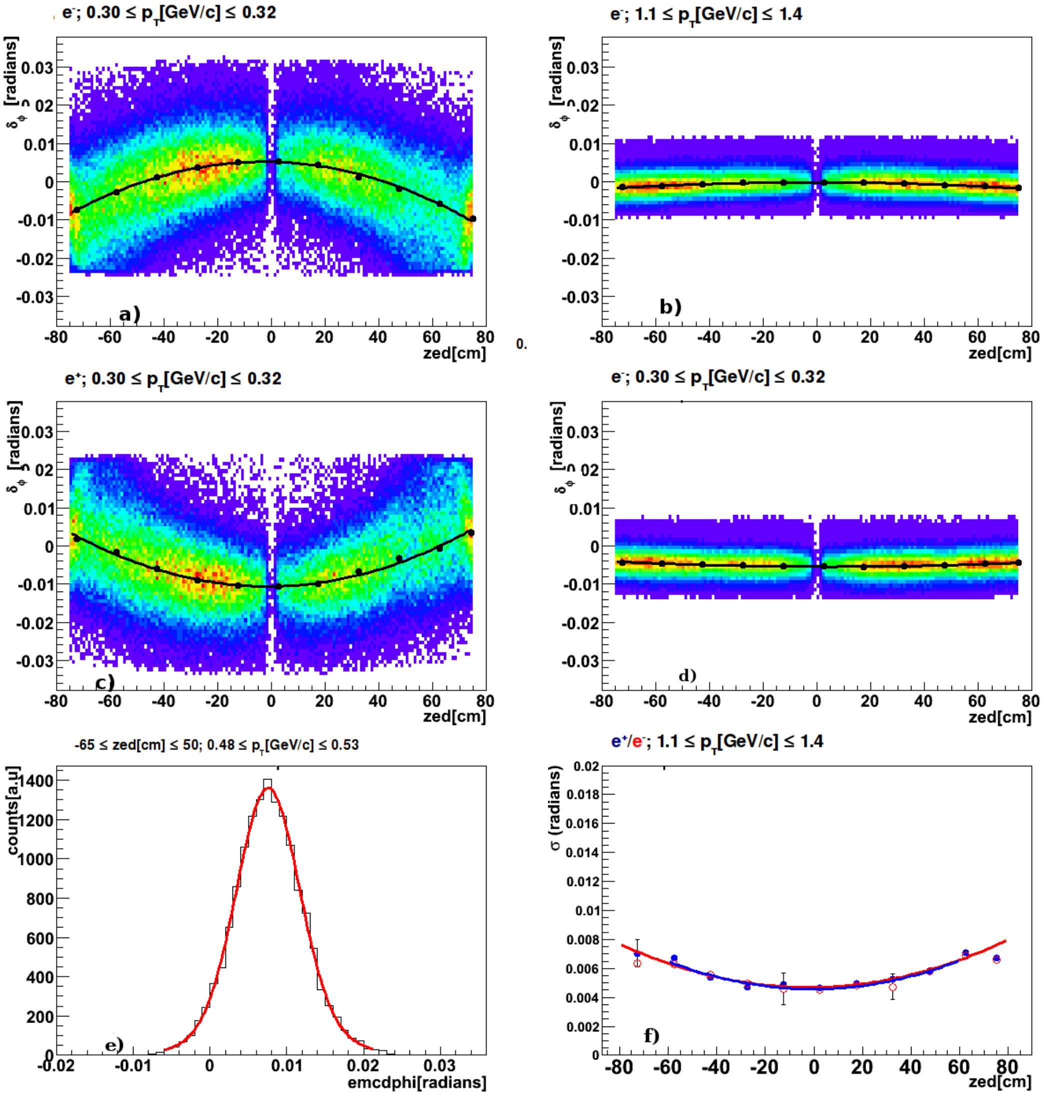

Figure 3.4: (a) and (b) show the δ_ϕ dependence on zed[cm] for electrons with $0.21 \leq p_T[GeV/c] < 0.22$ and $0.34 \leq p_T[GeV/c] < 0.37$ respectively, and (c) and (d) show the same for positrons. (e) shows the raw emcdphi distribution for $(0.48 \leq p_T[GeV/c] < 0.53)$ and $-65 \leq zed[cm] < 50$, fitted with a Gaussian function and (f) shows a fit to the zed-dependent extracted sigmas for one p_T bin. Blue and red points correspond to positrons and electrons.

The reduced variable *emcsdphi_e* is finally given by

$$\begin{aligned}
emcsdphi\_e &= \frac{\delta_\phi - \delta_{\phi 0}}{\sigma_\phi(p_T, zed)}; & (3.3)\\
where\ \ \delta_{\phi 0} &= p_0^{mean}(p_T) + p_1^{mean}(p_T)\cdot zed + p_2^{mean}(p_T)\cdot zed^2 & (3.4)\\
\sigma_\phi(zed, p_T) &= p_0^{\sigma}(p_T) + p_1^{\sigma}(p_T)\cdot zed + p_2^{\sigma}(p_T)\cdot zed^2; & (3.5)\\
with\ \ p_i^{mean}(p_T) &= c_0^i + c_1^i/p_T + c_2^i/p_T^2, i = 0,1,2; & (3.6)\\
and\ \ p_i^{\sigma}(p_T) &= c_0^{i\,\sigma} + c_1^{i\,\sigma}/p_T + c_2^{i\,\sigma}/p_T^2, i = 0,1,2; & (3.7)
\end{aligned}$$

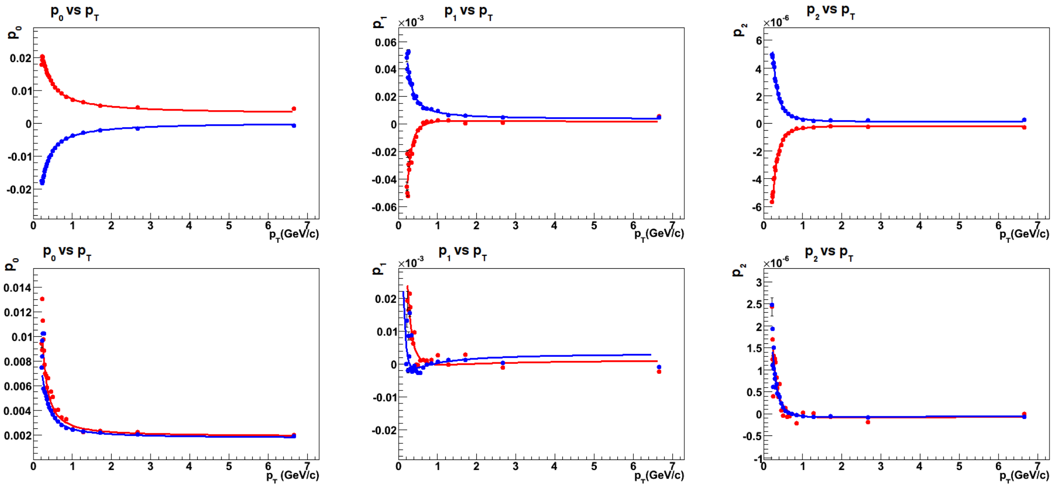

Figure 3.5: The top panels show the p_T dependence of the parameters p_0, p_1 and p_2 obtained from fitting the means of δ_ϕ vs zed, and the bottom panels show the same for the parameters obtained from fitting the extracted sigmas vs zed for the EMCal sector, $E1$. The lines are the fits to points (see text).

where Eq. 3.4 and Eq. 3.5 are the polynomial functions for a given zed bin described in step 3 and, Eq. 3.6 and Eq. 3.7 are the functions described in step 4.

Derivation of *emcsdz_e* To calculate *emcsdz_e*, we follow a similar procedure as for *emcsdphi_e*. Fig. 3.6 shows δ_z as a function of the track polar angle θ for two p_T bins, and for electrons and positrons separately. The extracted means of δ_z are fitted to the function $(p_0 + p_1 \cdot tan(\theta))$, whereas for the rest, the same functions as for δ_ϕ are used. The extracted fit parameters dependence on p_T for one EMCal sector is shown in Fig. 3.7. Mathematically, the *emcsdz_e* derivation can be expressed as follows:

$$emcsdz\_e = \frac{\delta_z - \delta_{z0}}{\sigma_z(p_T,\theta)}; \tag{3.8}$$

$$\delta_{z0} = p_0^{'mean}(p_T) + p_1^{'mean}(p_T) \cdot tan(\theta); \tag{3.9}$$

$$\sigma_z(p_T,\theta) = p_0^{'\sigma}(p_T) + p_1^{'\sigma}(p_T) \cdot \theta + p_2^{'\sigma}(p_T) \cdot \theta^2; \tag{3.10}$$

$$p_i^{'mean}(p_T) = c_0^{'i} + c_1^{'i}/p_T + c_2^{'i}/p_T^2, i = 0,1,2; \tag{3.11}$$

$$and \;\; p_i^{'\sigma}(p_T) = c_0^{'i\,\sigma} + c_1^{'i\,\sigma}/p_T + c_2^{'i\,\sigma}/p_T^2, i = 0,1,2; \tag{3.12}$$

Fig. 3.8 and Fig. 3.9 show the mean and sigma values of the reduced variables *emcsdphi_e* and *emcsdz_e* for the eight EMCal sectors, obtained after fitting the distributions to a Gaussian function. Blue and red symbols correspond to positrons and electrons. As expected the mean and sigma values are now p_T independent and centered around zero and one, respectively.

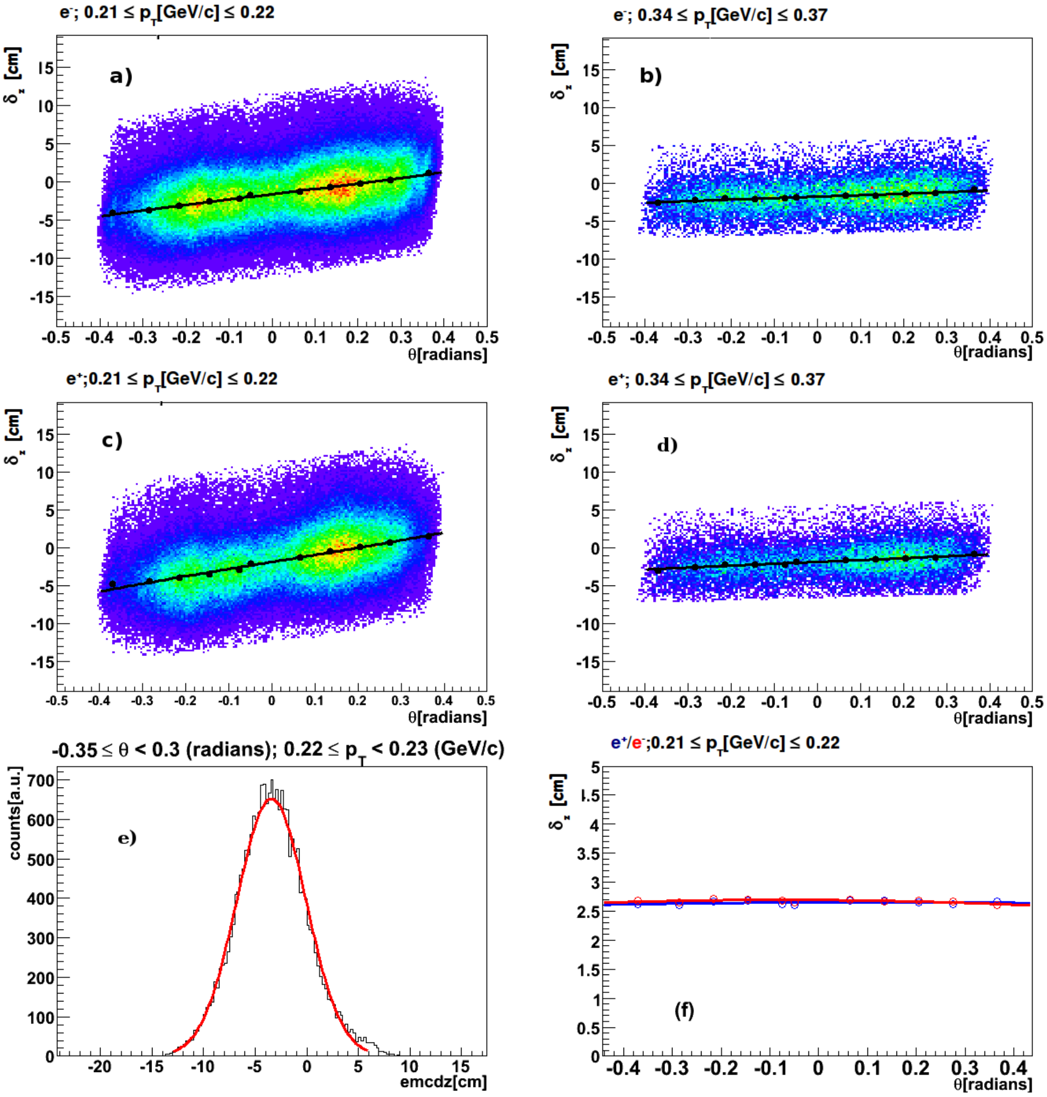

Figure 3.6: (a) and (b) show the δ_z dependence on the polar angle θ for electrons with $0.21 \leq p_T[GeV/c] < 0.22$ and $0.34 \leq p_T[GeV/c] < 0.37$ respectively and (c) and (d) show the same for positrons. (e) shows the raw emcdze distribution for electrons with $0.22 \leq p_T[GeV/c] < 0.23$) and $-0.35 \leq \theta[radians] < 0.3$, fitted with a Gaussian function, and (f) represents the θ dependence of δ_z for one p_T bin. Blue and red points represent positrons and electrons respectively.

For both the analyses, the reconstructed tracks were required to have a $\pm 3.5\ \sigma$ matching to the associated EMCal clusters.

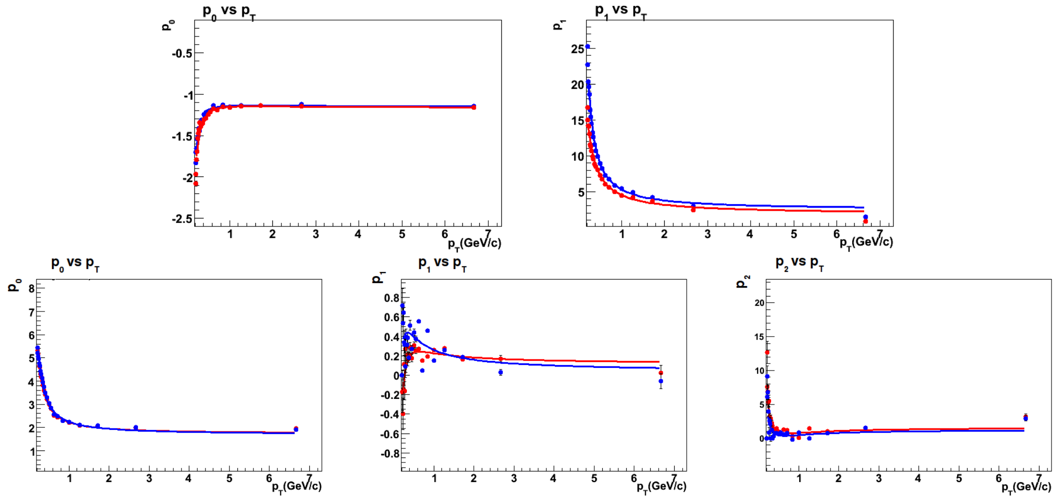

Figure 3.7: The top panels show the p_T dependence of the parameters p_0 and p_1, obtained from the fits of the δ_z centroids vs θ, and the bottom panel shows the same for the parameters corresponding to sigmas.

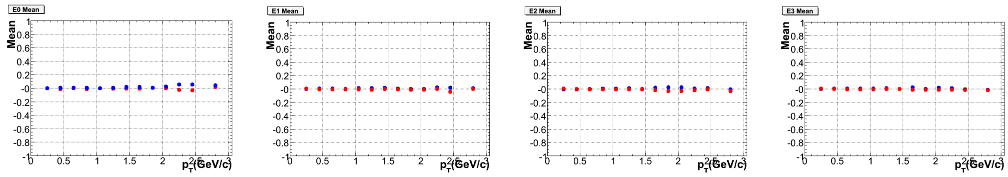

(a) E0 φ-mean (b) E1 φ-mean (c) E2 φ-mean (d) E3 φ-mean

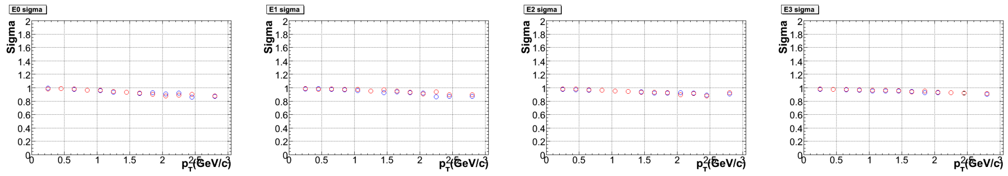

(e) E0 φ-sigma (f) E1 φ-sigma (g) E2 φ-sigma (h) E3 φ-sigma

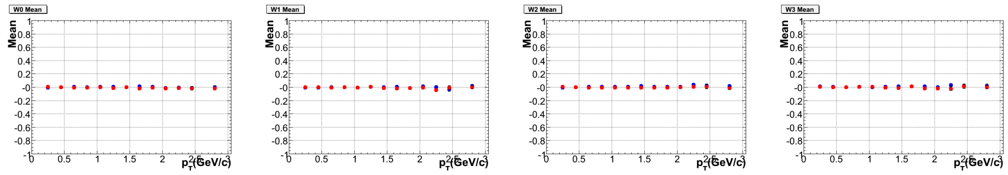

(i) W0 φ-mean (j) W1 φ-mean (k) W2 φ-mean (l) W3 φ-mean

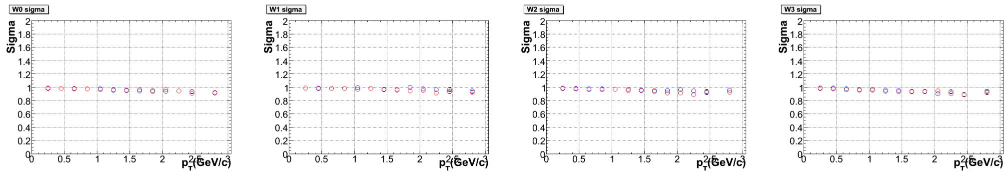

(m) W0 φ-sigma (n) W1 φ-sigma (o) W2 φ-sigma (p) W3 φ-sigma

Figure 3.8: Mean and sigma values of the track matching to the eight sectors of the EMCal along the φ coordinate as a function of p_T.

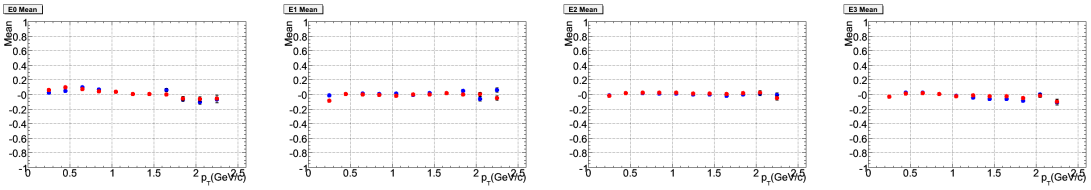

(a) E0 z-mean (b) E1 z-mean (c) E2 z-mean (d) E3 z-mean

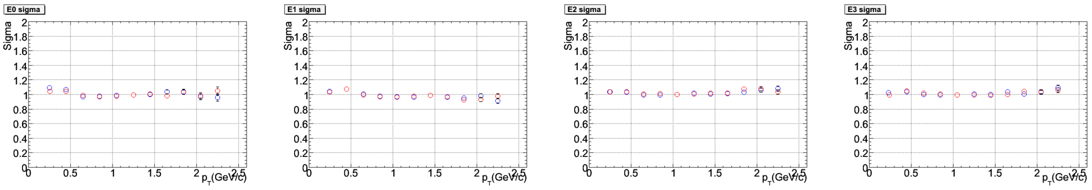

(e) E0 z-sigma (f) E1 z-sigma (g) E2 z-sigma (h) E3 z-sigma

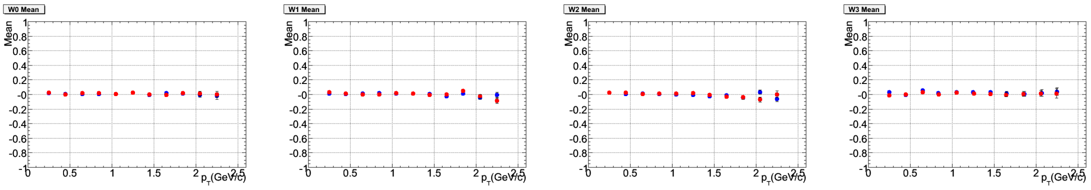

(i) W0 z-mean (j) W1 z-mean (k) W2 z-mean (l) W3 z-mean

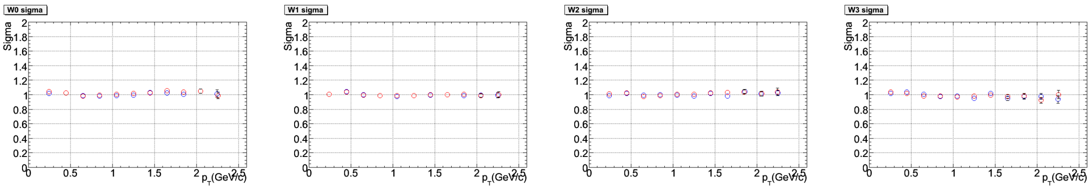

(m) W0 z-sigma (n) W1 z-sigma (o) W2 z-sigma (p) W3 z-sigma

Figure 3.9: Mean and sigma values of the track matching to the eight sectors of the EMCal along the z coordinate as a function of p_T.

3.4 Electron Identification

Here we discuss the variables that are used for electron identification. Together the RICH and EMCal provide an e/π rejection factor of about 1:10^4.

3.4.1 Electron Identification Using the RICH Detector

Tracks reconstructed using DC and PC1 and having a matched hit in the EMCal (see Section 3.3.2) are reflected by the RICH mirror into the RICH PMT plane. Then PMT hits are searched around the projection point as illustrated in Fig. 3.10.

The number of associated fired PMTs for a given track, designated as $n0$, is the primary variable for identifying electrons:

$$n0 \equiv \text{number of fired phototubes between } 3.4 \leq r^i_{cor} \leq 8.4 \text{ cm}$$

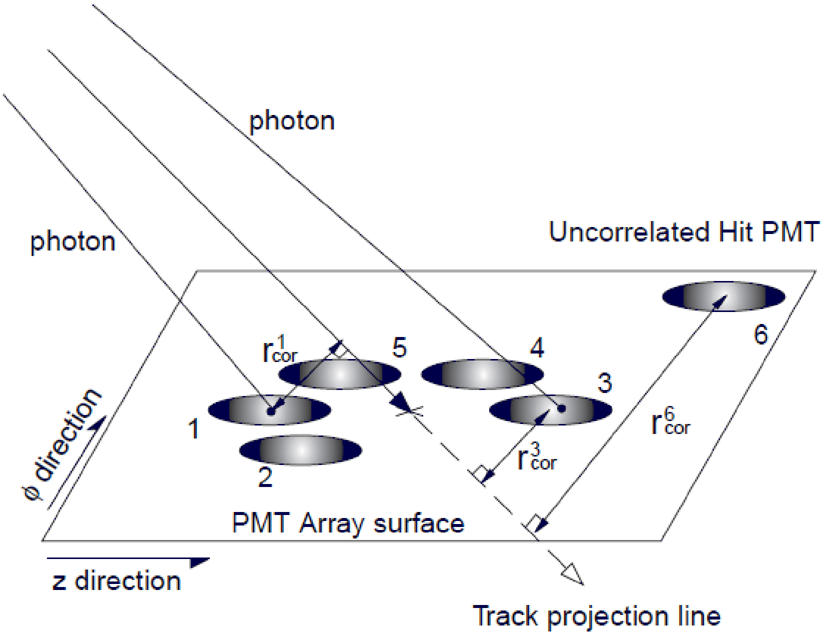

Figure 3.10: Schematic description of the definition of variable which characterizes the RICH ring. The track projection vector and five hit PMT are shown as an example. The distance between the center of the hit PMTs 1 and 3 and the track projection vector are represented as r^1_{cor} and r^3_{cor}, respectively.

where a phototube is considered to have a hit if it has a signal greater than 0.3 photo-electrons and r^i_{cor} is the distance between the center of phototube i and the track projection line. The pulse height measured in each PMT gives the number of photo-electrons ($N_{p.e}(i)$) associated with the hit. Using the position of the fired phototubes and $N_{p.e}(i)$, a weighted position of the ring center is calculated. The distance between the ring center and the track projection is called *disp* (displacement). Examples of the $n0$ and *disp* distributions are shown in Fig. 3.11 and Fig. 3.12 respectively. For the analyses discussed here, we use only the $n0$ variable and require it to have a value greater than one. In the $p+p$ and $d+Au$ collisions, we have a reasonably good S/B ratio and so to preserve the statistics and keep the analysis simpler, we do not use the *disp* variable. This variable is useful for $Au+Au$ analysis, where we have a very poor S/B ratio.

3.4.2 Electron Identification Using the EMCal

The EMCal provides the measurement of energy, which together with the momentum information provided by DC is used to identify electron as explained below.

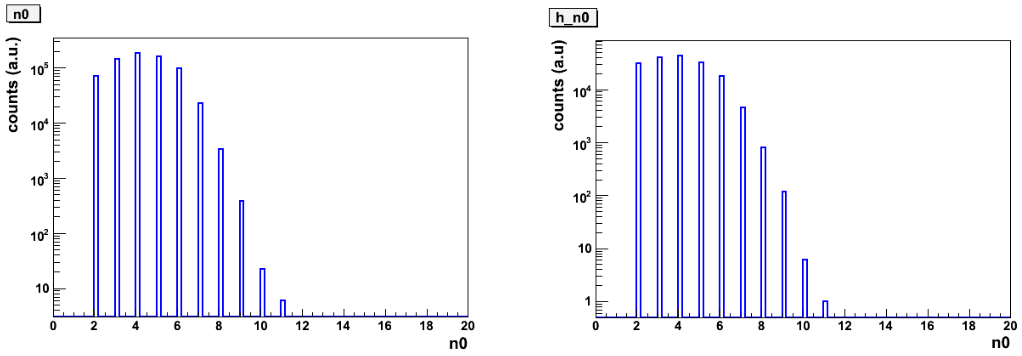

(a) $p+p$ (b) $d+Au$

Figure 3.11: n0 distribution

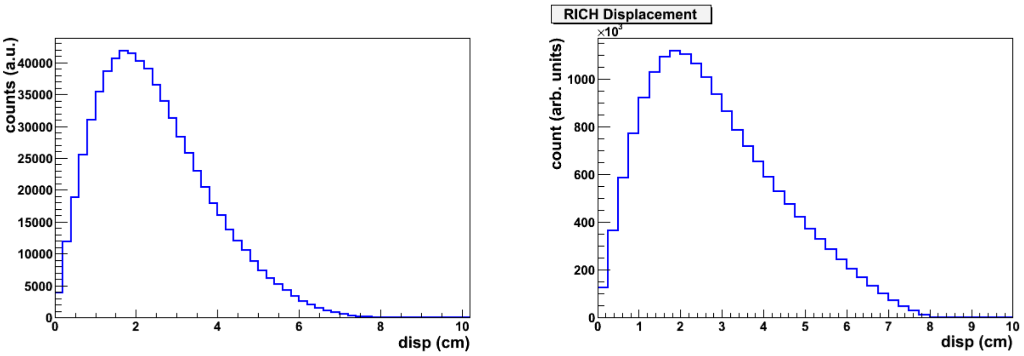

(a) $p+p$ (b) $d+Au$

Figure 3.12: Displacement distribution

Energy-Momentum Matching Since the electron mass ($m_{e^+e^-}$ = 511 KeV/c^2) is negligible compared to its momentum $p > 200$ MeV/c and all its energy is deposited in the EMCal, the ratio of the energy (E) measured by the EMCal and the total momentum (p) measured by the DC is about 1 ($E = \sqrt{p^2+m^2} \simeq p$). Hadrons, in contrast deposit only a fraction of their energy in the EMCal, leading to measured energies which are smaller than their momenta. Fig. 3.13 shows the *E/p* distribution in $p+p$ and $d+Au$ collisions for all charged tracks (black), tracks after requiring a matched hit in the RICH with $n0 > 1$ (blue), and also the contribution from accidental hit associations with the RICH (red). While the distribution of all charged tracks is almost structureless, a clear peak due to the electrons at $E/p \approx 1$ is seen when applying the RICH $n0$ cut.

The reconstructed energy does not match the momentum for all electrons. In some cases, when an electron shower overlaps with a photon shower in the EMCal, the reconstructed energy is large, causing the tail at $E/p > 1$. Also electrons from off-vertex decays or late conversions have a mis-reconstructed momentum, as the tracking algorithm assumes all tracks to originate from the collision vertex. Off-vertex decays traverse less magnetic field integral and are therefore bent less, which results in a larger reconstructed

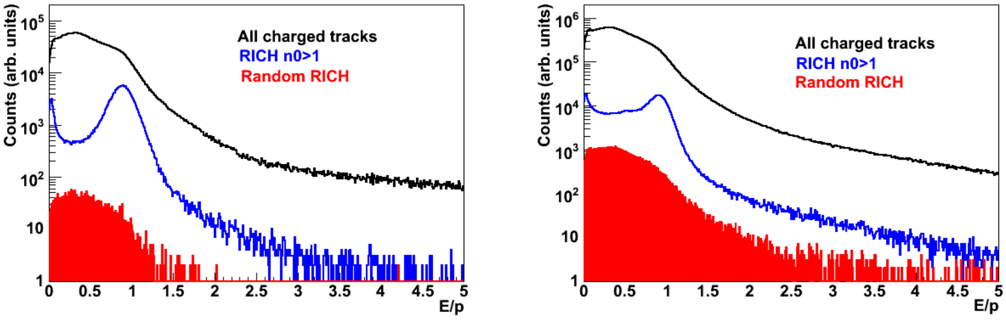

(a) $p+p$

(b) $d+Au$

Figure 3.13: E/p distribution in $p+p$ (left) and $d+Au$ (right), for all charged tracks (black), tracks after applying the RICH n0 cut (blue), and contribution of hadrons randomly associated to hits in the RICH (red). The *E/p* peak is not positioned exactly at 1, due to the reasons explained in the text.

momentum and an $E/p < 1$. In addition, at low p_T, the inclination angle of the track becomes significant. The EMCal cluster starts to spread spatially and we therefore measure only a fraction of the total deposited energy[1]. This also causes the mean of E/p to fall below one. Over the p_T range (≤ 5 GeV/c), covered in this analysis, the momentum resolution of the DC (Eq. 2.6) is better than the energy resolution of the EMCal (Eqs. 2.7 and 2.9), and therefore for the e^+e^- pair analysis, the invariant mass and p_T of the pair are calculated using the momentum information rather than the energy (See Eq. 3.17). As a consequence, we can keep electrons with a mismeasured energy ($E/p > 1$), but the ones with misrecostructed momenta are removed ($E/p < 0.5$).

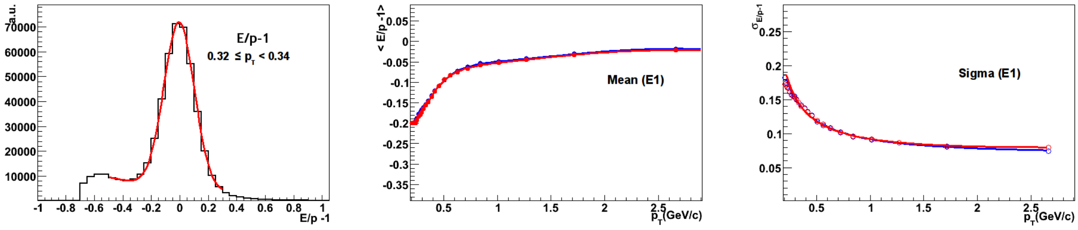

Figure 3.14: Left panel: *E/p-1* distribution for one p_T bin in one EMCal sector, fitted with a Gaussian function. Middle and right panels: the mean and sigma extracted from the Gaussian fit as a function of p_T for one EMCal sector. Blue (red) points represent positrons (electrons). The lines represent the empirical fits used to parameterize the mean and sigma values dependence on p_T.

In analogy to the EMCal matching variables discussed in Section 3.3.2, we express *E/p* also in terms of a reduced variable, that is centered at zero, with sigma around one. This

---

[1] The EMCal cluster algorithm is tuned for photons that hit at near-normal incidence

reduced variable is referred to as *dep*, and is p_T- and charge independent, and provides an easier way to apply the E/p cut in units of the sigma of its distribution.

To derive *dep*, we first accumulate the raw distributions of *E/p-1* separately, for the electrons and positrons, for each of the eight EMCal sectors, divided into several fine p_T bins. These raw distributions are then fit to a Gaussian function. This is illustrated in the left panel of Fig. 3.14, which shows the raw $E/p-1$ distribution for one p_T bin of one EMCal sector, fitted to a Gaussian function. The middle and right panels show respectively, the extracted centroid and sigma values from the Gaussian function, as a function of p_T for one EMCal sector. The p_T dependent centroid distribution is then fit to a polynomial function of second degree, whereas the distribution of sigma is fitted using the functional form $\sqrt{(p_0 \cdot p_T)^2 + (p_1/\sqrt{p_T})^2 + (p_2)^2}$, that takes into account the momentum resolution at high p_T. The lines in the middle and right panels of Fig. 3.14 represent examples of these fits.

The parameterizations of these fits are then used to calculate *dep* as:

$$dep = \frac{\Delta(E/p-1)}{\sigma} \tag{3.13}$$

where $\Delta(E/p-1)$ is the difference between the measured $E/p-1$ and the mean value of the Gaussian fit and σ corresponds to the extracted sigma value from the fit. Fig. 3.15 shows the reduced mean and sigmas for the dep distribution as a function of p_T and charge for all the EMCal sectors. The means are now centered around zero and the sigmas have a value ~ 1.

3.5 Quality Assurance

It is important to have stable performance and acceptance of the detectors involved in the analysis over the entire run, so as to avoid any extra corrections and systematic errors. Changes can occur by a variety of reasons, such as loss of active areas in the detector, unstable DAQ conditions, or high voltage problems. The acceptance variations of all the detectors involved in the analysis are checked and run dependent dead maps are prepared to mask out any noisy/unstable/inefficient region from the analysis. Finally, we examine the electron yield per event as a function of run number and remove the runs with too high or too low yield. The details of the method are presented below.

Acceptance Cuts For DC/PC1, we accumulate 2D histograms in the α versus wire net number (*board*) space for the east and west arms separately. The board number is related to the azimuthal angle ϕ and is a better choice for acceptance studies, since it directly

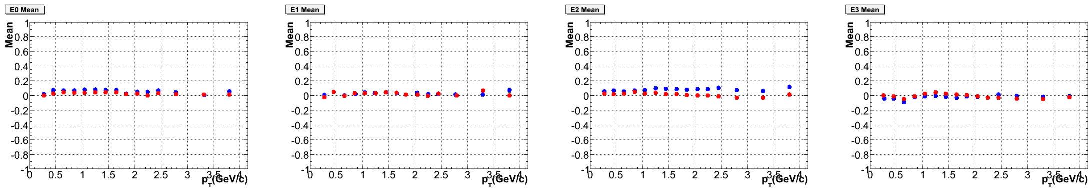

(a) E0-mean (b) E1-mean (c) E2-mean (d) E3-mean

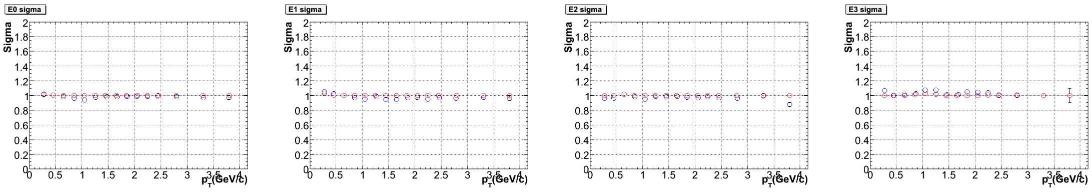

(e) E0-sigma (f) E1-sigma (g) E2-sigma (h) E3-sigma

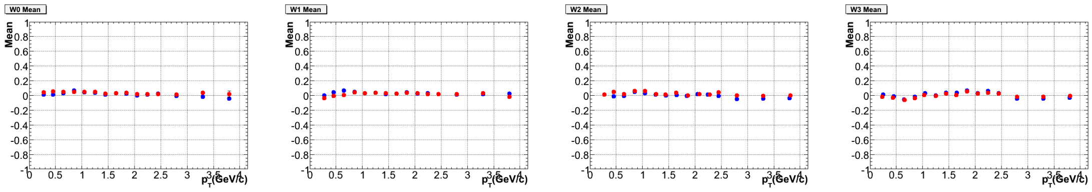

(i) W0-mean (j) W1-mean (k) W2-mean (l) W3-mean

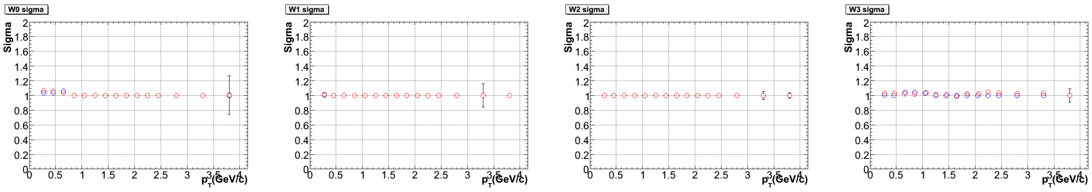

(m) W0-sigma (n) W1-sigma (o) W2-sigma (p) W3-sigma

Figure 3.15: Mean and sigma values of dep for the eight EMCal sectors as a function of p_T.

reflects the hardware condition. Cuts are applied to remove inefficient, dead or noisy areas of the detector. The 2D plots before and after applying the cuts are shown in Fig. 3.16. Also a cut of ±75 cm on DC *zed* was applied to remove edge effects in the DC.

For the EMCal/RICH, we look at the tower/PMT occupancy histograms and mask any tower/PMT that is noisy or has an occupancy lower than 4σ of the mean value. An example for one EMCal and RICH sectors showing the masked towers/PMTs is shown in Fig. 3.17.

Fluctuations of the Electron Yield Fig. 3.18 shows the number of electrons and positrons per event using the eID cuts described in Table 3.2 and with all the acceptance cuts implemented, for $p+p$ (left) and $d+Au$ (right) collisions, respectively. As can be seen for $d+Au$, there are few runs between 251000 to 252000, that have a high electron yield. This is due to the additional converter material around the beam pipe, that was introduced

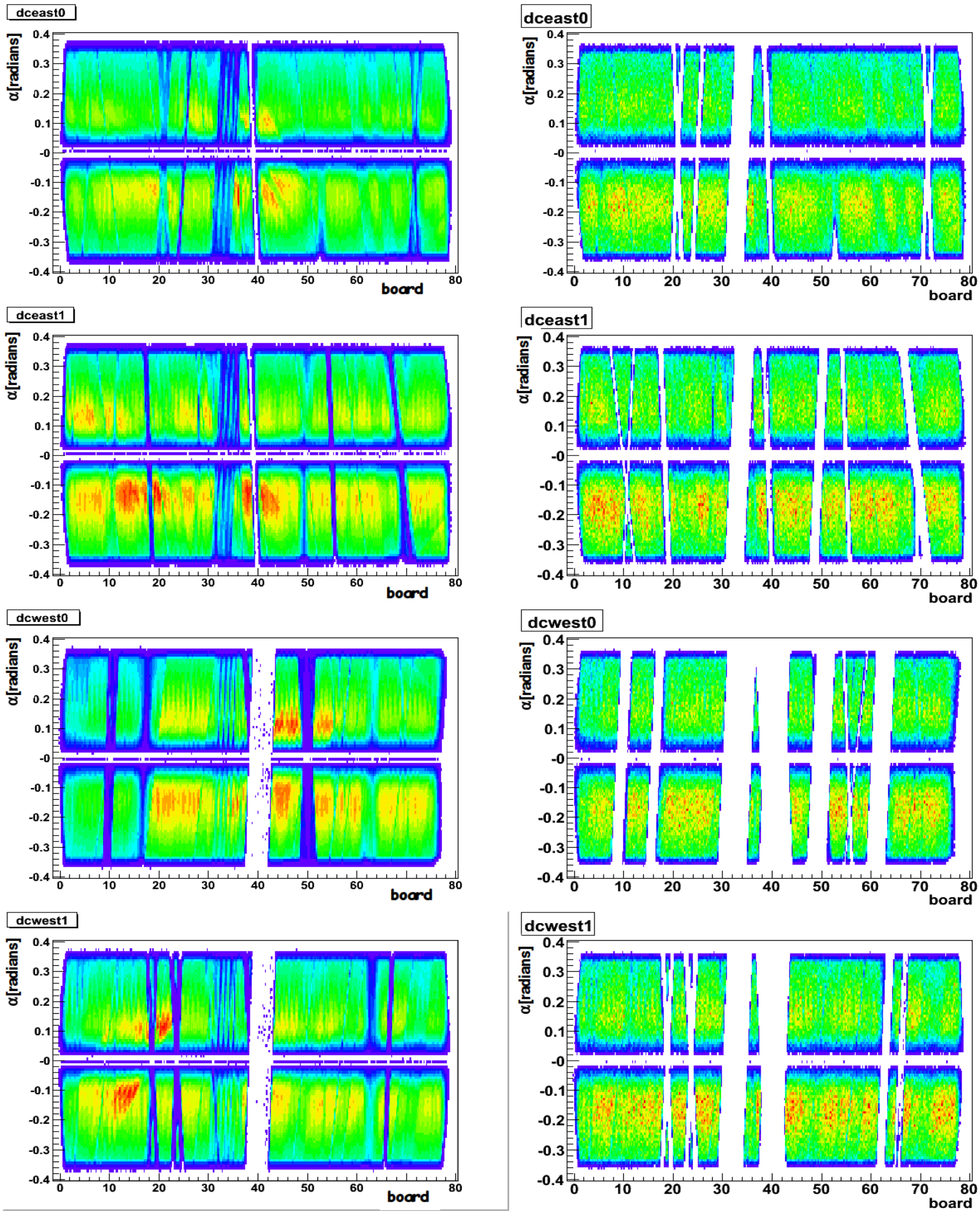

Figure 3.16: Alpha vs board distribution for DC/PC1 quality assurance studies before (left) and after (right) fiducial cuts. The south (0) and north (1) sectors of the east and west DC are shown separately.

in those runs for special studies. These runs and the others that lie outside the window $0.0008 \leq N_{e^{+}+e^{-}} \leq 0.0014$ are removed from the analysis. Also a small drop in the acceptance can be seen after run 249440 for $d+Au$, which was due to high voltage problems

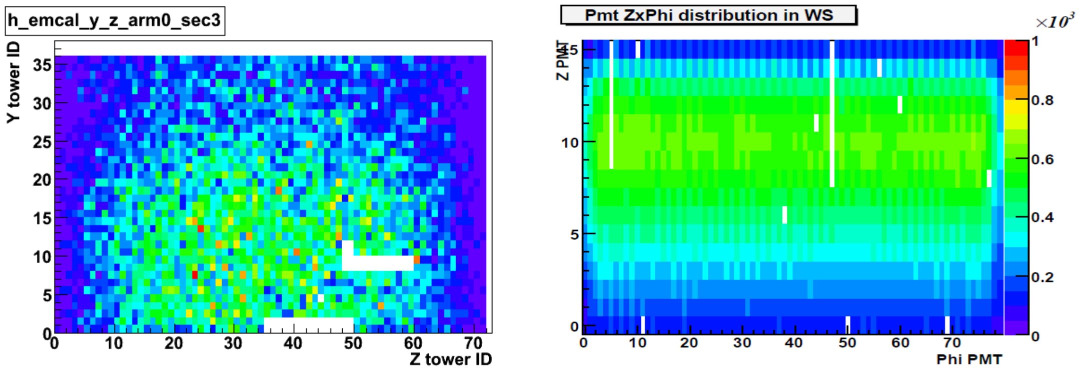

Figure 3.17: Left panel: the EMCal tower occupancy for one sector. Right panel: the same for the RICH PMTs. The masked towers/PMTs are shown as white boxes.

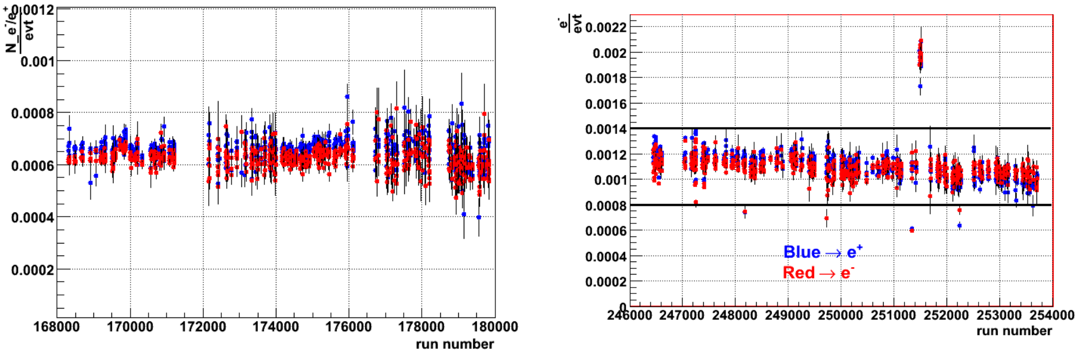

Figure 3.18: Left panel: the number of e^+ (blue) and e^- (red) per event as a function of run number for the $p+p$ collisions sample corresponding to good runs, Right panel: the same distribution for $d+Au$ collisions sample for all the runs (including bad runs).

in part of the PC1 detector. The distribution shown for $p+p$ corresponds to all the good runs used in the analysis after all the converter and other bad runs were removed. A small drop in acceptance can also be seen after run 178937. This was due to two bad RICH data packets that were disabled after this run. These extra dead areas are corrected for in the acceptance corrections as described later in Section 3.11.

3.6 Single Electron ERT Efficiency

Both the $p+p$ and $d+Au$ analysis require that in every event, at least one electron has fired the ERT trigger (see Section 2.2.6.2). The results in the e^+e^- pair analysis need therefore to be corrected for the pair trigger efficiency, derived from the single electron ERT efficiency. The single electron trigger efficiency is determined using the MB data sample only, since the ERT Level-1 trigger decision is also recorded in the MB events.

We first build the p_T spectrum, $dN^{\pm}_{MB}/dp^{\pm}_{T}$ of all electrons *i.e*, tracks that satisfy the eID cuts, from the MB data sample. This is then compared to the p_T distribution of electrons, obtained with the additional requirement of having an associated fired ERT trigger tile, *i.e.* $dN^{\pm}_{MB\&\&ERT}/dp^{\pm}_{T}$. The trigger efficiency is then given by the ratio of the two distributions:

$$\varepsilon_{ERT} = \frac{dN^{\pm}_{MB\&\&ERT}/dp^{\pm}_{T}}{dN^{\pm}_{MB}/dp^{\pm}_{T}} \tag{3.14}$$

For the $p+p$ analysis, the ERT efficiency was determined separately for each of the eight EMCal sectors. An example showing the p_T spectra for MB and ERT electrons, and ERT efficiency for the EMCal sector E3 is shown in Fig. 3.19. The ERT efficiency reaches a plateau at a higher value compared to the ERT threshold value (for Run5 $p+p$ E_{th}, was 400 MeV). The plateau level lies below 1 due to certain inactive ERT tiles, either in RICH or EMCal. The trigger efficiency points are then fitted with a Fermi function:

$$f(p_T) = \frac{\varepsilon_0}{(e^{-(p_T-p_0)/k})+1} \tag{3.15}$$

with ε_0, p_0 and k as the free parameters. The parameters of the fit thus obtained are used in the simulations to emulate the pair trigger efficiency (see Section 3.13).

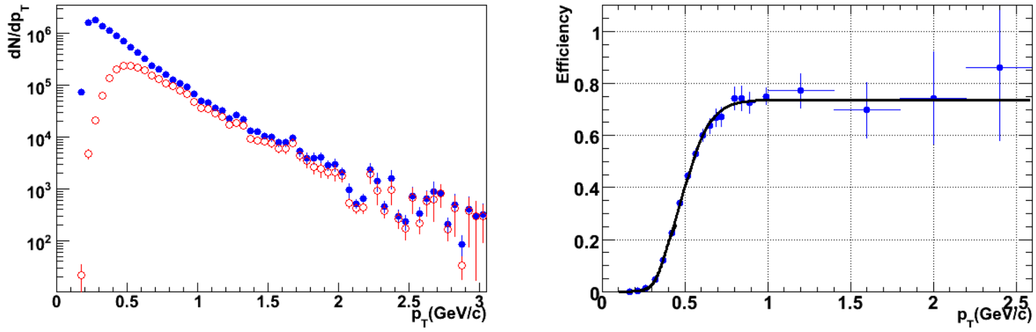

Figure 3.19: The left panel shows the MB (blue) and ERT (red) single electron p_T spectra from Run5 $p+p$ data for one EMCal sector. The right panel shows the ERT efficiency obtained by dividing the red to the black spectra.

In the $d+Au$ analysis, we improved the procedure and the single electron trigger efficiency was derived separately for each EMCal supermodule and each RICH supermodule. RICH has 8 sectors with 32 supermodules in each, resulting in a total of 256 SMs. EMCal has 2 sectors with 32 supermodules each, and 6 sectors with 18 supermodules each, resulting in a total of 172 SMs. Since during the $d+Au$ run, we had two data samples with different ERT thresholds (600 and 800 MeV), the ERT efficiencies were derived separately for the two cases. An example of p_T distributions for MB and ERT electrons

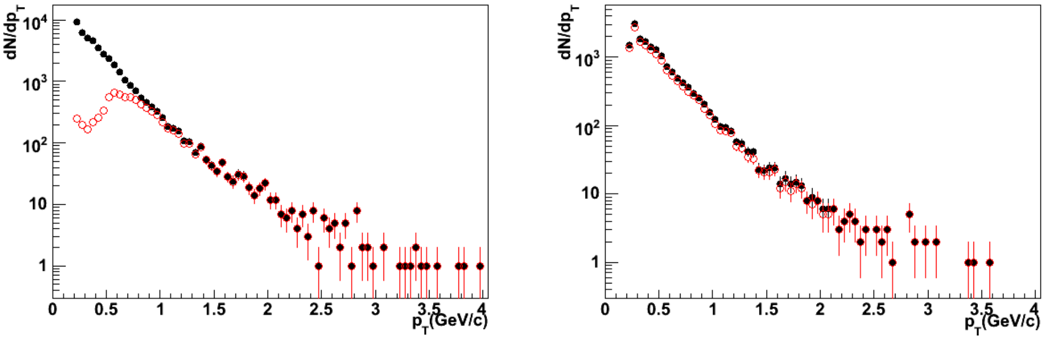

(a) EMCal SM

(b) RICH SM

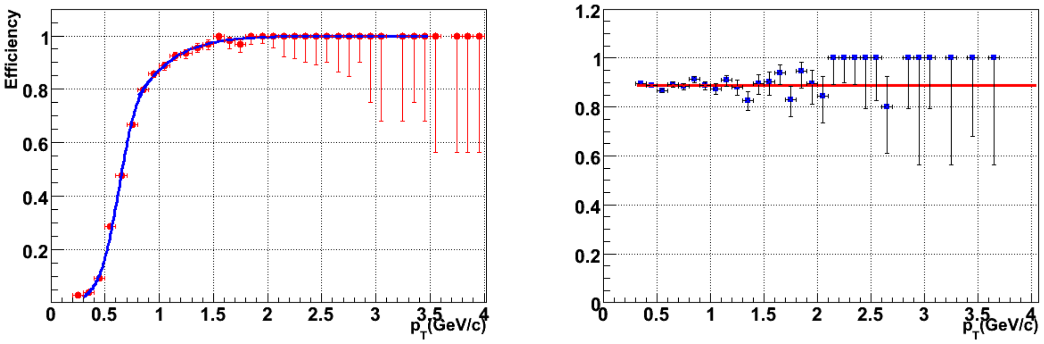

(c) EMCal SM Efficiency

(d) RICH SM Efficiency

Figure 3.20: (a) shows the p_T spectra for a single EMCal SM. The black symbols represent MB electrons falling into this SM acceptance and red symbols represent the cases when this SM has the trigger bit ON, for the 600 MeV data sample, (b) the same for one RICH SM. (c) and (d) show the EMCal and RICH ERT efficiencies, respectively for these SMs.

for the 600 MeV data sample is shown in Fig. 3.20(a) and Fig. 3.20(b) for a single EMCal and RICH supermodule, respectively. The resulting trigger efficiency can be seen in Fig. 3.20(c) and Fig. 3.20(d).

The trigger efficiency points for the EMCal supermodules were fitted to two fermi functions (Eq. 3.15), one to describe the lower p_T region (0-0.9 GeV/c) and the other to describe the high p_T region. The RICH trigger efficiencies were fitted to a constant function. As expected, the plateau for a given supermodule levels at 1.

3.7 Pair Cuts

In the pair analysis, we use two types of cuts: rejection of artificial tracks referred to as “ghost tracks” and removal of extra conversions arising in the detector material.

Rejection of Artificial Tracks Artificial tracks arise as a result of problems or ambiguities in the pattern recognition of the detectors. These tracks give rise to artificial pairs and hence should be rejected. There are two types of artificial tracks; DC ghost tracks and RICH ring sharing tracks. The DC ghost tracks are an artifact of the tracking algorithm discussed in Section 2.2.3.3, that occurs when the trajectory of a single particle is reconstructed twice and thus gives rise to two tracks with almost identical parameters. The DC ghost tracks are identified by looking at the Δz vs $\Delta\phi$ distribution of the differences in the z and ϕ of any pair of tracks in the same event. The left panel in Fig. 3.21 shows such a distribution with the characteristic peak at zero of the ghost tracks. The cut used to reject the DC ghost tracks is shown by the box in the figure.

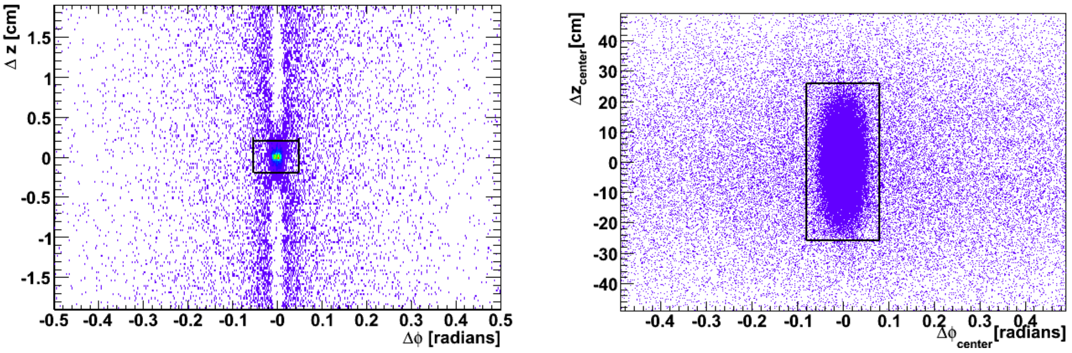

Figure 3.21: Left panel: Δz vs $\Delta\phi$ distribution for pairs of tracks in the DC. Right panel: Δz vs $\Delta\phi$ distribution for the ring centers of any pair of electron tracks in the same event. The boxes represent the cuts used for the $d+Au$ analysis.

The ring sharing effect in the RICH detector arises, when after the DC, an electron track is parallel to a hadron track in the same event. Due to the spherical geometry of the RHIC mirror, these two tracks are focussed onto the same photo-multipliers. Therefore the hits in the RICH due to the electron are also assigned to the parallel hadron track, which is then mis-identified as an electron. This ring sharing effect can be seen in the distance between the ring centers of any pair of electron tracks in the same event as illustrated in the right panel of Fig. 3.21. The box in the figure shows the cut used in the $d+Au$ analysis to reject such pairs.

For the $p+p$ analysis all the artificial pairs, from both the DC and the RICH detector were rejected using a variable called *Post Field Opening Angle (pfoa)*, which is defined as the angle between two tracks at the drift chamber. The *pfoa* is calculated by taking the inverse cosine of the scalar product of the two track unit vectors. The *cos(pfoa)* distribution for like sign pairs shows a strong peak at either 1 or -1 for the artificial pairs, depending on the magnetic field direction. An example of *cos(pfoa)* can be seen in Fig. 3.22. To

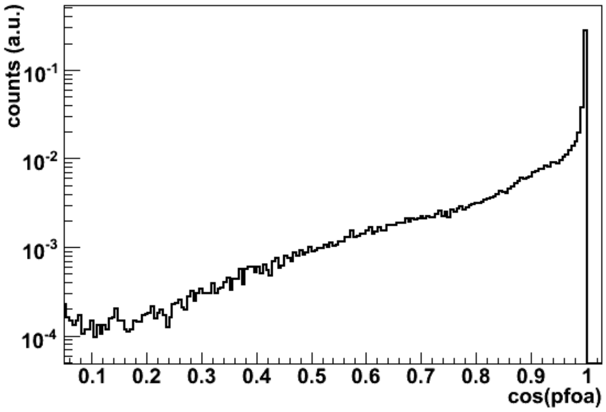

Figure 3.22: The distribution of *cos(pfoa)* for the like-sign pairs in each event.

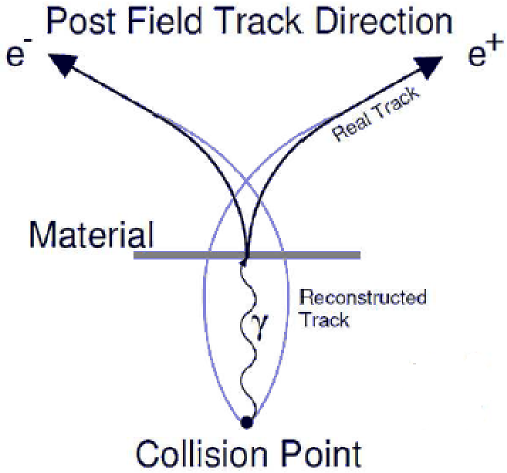

Figure 3.23: Schematics of conversion pairs.

reject these pairs, we require $|cos(pfoa)| < 0.99$. These cuts result in a loss of $\sim$ 1-2% in the raw yield of ϕ and ω and a similar loss is seen in the simulations also.

The effect of artificial pairs in the e^+e^- invariant mass distribution can be seen in Fig. 3.24. Such pairs result in a peak at $\approx$ 600 MeV. The artificial pairs affect the normalization of combinatorial background generated using mixed event technique (Section 3.9.2). This is because, when such a pair is constructed in same event, it is an artifact of the detector or reconstruction or analysis. However, for the mixed event there is no reason, and the probability that this happens is purely regulated by phase-space. As a consequence the same and mixed event distributions might be influenced in a different way by a pair cut, that can lead to over- or under-subtraction of the background in the region interested by the cut. Studies using a toy monte carlo [130] suggested that if one throws away the artificial pairs, both the real and mixed event spectrum reproduce same shape. But the normalization for this case results in a slight under-subtraction of the mixed event background. As will be discussed in later section (Section 3.9.2), we use a combined method of mixed event and fitting for the background subtraction and so this takes care of the slight residual background left, if any, after the mixed event subtraction.

Photon Conversions e^+e^- pairs resulting from photon conversions occurring off-vertex in the detector material e.g. the beryllium beam pipe (0.3 X_0), get reconstructed with an incorrect momentum. This is so because the track algorithm assumes that all the reconstructed tracks originate from the vertex, subjecting them to the same field integral as for particles originated at the vertex. Therefore, their reconstructed momentum is higher than in reality leading to a fake invariant mass which is proportional to the radial distance between the collision vertex and the conversion point. A schematic representation of the tracking algorithm for a conversion pair produced in the beam pipe is illustrated in Fig. 3.23.

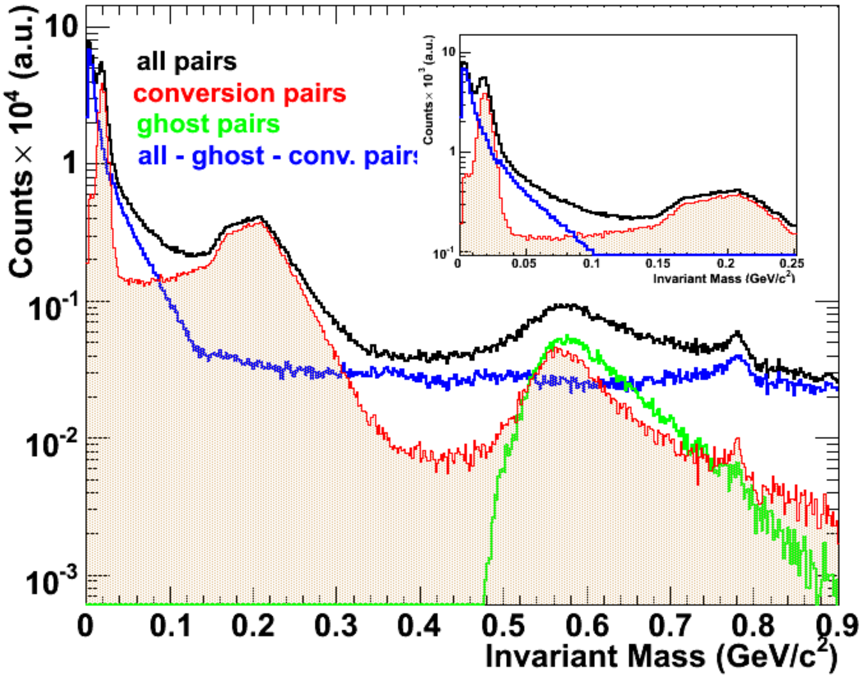

Figure 3.24: Invariant mass distribution of all e^+e^- pairs (black). The conversion pairs rejected using the ϕ_V cut are shown in red, the ghost pairs are shown in green, and the remaining pairs are shown in blue. The small insert shows a zoom into the low-mass region ($m_{e^+e^-} \leq 250\ MeV/c^2$).

Fig. 3.24 shows the e^+e^- invariant mass spectrum in the low-mass region ($m_{e^+e^-} \leq 0.9$ GeV/c^2) for $d + Au$ collisions highlighting the contributions from conversions. The peak at $m_{e^+e^-} \approx$ 20 MeV/c^2 is due to the conversions occurring in the beam pipe at a radius of 4 cm, the peak around 200 MeV/c^2 corresponds to the DC entrance window located at 2.2 m, and in between there is continuum from the conversions in air. The region beyond the DC entrance window is field-free and hence electrons from conversions within the DC do not bend. They follow a straight line trajectory and are rejected by a high p_T cut.

As photons are massless, conversion pairs do not have an intrinsic opening angle, but get opened up due to the axial magnetic field. Therefore the decay plane of conversion pairs is perpendicular to the magnetic field along the z- axis, and thus conversion pairs can be singled out by applying a cut on the orientation of the pairs. The orientation angle ϕ_V is defined as follows: Here $\vec{p}_1$ and $\vec{p}_2$ are the 3-momentum vector of the electron and positron, respectively. For an e^+e^- pair from a conversion, ϕ_V is distributed around 0

$$\vec{u} = \frac{\vec{p}_1 + \vec{p}_2}{|\vec{p}_1 + \vec{p}_2|} \tag{3.16a}$$

$$\vec{v} = \vec{p}_1 \times \vec{p}_2 \tag{3.16b}$$

$$\vec{w} = \vec{u} \times \vec{v} \tag{3.16c}$$

$$\vec{u}_a = \frac{\vec{u} \times \hat{z}}{|\vec{u} \times \hat{z}|} \tag{3.16d}$$

$$\phi_V = cos^{-1}\left(\frac{\vec{w} \cdot \vec{u}_a}{|\vec{w}||\vec{u}_a|}\right) \tag{3.16e}$$

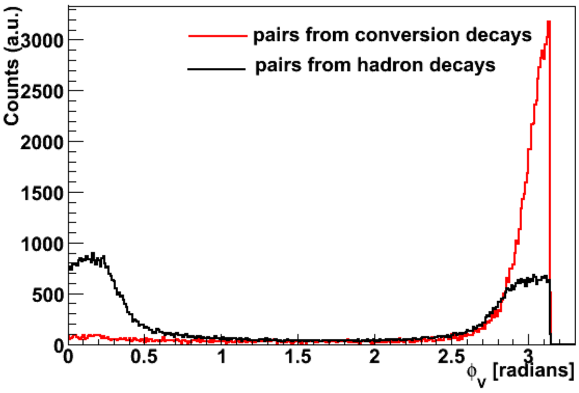

Figure 3.25: ϕ_V distributions for conversions pairs (red) and pairs from hadron decays (black).

or 180 degrees (depending upon the magnetic field direction), whereas e^+e^- pairs originating from hadron decays have no preferential direction. This can be seen in Fig. 3.25, where the pairs from conversions (red) show a clear peak around 3.14 radians, while for hadron decays, the distribution (black) does not have any such feature. A cut on the ϕ_V distribution is thus used to remove the conversion pairs, and the cut values used in this analysis are summarized in Table 3.2.

3.8 Summary of Cuts

Table 3.2 summarizes all the selection cuts used in the $p+p$ and $d+Au$ analyses.

3.9 Pair Analysis and Raw Yield Extraction

Since the source of any electron or positron is unknown, we combine all the electrons and positrons in a given event into pairs to generate the like sign (FG_{++}, FG_{--}) and unlike sign (FG_{+-}) foreground pairs. Since we use ERT data, it is required that at least one of the tracks in each pair fires the ERT trigger.

The invariant mass, $m_{e^+e^-}$ and transverse momentum p_T of the pair are calculated using the single track information as:

$$m^2_{e^+e^-} = (E_{e^+} + E_{e^-})^2 - (\vec{p}_{e^+} + \vec{p}_{e^-})^2 = 2[p_{e^+}p_{e^-}(1 - cos\alpha)]^{1/2} \tag{3.17a}$$

$$p_T^2 = (p_{x,+} + p_{x,-})^2 + (p_{y,+} + p_{y,-})^2 \tag{3.17b}$$

Cut	Run5 $p+p$	Run8 $d+Au$
Event Cut		
Event Trigger	MB, ERT	MB, ERT
BBC vertex cut	$-30 \leq bbcz \leq 28$ cm	$\lvert bbcz \rvert \leq 30$ cm
Track selection cuts		
DCH zed	$\lvert zed \rvert < 75$ cm	$\lvert zed \rvert < 75$ cm
DCH quality	All	31 || 51 || 63
p_T cut	$0.2 \leq p_T \leq 5.0$ GeV/c	$0.2 \leq p_T \leq 7.0$ GeV/c
eID cuts		
RICH n0	> 1	> 1
EMCal dep	> -2	> -2
EMCal matching	$\sqrt{emcsd\phi^2 + emcsdz^2} < 3.5$	$\sqrt{emcsd\phi^2 + emcsdz^2} < 3.5$
Pair cuts		
DC ghost rejection	$cos(pfoa) < 0.99$	$\Delta\phi < 0.08\ rad,\ \Delta z < 0.2\ cm$
RICH ghost rejection	$cos(pfoa) < 0.99$	$\Delta x\phi < 0.08\ rad,\ \Delta\, xz < 26\ cm$
Conversions	No cut	600 MeV $(m_{ee} < 0.03(\geq 0.03), \phi_V < 0.25(< 0.1)\ rad$ 800 MeV $(m_{ee} < 0.03(\geq 2.85), \phi_V < 0.25(< 3.0)\ rad$

Table 3.2: Summary of the cuts used in the $p+p$ and $d+Au$ analyses

where $E_{e^+(e^-)} = \sqrt{\vec{p}^{\,2}_{e^+(e^-)} + m_e{}^2}$, m_e = 511 keV/c^2, α is the pair opening angle and the 3-momentum vector $\vec{p}_{e^+(e^-)}$ is measured with the drift chamber (Section 2.2.3.4), with components expressed as follows:

$$p_x = psin\theta_0 cos\phi_0,\ p_y = psin\theta_0 sin\phi_0,\ p_z = pcos\theta_0$$

By construction, the unlike sign mass spectrum contains both the signal and an inherent combinatorial background, comprised of uncorrelated pairs and a small fraction of correlated pairs. The uncorrelated background arises from all the combinations where the origin of the two electrons is totally uncorrelated. The main source of this background comes from unrecognized π^0 Dalitz decays and γ-conversions, where one electron in the pair is lost, as a result of the limited azimuthal angular acceptance and the strong magnetic field beginning at $R = 0$. The correlated background occurs if there are two e^+e^- pairs in the final state of a meson. For example for the double π^0 Dalitz decay ($\pi^0 \rightarrow e_1^+ e_1^- e_2^+ e_2^-$), a Dalitz decay ($\pi^0 \rightarrow \gamma e_1^+ e_1^-$) followed by the γ converting into an $e_2^+ e_2^-$ pair in the detector material and the two photon decay ($\pi^0 \rightarrow \gamma\gamma$) in which both photons convert into e^+e^- pairs. *i.e.*, $\pi^0 \rightarrow \gamma_1\gamma_2 \rightarrow e_1^+ e_1^- e_2^+ e_2^-$. The e^+e^- pair with the same parent particle is considered physics signal (*i.e*, $e_1^+ e_1^-$ or $e_2^+ e_2^-$) and in the case of a real photon conversion in the detector material, the pair is removed by the ϕ_V cut (see Section 3.7). The "cross" combinations into two unlike-sign ($e_1^+e_2^-$ and $e_2^+e_1^-$) as well as into two like-sign ($e_1^+e_2^+$ and $e_1^-e_2^-$) are not purely combinatorial, but correlated via the π^0 mass. Another source of correlated pairs comes from hadrons, either within the same jet or in back-to-back jets, that decay into electron pairs. The first case results in pairs with low masses due to the small opening angles, while pairs correlated via back-to-back jets have large opening angles and so larger invariant masses.

A precise determination of contributions from these different types of background is essential for studying the continuum in the low mass pair region. For the ω and ϕ, one can use simpler methods for the background estimation. The signal to background ratio (S/B) increases with increasing pair p_T. For $p+p$, in the region of the ω (ϕ) meson it changes from 1:2 (2:1) to 3:1 (6:1), whereas for the $d+Au$ it varies from 1:5 (1:2) to 3:1 (4:1). In the present work, we use two methods for the background estimation. The first is simply a fitting procedure that was used in the $p+p$ analysis, and the second is a combination of event mixing technique and fitting that was used in the $d+Au$ analysis. The resonance yield (ω or ϕ) is extracted by subtracting the background estimated using either of these two methods and then summing the yield in a certain window around the peak. The details are given in the next section.

3.9.1 Raw Yield Extraction by Fitting Technique

The ϕ and ω yield in $p+p$ collisions were extracted using a fitting procedure. The resonance peak for a given p_T bin was fitted to a Relativistic Briet-Wigner (RBW) function for the signal, convoluted with a Gaussian function for the detector mass resolution, and a polynomial of 2^{nd} degree for the underlying background. The relativistic Breit-Wigner parameterization is given by:

$$Y(m) \sim \frac{m.m_{\phi/\omega} \cdot \Gamma_{\phi/\omega}}{(m^2 - m^2_{\phi/\omega})^2 + (m_{\phi/\omega} \cdot \Gamma_{\phi/\omega})^2} \tag{3.18}$$

The detector mass resolution as a function of p_T was determined using a zero-width Monte Carlo simulation for $\phi \rightarrow e^+e^-$ explained in Section 3.11, where the width of the input ϕ meson was set to be zero. The p_T dependent σ values thus obtained are used to constraint the σ parameter of the Gaussian function in the simulation and data. The Γ of the RBW was fixed to the PDG value, while the σ of the Gaussian function was allowed to vary within ± 10% around the zero-width value.

For ϕ, the raw yield is extracted by summing up the bins in a $\pm 3\sigma$- window around the peak position and subtracting the background determined by integrating the polynomial over the same window. The σ here corresponds to the value extracted from the fit.

For ω, we follow the same procedure as for ϕ, but add a second relativistic Breit-Wigner function to account for the contribution of the ρ-meson beneath the ω peak. The production ratio of ρ to ω meson was assumed to be 1 and so in the fit their ratio is given by the ratio of their branching ratios to e^+e^- in vacuum *i.e.* 1.53. Examples of the fits to ω and ϕ peaks for the several p_T bins used in the $p+p$ analysis are shown in Fig. 3.26.

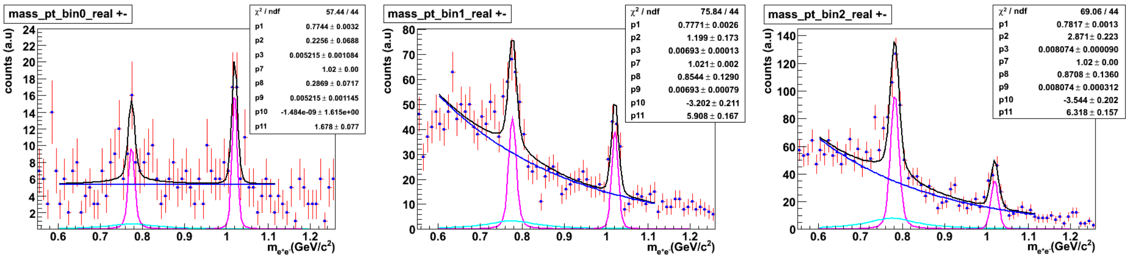

(a) $0 \leq p_T < 0.25$ (b) $0.25 \leq p_T < 0.5$ (c) $0.5 \leq p_T < 0.75$

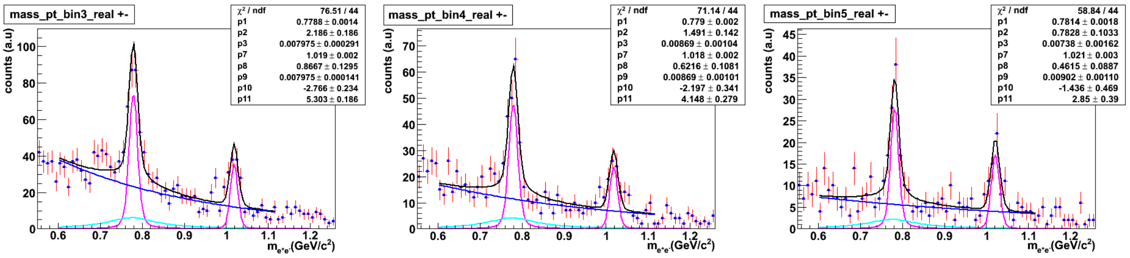

(d) $0.75 \leq p_T < 1.0$ (e) $1.0 \leq p_T < 1.25$ (f) $1.25 \leq p_T < 1.5$

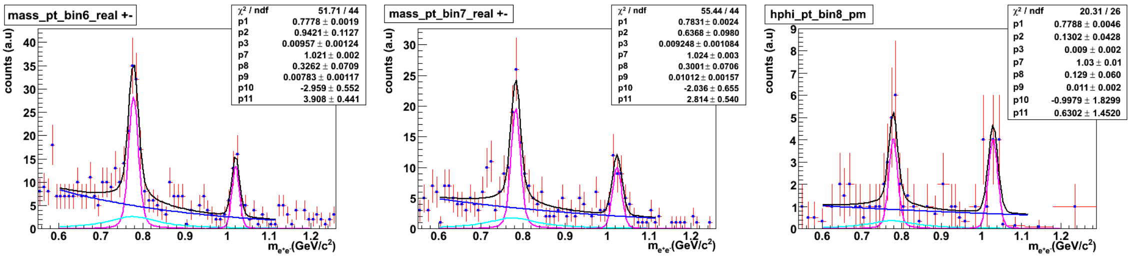

(g) $1.5 \leq p_T < 2.0$ (h) $2.0 \leq p_T < 3.0$ (i) $3.0 \leq p_T < 4.0$

Figure 3.26: Invariant e^+e^- mass spectra for the p_T bins used in the $p+p$ analysis, showing the ϕ and ω meson peaks, fitted to a RBW function convoluted with a Gaussian function and a polynomial function for the background. The cyan lines represent the ρ contribution.

If we denote the invariant mass distribution by FG_{+-}, the background function by f_{bg}, and the background integral by I, then the raw yield of ϕ/ω, $N_{\phi/\omega}$ for a given p_T bin is calculated as follows;

$$\begin{aligned}
N^{raw}_{\phi/\omega} &= N_{FG} - I \qquad (3.19)\\
\Delta N^{raw}_{\phi/\omega} &= \sqrt{N_{FG}+I} \qquad (3.20)\\
where\ N_{FG} &= \sum_{m_{min}}^{m_{max}} FG_{+-} \qquad (3.21)\\
for\ \phi,\ I &= I_{pol} = \int_{m_{min}}^{m_{max}} f_{bg}(m)dm\\
for\ \omega,\ I &= I_{\rho}\left(= \int_{m_{min}}^{m_{max}} f^{RBW}_{\rho}(m)dm\right) + I_{pol}\left(= \int_{m_{min}}^{m_{max}} f_{bg}(m)dm\right)
\end{aligned}$$

with $m_{min} = m_{\phi/\omega} - 3\sigma_{\phi/\omega}$; $m_{max} = m_{\phi/\omega} + 3\sigma_{\phi/\omega}$. $m_{\phi/\omega}$ and $\sigma_{\phi/\omega}$ are the resonance peak position and sigma values obtained from the fit and I_{ρ} corresponds to the rho yield beneath the ω peak.

3.9.2 Raw Yield Extraction by Event Mixing Technique

The uncorrelated part of the combinatorial background can be reproduced with high statistical accuracy using an event mixing procedure. The event mixing technique was originally proposed by Kopylov [131] and later by Drijard, Fischer, and Nakuba [132] and L'Hote [133]. The basic idea behind the event mixing technique is that the distributions of pairs from mixed events contains everything of the reaction and the experimental device, except the correlations. An artificial mixed event is generated by combining all the electrons from one event A, to all the electrons in another event B, provided that events A and B have the same event topology[1]. This procedure generates an unlike- and a like-sign mixed event invariant spectrum, which by construction do not contain any particle correlations. The main advantage of this technique is that one can generate as many mixed events as needed to get a precise determination of the shape of the combinatorial background spectrum, thereby practically eliminating the point-to-point statistical fluctuations in the combinatorial mass spectrum.

The event mixing method described above is valid for minimum bias events only. The ERT trigger used in the data collection biases the single electron distribution towards high p_T and as such the triggered events can not be mixed among each other. Thus to generate the correct combinatorial background shape of e^+e^- pairs, the mixed events are generated from the minimum bias data sample, but as the real events, they are required to satisfy the ERT trigger *i.e.*, in every mixed pair at least one of the electrons must satisfy the ERT condition. The mixing is done for events belonging to the same centrality and z-vertex

---

[1] In the present analysis we require the two events to belong to the same centrality and vertex classes.

classes. We used 5 centrality and 30 vertex bins. To achieve enough accuracy, every event is mixed to 2000 events of the same topology.

Normalization of the Background The mixed event distribution thus constructed reproduces the shape of the real combinatorial background, but needs to be properly normalized in order to subtract it from the measured unlike-sign spectrum. Under the assumption that the number of electrons or positrons per event follows a Poisson distribution, one can prove that the size of the combinatorial background is given by the geometrical mean of the like-sign pairs *i.e.*, $2\sqrt{N_{++}N_{--}}$, where N_{++} and N_{--} represent the real $++$ and $--$ like-sign pair yields.

To assess how well the mixed events reproduce the combinatorial background, we compare the like-sign distributions ($++$ and $--$ pairs) of the real and mixed events. The left panel in Fig. 3.27 shows an example of such a comparison for the 600 MeV $d+Au$ data set. The mixed events spectrum reproduces quite well the measured like-sign spectrum at masses around 1 GeV/c^2. A strong difference is observed at low masses. The peak at $\approx$ 100 MeV/c^2 in Fig. 3.27 is due to the cross pairs coming from correlated π^0 decays as already discussed in previous Section 3.9. Similar cross-pairs are possible for η decays, and hence the background from cross-pairs extends up to the mass of $m_\eta \approx$ 550 MeV/c^2. The differences in shape at high p_T are due to the correlated pairs from jets which were also discussed in Section 3.9.

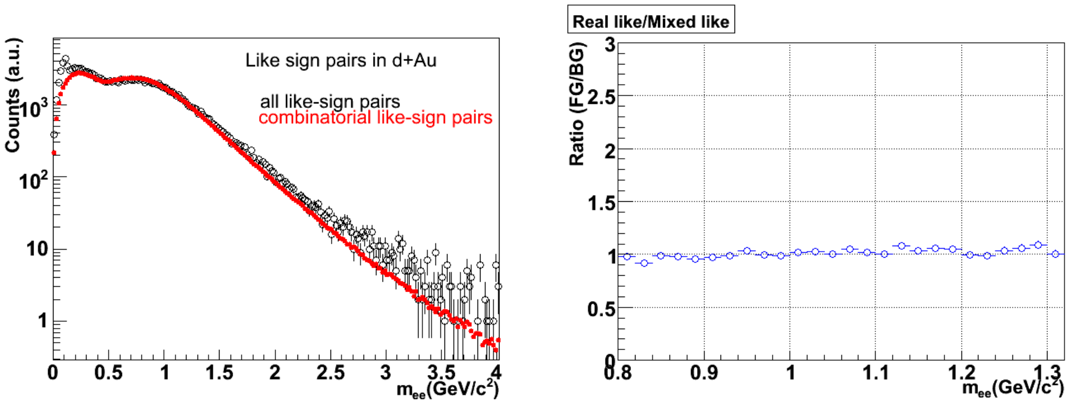

Figure 3.27: Left panel: measured (black) and mixed event (red) like-sign spectra in $d+Au$ collisions for 600 MeV data sample. Right panel: their ratios. The mixed events are normalized according to Eq. 3.22. A clear shape difference is observed at small and large masses indicating correlated background.

To derive the normalization factor, we therefore choose the region between 0.7 - 1.3 GeV/c^2 where the two distributions match well and do not have these correlations. The stability of the results was checked by varying the normalization region, and the difference in the normalization was included in the systematic errors. The normalization factor and the signal determination is explained below.

For a given p_T and centrality bin, we denote the real unlike-sign and like-sign mass distributions by FG_{+-}, FG_{++}, FG_{--}, and the mixed event unlike-sign and like-sign by ME_{+-}, ME_{++}, ME_{--}. The normalization factor α and subtracted unlike-sign signal distribution, S_{+-}, are then given by:

$$\begin{aligned}
\alpha &= \frac{2\cdot\sqrt{\sum_A FG_{++}\cdot\sum_A FG_{--}}}{\sum_A ME_{+-}}; && (3.22)\\
\Delta\alpha &= \alpha\cdot\sqrt{\frac{1}{4}\left(\frac{1}{\sum_A FG_{++}}+\frac{1}{\sum_A FG_{--}}+\frac{1}{\sum_A ME_{+-}}\right)} && (3.23)\\
S_{+-} &= FG_{+-}-\alpha\cdot ME_{+-} && (3.24)\\
\Delta S_{+-} &= \sqrt{FG_{+-}+\alpha^2\cdot ME_{+-}+(\Delta\alpha)^2\cdot(ME_{+-})^2} && (3.25)
\end{aligned}$$

where A denotes the normalization region, $\Delta\alpha$ and ΔS_{+-} represent the error on the normalization factor and the subtracted signal respectively.

The ratio of the real to the normalized mixed like-sign spectra is shown in the right panel of Fig. 3.27. As can be seen, the ratio is flat and around 1 in the region of interest for this analysis indicating the validity of the normalization.

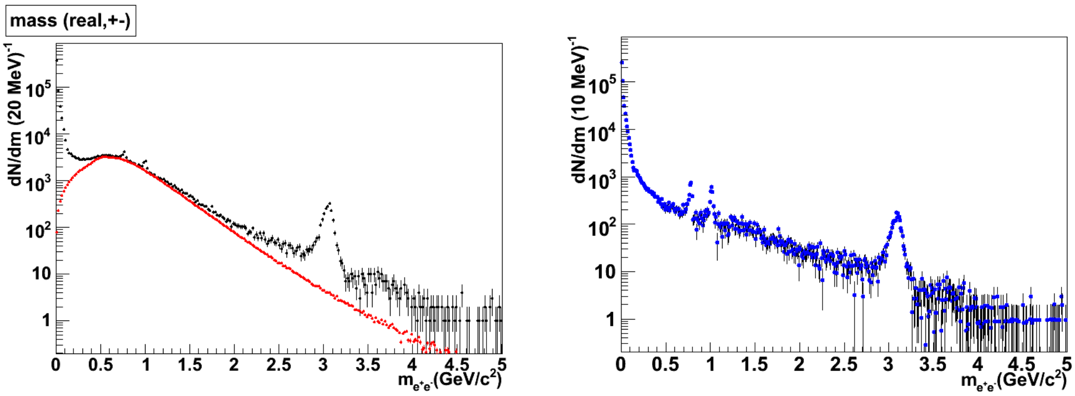

Figure 3.28: The measured (black) and mixed (red) unlike-sign e^+e^- invariant mass spectra (left) and subtraction of two (right) in $d+Au$ collisions.

The real unlike-sign and the normalized mixed unlike-sign spectra are shown in the left panel of Fig. 3.28, with the subtracted spectrum shown in the right panel. In the resulting dilepton spectrum, the main sources of dileptons in the region below 1 GeV/c^2, are the Dalitz decays of the mesons such as $\pi^0,\eta,\eta'\rightarrow\gamma e^+e^-$, $\omega\rightarrow\pi^0e^+e^-$, $\phi\rightarrow\eta e^+e^-$ and the resonance decays of the light vector mesons, $\rho,\omega,\phi\rightarrow e^+e^-$. In the mass region between 1-3 GeV/c^2, the dilepton yield is dominated by the semi-leptonic decay of D and B mesons and Drell-Yan pairs, whereas the region above 3 GeV/c^2 includes dileptons from hard processes and resonance decays of J/ψ and ψ' mesons.

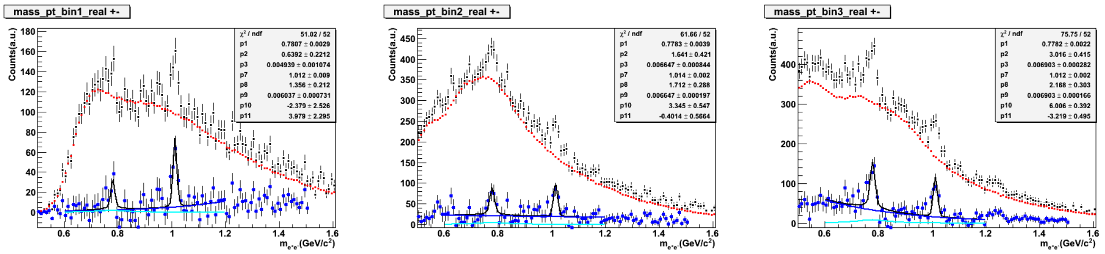

(a) $0.25 \leq p_T < 0.5$ (b) $0.5 \leq p_T < 0.75$ (c) $0.75 \leq p_T < 1.0$

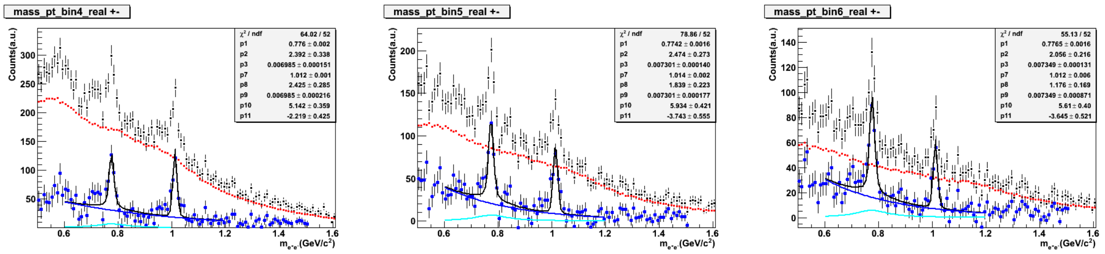

(d) $1.0 \leq p_T < 1.25$ (e) $1.25 \leq p_T < 1.5$ (f) $1.5 \leq p_T < 1.75$

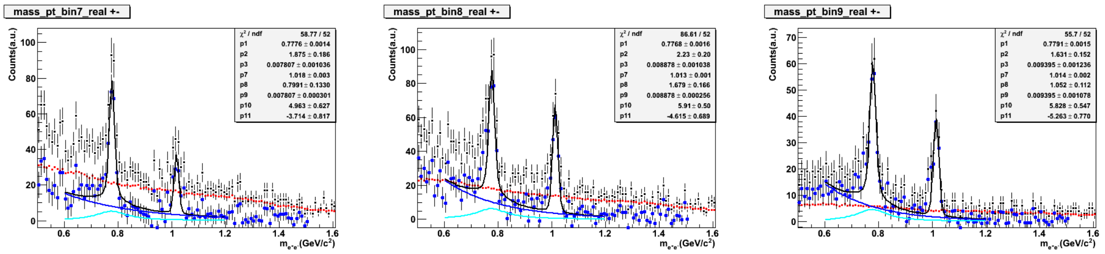

(g) $1.75 \leq p_T < 2.0$ (h) $2.0 \leq p_T < 2.5$ (i) $2.5 \leq p_T < 3.0$

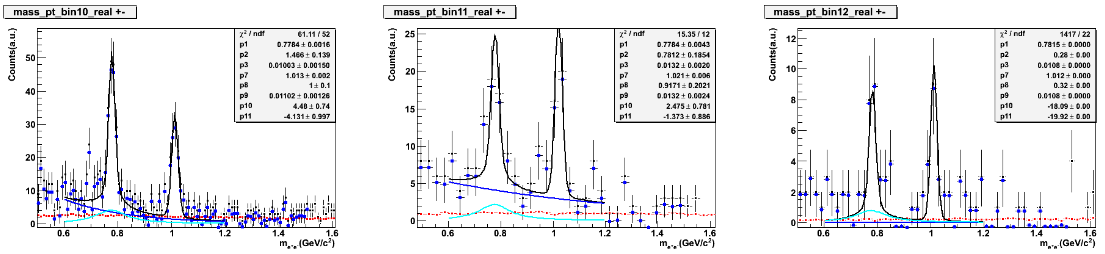

(j) $3.0 \leq p_T < 4.0$ (k) $4.0 \leq p_T < 5.0$ (l) $5.00 \leq p_T < 7.0$

Figure 3.29: The real unlike-sign (black) and the normalized mixed unlike-sign (red) e^+e^- spectra, together with the fits to the subtracted spectra (blue) to determine the underlying continuum beneath the ω- and ϕ-peaks, in the Run8 $d+Au$ 600 MeV data set.

Some of these sources give a continuum yield beneath the ω and ϕ peaks in the subtracted spectrum. This continuum was removed by a fitting method, using the same procedure, as described earlier (see Section 3.9.1). The raw yield for ϕ/ω for any p_T bin is given by the same Eq. 3.19. Examples of mass spectra in various p_T bins for minimum bias $d+Au$ collisions for the 600 MeV data set are shown in Fig. 3.29.

3.10 Invariant Yield

To get the absolute differential cross-section or the invariant yield for ϕ and ω, various corrections to the measured raw yield need to be applied. These include corrections for the limited PHENIX acceptance due to geometry and magnetic field, track reconstruction inefficiencies, multiplicity effects, and any variations in the detector performance over time. The invariant p_T yield is given by:

$$\frac{1}{2\pi p_T}\frac{d^2N}{dp_T dy} = \frac{N^C_{raw}(p_T)\cdot CF(p_T)}{2\pi p_T \cdot N^C_{events}\cdot BR\cdot \Delta p_T \cdot \varepsilon_{embedding}\cdot \varepsilon_{ERT}(p_T)\cdot \varepsilon_{RBR}}\cdot\frac{\varepsilon_{BBC}}{\varepsilon_{Bias}} \tag{3.26}$$

where

- $N^C_{raw}(p_T)$ is the raw yield of $\phi/$ or ω for a given centrality class 'C' or MB.(Section 3.9).
- $CF(p_T)$ is the p_T dependent correction factor obtained from the simulations that takes into account the acceptance and reconstruction efficiency and is discussed in Section 3.11).
- N^C_{events} is the total number of events corresponding to the ERT sample analyzed for the given centrality class C.
- BR is the branching ratio into e^+e^-, $7.18\pm0.12\times10^{-5}$ for ω and $2.97\pm0.04\times10^{-4}$ for ϕ [134].
- Δp_T is the p_T bin width.
- $\varepsilon_{embedding}$ is the pair embedding efficiency to account for the reconstruction losses due to detector occupancy effects. In $p+p$ and $d+Au$ collisions, it is 1, as the effects due to multiplicity are negligibly small.
- $\varepsilon_{ERT}(p_T)$ is the p_T dependent trigger efficiency (see Section 3.6).
- ε_{RBR} is the run-by-run efficiency to take account of any variations in the detector performance over time (see Section 3.15).
- ε_{BBC} is the BBC efficiency for the Minimum Bias collisions (see Section 2.2.6.1).
- ε_{Bias} is the BBC trigger bias (see Section 2.2.6.1).

All the factors in Eq. 3.26, with the exception of $CF(p_T)$ and ε_{RBR} (that will be presented in the next sections), have been discussed in earlier sections. The invariant yield can be converted into an invariant cross-section by multiplying with the inelastic cross-section, σ^{inel} (Section 2.2.6.1):

$$E\cdot\frac{d^3\sigma}{dp^3}=\frac{1}{2\pi p_T}\frac{d^2N}{dp_T dy}\sigma^{inel} \tag{3.27}$$

The ϕ, $\omega \rightarrow e^+e^-$ transverse momentum spectra in $d+Au$ collisions were calculated for the following centrality classes (Section 2.2.7): Minimum Bias *i.e.* 0-88%, 0-20%, 20-40%, 40-60% and 60-88%, and corrected separately for the 600 and 800 MeV data sets for each case. Since the 600 and 800 MeV data sets were completely independent, the two measurements were combined using a weighted procedure:

If $x_1^i \pm \sigma_1^i$ and $x_2^i \pm \sigma_2^i$ correspond to the 600 and 800 MeV invariant yields for the i^{th} p_T bin, with errors defined as

$$\sigma_1^i=\sqrt{(\sigma_{1stat}^i)^2+(\sigma_{1sys}^i)^2};\quad \sigma_2^i=\sqrt{(\sigma_{2stat}^i)^2+(\sigma_{2sys}^i)^2};$$

where $\sigma_{1stat}^i(\sigma_{2stat}^i)$ and $\sigma_{1sys}^i(\sigma_{2sys}^i)$ correspond to the statistical and uncorrelated systematic errors (ERT uncertainty) respectively (see Section 3.17), then the two measurements are combined using weights, that are inversely proportional to each measurement's variance σ_j^i [135–137]. The weighted average $\langle x^i\rangle$ and the associated combined error σ^i, is given by:

$$\begin{aligned}\langle x^i\rangle &= \frac{w_1^i\cdot x_1^i+w_2^i\cdot x_2^i}{w_1^i+w_2^i},\ \text{where weight } w_j^i=\frac{1}{(\sigma_j^i)^2}\\ &= \frac{(\sigma_2^i)^2\cdot x_1^i+(\sigma_1^i)^2\cdot x_2^i}{(\sigma_2^i)^2+(\sigma_1^i)^2} \qquad (3.28)\\ \sigma^i &= (w_1^i+w_2^i)^{-1/2}\\ &= \frac{\sigma_1^i\cdot\sigma_2^i}{\sqrt{(\sigma_2^i)^2+(\sigma_1^i)^2}} \qquad (3.29)\end{aligned}$$

3.11 Monte Carlo Simulations

The primary tool to correct for the PHENIX limited acceptance and the reconstruction efficiencies is the simulation software PISA ("PHENIX Integrated Simulation Application"), developed within the framework of GEANT3 [138]. PISA allows to reconstruct simulated particles using the same analysis software as for the real data. The hadron decays are generated using the PHENIX internal single particle generator, *EXODUS*. The general strategy to derive *acceptance* × *reconstruction* efficiency is described below.

Event Generation Using EXODUS In the first stage, the ϕ, $\omega \rightarrow e^+e^-$ decays were generated using *EXODUS*, with the following input specifications:

- flat vertex distribution within $|\, z \,| < 30$ cm.
- flat rapidity distribution within $|y| \leq 0.5$ and uniform in ϕ: $0 \leq \phi \leq 2\pi$.
- exponential transverse momentum distribution,

  $$dN/dp_T = p_T exp(-\frac{m_T}{T}),$$

  where T is the inverse slope equal to 366 MeV [61] for ϕ meson, whereas for ω a flat p_T distribution was used. A Gounaris Sakurai [139] parameterization with natural width parameter Γ set to the PDG value was used to define the resonance spectral shape.

Detector Simulation (PISA) In the next step, the generated ϕ, $\omega \rightarrow e^+e^-$ decays are passed through PISA. PISA tracks the primary particle, as well as secondaries produced from the interactions with the detector material, through the detector and simulates the detailed response of each subsystem to produce hit information, as it would appear in the data.

Reconstruction The PISA output hit information is then run through the PHENIX reconstruction software [115], that tunes the detector response to a set of characteristics (dead and hot channel maps, gains, noise levels etc) that describe the performance of each subsystem during a particular "reference run" selected from the real data, performs inter-detector hit association and builds tracks. The output format of the reconstructed simulated data is exactly the same as the real data format and thus the simulated data are processed with the same analysis code and the same cuts, that are used for the real data.

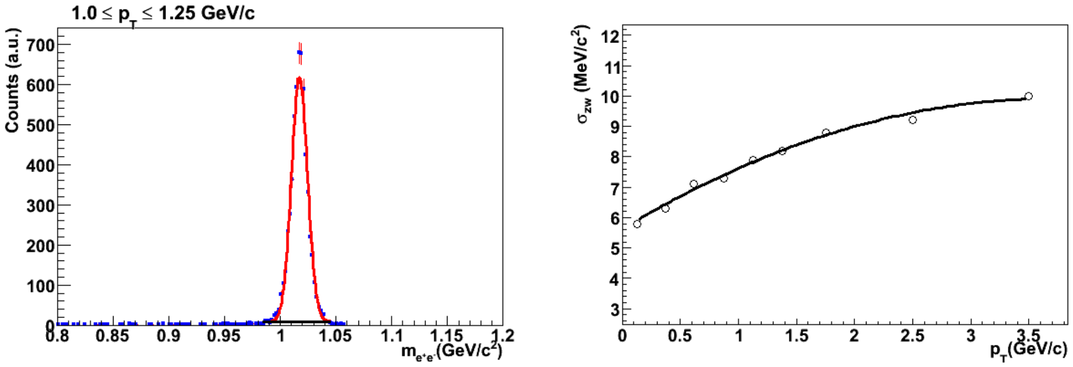

Figure 3.30: Left panel: an example of the $\phi \rightarrow e^+e^-$ reconstructed mass distribution for the p_T bin ($1.0 \leq p_T < 1.25$ GeV/c), in a zero-width simulation, fitted to a Gaussian function. Right panel: p_T dependence of the extracted detector mass resolution.

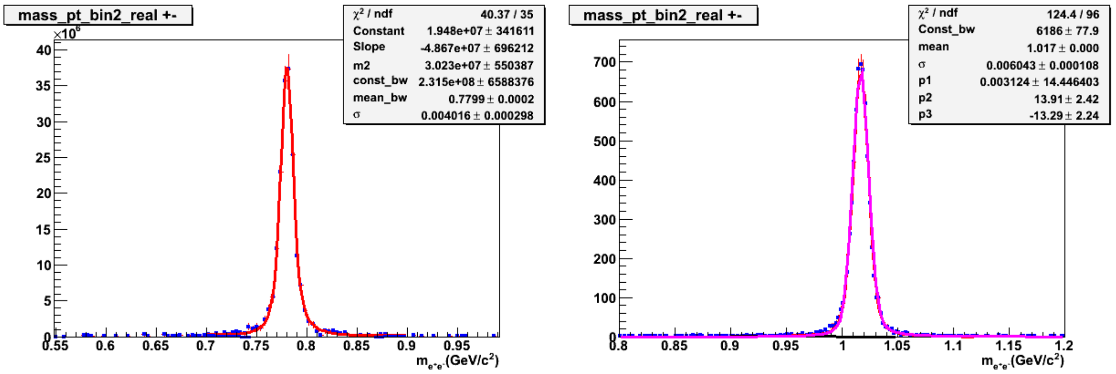

Figure 3.31: Left panel: an example of the $\omega \rightarrow e^+e^-$ reconstructed mass distribution in the simulation for the p_T bin ($1.0 \leq p_T < 1.25$ GeV/c), fit to a RBW convoluted with a Gaussian function. Right panel: the same for $\phi \rightarrow e^+e^-$.

Zero-width Simulation The spectral shape of the reconstructed resonance in the real data results from the convolution of the p_T-dependent detector mass resolution and the resonance natural width. In order to separate out the two effects, we run a special simulation by setting the natural width of the resonance to zero. The reconstructed resonance in this case has only detector resolution effects and thus fitting the resonance shape to a Gaussian function gives the detector mass resolution. An example of the reconstructed ϕ mass distribution for one p_T bin, obtained in this zero-width simulation is shown in the left panel of Fig. 3.30. The tail towards low masses on the left side of the peak is due to Bremsstrahlung and multiple scattering of the electrons in the detector. The resonance shape is fit to a Gaussian function having σ as a free parameter and a polynomial function of second degree for the background. The σ- values obtained from the fits are taken to represent the detector mass resolution. The p_T dependence of σ is shown in the right panel of Fig. 3.30. These σ values are used to constrain the fits used for the regular simulation and data (see Section 3.9.1). An example showing the fits to the $\omega \rightarrow e^+e^-$ and $\phi \rightarrow e^+e^-$ for the regular simulation for one p_T bin are shown in Fig. 3.31.

A summary of the various simulation projects used in this thesis is given in Table 3.3.

3.11.1 Comparison Between Data and Simulation

The matching of the reconstructed tracks to the EMCal along z and ϕ directions and the energy-momentum matching, $E/p-1$, in the simulation, need to be translated in terms of reduced variables in order to apply the same cuts in units of sigma as in the real data. This was done in the same way as explained in the Section 3.4.2 for the real data. An

Analysis	Configuration	$N_{evts}(\times 10^6)$	y	φ *radians*	$z_{vtx}(cm)$	p_T range(GeV)(shape)	Γ(MeV)
			$\phi \rightarrow e^+e^-$				
$p+p$	Run5	10	± 0.6	0-2π	± 30	0-5(exp)	0
$p+p$	Run5	10	± 0.6	0-2π	± 30	0-5(exp)	PDG
$d+Au$	Run8	10	± 0.5	0-2π	± 30	0-8(exp)	PDG
			$\omega \rightarrow e^+e^-$				
$p+p$	Run5	10	± 0.6	0-2π	± 30	0-5 (flat)	PDG
$d+Au$	Run8	10	± 0.5	0-2π	± 30	0-8 (flat)	PDG
			Single electrons (e^+), (e^-)				
$d+Au$	Run8	10	± 0.5	0-2π	± 30	0-5 (flat)	

Table 3.3: Summary of the various simulation projects used, (exp stands for exponential)

example showing these reduced variables for one EMCal sector $E0$ is shown in Fig. 3.32. Fig. 3.33 shows a comparison of the eID variables, $n0$, $emcd\phi$, $emcdz$ and dep in data and simulation. Good agreement between them can be seen.

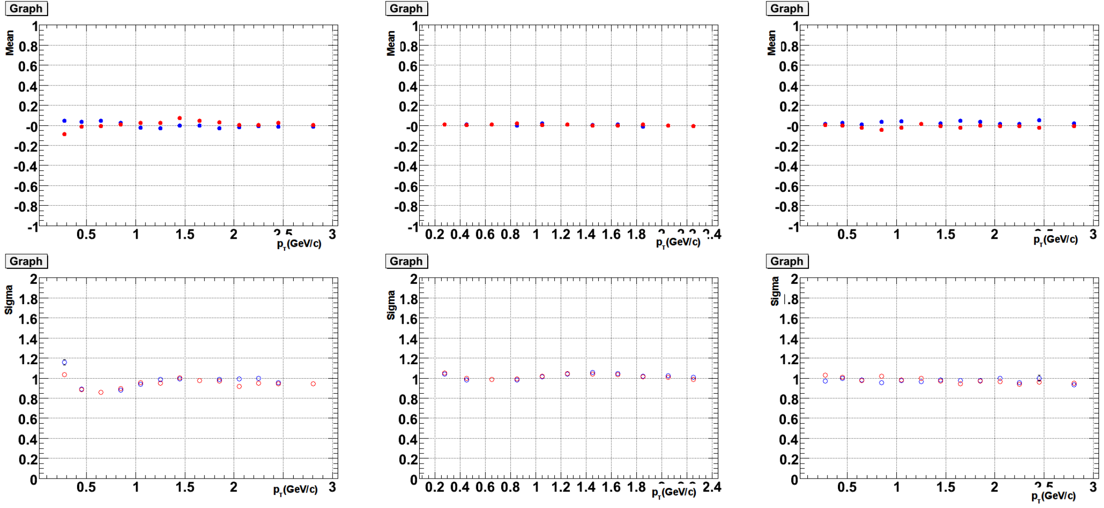

Figure 3.32: The top panel shows the mean of $emcd\phi$, $emcdz$ and dep variables as a function of p_T for e^+ (blue) and e^- (red) for $d+Au$ simulation and the bottom panel shows the corresponding sigma values.

3.11.2 Acceptance Comparison

It is important that the simulation has the same acceptance as that of the real data for all the subsystems involved in the analysis. Therefore we apply the same DC/PC1 fiducial cuts, and the same RICH and EMCal dead/noisy towers maps, that were used in the real data analysis, as explained in Section 3.5. For these studies, we use the simulation

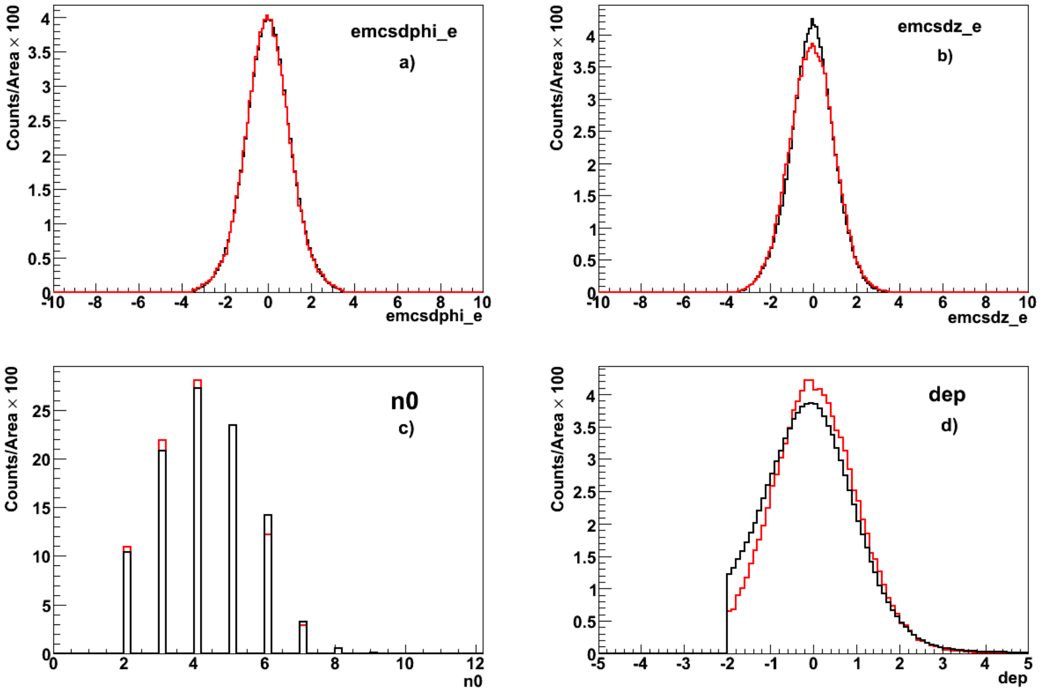

Figure 3.33: Comparison of eID variables *emcd*ϕ, *emcdz*, $n0$ and *dep* in data (black) and in simulation (red).

of single electrons, generated with the specifications mentioned in Table 3.3. Since the electrons are generated with a flat p_T distribution, we weigh the p_T of the reconstructed electrons according to the distribution from the real data of MB electrons. Fig. 3.34 shows an example of acceptance comparison for the $p+p$ analysis in terms of ϕ (bottom panel) and *zed* (top panel) of the DC, between simulation and data, after all the cuts were implemented. The MC histograms were normalized to represent the same total integral as in the data. The acceptance in simulation seems to be in good agreement with that of the data.

3.12 Acceptance and Reconstruction Efficiency Correction

The reconstructed simulated files are passed through the same analysis chain as that applied to the real data. For the cases, where the input p_T distribution was flat, we weigh both the generated and reconstructed p_T distribution of the meson, using the measured p_T distribution of the resonance. The weighing takes cares of the momentum smearing effect, which is significant in the low p_T region as compared to high p_T (> 1 GeV/c)

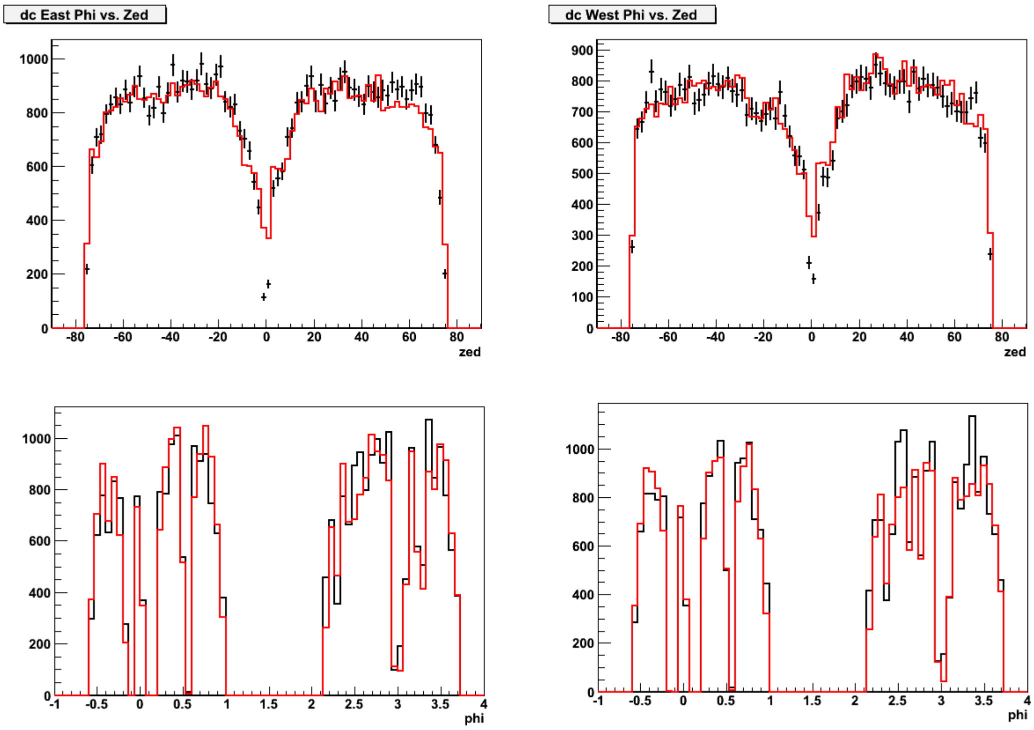

Figure 3.34: The top two panels show a comparison between MC (red) and data (black) for the DC (zed) distribution for the east and west arm, and the bottom two panels represent the comparison of DC (ϕ) distribution.

where it is negligible.

The correction factor for a given p_T bin is then defined as $CF = \frac{N^{gen}(p_T)}{N^{rec}(p_T)}$, where N^{gen} and N^{rec} correspond to the number of generated and reconstructed mesons in the given p_T bin, respectively. This correction factor represents the geometrical acceptance and pair reconstruction efficiency and also has detector mass resolution effects. Fig. 3.35 shows the correction function for Run5 $p+p$ and Run8 $d+Au$ collisions, for both ω and ϕ mesons. The differences in the CF between the two runs are due to differences in the inactive/noisy areas and analysis cuts.

3.13 Pair ERT Efficiency

The measured p_T spectra need to be corrected for the ERT trigger bias (Section 3.6) effects. This is done by passing the reconstructed simulated e^+e^- decays of the meson through an emulator of the ERT trigger. For the $d+Au$ collisions, this emulator uses the RICH and EMCal supermodule dependent single electron ERT efficiency curves, determined as explained in Section 3.6. For the Run5 $p+p$ data, this was done for each arm

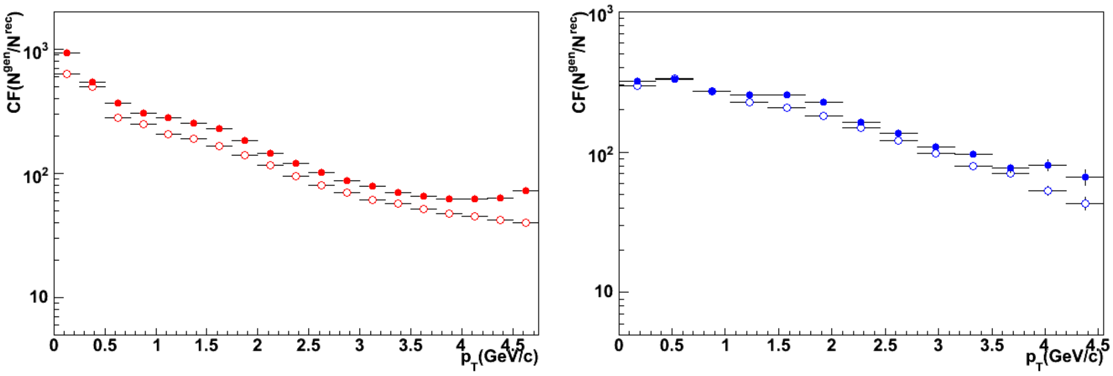

Figure 3.35: Left panel: *CF* for ω. Right panel: *CF* for ϕ. Open and closed symbols correspond to Run5 $p+p$ and Run8 $d+Au$, respectively.

and each sector separately. Since the ERT trigger is a single electron trigger, it works for the given meson as a logical *OR*. Both electron and positron of each reconstructed meson are examined for the trigger condition as follows:

- Both electron and positron are assigned an individual weight w, generated randomly with a flat distribution between 0 and 1.
- The meson satisfies the ERT trigger if either the electron or the positron fulfills the trigger condition $w \geq \varepsilon_{ERT}$, where ε_{ERT} is the ERT efficiency for the momentum of the electron or positron considered, determined using the ERT curves (Section 3.6) for the given EMCal or RICH supermodule, that is pointed to by the given electron or positron.

The ϕ/ω-meson trigger efficiency is then obtained by dividing the number of ϕ/ω surviving the ERT trigger to the total number of ϕ/ω without emulating the trigger. Fig. 3.36 shows the pair trigger efficiency determined using the above mentioned procedure in $p+p$ and $d+Au$ collisions. These efficiencies are fitted to a Fermi function and the parameterized curves are used to calculate the trigger efficiency correction (ε_{ERT}) to be applied to the final invariant p_T spectrum.

3.14 eID Efficiency

Slight differences in the distributions of the eID parameters in real data and simulation can lead to a different fraction of signal loss in real data and simulation and hence needs to be corrected. To study these possible effects, we compare the electron identification efficiency in data and simulation. The absolute electron identification efficiency is directly

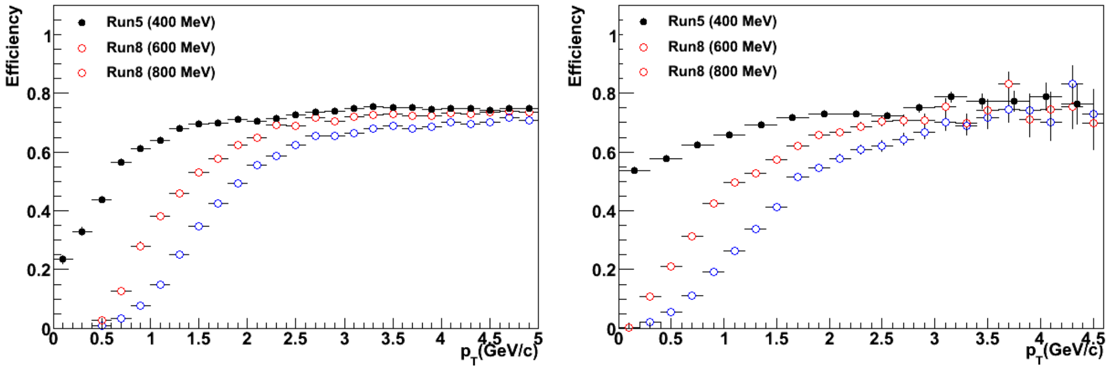

Figure 3.36: The pair ERT efficiency for ω (left) and ϕ (right), for Run5 (400 MeV), Run8 (600 MeV) and Run8 (800 MeV) data samples.

determined using data taken in a special set of runs with a 1.7% X_0 brass converter material installed around the beam pipe, so as to have a high yield of conversion pairs. These special runs can be seen in the left panel of Fig. 3.18 with a high electron yield. The basic idea is to reconstruct the photons that get converted in this material giving us a pure electron sample to study the electron identification efficiency. In the mass spectrum in the left panel of Fig. 3.37 (black line), it is seen that the converter produces a significant increase in the 20 MeV peak w.r.t the Dalitz peak, as compared to the case with no converter (see Fig. 3.24).

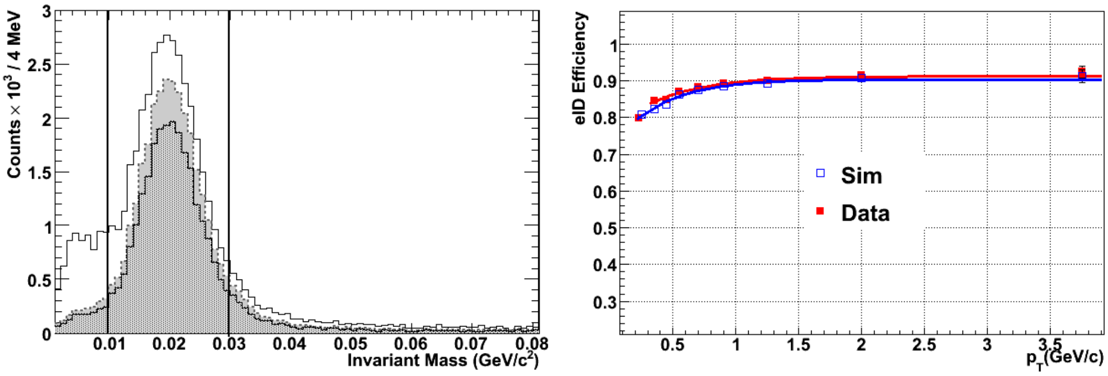

Figure 3.37: Left panel: the peak due to conversion electrons in the converter runs for the different cases discussed in the text. The vertical lines correspond to the mass window for counting e^+e^- pairs. Right panel: the eID efficiency obtained in the simulation (blue) and data (red).

To determine the electron identification efficiency, we apply a ϕ_V cut (see Section 3.7 for details) to select the conversion pairs in the 20 MeV peak and count the number of e^+e^- pairs in the window indicated by the two vertical lines, for two cases. In the first case, we apply strong eID cuts only on one leg of the pair (dashed line), whereas the second leg has a very loose eID cut ($n0 > 0$ (see Section 3.4.1) which practically eliminates the tracks that do not have matching hit in RICH PMTs). For the second case we apply the same eID cuts as in the analysis to the second leg in the pair (filled histogram). The ratio of these two cases gives us the eID efficiency, which comes to about 86% on average for the eID cuts used in the present analysis. The same procedure is applied to the simulation where we count the ϕ signal for the two cases. The two efficiency curves obtained from simulation and data, fitted with a Fermi function are shown in the right panel of Fig. 3.37. The simulation and data show very good agreement and hence no extra correction was applied.

3.15 Run-by-Run Correction

Th data used in the analysis is collected over a large period of time and uses several subsystems needed for the tracking and the electron identification. The performance of the different subsystems can change over time which leads to variations in the yield. These run-by-run variations are corrected by monitoring the average number of inclusive electrons per event for each run i (ε^i_{e+}, ε^i_{e-}) and normalizing it to the same quantity in the reference run that was used in the simulations for reconstruction. This is done as follows:

We denote the number of electrons in a given run i by N^i_{e+}, N^i_{e-}, the number of events as N^i_{evt}, and the same quantities in the reference run by $N^{ref.run}_{e+}$, $N^{ref.run}_{e-}$ and $N^{ref.run}_{evt}$. Then:

$$\varepsilon^i_{e+} = \frac{N^i_{e+}/N^i_{evt}}{N^{ref.run}_{e+}/N^{ref.run}_{evt}}; \quad \varepsilon^i_{e-} = \frac{N^i_{e-}/N^i_{evt}}{N^{ref.run}_{e-}/N^{ref.run}_{evt}} \tag{3.30}$$

$$\varepsilon^i = \varepsilon^i_{e+} \cdot \varepsilon^i_{e-} \tag{3.31}$$

The global RBR efficiency is then calculated as the weighted average of the electron yield per event in each run i.

$$\varepsilon_{RBR} = \frac{\sum \varepsilon^i \cdot N^i_{evt}}{\sum N^i_{evt}} \tag{3.32}$$

Fig. 3.38 shows the run-by-run variation of ε^i as a function of run number for Run5. ε_{RBR} was calculated to be 0.96 for Run5 $p+p$.

3.16 Bin-width Correction

Plotting the extracted yield for a given p_T bin at the center of the bin, for the case of an exponentially falling spectrum introduces an error, as it does not represent the center of

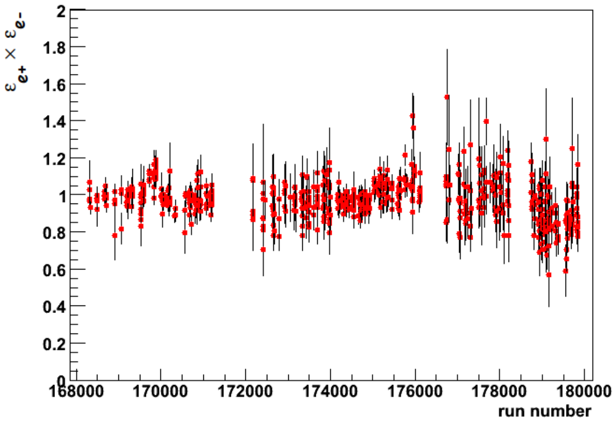

Figure 3.38: Run-by-run variation of the e^+ and e^- yield per event in the $p+p$ analysis.

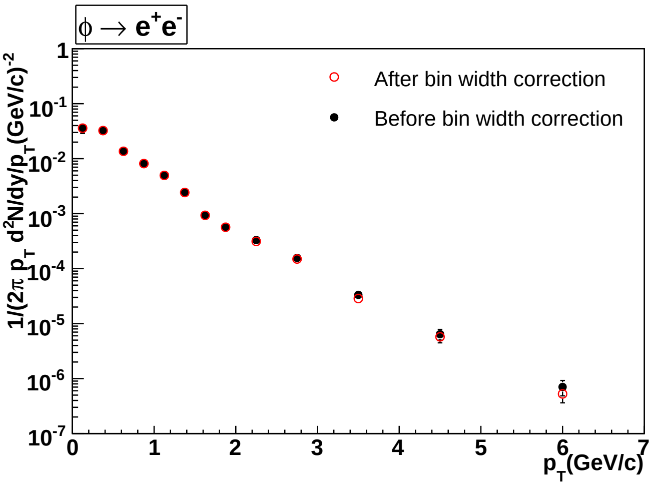

Figure 3.39: Example showing the effect of the bin-width correction.

gravity of the distribution within the bin [140]. This effect is more significant for bins with large width and steeper falling slope and results in a shift of the average p_T of the data relative to the center of the bin. In general, one can follow either of the two approaches mentioned below, to correct for this effect:

1. move the yield for a given point vertically and leave the data point along the p_T-axis unchanged, at the center of the bin.
2. move the data point along the p_T-axis and leave the yield unchanged.

The results presented here are corrected following the first approach. We first fit the measured spectrum with a function f, which should be an approximation to the true function. Here we used an exponential or Levy function [141]. For a given p_T bin, using this fitted function, we calculate the ratio r between the average yield in this bin and the value of the function at the bin center p_T^c *i.e*,

$$r = \frac{\frac{1}{\Delta}\int\limits_{p_T^c-\Delta/2}^{p_T^c+\Delta/2} f(p_T)dp_T}{f(p_T^c)} \tag{3.33}$$

where Δ represents the bin width. The corrected yield for a given p_T bin is then calculated as:

$$\left.\frac{dN}{dp_T}\right|_{corrected} = \frac{\left.\frac{dN}{dp_T}\right|_{uncorrected}}{r} \tag{3.34}$$

An example showing the effect of bin-width correction can be seen in Fig. 3.39. The effect is negligible for small sized bins as seen at low p_T, whereas the effect is relatively larger for the wider bins at high p_T.

3.17 Systematic Uncertainties

The present section summarizes the various sources of systematic uncertainties that contribute to the invariant spectra and cross-section determination. In most cases, the systematic errors on the invariant spectra were estimated by varying the parameters, recalculating the invariant cross-section and monitoring their deviations from the baseline value. The RMS of the resulting variation is assigned as systematic error. The main sources of systematic uncertainties are:

Raw Yield Extraction Uncertainty For both $p+p$ and $d+Au$ analyses, the uncertainty due to the fit procedure in the yield extraction was estimated by a) varying the fit function that describes the combinatorial background, by a second or third degree polynomial or an exponential. Also a combined fit to both ω and ϕ was considered, b) varying the size of the window to count the signal (2σ *or* 2.5σ *or* 3σ), iii) varying the mass range used in the fit to determine the shape of the background under the ϕ/ω-peak. For the $d+Au$ analysis, the error due to the uncertainty in the normalization on the mixed event background was estimated by varying the region of normalization. For each case, the whole analysis chain to extract the invariant yield was repeated and the resulting RMS/mean for each p_T bin was assigned as systematic uncertainty.

Monte Carlo Simulation The main sources of the systematic uncertainties in the simulation are due to the fiducial mismatch between data and Monte Carlo as discussed in Section 3.11.2. This was evaluated by taking the ratio of the integral yield of electrons that fall into the acceptance in data, to the corresponding integral yield in MC, obtained from the comparison of DC *zed* and ϕ distributions, shown in Fig. 3.34. In these figures, the MC was normalized to the data in a small two-dimensional $\varphi - zed$ window, where there are no dead areas. The variation of the data to the MC ratios, determined outside the normalization window for different normalization windows gives an estimation of the systematic error.

Uncertainty Due to Electron Identification The uncertainty due to electron identification cuts was determined by varying the eID parameters ($n0$, dep, $emcd\phi, emcdz$) one at a time, both in the data and simulation. Each of the variable was varied between 1.0 σ to 3.5 σ values. For each set of parameters, the whole procedure (yield extraction, correction function etc.) was repeated. The RMS/mean of all the combinations as a function of p_T is fitted to a constant function as shown in Fig. 3.40. The resulting value of the fit is assigned as systematic error, which came to be about 10% for ω and 9% for ϕ.

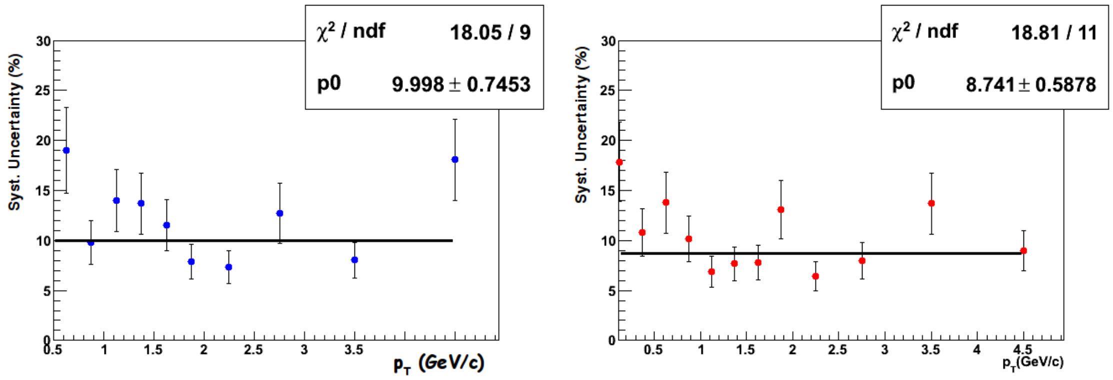

Figure 3.40: Left panel: systematic uncertainties due to eID cuts for ω. Right panel: same for ϕ. The points are fitted to a constant function.

ERT Efficiency Uncertainty The systematic uncertainties in the ERT efficiency are evaluated by varying the single electron efficiency curves for every EMCal and RICH supermodule. Every point on a given EMCal/RICH supermodule trigger efficiency curve, as shown in Fig. 3.41, is varied randomly according to a Gaussian distribution, with mean and sigma given by the point and its statistical error, respectively.

The new points thus obtained are fitted again and a new pair efficiency curve is generated following the same procedure as described in Section 3.13. This procedure was repeated 20 times and the resulting RMS/mean of the pair efficiencies for a given p_T bin was assigned as its error. An example showing the variations of points for one EMCal and RICH supermodule is shown in Fig. 3.41. For the $p+p$ analysis, the same procedure was followed, but it was done for the ERT efficiency curves obtained for each sector separately.

Momentum Scale Uncertainty To estimate the errors related to the uncertainty of the DC-PC1 momentum scale, we varied the momenta of reconstructed particles in simulation by ±0.7% (DC momentum resolution), and calculated the corresponding variation in the

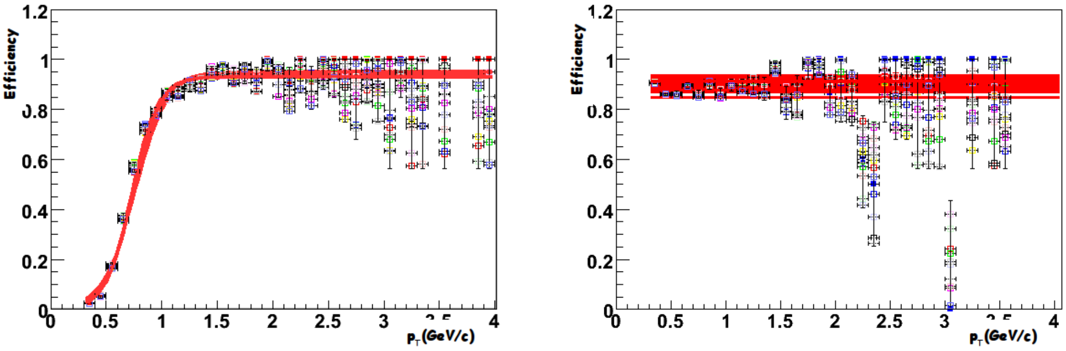

Figure 3.41: Left panel: random variation of points for one EMCal SM, together with the fits. Right panel: same for one RICH SM.

correction factor. The results are summarized in Table 3.6 and Table 3.7 for ω and ϕ, respectively.

Run-by-Run Efficiency Uncertainty For the $p+p$ analysis, this uncertainty was estimated by taking the RMS of the spread of number of electrons and positrons pairs per event selected using the standard eID cuts from the MB data sample. This came to be about 5%.

Branching Ratio Uncertainty The branching ratio uncertainty for $\omega \rightarrow e^+e^-$ and $\phi \rightarrow e^+e^-$ is equal to 1.7% and 1.3% respectively [142].

Summary The total systematic error on the invariant p_T spectra were obtained by the quadratic sum of the individual contributions. Table 3.4 gives a summary of the systematic errors in $p+p$ for ω and ϕ. Table 3.5 gives the systematic errors for 600 and 800 MeV $d+Au$. Table 3.6 and Table 3.7 summarize the combined (600+800 MeV) systematic errors on ω and ϕ for the $d+Au$ analysis.

All the systematic error contributions mentioned above, are classified into three different categories:

- Type A: errors that fluctuate from point to point, such as the statistical error, and errors where the p_T correlation is unknown, *e.g.* the uncertainty in the raw yield extraction.
- Type B: errors that are correlated in p_T and move all points into the same direction, but potentially by different relative amounts, such as the uncertainty on the ERT efficiency and momentum scale.

- Type C: global scale uncertainties, which move all points by the same relative amount. This includes *e.g.* the normalization error of 9.6% in the case of the $p+p$ measurement. The uncertainty in the determination of N_{coll} also belong to this category of errors.

p_T bin	Type	0-0.25	0.25-0.5	0.5-0.75	0.75-1	1-1.25	1.25-1.5	1.5-2	2-3	3-4
$\omega \rightarrow e^+e^-$										
Bkg. Shape	A	19.2	5.2	6.4	4.8	2.1	3.0	4.0	9.2	4.5
ert eff		2.4	2.4	2.3	2.0	1.8	1.6	1.3	1.0	0.9
eID		10%								
Fiducials		5%								
RBR		5%								
BR		1.7%								
$\sqrt{(\delta\varepsilon_{bias}2+\delta\sigma_{BBC}2)}$		9.9%								
Total		25.0	16.9	17.3	16.7	16.1	16.2	16.4	18.4	16.5
$\phi \rightarrow e^+e^-$										
Bkg shape		4.4	3.8	3.1	2.9	7.0	1.0	4.2	1.0	2.0
ert eff		0.7	0.5	0.4	0.4	0.4	0.5	0.7	1.2	1.7
eID		9%								
Fiducials		5%								
RBR		5%								
BR		1.3%								
$\sqrt{(\delta\varepsilon_{bias}2+\delta\sigma_{BBC}2)}$		9.9%								
Total		15.8	15.7	15.5	15.5	16.7	15.3	15.8	15.3	15.4

Table 3.4: Summary of the systematic errors for ω and ϕ in $p+p$ collisions

p_T bin	0-0.25	0.25-0.5	0.5-0.75	0.75-1	1-1.25	1.25-1.5	1.5-1.75	1.75-2	2-2.5	2.5-3	3-4	4-5	5-7
ω (600 MeV)													
raw yield(0-88)		8.4	8.0	7.6	7.2	6.9	6.6	6.3	5.9	5.6	5.3	5.3	5.2
raw yield(0-20)		21.4	18.1	15.3	12.8	10.8	9.02	7.63	6.19	5.48	7.01	13.9	10
raw yield(20-40)		9.0	8.0	7.19	6.57	6.11	5.79	5.61	5.62	6.14	8.02	12.6	12
raw yield(40-60)		13	11	9.3	7.7	6.4	5.4	5.5	4.6	4.2	4.3	8.8	16.3
raw yield(60-88)		17.3	15.9	14.5	13.3	12.1	11	10	8.7	7.3	5.7	7.9	19.6
ert		18	7.2	5.3	2.6	1.7	1.1	1.0	0.8	0.7	0.7	0.8	0.8
ω (800 MeV)													
raw yield(0-88)			15	12.5	10.6	9	7.59	6.4	5.04	4	4.12	7.4	6.0
raw yield(0-20)			16	14.7	12.6	10.7	8.99	7.5	5.66	3.92	2.87	4.4	4.5
raw yield(20-40)			12	10.3	9.95	9.61	9.28	8.95	8.47	7.84	6.92	5.74	5.7
raw yield(40-60)			18.9	15.7	12.8	10.5	8.5	6.97	5.49	5.02	7.52	9.9	8.9
raw yield(60-88)			10.7	9.17	7.8	6.6	5.59	4.76	4.86	5.3	5.83	7.09	9.4
ert			19.0	7.6	2.9	3.8	1.8	1.9	1.7	1.0	1.0	1.2	1.2
ϕ (600 MeV)													
raw yield(0-88)	7.16	6.84	6.53	6.22	5.92	5.63	5.34	5.07	4.66	4.16	3.45	2.62	6
raw yield(0-20)	12.9	11.4	9.98	8.7	7.56	6.55	5.69	4.95	4.11	3.46	3.51	5.48	7
raw yield(20-40)	10.1	9.01	7.99	7.06	6.22	5.47	4.82	4.26	3.59	3.02	2.87	3.98	6
raw yield(40-60)	9.94	8.22	6.71	5.4	4.3	4.0	4.1	3.5	3.5	3.0	4.07	9.51	10.9
raw yield(60-88)	5.94	5.91	5.91	5.94	5.99	6.06	6.17	6.29	6.53	6.94	7.74	9.16	9.96
ert	21	1.7	0.6	0.5	0.5	0.6	0.8	1.0	1.2	1.4	1.51	1.5	1.5
ϕ (800 MeV)													
raw yield(0-88)	15.8	14.1	12.6	11.1	9.82	8.63	7.57	6.62	5.44	4.28	3.47	4.09	4.0
raw yield(0-20)			11.9	10.8	9.71	8.75	7.86	7.06	6.01	4.88	3.8	3.49	4.0
raw yield(20-40)		12.2	10.8	9.62	8.51	7.52	6.63	5.86	4.9	4.02	3.52	4.42	5.0
raw yield(40-60)		8.64	7.07	6.44	6.76	6.03	6.25	6.41	5.54	5.54	5.14	3.84	5.0
raw yield(60-88)		9.6	8.25	6.95	5.71	5.52	5.38	5.31	4.29	4.47	5.15	5.83	5.24
ert		5.4	3.3	2.0	1.7	1.7	1.5	1.4	1.5	1.7	1.8	1.8	1.8

Table 3.5: Summary of the raw yield and ERT systematic errors for 600 and 800 MeV for the ω and ϕ in $d+Au$ collisions.

p_T bin	0-0.25	0.25-0.5	0.5-0.75	0.75-1	1-1.25	1.25-1.5	1.5-1.75	1.75-2	2-2.5	2.5-3	3-4	4-5	5-7
raw yield(0-88)		8.4	17.0	14.6	12.8	11.3	10.0	9.0	7.8	6.9	6.8	9.1	8.0
raw yield(0-20)		21.4	24.1	21.2	18.0	15.2	12.7	10.7	8.4	6.7	7.6	14.6	11
raw yield(20-40)		9	14.4	12.6	11.9	11.4	10.9	10.6	10.2	10.0	10.6	13.8	13.3
raw yield(40-60)		13	21.9	18.2	15.0	12.3	10.0	8.9	7.2	6.6	8.7	13.3	18.6
raw yield(60-88)		17.3	19.2	17.2	15.4	13.8	12.3	11.1	10.0	9.0	8.2	10.6	21.7
ert		18	7.2	9.3	3.9	4.2	2.1	2.1	1.9	1.2	1.2	1.4	1.4
eID	10%												
Mom. scale	1.6	2.1	2.2	1.2	1.7	1.5	1.7	2.2	2.1	2.8	3.3	4.8	5.3
Fiducials	7.0%												
BR	1.7%												
$\sqrt{(\delta^2_{\varepsilon_{bias}}+\delta^2_{\sigma_{BBC}})}$	7.86%												
Total(0-88)		24.8	30.3	22.7	19.9	19.0	17.9	17.4	16.8	16.4	16.5	17.9	17.4
Total(0-20)		31.6	34.8	27.4	23.6	21.5	19.6	18.4	17.1	16.4	16.8	21.2	19
Total(20-40)		25.0	29.0	21.4	19.3	19.1	18.5	18.3	18.0	18.0	18.4	20.7	20.4
Total(40-60)		26.7	33.3	25.2	21.3	19.6	18.0	17.4	16.5	16.3	17.4	20.4	24.2
Total(60-88)		29.0	31.6	24.4	21.6	20.6	19.3	18.6	17.9	17.4	17.1	18.8	26.7

Table 3.6: Summary of the systematic errors for the ω in $d+Au$ collisions

p_T bin	0-0.25	0.25-0.5	0.5-0.75	0.75-1	1-1.25	1.25-1.5	1.5-1.75	1.75-2	2-2.5	2.5-3	3-4	4-5	5-7
raw yield (0-88)	17.3	15.7	14.2	12.8	11.5	10.3	9.3	8.3	7.2	6.0	4.9	4.9	7.2
raw yield (0-20)	12.9	11.4	15.5	13.8	12.3	10.9	9.7	8.6	7.3	6.0	5.2	6.5	8.1
raw yield (20-40)	10.1	15.2	13.5	11.9	10.5	9.3	8.2	7.2	6.1	5.0	4.6	6.0	7.8
raw yield (40-60)	9.9	11.9	9.8	8.4	8.0	7.2	7.5	7.3	6.6	6.3	6.6	10.3	12.0
raw yield (60-88)	5.9	11.3	10.2	9.1	8.3	8.2	8.2	8.2	7.8	8.3	9.3	10.9	11.3
ert	21	5.7	3.4	2.0	1.8	1.8	1.7	1.7	1.9	2.2	2.3	2.4	2.4
eID	9%												
Mom. scale	2.0	2.2	1.3	1.4	1.8	1.4	1.7	2.1	2.9	2.1	3.4	4.4	5.3
Fiducials	7.0%												
BR	1.3%												
$\sqrt{(\delta^2_{\varepsilon_{bias}}+\delta^2_{\sigma_{BBC}})}$	7.86%												
Total(0-88)	30.7	21.8	20.3	19.0	18.2	17.5	16.9	16.4	16.0	15.4	15.3	15.6	16.6
Total(0-20)	28.4	19.0	21.2	19.8	18.8	17.8	17.1	16.6	16.1	15.5	15.4	16.1	17
Total(20-40)	27.2	21.5	19.8	18.5	17.6	16.9	16.3	15.9	15.6	15.1	15.2	15.9	16.9
Total(40-60)	27.2	19.3	17.5	16.4	16.3	15.8	16.0	15.9	15.8	15.6	15.9	18.0	19.2
Total(60-88)	26.0	18.9	17.7	16.8	16.4	16.3	16.3	16.4	16.3	16.5	17.2	18.3	18.7

Table 3.7: Summary of the systematic errors for ϕ in the $d+Au$ collisions.

Chapter 4

Results and Discussion

The main aim of this thesis is to study the production of the ϕ and ω mesons via their dielectron decay channel in $p+p$ and $d+Au$ collisions. The results include invariant p_T spectra, the extraction of the rapidity density ($\frac{dN}{dy}$) and mean transverse momentum ($\langle p_T \rangle$), and a comparison to the hadronic decay modes. The nuclear modification factor R_{dAu} is also extracted and results are compared to charged hadrons results.

4.1 ϕ and ω Transverse Momentum Spectra

4.1.1 $p+p$ Collisions

The fully corrected invariant cross-sections of the ϕ and ω mesons in $p+p$ collisions are shown in the top panel of Fig. 4.1. The statistical errors are indicated by vertical lines and the filled boxes correspond to the systematic errors.

In the bottom panel, we show a compilation of meson cross-sections via several decay channels in $p+p$ collisions measured by PHENIX, at $\sqrt{s_{NN}}$ = 200 GeV [84, 85, 143–146]. The differential cross-sections exhibit an almost exponential shape at low p_T, a characteristic of soft processes, whereas at high p_T they exhibit a power law behavior as expected for particles produced in hard scattering processes. The lines in the figure show Levy fits [141, 147] to each individual data set. The Levy function is defined as:

$$E\frac{d^3\sigma}{dp^3} = \frac{d\sigma}{dy}\frac{(n-1)(n-2)}{2\pi nT(nT+m_0(n-2))}\left(1+\frac{\sqrt{p_T^2+m_0^2}-m_0}{nT}\right)^{-n} \tag{4.1}$$

where $\frac{d\sigma}{dy}$ is the absolute differential cross section, m_0 is the mass of the particle, T is the inverse slope parameter, and n is the additional Levy parameter. All parameters but m_0 are left free in the fit. The Levy function has an exponential behavior at low p_T, while at high p_T it exhibits a power law behavior. The Levy function describes pretty well all the mesons over their respective measured p_T range.

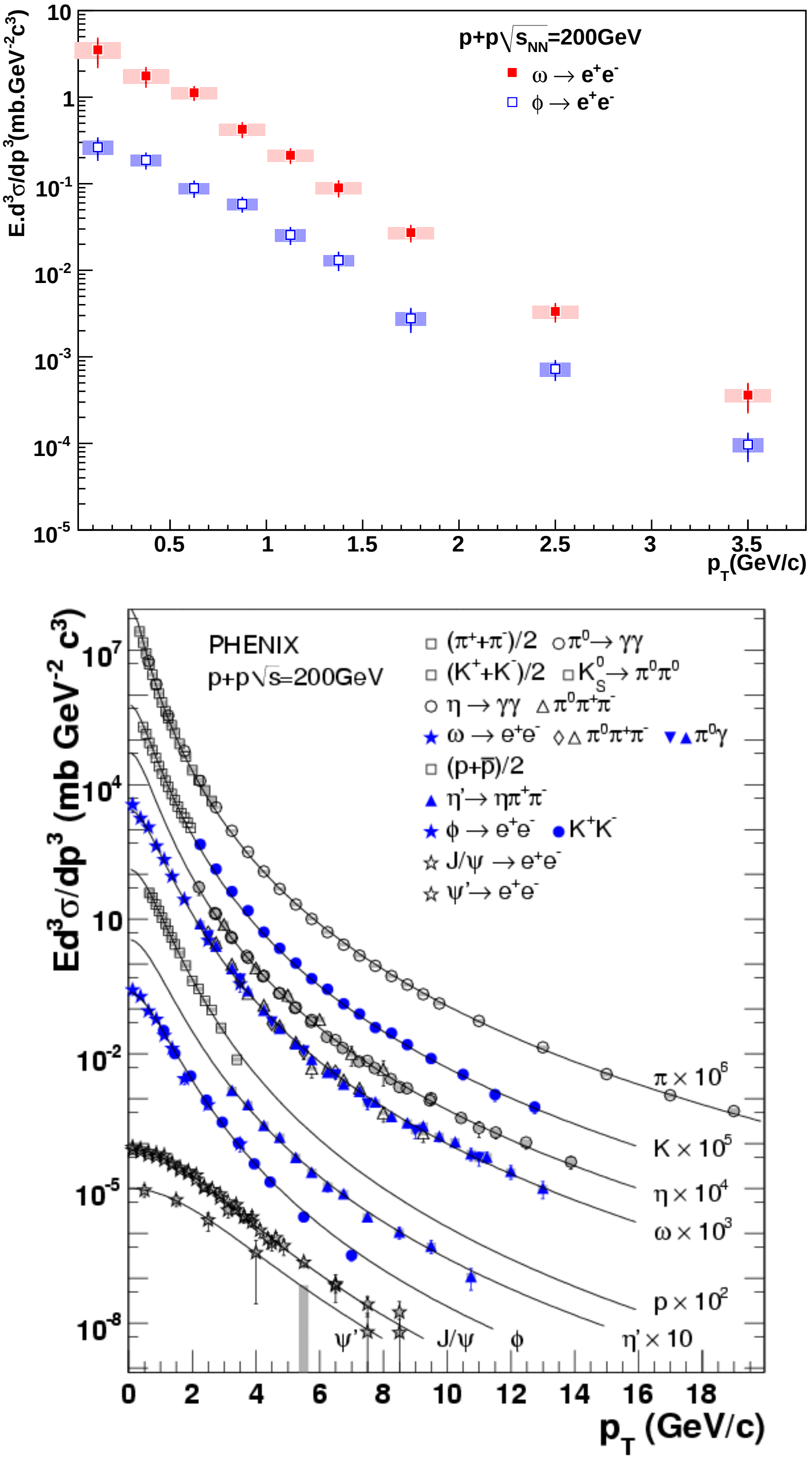

Figure 4.1: Top Panel: invariant cross section of the ω and ϕ mesons measured via their e^+e^- decay channel in $p+p$ collisions. The statistical errors are indicated by vertical lines, and the boxes represent the systematic errors. Bottom panel: compilation of meson production cross-sections in $p+p$ collisions at $\sqrt{s_{NN}}$ = 200 GeV, measured by PHENIX in different decay modes. The data are fitted to a Levy functional form (Eq. 4.1).

4.1.2 $d+Au$ collisions

As discussed in Section 3.10, the $d+Au$ data were taken with the ERT threshold settings of 600 and 800 MeV. The consistency between the two data sets is demonstrated in Fig. 4.2. The top panel shows the corrected invariant p_T spectra for the minimum bias case for the 600 and 800 MeV data sets, for both ω and ϕ. Good agreement is observed between the two data sets in the region of overlap. For a more precise comparison, the 600 MeV points are fitted to a Levy function (Eq. 4.1) and the bottom panel shows the ratios of the two sets (600 and 800 MeV) of points to this fit. As can be seen, the two analyses show good agreement within 1-2 σ. The final $d+Au$ results are obtained by taking the weighted average of the two data sets as was explained in Section 3.10.

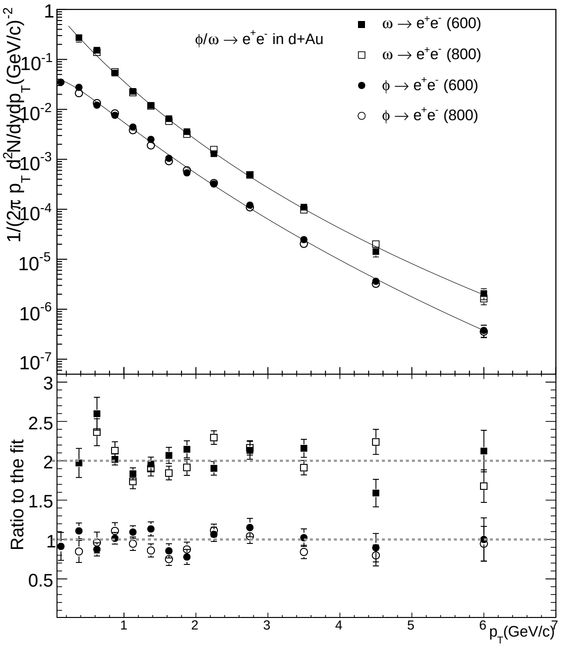

Figure 4.2: The top panel shows the measurements with the ERT threshold of 600 and 800 MeV, plotted together for each of the ω and ϕ meson. The 600 MeV measurements are fitted to a Levy function. The bottom panel shows the ratio of two measurements to this fit. For clarity, the ratios for ω are scaled by a factor of two.

The invariant transverse momentum spectra in $d+Au$ collisions are derived for minimum bias events, and for centrality classes 0-20%, 20-40%, 40-60%, 60-88%. They are shown in Fig. 4.3 and Fig. 4.4 for the ω and ϕ mesons, respectively. For clarity, the spectra are scaled vertically as quoted in the figures. The statistical errors are indicated by the vertical lines and the systematic errors are shown by the boxes. As in $p+p$ collisions, both ω and ϕ appear to have an exponential shape at low p_T and a power law at high p_T.

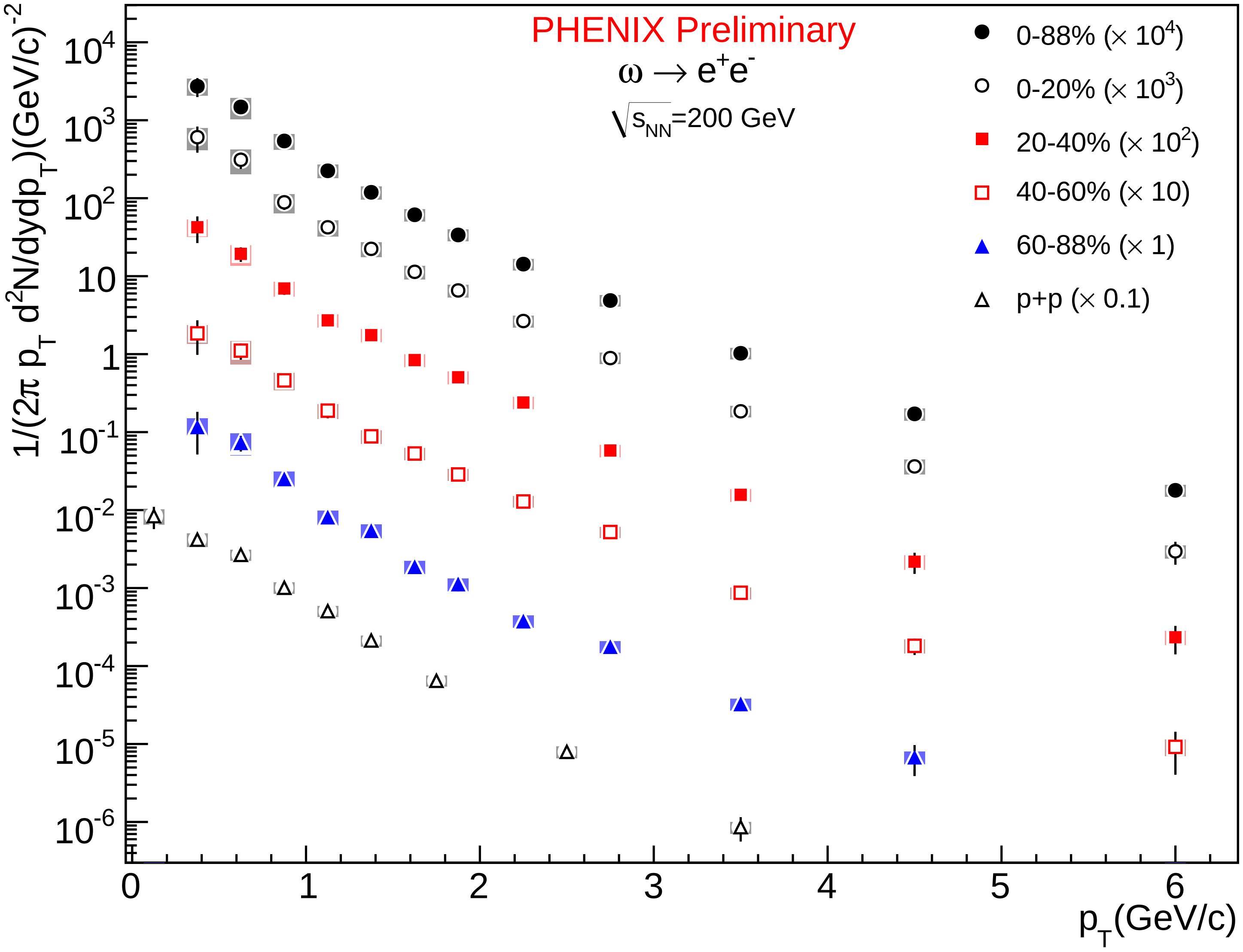

Figure 4.3: Transverse momentum spectra of the ω meson obtained in MB events and different centrality classes in $d+Au$ collisions. The spectra are scaled as quoted in the figure for clarity. The vertical bars correspond to the statistical errors and the boxes represent the systematic errors. The $p+p$ results are also shown for comparison.

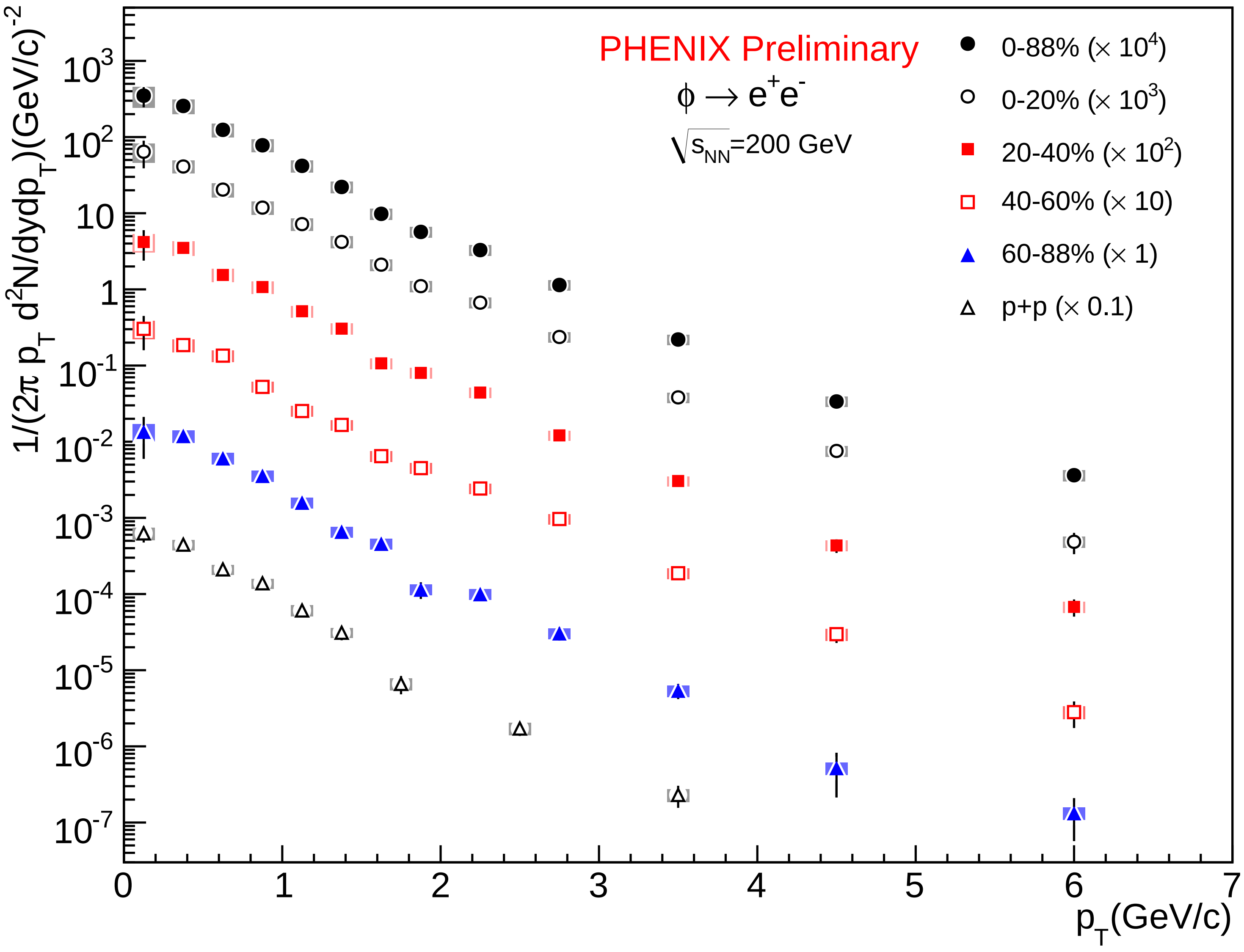

Figure 4.4: Transverse momentum spectra of the φ meson obtained in MB events and different centrality classes in $d+Au$ collisions. The spectra are scaled as quoted in the figure for clarity. The vertical bars indicate statistical errors and the boxes correspond to the systematic errors. The $p+p$ results are also shown for comparison.

4.2 Integrated Cross-section ($\frac{d\sigma}{dy}$) and Rapidity Density ($\frac{dN}{dy}$)

The particle rapidity density, $\frac{dN}{dy}$ (or integrated cross-section, $\frac{d\sigma}{dy} = \frac{dN/dy}{\sigma}$), in general can be determined via two methods:

1. fitting the measured invariant p_T or m_T spectra to a certain functional form and integrating the fit function to obtain $\frac{dN}{dy}$.
2. directly integrating the measured $\frac{d^2N}{dp_T dy}$ points, provided the measurements extend to low p_T region.

The first method is used when there are no measurements at low p_T, and it is widely applied. The derived values of $\frac{dN}{dy}$ are model dependent, since a specific functional form of the spectra is assumed, which may or may not correspond to the true shape in the extrapolated region. Furthermore, since most of the particle yield is at low p_T, the extrapolation in this region leads to large uncertainties. The second method, of course, does not suffer from these extrapolation uncertainties and is therefore the preferred method if it can be applied.

The ω, $\phi \rightarrow e^+e^-$ measurements in $p+p$ and $d+Au$ collisions carried out in this work, extend the coverage down to a $p_T = 0$. This enables us to make a direct and accurate measurement of the invariant cross section ($\frac{d\sigma}{dy}$) or the rapidity density ($\frac{dN}{dy}$) using the second method, without requiring any model dependent extrapolations.

We calculate the integrated $\frac{d\sigma}{dy}$ or $\frac{dN}{dy}$ directly, by summing up the $\frac{d^2\sigma}{dp_T dy}$ or $\frac{d^2N}{dp_T dy}$ over the measured p_T range. Mathematically it can be expressed as follows:

$$\frac{d\sigma}{dy} = 2\pi \sum_i \left(\left.\frac{d^2\sigma}{dy dp_T}\right|_i \times \Delta p_T^i \right) \tag{4.2}$$

$$or\ \frac{dN}{dy} = 2\pi \sum_i \left(\left.\frac{d^2N}{dy dp_T}\right|_i \times \Delta p_T^i \right) \tag{4.3}$$

The statistical and systematic errors on the data points are added in quadrature. The p_T spectra of $\phi \rightarrow e^+e^-$ and $\omega \rightarrow e^+e^-$ spectra in $p+p$ collisions are shown in Fig. 4.5, plotted in the form of $\frac{d^2\sigma}{dp_T dy}$. The resulting integrated values of $\frac{dN}{dy}$ for ω and ϕ obtained in $p+p$ and $d+Au$ collisions are summarized in the Table 4.2.

4.2.1 Comparison to the Results Obtained Using Different Functional Forms

Extracting the rapidity density using the first method described above is the usual practice. We therefore use commonly used functional forms to fit the measured spectra and

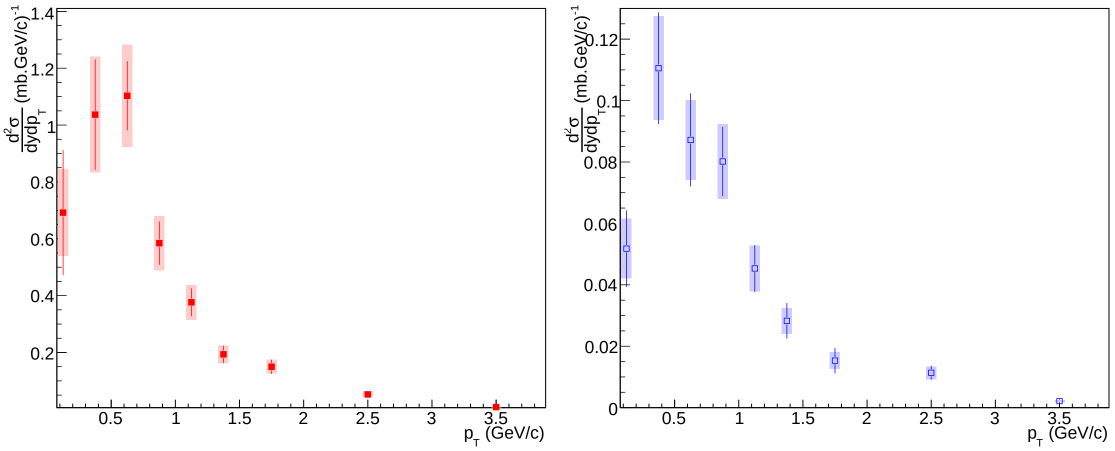

Figure 4.5: p_T spectra of ω (left panel) and ϕ (right panel) meson measured in $p+p$ collisions.

		$\omega \to e^+e^-$	$\phi \to e^+e^-$
	Centrality	$\frac{dN}{dy}$	$\frac{dN}{dy}$
$p+p$		$0.0995 \pm 0.0079 \pm 0.0079$	$0.0102 \pm 0.0007 \pm 0.0007$
$d+Au$	0-20%	$0.9877 \pm 0.1519 \pm 0.1602$	$0.1114 \pm 0.0079 \pm 0.0085$
	20-40%	$0.6836 \pm 0.1031 \pm 0.0866$	$0.0846 \pm 0.0058 \pm 0.0067$
	40-60%	$0.3715 \pm 0.0584 \pm 0.0499$	$0.0514 \pm 0.0041 \pm 0.0039$
	60-88%	$0.2140 \pm 0.0421 \pm 0.0316$	$0.0274 \pm 0.0023 \pm 0.0021$
	0-88%	$0.4439 \pm 0.0478 \pm 0.0594$	$0.0619 \pm 0.0029 \pm 0.0051$

Table 4.1: The final rapidity density values for ω and ϕ mesons in $p+p$ and $d+Au$ collisions, obtained by summing up the measured yields in e^+e^- decay channel. The first error is statistical and the second is systematic.

compare the results to the results obtained by summing up the points as discussed in the previous section. The following three functional forms are considered for these studies:

1. The first is a Levy function which is defined in Section 4.1.1. With the exception of m_0, all other parameters are left free in the fit.
2. The second is an exponential function based on the assumption that the particle production is exponential in p_T:

$$E\frac{d^3\sigma}{dp^3} = \frac{1}{2\pi T^2}\frac{d\sigma}{dy}e^{-p_T/T} \tag{4.4}$$

   with both $\frac{d\sigma}{dy}$ and T as free parameters
3. The third is also an exponential function, that assumes that the particle production

is exponential in $m_T = \sqrt{p_T^2 + m_0^2}$. $\frac{d\sigma}{dy}$ and T are free parameters.

$$E\frac{d^3\sigma}{dp^3} = \frac{1}{2\pi T(T+m_0)}\frac{d\sigma}{dy}e^{-(m_T-m_0)/T} \tag{4.5}$$

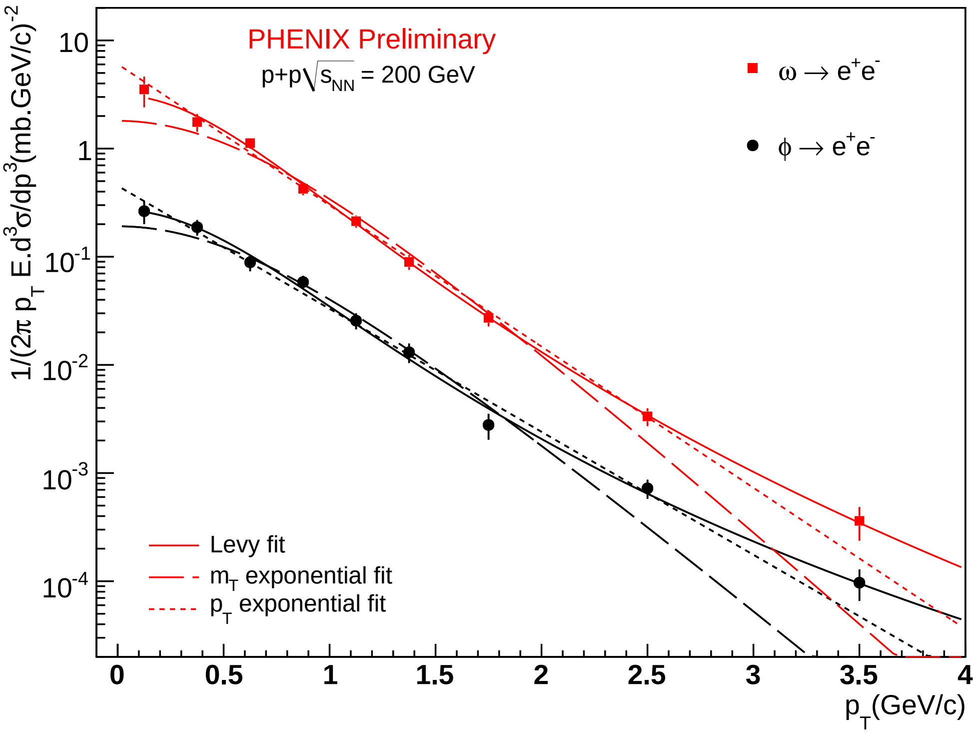

Figure 4.6: $\omega \rightarrow e^+e^-$ and $\phi \rightarrow e^+e^-$ spectra in $p+p$ collisions, fit to Levy, p_T- and m_T-exponential functions.

Fitting e^+e^- Measurements Only Fig. 4.6 shows the $\omega \rightarrow e^+e^-$ and $\phi \rightarrow e^+e^-$ distributions obtained in $p+p$ collisions together with fits to the Levy (solid line), p_T-exponential (small dashed line) and m_T-exponential (big dashed line) functions. As can be seen, the Levy function describes both the ω and ϕ spectra quite well over the entire measured region. Both exponential fits underestimate the yield at high p_T. At low p_T, the m_T-exponential fit systematically underestimates the first points, resulting in a $\frac{d\sigma}{dy}$ value that is lower by $\sim$ 5 - 12% compared to the values obtained by the integrated method. As the data do not follow the exponential behavior at high p_T, we also tried the fits using a restricted range (0-2.5 GeV/c for the ϕ and 0-3.0 Gev/c for the ω). Since the rapidity density is dominated by the yield at low p_T, the $\frac{d\sigma}{dy}$ values obtained with the restricted range are more realistic as compared to those obtained with the full range fit.

Data set	Method	$\frac{d\sigma}{dy}$ (mbarns)	χ^2/NDF
$\phi \to e^+e^-$	Summing the points	0.432 ± 0.031 (stat.) ± 0.028 (sys.)	-
$\phi \to e^+e^-$	Levy Fit (Full Range)	0.430 ± 0.031	5.12/6
$\phi \to e^+e^-$	p_T-exponential (Full Range)	0.415 ± 0.030	12.8/7
$\phi \to e^+e^-$	p_T-exponential (0-2.5 GeV/c)	0.417 ± 0.030	9.9/6
$\phi \to e^+e^-$	m_T-exponential (Full Range)	0.404 ± 0.031	23.2/7
$\phi \to e^+e^-$	m_T-exponential (0-2.5 GeV/c)	0.416 ± 0.030	3.0/5
$\phi \to K^+K^-$	Levy Fit (Full Range)	0.437 ± 0.022	52/20
$\phi \to K^+K^-$	p_T-exponential (Full Range)	0.396 ± 0.012	164/22
$\phi \to K^+K^-$	p_T-exponential (0.8-3.0 GeV/c)	0.469 ± 0.017	62/14
$\phi \to K^+K^-$	m_T-exponential (Full Range)	0.257 ± 0.007	252/22
$\phi \to K^+K^-$	m_T-exponential (1.3-3.0 GeV/c)	0.334 ± 0.011	42.5/12
$\omega \to e^+e^-$	Summing the points	4.20 ± 0.33 (stat.) ± 0.33 (sys)	-
$\omega \to e^+e^-$	Levy Fit (Full Range)	4.14 ± 0.29	2.05/6.0
$\omega \to e^+e^-$	p_T-exponential (Full Range)	4.20 ± 0.29	7.0/7.0
$\omega \to e^+e^-$	p_T-exponential (0-3.0 GeV/c)	4.25 ± 0.28	4.2/6.0
$\omega \to e^+e^-$	m_T-exponential (Full Range)	3.64 ± 0.26	17.5/7.0
$\omega \to e^+e^-$	m_T-exponential (0-2.0 GeV/c)	3.88 ± 0.26	4.4/5.0
$\omega \to \pi^+\pi^-\pi^0, \gamma\pi^0$	Levy Fit (Full Range)	21.5 ± 10.3	36.4/25
$\omega \to \pi^+\pi^-\pi^0, \gamma\pi^0$	p_T-exponential (Full Range)	0.476 ± 0.049	281.9/26
$\omega \to \pi^+\pi^-\pi^0, \gamma\pi^0$	p_T-exponential ($\leq$ 5.1 GeV/c)	1.33 ± 0.15	10.2/7.0
$\omega \to \pi^+\pi^-\pi^0, \gamma\pi^0$	m_T-exponential (Full Range)	0.346 ± 0.033	291/26
$\omega \to \pi^+\pi^-\pi^0, \gamma\pi^0$	m_T-exponential ($\leq$ 5.1 GeV/c)	0.89 ± 0.09	11.1/7.0

Table 4.2: Comparison of $\frac{d\sigma}{dy}$ of the ϕ and ω meson obtained using various methods in $p+p$ collisions. The errors quoted are those obtained from the fit.

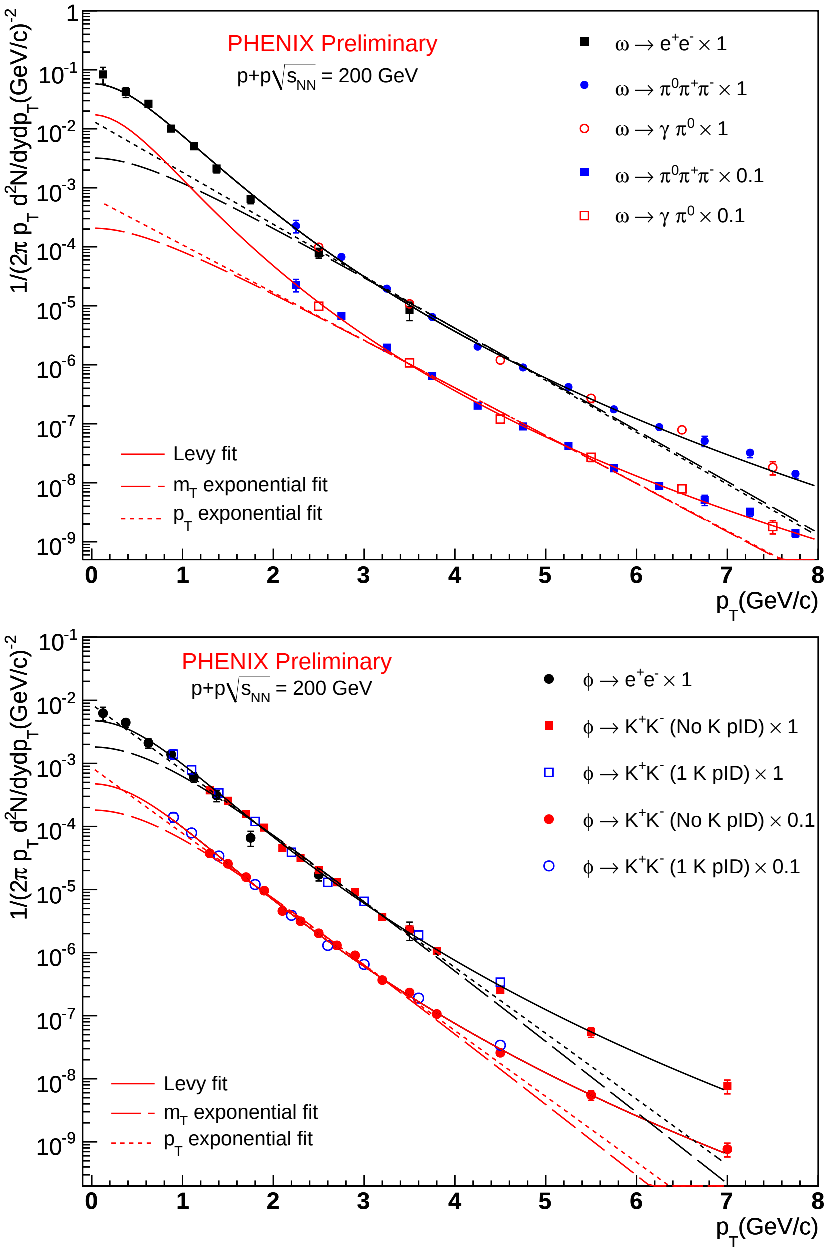

Figure 4.7: Top panel: ω meson spectra in $p+p$ collisions, fitted to Levy, p_T- and m_T-exponential functions. The fits are done for two combinations of data sets: hadronic channel (red lines) only and hadronic and leptonic channel together (black lines). The omega $\omega \rightarrow \pi^+\pi^-\pi^0, \gamma\pi^0$ results are taken from [145]. Bottom panel: same for the ϕ meson. The $\phi \rightarrow K^+K^-$ results are from [84]. The errors plotted are statistical only.

The $\phi \rightarrow e^+e^-$ and $\omega \rightarrow e^+e^-$ results obtained using the various fits described above are summarized in Table 4.2. The Levy function gives results which are in very good agreement with the measured values. The p_T-exponential results are consistent within errors whereas the m_T-exponential values are lower by ~ 4 - 8%.

Fitting Hadronic Measurements Only We also compared our e^+e^- results of $\frac{d\sigma}{dy}$ to the ones obtained by fitting the hadronic decay measurements with the above mentioned three functional forms. The method of summing up the measured points can not be used in this case, since there are no measurements at low p_T. Fig. 4.7 shows the fits to hadronic decay channel measurements only (red line) in $p+p$ collisions. The extracted $\frac{d\sigma}{dy}$ values from hadronic channel fits are also summarized in Table 4.2. For $\phi \rightarrow K^+K^-$, the results obtained are consistent with the measured $\phi \rightarrow e^+e^-$ values within 5-20%, depending upon the fit model used. However for $\omega \rightarrow \pi^+\pi^-\pi^0, \gamma\pi^0$, since there are no measurements below 2.0 GeV/c, the fits become very unreliable in this region. Consequently the extracted values do not agree to the measured $\omega \rightarrow e^+e^-$ results and all the three functions give very different results.

However, by adding the low p_T e^+e^- measurements, the fits get constrained as shown by the black lines in Fig. 4.7 and a combined fit to e^+e^- and hadronic measurements gives realistic results and describes both the data sets equally well.

Fit Results For $\frac{dN}{dy}$ in $d+Au$ Examples of $\omega \rightarrow e^+e^-$ and $\phi \rightarrow e^+e^-$ distributions for minimum bias and centrality selected $d+Au$ collisions, fitted to Levy, p_T-exponential and m_T-exponential functions are shown in Fig. 4.8. The $\frac{dN}{dy}$ values extracted using these fits are summarized in Table 4.3. As in $p+p$, the Levy function and the p_T-exponential results are consistent within errors to the measured values. The m_T exponential underestimates the yields by 8-20% in case of ϕ and by 7-40% for ω.

Table 4.3 also contains results obtained by fitting hadronic channel measurements only. The results for $\phi \rightarrow K^+K^-$ are consistent with $\phi \rightarrow e^+e^-$ results, within errors. For ω, as in $p+p$, there are no measurements below 2.0 GeV/c and so none of the models yields any reliable $\frac{dN}{dy}$ values.

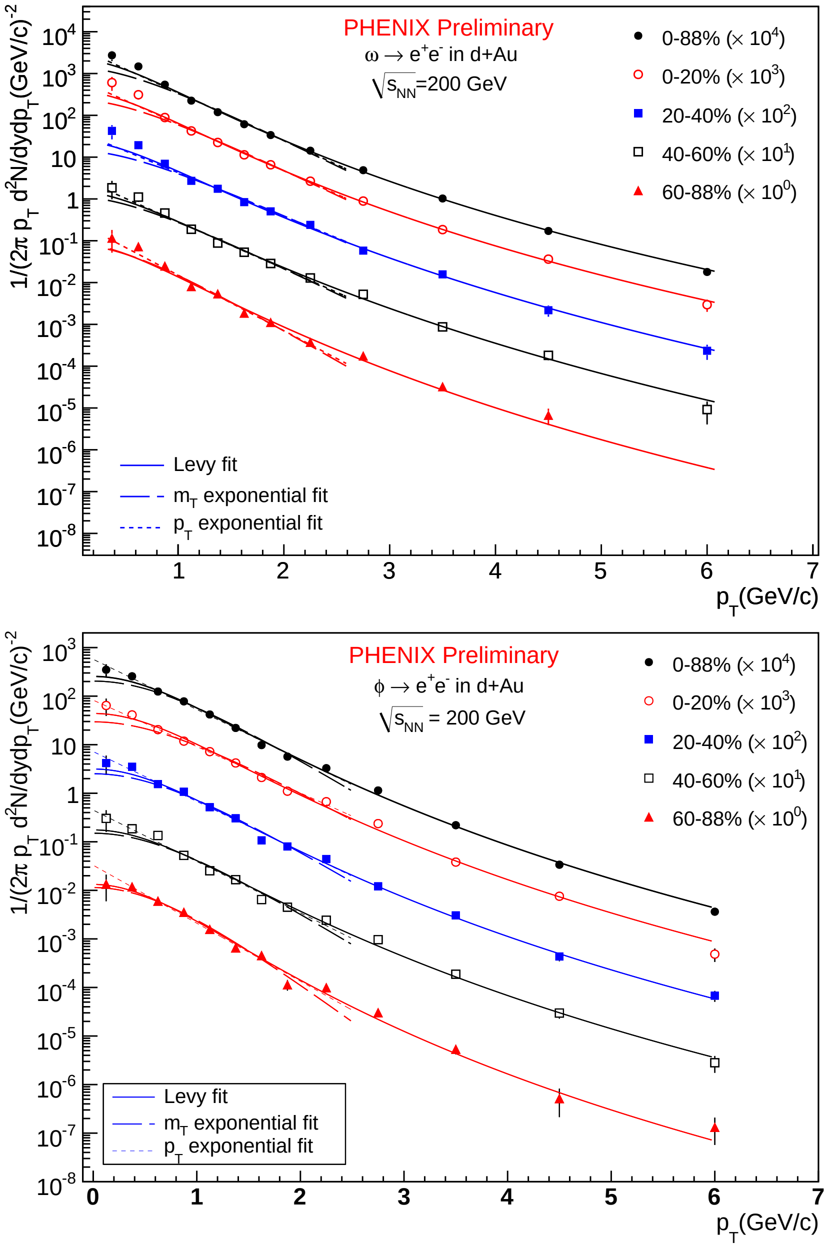

Figure 4.8: Top panel: The $\omega \rightarrow e^+e^-$ p_T spectra in the $d+Au$ collisions, fit to Levy, p_T- and m_T-exponential functions. Bottom panel: same for the $\phi \rightarrow e^+e^-$ p_T spectra. Only statistical errors are shown.

		$\frac{dN}{dy}$ ($\sum_i pts$)	Levy		p_T-exponential		m_T-exponential	
Data set	Event class	$\frac{dN}{dy}$	$\frac{dN}{dy}$	χ^2/NDF	$\frac{dN}{dy}$	χ^2/NDF	$\frac{dN}{dy}$	χ^2/NDF
$\phi \rightarrow e^+e^-$	0-88% (MB)	0.0619 ± 0.0029 ± 0.0051	0.05704 ± 0.00238	32.67/10	0.06034 ± 0.00243	19.5/7.0	0.05266 ± 0.00215	49.15/7.0
	0-20%	0.1114 ± 0.0079 ± 0.0085	0.09852 ± 0.00507	16.35/10	0.10717 ± 0.00640	5.88/7.0	0.09236 ± 0.00544	17.31/7.0
	20-40%	0.0846 ± 0.0058 ± 0.0067	0.07876 ± 0.00493	20.5/10	0.08102 ± 0.00495	18.7/7.0	0.06981 ± 0.00435	34.30/7.0
	40-60%	0.0514 ± 0.0041 ± 0.0039	0.04478 ± 0.0034	22.8/10	0.04758 ± 0.00335	13.3/7.0	0.04015 ± 0.00290	28.86/7.0
	60-88%	0.0274 ± 0.0023 ± 0.0021	0.01900 ± 0.00248	17.1 /10	0.02736 ± 0.00206	17.5/7.0	0.02434 ± 0.00187	22.57/7.0
$\phi \rightarrow K^+K^-$	0-88% (MB)		0.07330 ± 0.00393	7.83/7.0	0.07006 ± 0.00241	41.3/5.0	0.04553 ± 0.00136	81.13/5.0
	0-20%		0.13467 ± 0.00680	7.81/7.0	0.12660 ± 0.00725	15.1/5.0	0.08280 ± 0.00415	29.28/5.0
	20-40%		0.08547 ± 0.00450	3.32/7.0	0.08794 ± 0.00506	9.30/5.0	0.05680 ± 0.00280	20.98/5.0
	40-60%		0.04459 ± 0.00307	9.37/7.0	0.04560 ± 0.00346	19.4/5.0	0.02966 ± 0.00195	29.75/5.0
	60-88%		0.02431 ± 0.00181	5.46/7.0	0.02500 ± 0.00199	12.1/5.0	0.01582 ± 0.00109	22.70/5.0
$\omega \rightarrow e^+e^-$	0-88% (MB)	0.4439 ± 0.0478 ± 0.0594	0.4216 ± 0.0223	16.02/9.0	0.4141 ± 0.0295	13.7/6.0	0.3166 ± 0.0198	26.61/6.0
	0-20%	0.9877 ± 0.1519 ± 0.1602	0.82167 ± 0.06840	9.60/9.0	0.78111 ± 0.08884	7.15/6.0	0.59221 ± 0.05850	12.24/6.0
	20-40%	0.6836 ± 0.1031 ± 0.0866	0.57619 ± 0.04452	17.3/9.0	0.51158 ± 0.05244	12.1/6.0	0.40213 ± 0.03556	17.98/6.0
	40-60%	0.3715 ± 0.0584 ± 0.0499	0.37167 ± 0.03180	16.3/9.0	0.35582 ± 0.04210	7.03/6.0	0.27606 ± 0.02961	12.74/6.0
	60-88%	0.2140 ± 0.0421 ± 0.0316	0.18208 ± 20.5843	11.2/8.0	0.21630 ± 0.03085	7.56/6.0	0.15494 ± 0.01964	12.07/6.0
$\omega \rightarrow \pi^+\pi^-\pi^0, \gamma\pi^0$	0-88% (MB)		1.86610 ± 1.60632	5.93/6.0	0.06024 ± 0.02477	8.99/7.0	0.04518 ± 0.01719	9.17/7.0
	0-20%		4.05847 ± 7.97080	0.31 / 1.0	0.23659 ±0.23476	0.69/2.0	0.16640 ± 0.14761	0.72/2.0

Table 4.3: Parameters from the Levy (Eq. 4.1), p_T-exponential (Eq. 4.4) and m_T-exponential (Eq. 4.5) fit for the ϕ and ω meson in $d+Au$ collisions.

4.3 Mean $\langle p_T \rangle$ calculation

Another global observable that can be extracted from the p_T spectra is the mean p_T ($\langle p_T \rangle$) of all the particles coming from the collision. Similar to the $\frac{dN}{dy}$ estimation, we calculate it by the simple arithmetic mean of all the measured points *i.e.*,

$$\langle p_T \rangle = \frac{\sum_i p_T^i \frac{dN^i}{dy}}{\sum_i \frac{dN^i}{dy}} \tag{4.6}$$

$$\frac{dN^i}{dy} = \frac{d^2N^i}{dy\,dp_T} \times \Delta p_T^i \tag{4.7}$$

where p_T^i, $\frac{dN^i}{dy}$, $\frac{d^2N^i}{dydp_T}$ represent the measured values for a given point i. The uncorrelated error (statistical + type A added in quadrature) (see Section 3.17 for details) are propagated assuming independence of the data points.

$$\sigma_{p_T}^2 = \sum_i \left[\frac{p_T^i \sum_{j\neq i} \frac{dN^j}{dy} - \sum_{j\neq i}(p_T^j \frac{dN^j}{dy})}{(\sum_i (\frac{dN^i}{dy})^2)} \cdot \sigma_i \right]^2 \tag{4.8}$$

where σ_i corresponds to statistical + type A error on $\frac{dN_i}{dy}$ for the point i. The point to point correlated errors on data points were propagated separately. For this, we moved the points in two ways such that the variation takes into account the maximum variation in shape of the p_T distribution.

- all the points are moved such that the first point is placed $1\sigma_{corr}$ above the original value and the last point stays unchanged.
- repeat the same but this time the last point is moved by $1\sigma_{corr}$ and the first point stays at the original value.

The $\langle p_T \rangle$ is calculated for both cases. The difference between them corresponds to 2σ of the propagated point-to-point systematic correlated error.

$$\sigma\langle p_T \rangle_{corr} = |\langle p_T \rangle_1 - \langle p_T \rangle|_2/2 \tag{4.9}$$

The resulting mean transverse momentum ($\langle p_T \rangle$) values thus obtained for the ω and ϕ mesons in $p+p$ and the various centrality classes of $d+Au$ collisions are summarized in Table 4.4.

		$\phi \to e^+e^-$	$\omega \to e^+e^-$
	Centrality	$\langle p_T \rangle$ (GeV/c)	$\langle p_T \rangle$ (GeV/c)
$p+p$		$0.752 \pm 0.032 \pm 0.014$	$0.664 \pm 0.037 \pm 0.012$
	0-20%	$0.8927 \pm 0.0465 \pm 0.0206$	$0.7585 \pm 0.0616 \pm 0.0149$
	20-40%	$0.8563 \pm 0.0432 \pm 0.0183$	$0.7789 \pm 0.0588 \pm 0.0161$
$d+Au$	40-60%	$0.8293 \pm 0.0477 \pm 0.0188$	$0.8294 \pm 0.0687 \pm 0.0167$
	60-88%	$0.7844 \pm 0.0452 \pm 0.0149$	$0.7499 \pm 0.0723 \pm 0.0133$
	0-88%	$0.8572 \pm 0.0368 \pm 0.0196$	$0.7889 \pm 0.0418 \pm 0.0161$

Table 4.4: The $\langle p_T \rangle$ values for ω and ϕ mesons in $p+p$ and $d+Au$ collisions, obtained by summing up the measured yields in e^+e^- decay channel. The first error is statistical and the second is systematic.

4.4 $\frac{dN}{dy}$ and $\langle p_T \rangle$ versus Participating Nucleons N_{part}

We present here the dependence of $\frac{dN}{dy}$ and $\langle p_T \rangle$ as a function of the participating nucleons (N_{part}). The left panel of Fig. 4.9 shows the $\frac{dN}{dy}$ values in $p+p$ and $d+Au$ collisions, and the right panel shows the $\frac{dN}{dy}$ values per pair of participating nucleons for the same systems vs N_{part}. Due to the nature of the steeply falling particle spectra, most of the yield comes from the low p_T region, below 1 GeV/c, which is dominated by soft particle production, so the apparent scaling of $\frac{dN}{dy}$ with N_{part} is a property of soft particle production. For higher p_T, the yield is dominated by point-like processes which should scale with the number of binary collisions in the absence of any nuclear effects. This is studied in terms of the *nuclear modification factor* R_{dAu} and will be discussed in Section 4.6. Also shown in Fig. 4.10 is the $\langle p_T \rangle$ plotted as a function of the number of participating nucleons in

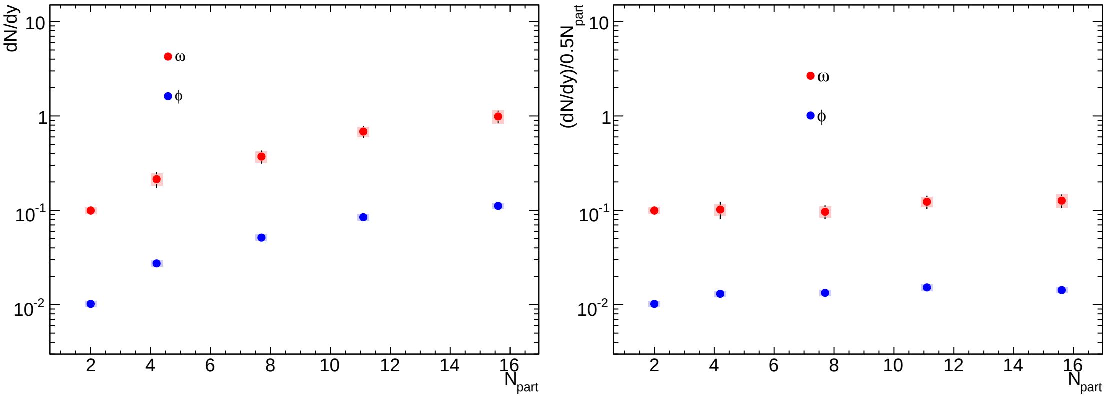

Figure 4.9: Left panel: $\frac{dN}{dy}$ as a function of the number of participating nucleons (N_{part}) in $p+p$ and $d+Au$ collisions. Right panel: $\frac{dN}{dy}$ per pair of participating nucleons for the same systems.

$p+p$ and $d+Au$ collisions. A very small increase in the mean p_T is observed from $p+p$ to central $d+Au$ collisions.

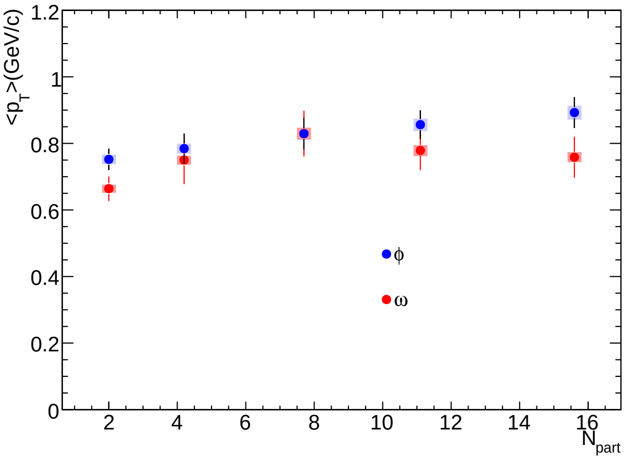

Figure 4.10: $\langle p_T \rangle$ for ω and ϕ plotted as a function of number of participants N_{part} in $p+p$ and $d+Au$ collisions.

4.5 Comparison to Hadronic Decay Channel Results

We compare the results of the measurements obtained via the e^+e^- decay channel in this work to the corresponding hadronic decay channel results *i.e.*, $\omega \rightarrow \pi^+\pi^-\pi^0, \gamma\pi^0$ and $\phi \rightarrow K^+K^-$. As discussed in Section 1.5, a comparison between the $\phi \rightarrow e^+e^-$ and $\phi \rightarrow K^+K^-$ decay channels is a powerful tool to search for the in-medium modifications in $Au+Au$ collisions. But before making such a comparison, it needs to be established that the reference measurements in the baseline $p+p$ and $d+Au$ systems are well understood and checked for any underlying effects.

Fig. 4.11 shows the comparison between $\phi \rightarrow e^+e^-$ and $\phi \rightarrow K^+K^-$ [84, 148], and $\omega \rightarrow \pi^+\pi^-\pi^0, \gamma\pi^0$ [145] and $\omega \rightarrow e^+e^-$ decay channels in $p+p$ and $d+Au$ collisions. The ω in $d+Au$ collisions via hadronic channel is only measured for minimum bias and 0-20% centrality classes. The $\phi \rightarrow e^+e^-$ and $\phi \rightarrow K^+K^-$ measurements have a significant overlap region in p_T in $p+p$ (1.0 – 3.5 GeV/c) and $d+Au$ (1.0 – 6.0 GeV/c) collisions. For $\omega \rightarrow e^+e^-$ and $\omega \rightarrow \pi^+\pi^-\pi^0, \gamma\pi^0$ measurements, the overlap region is small (2.0 – 3.5 GeV/c in $p+p$ and 3.0 – 6.0 GeV/c in $d+Au$ collisions). To demonstrate the consistency between the two decay channel measurements, we fit the e^+e^- measurements for each case to a Levy function (Eq. 4.1) and then plot the ratios of the data points to this fit, as shown in the right panels. The measurements in the two decay channels for both ω and ϕ show a reasonable agreement in the region of overlap. This implies that in $p+p$

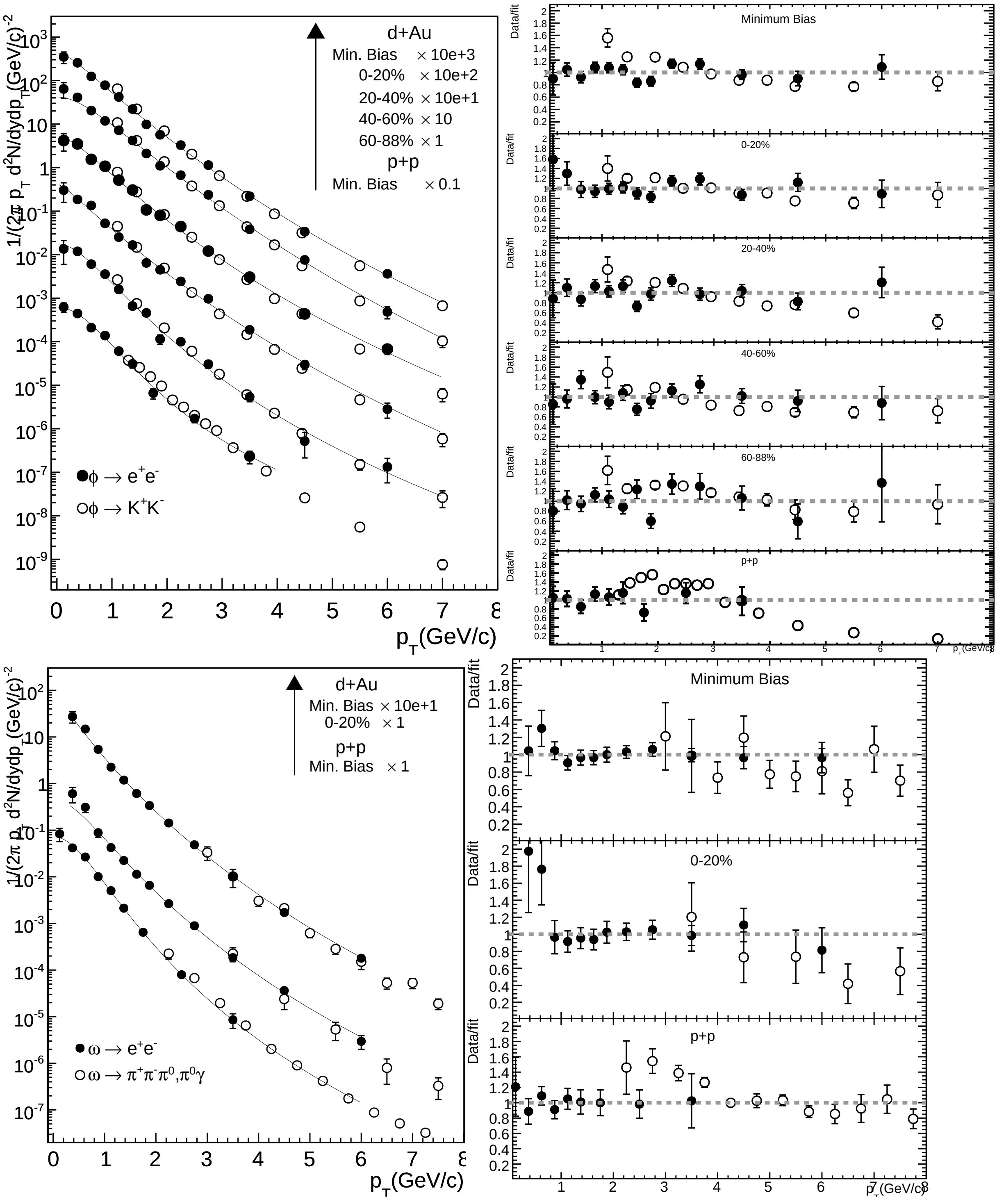

Figure 4.11: The top left panel shows $\phi \rightarrow e^+e^-$ and $\phi \rightarrow K^+K^-$ measurements [84] plotted together. The e^+e^- points are fit to a Levy function (Eq. 4.1). The top right panel shows the ratio of the two measurements to the fit. The bottom panels show the same type of comparison for $\omega \rightarrow e^+e^-$ and $\omega \rightarrow \pi^+\pi^-\pi^0, \gamma\pi^0$ results [145]. Only statistical errors are shown for each case.

and $d+Au$ collisions, the leptonic and hadronic channel measurements are consistent to each other. This agreement also demonstrates a good control of the systematic uncertainties associated with the different analysis techniques and different detectors, used in the different decay channels.

4.6 Nuclear Modification Factor R_{dAu}

Possible nuclear effects on hadron production in $d+Au$ collisions are measured through a comparison to the production in $p+p$ collisions, scaled by the number of underlying nucleon-nucleon inelastic collisions via the nuclear modification factor R_{dAu} as explained in Section 1.6 and Section 1.7. As was discussed in those sections, R_{dAu} reveals the size of cold nuclear matter effects, like Cronin enhancement [89, 95], shadowing [90] and possible parton saturation phenomenon [102], which occur in the initial state and should therefore establish the initial conditions for the $Au+Au$ system.

The R_{dAu} of ϕ and ω is derived by dividing point-by-point the $e^{+}e^{-}$ (or hadronic) spectra in $d+Au$ collisions, by the $e^{+}e^{-}$ (or hadronic) spectra in $p+p$ collisions, scaled by the corresponding number of binary nucleon-nucleon collisions, N_{coll} (Eq. 1.4). The nuclear modification factors R_{dAu} thus obtained, for ω and ϕ in the four centrality bins and for minimum bias $d+Au$ collisions at $\sqrt{s_{NN}}$ =200 GeV are shown in Fig. 4.12. The results from both the leptonic and hadronic channels are shown in these plots. The N_{coll} values derived from Glauber calculations were taken from Table 2.4 presented in Section 2.2.7. The statistical errors are propagated by adding in quadrature the errors on the numerator and denominator and are shown by the vertical error bars. The type A and type B systematic errors (Section 3.17) are added in quadrature and are shown by filled boxes in the plots. In all the plots, the boxes around 7.8 correspond to the uncertainty in the N_{coll} determination. In addition, there is also a 9.6% overall normalization error of the $p+p$ reference spectrum which is not shown on the plots.

From these plots, the following conclusions can be drawn:

- Clearly there is is no suppression in $d+Au$ collisions for $p_T > 1.5$ GeV/c, in the mid-rapidity window $|\eta| < 0.35$. As for other mesons, the high-p_T suppression of the ϕ and ω observed in $Au+Au$ collisions [79–83] is not an initial or cold nuclear matter effect, but a final state effect occurring in the hot and dense medium.
- There is a good agreement between the R_{dAu} obtained independently via $e^{+}e^{-}$ and hadronic decay channels, that reflects the good agreement observed both in the $p+p$ and $d+Au$ invariant cross-sections.

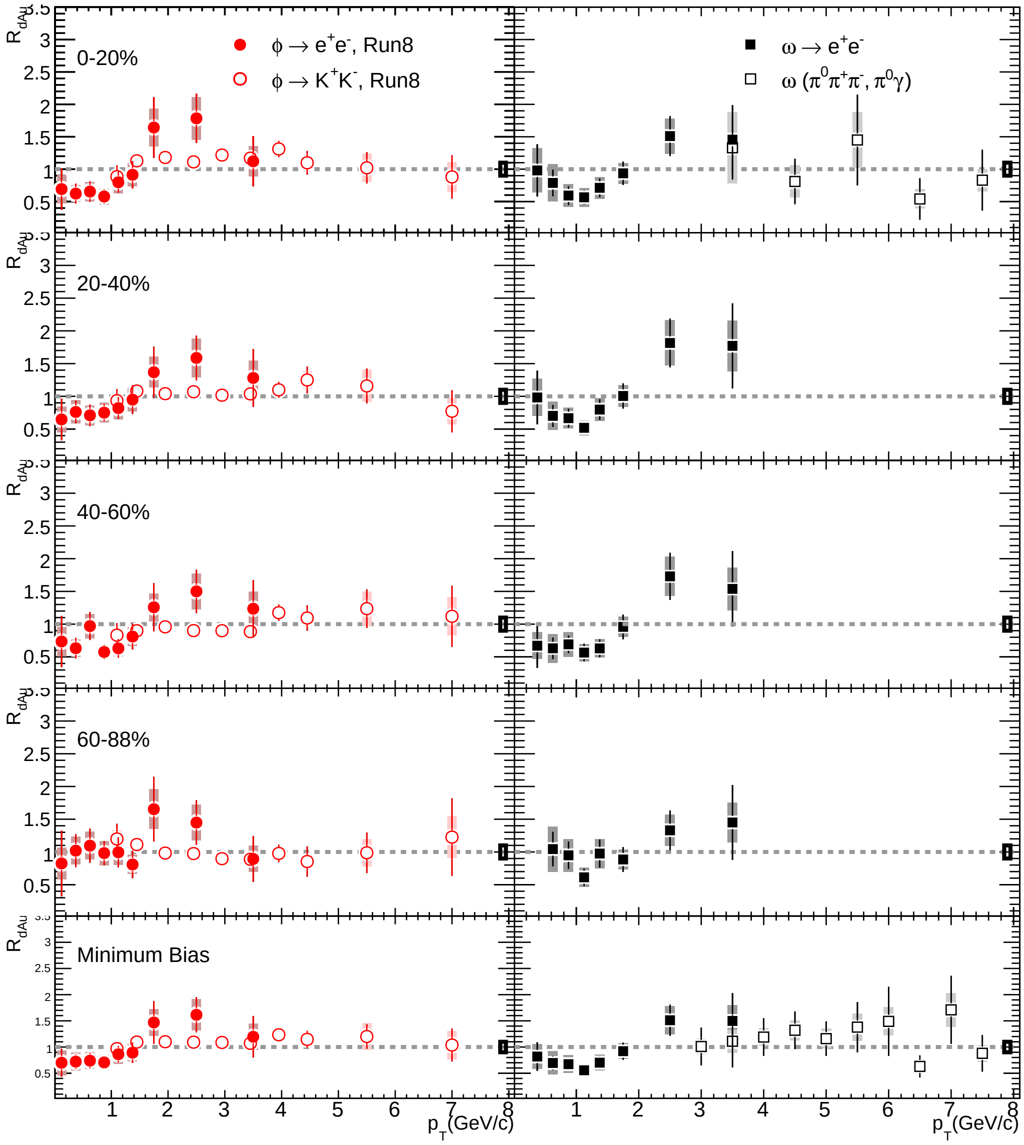

Figure 4.12: R_{dAu} of ϕ (left) and ω (right). The statistical errors are indicated by the vertical error bars and the filled boxes correspond to the systematic errors. The black boxes around 7.8 corresponds to the uncertainty in N_{coll}. In addition, there is a 9.6% normalization uncertainty on the $p+p$ reference which is not shown.

- Taking together the e^+e^- and the hadronic channel results, it can be concluded that there is no evidence of any significant Cronin enhancement.

In Fig. 4.13, we show a comparison of the R_{dAu} of ϕ and ω with that of π^0, as measured by PHENIX [99]. The R_{dAu} of π^0 has been measured up to 16 GeV/c. For the comparison shown here, we plot only up to 8 GeV/c. The R_{dAu} of π^0 have very small uncertainties, and for all the centralities do not show any considerable *Cronin enhancement*. The R_{dAu} values of ϕ and ω are consistent with those of π^0 within the uncertainties of the measurements.

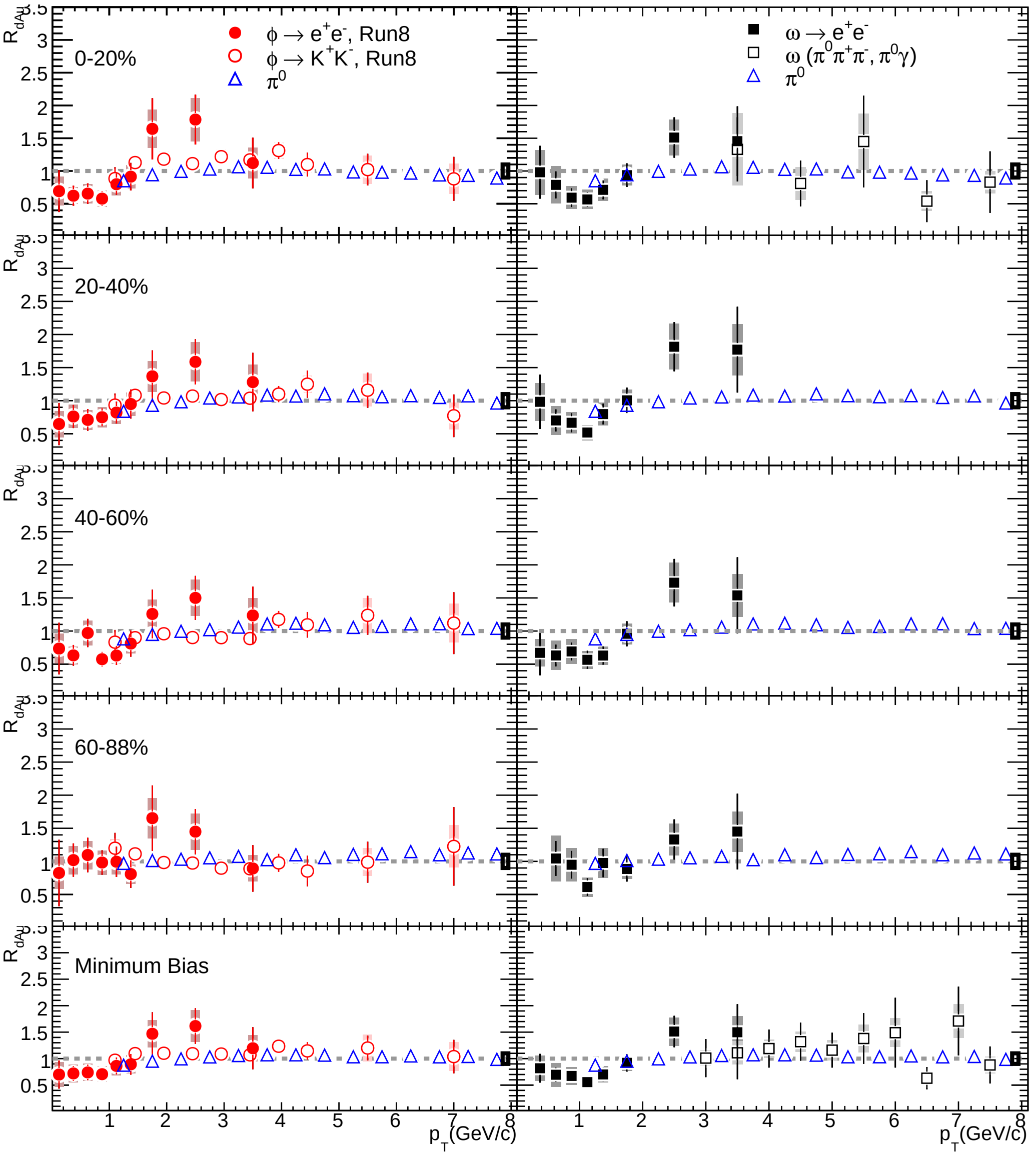

Figure 4.13: R_{dAu} of ϕ (left) and ω (right) overlayed with that of π^0. The π^0 results are from Ref. [99]. The N_{coll} uncertainty is shown by black boxes around 7.8.

A comparison of the R_{dAu} for various hadrons measured by PHENIX, for minimum bias $d+Au$ collisions can be seen in Fig. 4.14. The $\phi \rightarrow e^+e^-$ and $\omega \rightarrow e^+e^-$ are from this work, K^+, K^-, π^+, π^-, p results are taken from Ref. [85], $\phi \rightarrow K^+K^-$ is taken from Ref. [84], ω ($\pi^+\pi^-\pi^0$, $\pi^0\gamma$) is taken from Ref.[145], and π^0 and η are from Ref. [99]. The R_{dAu} of proton exhibits an enhancement in the range, $2 \leq p_T \leq 4$ GeV/c, usually associated with the *Cronin effect*. In the same p_T range, all other mesons π^0, η, ϕ, ω show very little or no enhancement.

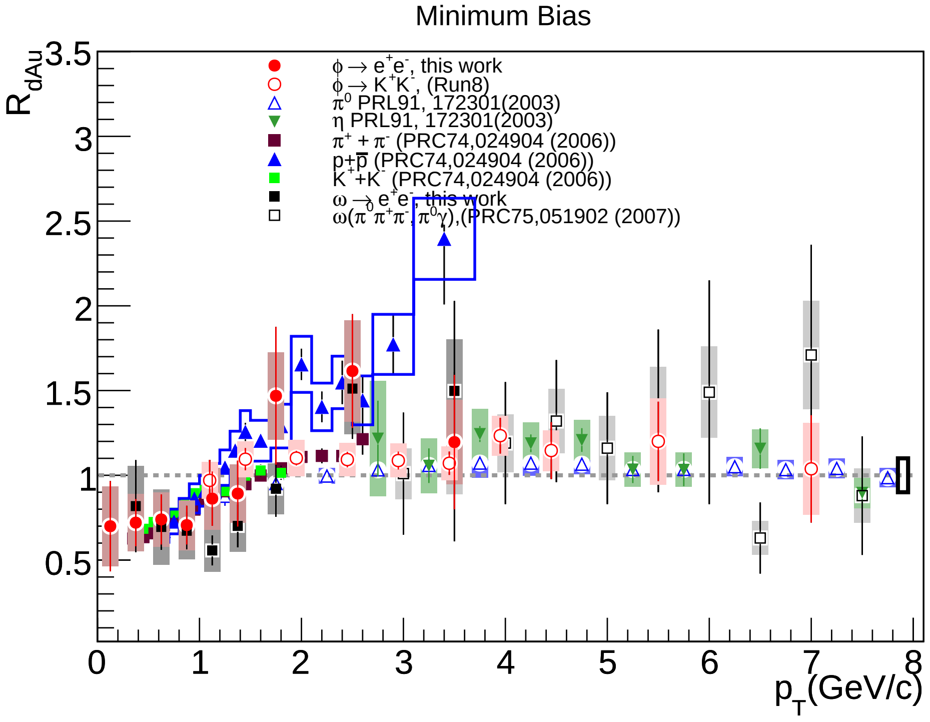

Figure 4.14: R_{dAu} of ϕ and ω in minimum bias $d+Au$ collisions, overlayed with the R_{dAu} of $p+\bar{p}$, $\pi^+ + \pi^-$, $K^+ + K^-$ taken from Ref. [85], and π^0, η from Ref. [99]. The $\phi \to K^+K^-$ points are taken from Ref. [84] and the $\omega \to \pi^+\pi^-\pi^0, \gamma\pi^0$ results are from Ref. [145].

Chapter 5

Hadron Blind Detector

5.1 Low mass dielectrons at RHIC

Electron pairs are a promising observable in the quest for the phenomena of chiral symmetry restoration and deconfinement expected to take place in the early stages of heavy ion collisions [149]. They can provide a direct measure of the temperature of the plasma by identifying the thermal radiation emitted from the QGP via $q\bar{q}$ annihilation ($q\bar{q} \rightarrow \gamma^* \rightarrow e^+e^-$). Also the decay of the resonances ρ, ω and ϕ into electron-positron pairs allows the study of possible changes of their mass and width in the medium as a result of chiral symmetry restoration.

The measurement of low-mass electron pairs in heavy-ion collisions is a very challenging task. The PHENIX detector in its original configuration suffers from a huge combinatorial background, arising from the large number of unrecognized π^0 Dalitz decays and γ conversions. This is due to the limited azimuthal angular acceptance of PHENIX in the central arms and the strong magnetic field beginning radially at R=0, that very often results in only one of the two tracks of an e^+e^- pair being detected. This leads to a huge combinatorial background that increases quadratically with the number of charged tracks N_{ch}, making the signal extraction extremely difficult at the high multiplicities of RHIC. The S/B ratio from the di-electron measurements in $Au+Au$ collisions [52], obtained with the PHENIX original set-up is $\sim$ 1/200 at mass $m_{e^+e^-} \approx 500$ GeV/c^2 for a single electron p_T cut of 200 MeV/c. Fig. 5.1 shows the dilepton spectrum in minimum bias $Au+Au$ collisions at $\sqrt{s_{NN}} = 200$ GeV. It is clear that statistical and systematic uncertainties in the low-mass region are huge, and simply increasing the statistics will be insufficient to allow a precise measurement. Improvement of the signal to background is imperative.

In order to overcome the problem of the huge background, the Weizmann group proposed to upgrade the PHENIX detector by adding a Hadron Blind Detector [150–152]

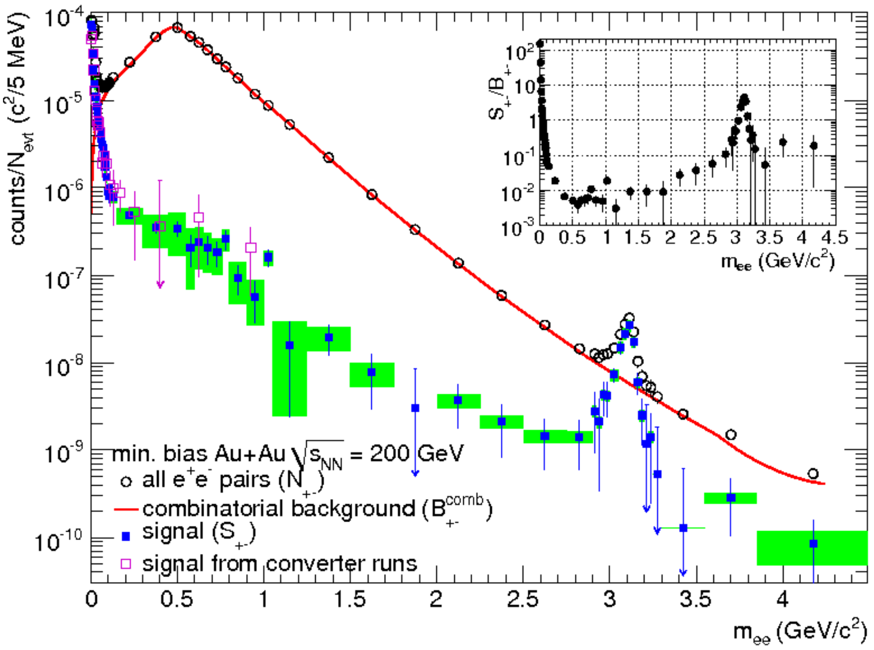

Figure 5.1: Uncorrected mass spectra (black) of all $e^{+}e^{-}$ pairs , mixed-event background (B^{comb}(red)) and signal S (blue) obtained by subtracting the two, in minimum bias $Au+Au$ collisions. Statistical (bars) and systematic (boxes) are shown separately. The insert shows the S/B^{comb} ratio.

that will reconstruct and reject Dalitz decays and conversion pairs.

5.2 The HBD Concept

The HBD is a conceptually novel Čerenkov detector. Its primary aim is to recognize and reject tracks originating from π^0 Dalitz decays and γ-conversions, thus allowing to measure low mass ($m_{e^+e^-} \leq 1$ GeV/c^2) electron-positron pairs produced in central $Au+Au$ collisions at RHIC energies. The main idea is to exploit the fact that the opening angle of electron pairs from these sources is very small compared to pairs from the vector mesons. The HBD is therefore located in a field-free region, where the pair opening angle is preserved. The field free region is created by the inner coil installed in the central arms of PHENIX (see Section 2.2.2). This coil counteracts the main field of the outer coils and creates an almost field-free region close to the vertex and extending to $\approx$ 50-60 cm in the radial direction (see Fig. 5.2).

Conceptual Monte Carlo simulations [150] were done at the ideal detector level to quantify the potential benefit and define the system specifications of the HBD. The results of the study indicated that a reduction of the combinatorial background, originating from

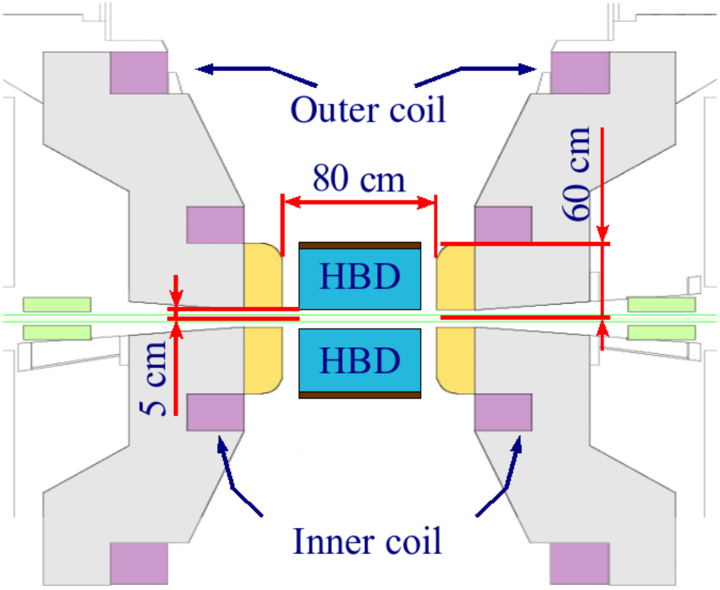

Figure 5.2: Layout of the inner part of the PHENIX detector showing the location of the HBD.

conversions and π^0 Dalitz decays, of two orders of magnitude can be achieved with a detector that provides electron identification with a very high efficiency, of at least 90%, double (electron) hit recognition at a comparable level, and a moderate π rejection factor of ~ 50.

A careful evaluation of the relevant options for the key elements (gases, detector configuration and readout chambers) led to the following layout for the HBD: a 50 cm long Čerenkov radiator directly coupled in a windowless configuration to a triple GEM (Gas Electron Multiplier) detector element [153], operated with pure CF_4, with a *CsI* photocathode evaporated on the top face of the top GEM foil, and a pad readout at the bottom of the GEM stack.

Each triple GEM detector element consists of one gold plated GEM with the *CsI* film evaporated on the top face of the top GEM, and two standard copper GEMs. A stainless steel mesh placed 1.5 mm above the top GEM provides a positive or negative voltage with respect to it. A schematic configuration of the triple GEM detector element, illustrating the two modes in which it can be operated is shown in Fig. 5.3. Depending on the direction of the bias field, charge produced by ionizing particles in the upper gap (drift gap) can either be collected by the GEM (FB = Forward Bias) (right panel), or by the mesh (RB = Reverse Bias) (left panel). In either configuration, photoelectrons produced on the photocathode are collected with good efficiency into the GEM due to the strong electric field inside the holes, which is typically of the order of 100 kV/cm. Only a very small amount of ionization charge produced very near the photocathode (within $\sim$ 100 μm) is collected by the GEM in RB mode. The FB mode is therefore sensitive to hadrons and other charged particles, while the RB mode is essentially sensitive only to the Čerenkov light produced by electrons (hence the term “Hadron Blind”), and thus the HBD is normally operated in RB mode. Various tests carried out in the lab demonstrated that one can maintain a high photoelectron detection efficiency, while the ionization charge is suppressed using a slightly reverse bias across the drift gap [154, 155].

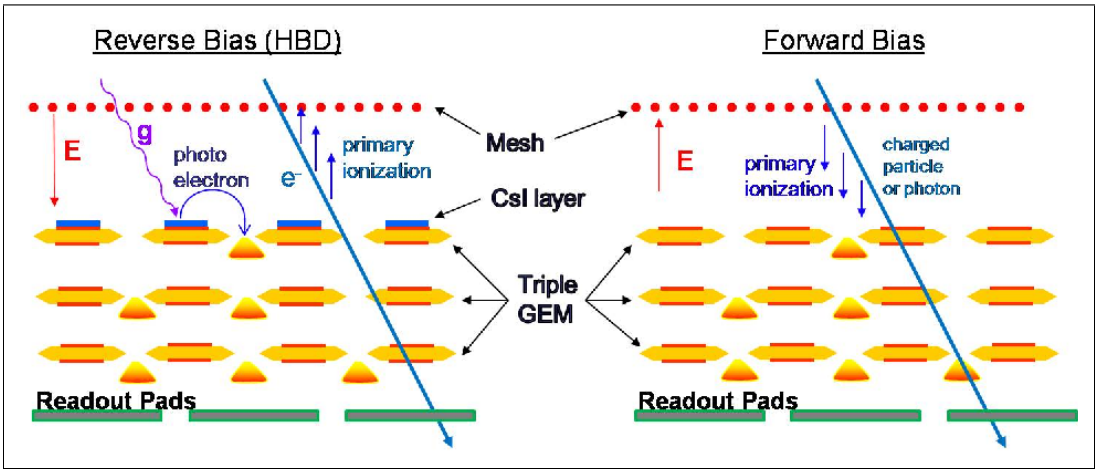

Figure 5.3: GEM operation modes: Left panel (RB) and Right panel (FB)

A high voltage, $\sim$ 500 V is applied across the GEM foil, which creates regions of extremely high electric field density inside the holes. The Čerenkov photons striking the photocathode surface, eject photoelectrons that get sucked by the field lines into the holes, creating an electron avalanche in the CF_4 operating gas. The avalanche process continues across the three layers of GEMs, in series, creating a measurable signal which is read out on a pad plane at the bottom of GEM stack.

This scheme exhibits a number of attractive features:

- The use of CF_4 both as radiator and detector gas in a windowless geometry results in a large bandwidth (from $\sim$ 6 eV given by the CsI threshold to $\sim$ 11.5 eV given by the CF_4 cut-off) which eventually leads to a large figure of merit N_0 estimated to be close to 800 cm^{-1} [150]. Under ideal conditions of 100% gas transparency and 100% photoelectron collection efficiency, the expected number of photoelectrons N_{pe} per incident electron, from a 50 cm long radiator is $\approx$ 36. The large value of N_{pe} ensures a very high electron efficiency and makes it possible to achieve a double-hit recognition of about 90%.

- The proposed design uses a reflective photocathode. The top face of the first GEM is coated with a thin layer of CsI and the photoelectrons are pulled into the holes of the GEM by their strong electric field. In this configuration photon feedback effects are avoided.
- The readout scheme foresees the detection of Čerenkov photoelectrons in a pad plane with large hexagonal pads of size comparable to, but smaller than the blob size ($\sim$10 cm^2), such that there is a very small probability for a single-pad hit by an electron entering the HBD. On the other hand, hadrons will produce a single pad hit with a $>$90% probability, thus providing a simple and strong handle for hadron rejection in the HBD.
- The relatively large pad size results in a low granularity, and hence low cost, detector. In addition, the photoelectrons produced by a single electron will be distributed mostly over three pads. One can thus expect a primary charge of a few electrons/pad, which allows the operation of the detector at a relatively moderate gain of a few times 10^3. This is a crucial advantage for the stable operation of a UV photon detector.

The concept discussed above was new and involved many new elements, which had never been tested before in the laboratory. A comprehensive R&D program was thus carried out, that included studies performed in the lab and also a beam test at KEK.

5.3 Summary of R&D results

The validity of the HBD concept was demonstrated in a comprehensive R&D program[154, 155]. The R&D set-up consisted of a triple GEM detector mounted inside a stainless steel box that can be pumped down to 10^{-6} before gas filling. Measurements were done with X-rays using an Fe^{55}, α-particles using an ^{241}Am source, and with UV photons using a Hg-lamp (see Fig. 5.4. All measurements were done with GEMs produced at CERN having 50 μm kapton thickness, 5μm thick copper layers, 60-80 μm diameter holes and 140 μm pitch, with a sensitive area of either 3×3 or 10×10 cm^2. The results are summarized as follows:

- A triple GEM detector can operate in a very stable mode with pure CF$_4$ at gains in excess of 10^4 (see top left panel in Fig. 5.5).
- A charge saturation effect occurring in CF$_4$ (see top left panel in Fig. 5.5) makes the HBD relatively robust against discharges. The measurements reveal that the limit of stability is dictated by the quality of the GEM foils rather than by the presence of heavily ionizing particles.

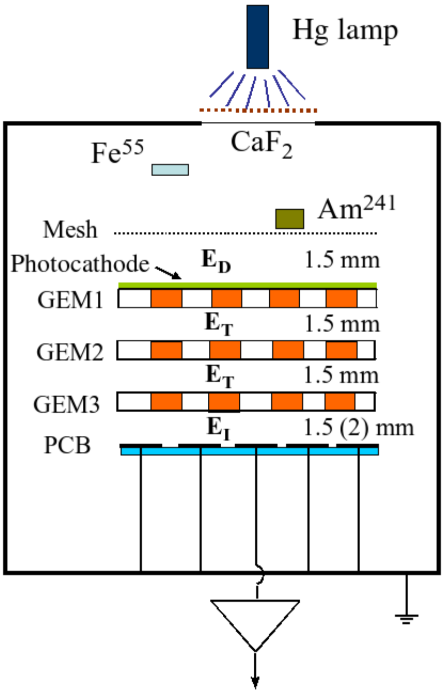

Figure 5.4: Set up of the triple GEM detector for R&D studies. A Hg lamp, ^{55}Fe and ^{241}Am sources were used for measurements with UV photons, X-rays and α-particles, respectively.

- Aging studies of the CsI photocathode as well as GEM foils showed no sizable deterioration of the detector gain and CsI quantum efficiency for irradiation levels of $\sim$ 150 μC/cm^2 that correspond to $\sim$ 10 years of normal PHENIX operation at RHIC.
- The CsI quantum efficiency in CF_4 was measured in the range 6-10.3 eV (120-200 nm). A linear extrapolation to the expected operational bandwidth of the device (6 - 11.5 eV) gives a figure of merit N_0 = 822 cm^{-1} and $\sim$ 36 photoelectrons over a 50 cm long radiator under ideal conditions.
- Systematic measurements of the detector response to electrons, mip's and α- particles as a function of the drift field E_D (the field in the gap between the mesh and the upper GEM) were done. A slightly reversed field in this gap strongly suppresses the charge collection from this gap as shown in the top right panel of Fig. 5.5, while the photoelectrons are effectively collected by the strong field inside the GEM holes (see bottom panel of Fig. 5.5). A combination of amplitude response, with hit size leads to large hadron rejection factors of $\sim$ 100, with a single electron detection efficiency of $\sim$ 90%.

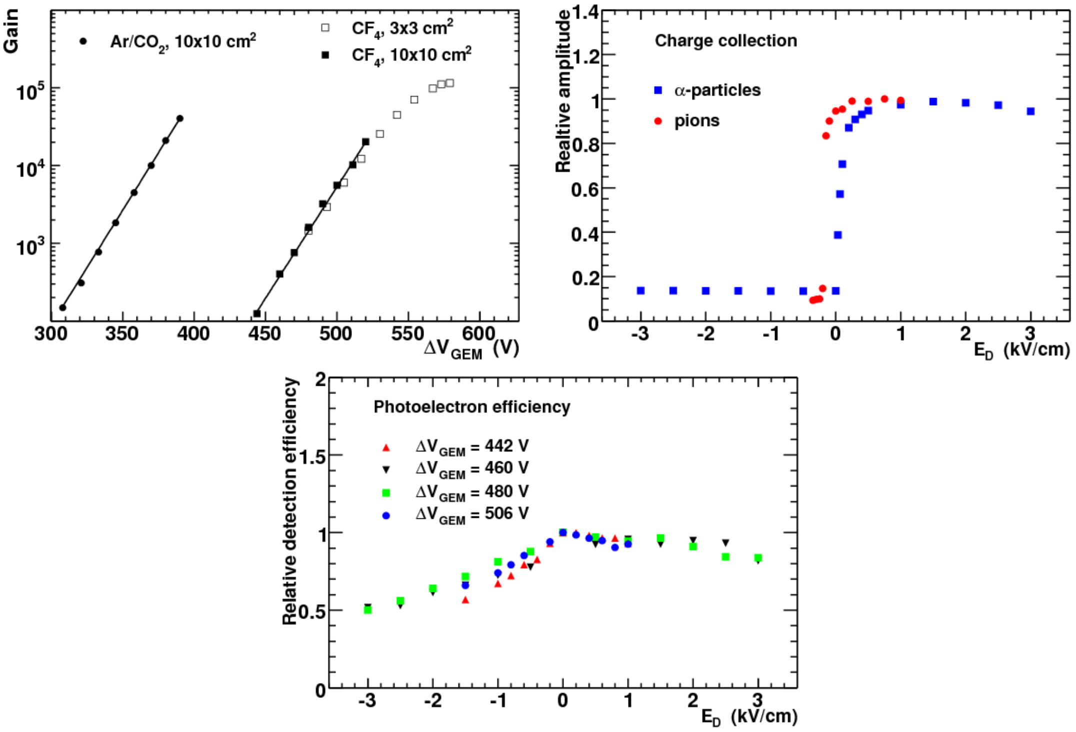

Figure 5.5: The top left panel shows gain as a function of ΔV_{GEM} for Ar/CO$_2$ and CF$_4$ measured with a Hg UV lamp. For CF$_4$, the gain curve with X-rays from ^{55}Fe is also shown. The lines are exponential fits to the data [154]. The top right panel shows the collection of ionization charge from 1 GeV/c pions and α particles from ^{241}Am vs. the drift field E$_D$ in the gap between the mesh and the upper GEM and the bottom panel shows the photoelectron detection efficiencies for different gains vs the drift field E$_D$ [155].

5.4 Construction of the final HBD

The design and construction of the detector vessel as well as assembly and preliminary test of the GEM foils were carried out at the WIS whereas the *CsI* evaporation, final assembly and test of detector modules were done at Stony Brook University. The analog and digital electronics were developed and built by BNL Instrumentation and Columbia University.

Vessel Construction The HBD consists of two identical vessels, located close to the interaction vertex. The entrance window is right after the beam pipe at r ∼5 cm and the detector extends radially up to r ∼60 cm and up to 63 cm along the beam axis. Each arm covers 135^0 in ϕ and ±0.45 units in pseudorapidity (η). This extended acceptance with respect to the central arm acceptance provides a generous veto area for the efficient rejection of close pairs, where only one partner is inside the central arm acceptance.

A 3-d view of the final HBD design can be seen in the left panel of Fig. 5.6 and an exploded view of one HBD vessel displaying various elements of the detector is shown in the right panel. Each vessel has a polygonal shape formed by the 10 panels (6 active panels, 2 HV panels and 2 vertical panels) glued together. These panels consist of a 19 mm thick honeycomb core sandwiched between two 0.25 mm thick FR4 sheets. Each of the six active back panels is equipped with two triple GEM photon detectors on the inside and to the Front End Electronics on the outer side. These panels have small holes for the wires that connect the pads to the motherboard into which the individual preamplifiers are plugged (see below). The two panels, outside the active area are used for detector services such as gas in/out, high voltage connectors serving the GEMs, and a UV transparent window. The entrance window to the detector is a 125 μm thick mylar foil coated with 100 nm aluminum and is placed between two FR4 supports bolted to each other with an O-ring seal. An FR4 frame, 19 mm wide and 7 mm thick connect all panels together on each side and provide mechanical stability and rigidity to the entire box. The vessel is closed by two side covers (made of 12.5 mm thick honeycomb sandwiched between two 0.25 mm thick FR4 sheets) which are bolted on the vessel frames with an O-ring seal. The various operations like gluing, assembling the panels etc, were done with specially designed jigs and tools. The vessel construction involved ~350 gluing operations per box.

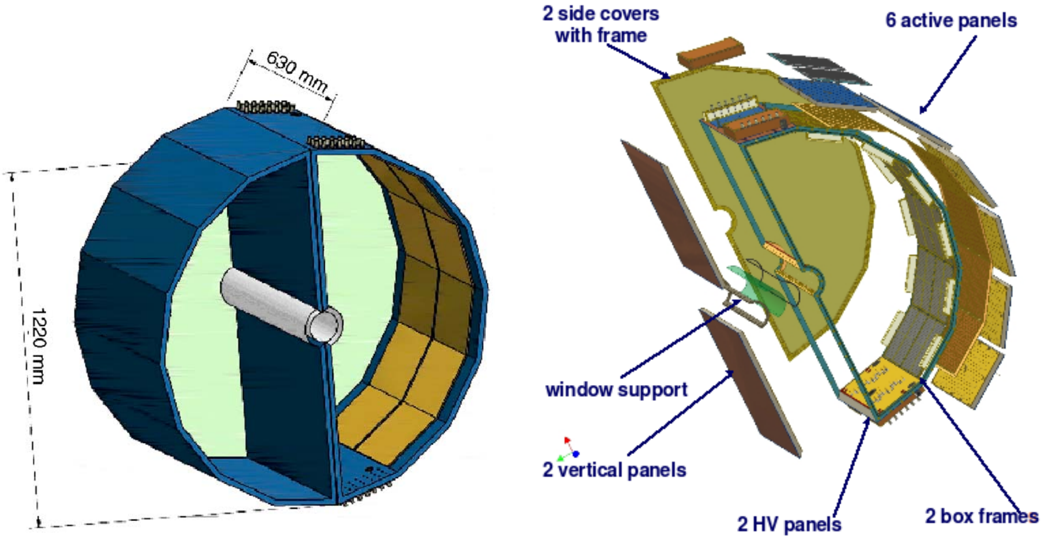

Figure 5.6: Left: a 3-d view of the HBD final design. Right: an exploded view of one HBD vessel showing the main elements.

The detector anode is a double-sided printed circuit board (PCB) made of a 50 μm thick Kapton foil in one single piece (140×63 cm^2). The PCB has 1152 hexagonal pads on the inner side and short (1.5 cm long) signal traces on the outer side, connected to the pads by plated-through holes in the PCB. Short wires are soldered at the edges of the signal traces and passed through small holes in the panels to bring the pad signals to the outer side, where the wires are soldered to a thin readout board containing the preamplifiers.

It is extremely important to have a leak-tight detector. Both water and oxygen have absorption bands in the deep UV region that absorb *Č*erenkov light and reduce the overall photoelectron yield[1]. Special attention was taken in the design to ensure the tightness of the vessel. The plated-through holes are effectively sealed by the panels glued on the back side of the PCB. Furthermore making the PCB as one single piece and gluing it to the panels provide a good seal at the junctions between the panels. The other panel junctions of the vessel are easily sealed by gluing a 50 μm thick mylar stripe along the inner side of the junction. The leak-rate in each one of the 311 liters vessel was measured to be < 0.12 cc/min.

Special care was taken in the design to minimize the dead areas, and the amount of material within the central arm acceptance. Each box weighs $\sim$5 Kg. Adding all accessories, HV connectors, gas in/out, GEM foils, preamplifier cards etc, results in a total weight of less than 10 Kg. The HBD contributes a total radiation length of about 3.34%, inside the central arm acceptance out of which 0.92% comes from the vessel, $\sim$ 1.88% from the electronics installed on the back of vessel and 0.54% from the 50 cm long CF_4 radiator.

Assembly and Testing of triple GEM detector modules The HBD consists of 24 identical detector modules, 12 in each arm, 6 along $\varphi\times$ 2 along z, each one with a size of 22.1×26.7 cm^2. Each detector module is comprised of a 91% transparent stainless steel mesh and three GEM foils. A standard GEM foil is a thin (50 μm) Cu-clad (5 μm) kapton foil perforated with holes of 80 μm diameter at a pitch of 150 μm. The top GEM facing the detector volume has a 0.2-0.4 μm layer of *CsI* evaporated on its surface previously coated with thin Gold and Nickel layers. The Gold layer prevents chemical reaction of the *CsI* with the copper of the GEM and the Ni acts as an adhesive agent between gold and copper. One face of the GEM foil is divided into 28 HV segments, 26 of which are of the same width (7.5 mm) and 2 segments (the first and last are of 6.5 mm width), to reduce the capacitance and the stored energy in case of discharge. The entrance mesh and the three GEM foils are mounted on FR4 fiberglass frames. The frames have a width of

---

[1] Every 10 ppm of either oxygen or water result in a loss of approximately 1 photoelectron by absorption in the 50 cm long CF_4 radiator

5 mm and a thickness of 1.5 mm that defines the inter-gap distance. They also have a supporting cross shape (0.3 mm thick in the middle), which prevents sagitta of the foils in the electrostatic field. The three GEM foils and mesh are stacked together and attached to the detector vessel by 8 pins, located at the corners and middle of the frames, that allow to keep the GEM foils and the mesh stretched while maintaining a minimum deformation of the 5 mm wide frames. The design allowed for only 1 mm clearance between two adjacent detectors. With this design, the resulting total dead area within the central arm acceptance is calculated to be 6%.

The different operations like gluing, stretching and high voltage testing of the GEM foils, were done either in a clean room or in a stainless steel box. The GEM foil was first stretched on a special stretching device and while stretched, glued onto the FR4 frames using epoxy[1]. Once the epoxy was cured, the GEM foil was cut from the stretching device and 20 MΩ SMD resistors were soldered across each HV segment. The GEMs were monitored for leakage current and discharges at every step *i.e.* before and after framing/gluing, and after soldering the resistors. A voltage of 550 V was applied in air across the GEM and a good GEM was required to draw a leakage current below 5 nA. A GEM that passed all these quality control tests, was then mounted inside a stainless steel vessel and tested up to 520V in CF_4. It was then mapped for gain variations in Ar/CO_2 using a collimated ^{55}Fe source, positioned inside the box. The measured gain values (corrected for pressure and temperature variation) were then stored in the PHENIX database.

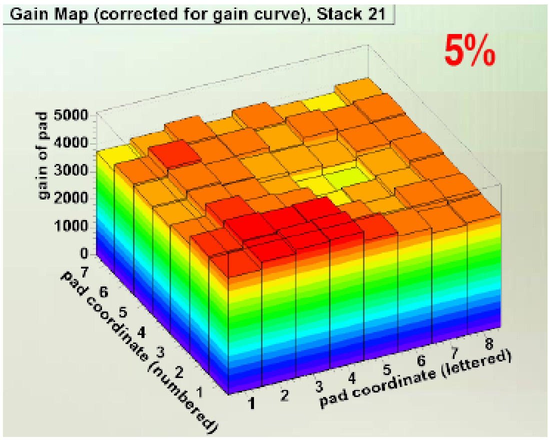

Figure 5.7: Gain map of one of the triple GEM stacks installed in the HBD

Due to small differences in the hole diameters, the GEMs have local gain variations that lead to an additive effect in the triple GEM assembly. A random combination of GEMs for the triple GEM assembly thus led to local gain variations which could be as high as 50%. In order to have the lowest possible gain variations between modules, the gain maps of the single GEMs were used to determine the gain of all possible triplets combinations and the best ones leading to the smallest gain variations were selected. The resulting gain spread from module to module varied from 5% to 20% in all the 24 modules. Fig. 5.7 shows the measured gain uniformity of an

---

[1] The epoxy used is Araldite AY-103/HY-991 from Huntsman Advanced Materials

installed stack in the HBD using this selection strategy. Out of a total of 65 standard and 47 gold plated GEMs that passed all the quality assurance tests, 48 standard and 24 Gold GEMs were used to construct the final detector.

***CsI* evaporation and readout electronics** The *CsI* evaporation on the top *Au* plated GEMs was performed at Stony Brook University [156], using a special evaporator system. The quantum efficiency of the photocathodes was measured inside the evaporator over the entire area of the GEM using a remote controlled movable UV light source and current monitor. The measured quantum efficiency was found to be in agreement with the R&D results [155] and uniform across the entire area of GEM to better than 5%.

Circuit boards containing the readout electronics [157] were installed on the back side of the vessel. The readout board is a multilayer board which contains the charge sensitive preamps and has a signal layer that drives the differential output signals from the preamps to connectors located at the edge of the board. The preamps used are hybrid preamplifiers, the $IO1195-1$, developed by the Instrumentation Division at BNL. The gain is set to give an output signal of ±50 mV for an input signal of 16 fC (100,000 e's), corresponding to an average signal of 20 photoelectrons per pad at a gas gain of 5×10^3. The preamp produces a differential signal in the range from 0 to ±1 V, that is delivered to a receiver and front end module (FEM). The FEM contains a 12 bit, 65 MHz flash-ADC for each channel which digitizes the signal. The FEM and all the digital electronics were designed and constructed by Nevis Laboratories.

5.5 HBD Performance in Run7 and Run9

The HBD was first installed into PHENIX in the year 2007, that served as an engineering run, and a series of studies were performed to test this new detector technology. The detector showed problems in holding high voltage, which was later confirmed to be due to trapped dust inside the detector. Besides, an inherent flaw in the LeCroy firmware was discovered. It was found that the mesh voltage was momentarily reapplied 200 ms after a trip, leading to a large HV difference in the 1.5 mm gap between the mesh and the top GEM, resulting in sparks. Many times the UV light from a single discharge would induce discharges on other GEM stacks in the line of sight, making several stacks to trip simultaneously. These massive discharges produced irreparable damage to several GEMs. The problem with the high voltage hardware was fixed during the run by installing zener diodes between the mesh and top GEM to remove the possibility of large voltage differences. More details can be found in [158]. These fixes prevented the massive trips and the detector operated rather stably for the rest period of the run.

The entire detector was rebuilt after Run7 and extreme care was taken to maintain a clean environment during the GEM assembly. A considerable fraction of the damaged GEMs was successfully recuperated by washing them with de-ionized water, and the rest were replaced with spare ones. The HBD was re-integrated into PHENIX in the summer of 2008 and successfully took physics data in $p+p$ collisions during Run9 and in the currently ongoing Run10, the HBD is successfully collecting data in $Au+Au$ collisions.

5.5.1 Calibration of the Detector

To optimize the performance of the HBD, a number of operational parameters like detector noise, adjusting gain and drift bias, need to be determined and well calibrated. A summary of the techniques that were developed to study and optimize these parameters during Run7 and Run9 are presented in the following sections.

5.5.1.1 HBD Noise Studies

The HBD is read out by a 2300 channel compact bit 12-bit 60 MHz digitizer system. The raw signals are shaped with 70 ns rise time and are directly digitized. An example of a 12 $\times$ 16 ns sample TDC signal for one HBD pad can be seen in top left panel in Fig. 5.8. The algorithm for signal processing used in Run7 and Run9 was $(S[8]+S[9]+S[10])/3-(S[0]+S[1]+S[2])/3$.

Fig. 5.8(b) (linear scale) and Fig. 5.8(c) (logarithmic scale) show a typical baseline noise distribution for one single pad, very nicely fitted with a gaussian. The detector exhibited an excellent performance of the noise level as can be seen Fig. 5.8(d)), with a typical $\sigma \sim 1.5$ ADC counts corresponding to ~ 0.1 primary electrons at a gain of 10^4. A zero suppression algorithm requiring a pad signal larger than 3σ or 5 ADC counts was implemented to reduce the event size.

5.5.1.2 Gain Determination and Calibration

One of the basic requirements of the HBD is to have an excellent ability to differentiate between single and double electrons based on the signal amplitude from the GEMs. The gain variations across the detector and over time due to temperature and pressure variations can lead to a smearing of the detector response and hence no clear separation between single and double hits. It is therefore crucial to monitor the absolute gain of each module and equilibrate the gain over the whole detector, and also over time.

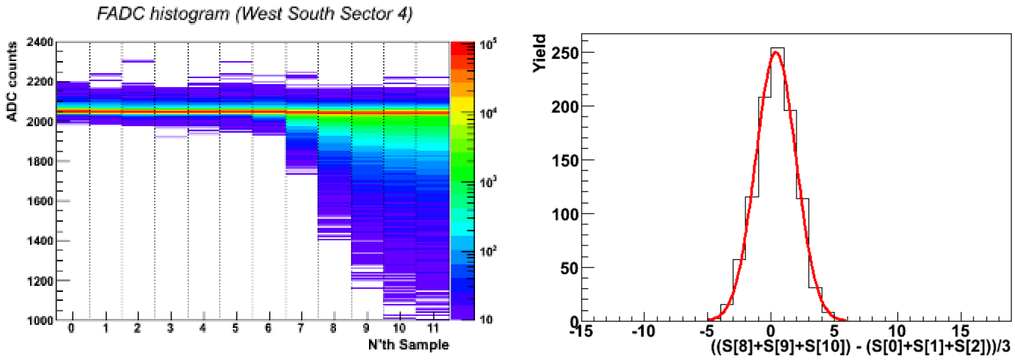

(a) ADC 12 × 16 ns samples

(b) Baseline ADC distribution (linear scale)

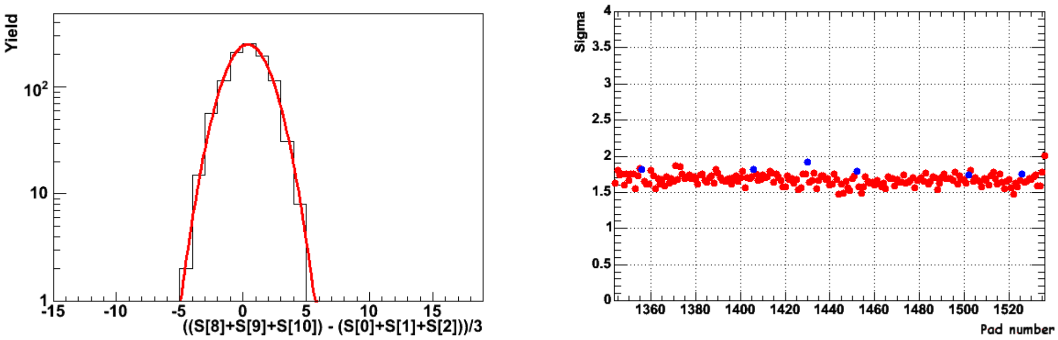

(c) Baseline ADC distribution (logarithmic scale)

(d) σ-values of the ADC distribution for a few HBD channels

Figure 5.8: The top left panel shows 12 × 16 ns ADC samples. The top right panel shows the distribution of ADC baseline values after pedestal subtraction for one single pad fitted to a Gaussian, in linear scale. The bottom left panel shows the same in logarithmic scale. The bottom right panel shows the distribution of the noise sigma values for a few pads.

The method used to determine the gas gain exploits the scintillation light produced in CF_4 by the charged particles traversing the radiator. The scintillation photons are identified by their expected characteristics: they should produce single pad hit signals on the readout plane with an exponential distribution, the signal does not depend on the detector bias (FB or RB), and the single fired pads from scintillation do not belong to any valid track. The scintillation component is clearly seen in Fig. 5.9, which shows the pulse height spectra for one module WS5 (West South sector 5) obtained from Run9 $p+p$ data. The FB and RB cases are overlayed and for a meaningful comparison, the ordinate is normalized to represent the number of hits per event. In the FB case, one can clearly see two components, a fast exponential from the scintillation photons and, a slow exponential due to charged particles. In the RB mode, as expected, the fast component due to scintillation survives completely whereas the tail due to charged particles is strongly suppressed.

Under the assumption that the number of scintillation photons per pad follows a Pois-

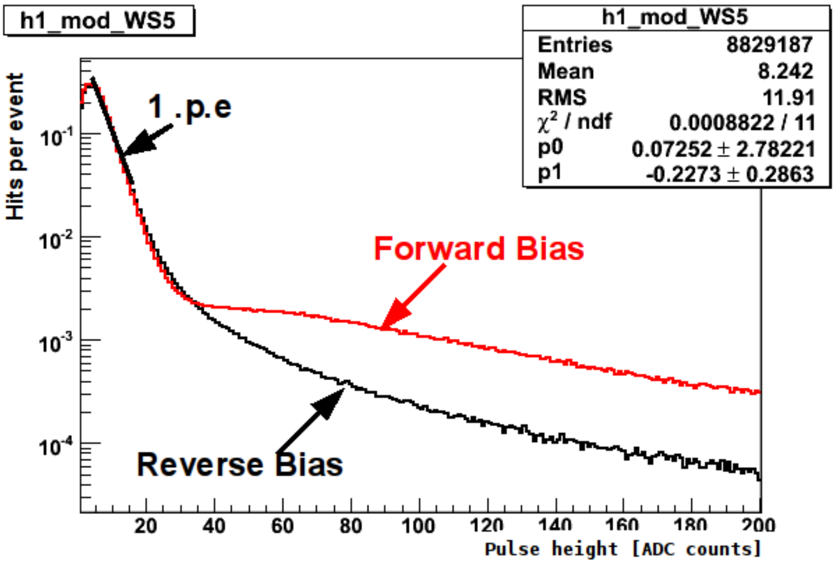

Figure 5.9: An example showing the FB and RB spectra for scintillation photons, for one HBD module (WS5) from Run9, used for the gain extraction.

son distribution,

$$P(n) = \frac{\mu^n e^{-\mu}}{n!} \tag{5.1}$$

the average number of scintillation photons in a given pad, $< m >$ is given by:

$$\langle m \rangle = \frac{\sum_{n\geq 1}^{\infty} nP(n)}{\sum_{n\geq 1}^{\infty} P(n)} = \frac{\mu}{1-P(0)} = \frac{\mu}{1-e^{-\mu}} \tag{5.2}$$

where P(0) = $e^{-\mu}$, is the probability to have no hit in the pad. The gain value is then given as

$$Gain = \frac{1/p_1}{\langle m \rangle} \tag{5.3}$$

where p_1 is the slope parameter obtained by fitting the scintillation part of the charge spectra to an exponential fit ($e^{p_1 \cdot x}$), as shown by the black line fit to the ADC charge distribution in Fig. 5.9.

For the case of $p+p$ collisions, due to the low multiplicity, the probability to have more than one scintillation hit in a given pad is very small and so $\langle m \rangle$ is ≈ 1. But for the $Au+Au$ collisions, $\langle m \rangle$ is a function of the event multiplicity and so needs to be calculated.

For small values of μ, we can rewrite Eq. 5.2 as follows:

$$\langle m \rangle = \frac{\mu}{1-e^{-\mu}} \approx 1 + \frac{\mu}{2} = 1 - \frac{ln(P(0))}{2} \tag{5.4}$$

The probability for no pad hit, $P(0)$, can not be measured directly, because the signal processing algorithm has a threshold on ADC counts for noise suppression and this information is not written out into the data stream. Instead, we can measure the probability to have a no hit in a given pad for several pad thresholds, which can then be extrapolated to zero pad threshold to obtain $P(0)$.

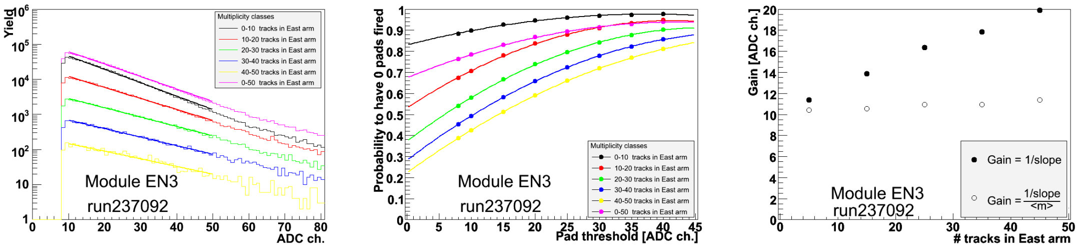

Figure 5.10: Left panel: ADC spectra for various event centralities defined on the basis of number of tracks in one central arm. Middle panel: the probability curve for $P(0)$ extraction as a function of pad threshold for each centrality. Right panel: uncorrected gain defined as Gain = $1/slope$ and the corrected gain defined as Gain = $\frac{1/slope}{\langle m \rangle}$.

The gain, if properly corrected for the multiple photon hits in a pad, should come independent of event multiplicity. This procedure for gain determination in $Au+Au$ collisions is demonstrated in Fig. 5.10 for one HBD module. The left panel shows the pulse height distributions for single fired pads with no associated central arm track, for various event multiplicities along with exponential fits. The middle panel shows the probability to have no pad fired, as a function of pad threshold for the same centralities shown in the left panel. These probabilities are fitted with a polynomial, which is extrapolated to zero threshold to get P(0). The right panel shows the uncorrected gains (Gain = $1/p_1$) (solid circles) and the corrected gains (Gain = $\frac{1/p_1}{<m>}$) (open circles) as a function of event multiplicity. The corrected gain, as expected, is independent of event multiplicity. For the most peripheral collisions, this correction becomes negligibly small and uncorrected gain approaches the absolute gain value.

5.5.1.3 Gain Equilibration

As already discussed in the previous section, the variations in gain affect the detector performance and make the analysis complicated. It is therefore in the best interest to minimize these gain variations. In general, we have two types of gain variations. The first one is due to spatial gain variations across the GEM area that could arise from different hole sizes, non-uniformities in the drift gap *etc*. To correct for these variations, we perform pad-by-pad gain calibrations, that are done once using a high statistics run. For this, we determine the gain of each pad G_i of a given module and the average gain $\langle G \rangle$ of that module, following the same procedure discussed in Section 5.5.1.2. Each signal a_i on pad is then corrected by:

$$a_i \longrightarrow a_i \frac{G}{G_i}$$

An example showing the spread of gains across the pads for one module, before and after the pad gain equilibration, is shown in Fig. 5.11. One can see that after equilibration, the spread of gains across all the pads has become smaller ($\sim$ 3-4%).

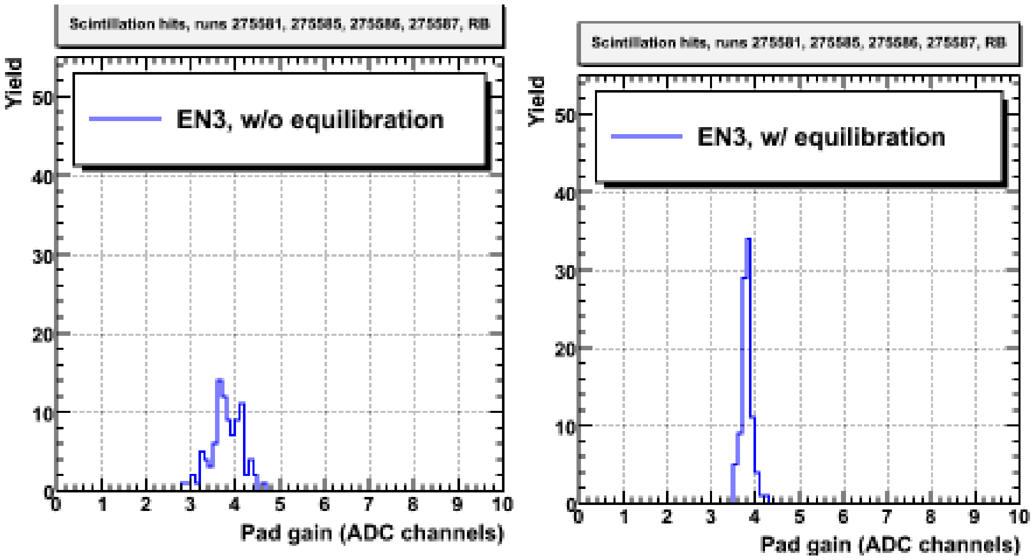

Figure 5.11: Left panel: gain distribution across all the pads in modules EN3 before equilibration. Right panel: the same after gain equilibration.

The second type of gain variations are due to changes over time. Slight changes in pressure (P) and/or temperature (T) significantly affect the detector gain. A change of 1% in P/T value causes a gain variation of $\sim$ 26% in CF_4 [154]. These changes in gain due to P/T variations can be compensated by changing the high voltage. Five P/T windows were defined, with each bin representing a variation of ± 13% in the gain, relative to center of the bin. Using gain curves measured with cosmic rays prior to the HBD installation in the laboratory, a look-up table was generated between these P/T bins and the high voltage (corresponding to center of the P/T bin) for several set of gains, for all 20 HBD modules. During the run, the P/T was monitored continuously online and whenever the measured P/T value crossed the window boundary, the high voltage was changed according to the look-up table for the new window. Using this procedure, we were able to limit the variations of gain to within 5-15%. This can be seen in Fig. 5.12

that shows the gains for all the modules in the west arm for the entire Run9. One can see that all the modules had relatively similar gains to each other and also over the entire Run9.

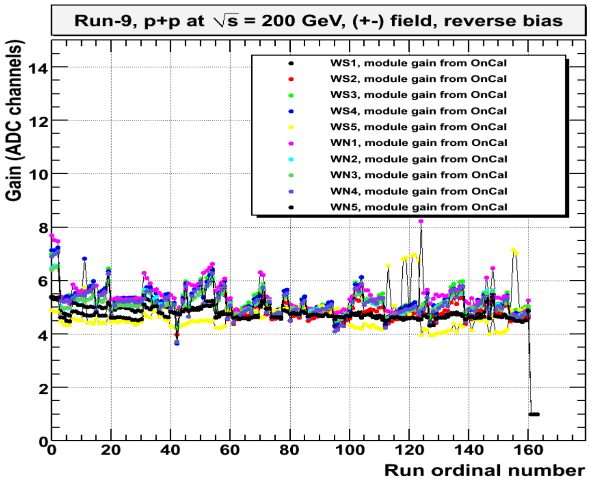

Figure 5.12: Gains of the HBD modules in west arm plotted as a function of run number for Run9 data.

5.5.1.4 Adjusting the Drift Bias Between the Mesh and Top GEM

As evident from Fig. 5.9, the ionization signal is much larger in the FB mode, due to the charge collected in the drift gap between the top GEM and the mesh. The ionization signal, as well as the photoelectron collection efficiency, depend strongly on the voltage across this gap. As soon as E_D is reversed, *i.e.*, set to negative values, there is a sharp drop in the pulse height as the primary charges get repelled towards the mesh, whereas the photoelectron collection efficiency drops much more slowly (see the bottom panel of Fig. 5.5).

From the R&D results (Fig. 5.5), we know that the optimum drift voltage (E_D) across the gap that gives a minimal hadron response, while keeping the photoelectron collection efficiency high, corresponds to zero volts. Since we use two separate HV power supplies for each module, one for the mesh and one for the GEM stack, and the absolute zero of a power supply has some uncertainty of few volts, the two power supplies need to be adjusted relative to each other.

This was achieved by performing a series of special runs where the voltage applied to the mesh of a given module was varied while keeping its gain constant. The relative voltage that corresponds to the zero drift field across the mesh to top GEM gap, was then

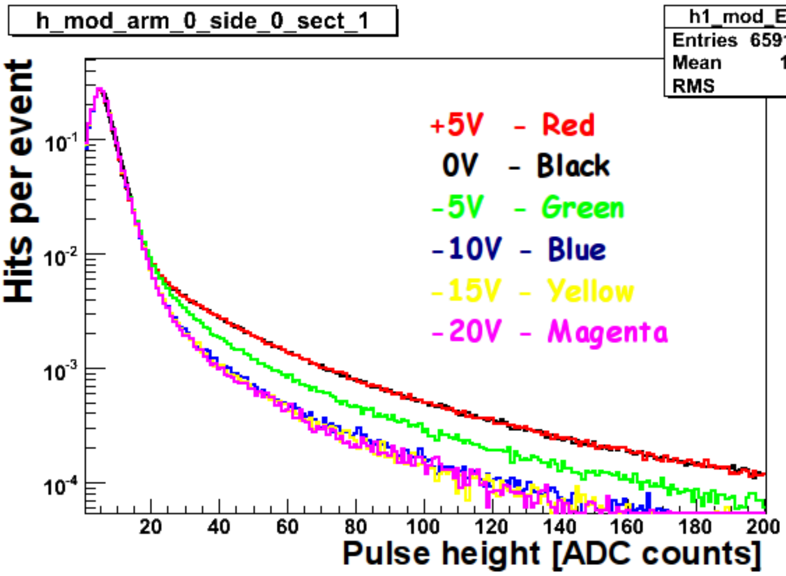

Figure 5.13: Example of a typical voltage scan for one module (ES1) performed in order to optimize the drift voltage (E_D) in the gap between the mesh and top GEM, for minimum sensitivity to hadrons and maximum photoelectron efficiency. The numbers refer to the nominal voltage difference between the two HV power supplies used for the mesh and the GEMs.

determined by looking at the pulse height spectra for different cases, and selecting the voltage that resulted in the minimal ionization tail. This is illustrated in Fig. 5.13 for one module ES1, where one can see different curves for the different voltages and it is evident that $E_D \approx 0$ should correspond to the set with $-15V$, because a further increase in negative relative voltage, does not reduce the ionization tail any more. This procedure of bias adjustment was done online for each individual module.

5.5.2 Results

The HBD was successfully operated in Run9 and took data for 200 GeV $p+p$ collisions in the "$+-$" magnetic field configuration. Currently only a fraction of the data (less than 10%) has been analyzed. However, the results from this preliminary analysis obtained so far show a much improved performance, compared to the engineering run in 2007, close to the anticipated one.

The HBD performance studies were done using a sample of events that satisfied a BBC vertex cut of $|bbcz| \leq 20$ cm. Reconstructed good quality (31||63) DC-PC1 tracks were selected and the analysis was restricted to events containing two electrons, identified using the standard eID cuts mentioned in Table 3.2, and that formed a pair with mass

$m_{e^+e^-} \leq 150$ MeV/c^2. This mass region is dominated by the π^0 Dalitz decays and has a high S/B ratio, thus providing a relatively clean sample of electrons that is suitable for detector performance studies.

Position Resolution The electron tracks selected in the central arms are projected onto the HBD plane and matched to the closest HBD hit. An example showing the distribution of residuals between identified electron tracks and associated hits in the HBD along the ϕ (azimuthal angle) and z (along the beam) axes is shown in Fig. 5.14. The matching resolution along z is $\sigma_z \approx 1.0$ cm and along ϕ, it is $\sigma_\phi \approx 8.0$ mrad. This is consistent with the resolution one would expect from the pad size (hexagonal pad dimension of a = 1.55 cm, implying $\sigma \sim 2a/\sqrt{12} = 0.9$ cm).

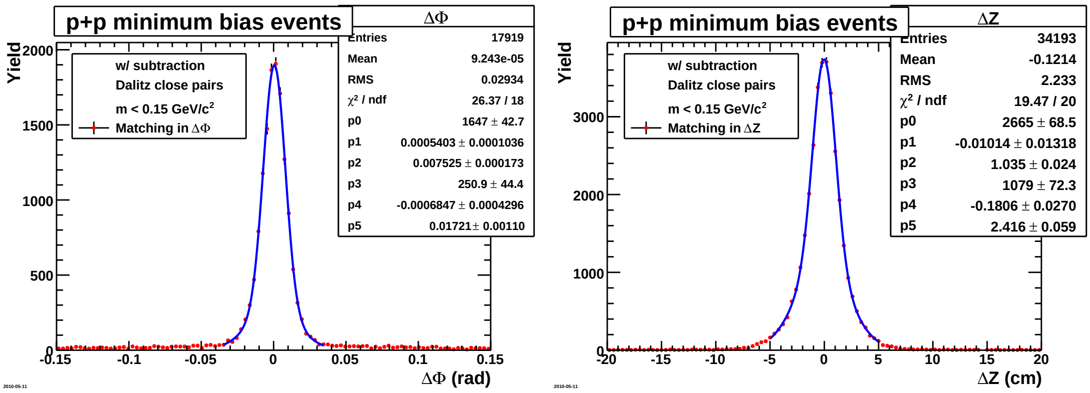

Figure 5.14: Matching distributions for electrons identified in the central arms, with clusters in the HBD along ϕ (left) and z (right).

Singles vs doubles One of the crucial requirements of the HBD performance is the ability to differentiate between single and double electron hit clusters. For studying this, as mentioned earlier, we use electrons from pairs that correspond to π^0 Dalitz region and then look at the charge distributions for single and double electrons. The charge distribution for single electrons was built, when the e^+ and e^- from a pair point to separate clusters in HBD. For doubles, those clusters were selected when the e^+ and e^- from a pair pointed to the same one cluster. The resulting charge distributions, calibrated in terms of photoelectrons, for single and double electron hit clusters are shown in Fig. 5.15. The distribution for singles peaks at ~ 20 p.e. while for doubles it peaks around ~ 40 p.e, which is double of the single electron's value. This gives a very good separation between the two cases and provides an excellent ability to identify single and double electrons in the final physics analysis. The value of ~ 20 photoelectrons for a single electron is

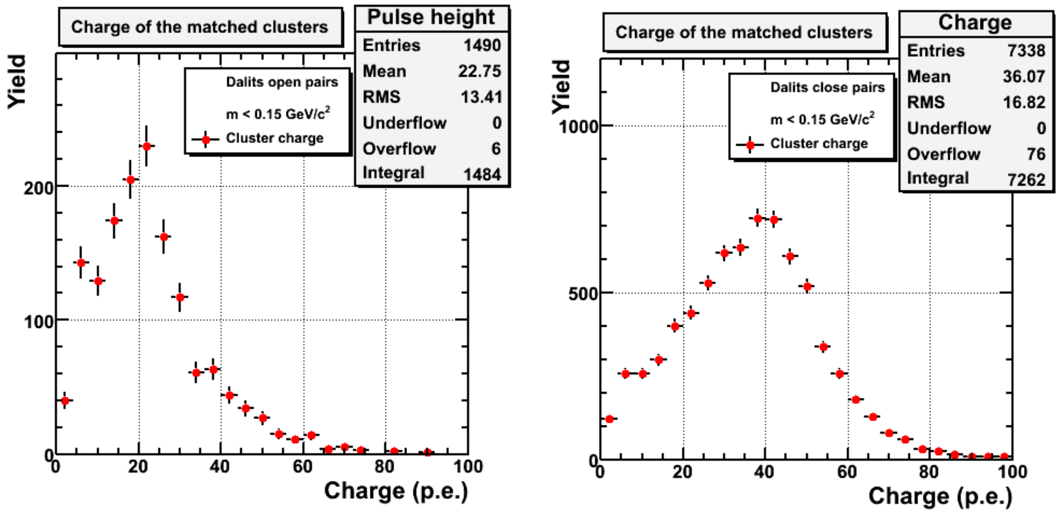

Figure 5.15: Photoelectron spectrum for single (left) and double electrons (right) in the HBD using e^+e^- pairs identified in the central arms with mass $m_{e^+e^-} \leq 150$ MeV/c^2.

essentially in agreement with what we expect, if we account for the known inefficiencies like gas transparency (dependent on the ppm levels of water and oxygen), wavelength dependent photoelectron efficiency ($\sim$ 66%) [159] etc. This gives us a good confidence that we have reached the optimal limit of performance of the detector.

Hadron Rejection factor The left panel in Fig. 5.16 shows the HBD response to hadrons identified in the central arms, in the reverse bias configuration. The photoelectron yield in this case peaks at around $\sim$ 1 p.e. as compared to 22, corresponding to single electrons. This will therefore provide an excellent hadron rejection while preserving good electron efficiency. The hadron rejection factor as a function of the cut on the number of photoelectrons in the hadron response is shown in the right panel of Fig. 5.16. A rejection factor of $\sim$ 50 can be achieved with a cut of about 11 p.e. The hadron rejection factor will further increase, when the cluster size cut is applied.

Electron efficiency The single electron efficiency was determined by selecting Dalitz pairs in the very low mass region ($25 \leq m_{e^+e^-} \leq 50$ MeV), and calculating the efficiency for finding clusters in the HBD, compared with the tracks found in the central arm. Fig. 5.17 shows the efficiency thus derived for singles as a function of the opening angle of the pair. It levels at around $\sim$ 90%, which is at the level required to have a good efficiency for detecting low mass pairs and vector mesons.

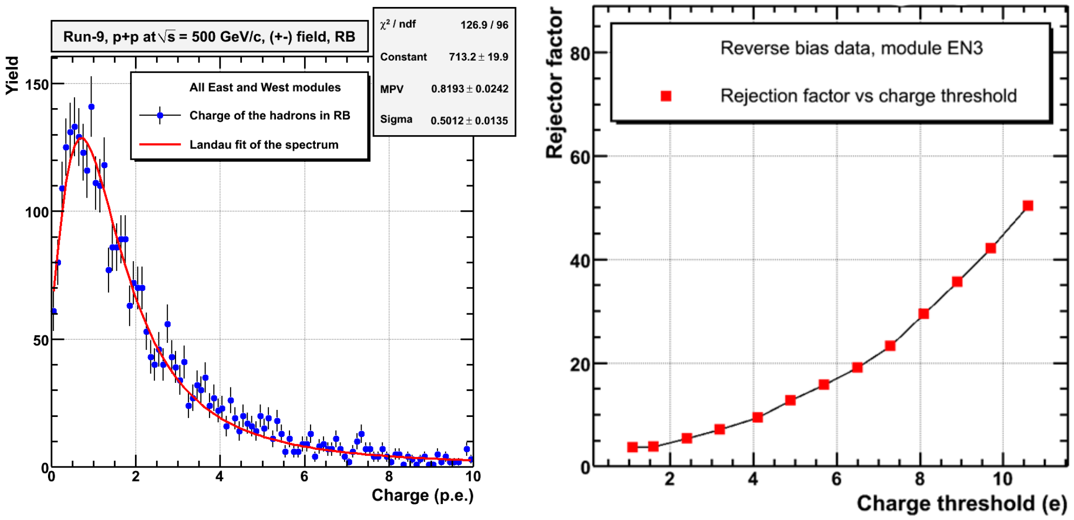

Figure 5.16: Left panel: the hadron response in photoelectron units in reverse bias mode. Right panel: the hadron rejection factor as a function of the cut on the photoelectron yield for one module, EN3.

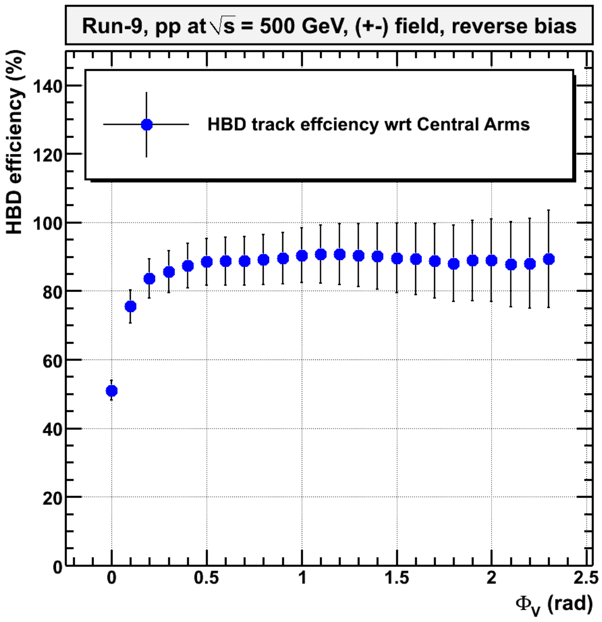

Figure 5.17: HBD single electron efficiency with respect to the central arms.

5.6 Summary

The HBD is a state-of-the-art detector developed for the measurement of low-mass electron pairs at RHIC with the PHENIX detector. It was rebuilt prior to the 2009 $p+p$ run at RHIC and was operated successfully for more than six months during the entire Run9. A lot of care was taken during assembling of GEMs, to maintain a very high level of cleanliness and minimal exposure to dust, which led to a much improved high voltage stability during the Run9 as compared to its operation in year 2007. An increased flow rate of ~ 4 lpm improved the UV transmission of gas and helped to preserve the quantum efficiency of the CsI photocathodes, leading to an overall increased photoelectron yield. We believe that we have reached the expected theoretical limit of photoelectron yield for single electrons, given the known efficiencies of the detector. This yield gives a good electron efficiency and separation between single and double electrons, that are required for efficient Dalitz pair rejection. The response to hadrons is highly suppressed compared to electrons, as is needed for hadron blind operation. The HBD is presently operational and taking data in the ongoing $Au+Au$ collisions at RHIC (Run10), which is a dedicated HBD run for the measurement of low mass electron pairs.

Appendix A

Publications that include this work

1. D. Sharma, ϕ-meson Production at RHIC energies using the PHENIX Detector, J. Phys. G36: 064023 (2009), arXiv:0901.3362.
2. D. Sharma, Low Mass Vector Meson Measurements via Di-electrons at RHIC by the PHENIX Experiment, arXiv:0901.3360; *Parallel Talk at 18th International Conference and Nuclei (PANIC08).*
3. PHENIX Collaboration: Scaling properties of particle production in $p+p$ collisions at 200 GeV measured by PHENIX, in preparation (D. Sharma is a memeber of the paper preparation committee).
4. PHENIX Collaboration: Measurement of ϕ mesons in $p+p$, $d+Au$ and $Au+Au$ collisions at $\sqrt{s_{NN}}$ = 200 GeV, in preparation (D. Sharma is a member of the paper preparation committee).
5. Design, Construction, Operation and Performance of a Hadron Blind Detector for the PHENIX Experiment, in preparation (D. Sharma is a member of the paper preparation committee).
6. I. Ravinovich *et al.* (including D. Sharma), A hadron blind detector for the PHENIX experiment at RHIC, Nucl. Phys. A774, 903 (2006); arXiv:nucl-ex/0510024, *Proceedings of 18th International Conference on Ultrarelativistic Nucleus-Nucleus Collisions: Quark Matter 2005 (QM 2005), Budapest, Hungary, 4-9 Aug 2005*"
7. A. Milov *et al.* (including D. Sharma), Construction and expected performance of the hadron blind detector for the PHENIX experiment at RHIC, J.Phys.G34:S701-S703 (2007), arXiv:physics/0701273, *Proceedings of 19th International Confer-*

ence on Ultra-Relativistic Nucleus-Nucleus Collisions: Quark Matter 2006 (QM2006), Shanghai, China, 14-20 Nov 2006

8. C. Woody *et al.* (including D. Sharma), Initial Performance of the PHENIX Hadron Blind Detector at RHIC., IEEE Nuclear Science Symposium Conference Record NSS/MIC, 1002-1008(2009).
9. W. Anderson *et al.* (including D. Sharma), Understanding the gain characteristics of GEMs inside the Hadron Blind Detector in PHENIX., IEEE Nuclear Science Symposium Conference Record NSS'07,6, 4662-4665(2007).
10. C.Y. Chi *et al.* (including D. Sharma), A faster digitizer system for the Hadron Blind Detector in PHENIX., IEEE Nuclear Science Symposium Conference Record NSS'07,3, 1997-2000(2007).
11. C. Woody *et al.* (including D. Sharma), Prototype Tests and Construction of the Hadron Blind Detector for the PHENIX Experiment., IEEE Nuclear Science Symposium Conference Record NSS'06,3, 1557-1561(2006).

Bibliography

[1] E. Rutherford and Hans Geiger. *The charge and nature of the α-particle*. Proc. Roy. Soc. Lond. A, **81** (1908) 162–173. 1

[2] J. Chadwick. *The existence of a neutron*. Proc. Roy. Soc. Lond. A, **136** (1932) 692–708. 1

[3] M. Gell-Mann. *A schematic model of baryons and mesons*. Phys. Lett., **8** (1964) 214–215. 1

[4] G. Zweig. *An SU(3) model for strong interaction symmetry and its breaking*. CERN preprint TH-412, unpublished., (1964). 1

[5] M. Gell-Mann. *The eightfold way: A theory of strong interaction symmetry*. Cornell preprint CTSL-20, unpublished, (1961). 1

[6] Y. Ne'eman. *Derivation of strong interactions fom a gauge invariance*. Nucl. Phys., **26** (1961) 222–229. 1

[7] J. J. Aubert *et.al.* *Experimental observation of a heavy particle*. Phys. Rev. Lett., **33** (1974) 1404–1406. 1

[8] J. E. Augustin *et.al.* *Discovery of a narrow resonance in e^+e^- annihilation*. Phys. Rev. Lett., **33** (1974) 1406–1408. 1

[9] S. W. Herb *et.al.* *Observation of dimuon resonance at 9.5-gev in 400-gev proton-nucleus collisions*. Phys. Rev. Lett., **39** (1977) 252–255. 1

[10] F. Abe *et.al.* *Observation of top quark production in $p\bar{p}$ collisions*. Phys. Rev. Lett., **74** (1995) 2626–2631. 1

[11] S. Abachi *et.al.* *Observation of the top quark*. Phys. Rev. Lett., **74** (1995) 2632–2637. 1

[12] C. Amsler *et.al. Review of Particle Physics*. Phys. Lett., **B667** (2008) 36–37. 2

[13] H. Fritzsch, M. Gell-Mann, and H. Leutwyler. *Advantages of the Color Octet Gluon Picture*. Phys. Lett., **B47** (1973) 365–368. 3

[14] J. C. Collins and M. J. Perry. *Superdense matter: Neutrons or asymptotically free quarks ?* Phys. Rev. Lett., **34** (1975) 1353–1356. 3

[15] L. D. McLerran and B. Svetitsky. *A Monte Carlo Study of SU(2) Yang-Mills Theory at Finite Temperature*. Phys. Lett., **B98** (1981) 195–198. 4

[16] Edward V. Shuryak. *Quantum Chromodynamics and the Theory of Superdense Matter*. Phys. Rept., **61** (1980) 70–158. 4

[17] F. Karsch. *Lattice Results on QCD Thermodynamics*. Nucl. Phys., **A698** (2002) 199–208. 4

[18] P. Braun-Munzinger and J. Stachel. *Dynamics of Ultra-Relativistic Nuclear Collisions with Heavy Beams: An Experimental Overview*. Nucl. Phys., **A638** (1998) 3–18. 4

[19] P. Braun-Munzinger, K. Redlich, and J. Stachel. *Particle production in heavy ion collisions*. Invited review of Quark Gluon Pasma 3, eds. R. C. Hwa and Xin-Nian Wang, World Scientific Publishing, (2003). 4, 5

[20] Z. Fodor and S. D. Katz. *Finite T/mu lattice QCD and the critical point*. Prog. Theor. Phys. Suppl., **153** (2004) 86–92. 4

[21] Shinji Ejiri *et.al. Study of QCD thermodynamics at finite density by Taylor expansion*. Prog. Theor. Phys. Suppl., **153** (2004) 118–126. 4

[22] A. Chodos, R. L. Jaffe, K. Johnson, C.B. Thorn, and V. F. Weisskopf. *New extended model of hadrons*. Phys. Rev., **D9** (1974) 3471–3495. 5

[23] C.-Y. Wong. *Introduction to High-Energy Heavy-Ion Collisions*. World Scientific, Singapore, (1994). 5

[24] J. Goldstone. *Field Theories with Superconductor solutions*. Il Nuovo Cimento., **19** (1961) 154–164. 7

[25] Michael C. Birse. *Chiral Symmetry in Nuclei: Partial Restoration and its Consequences*. J. Phys., **G20** (1994) 1537–1576. 7

[26] W. Weise. *Nuclear Aspects of Chiral Symmetry.* Nucl. Phys., **A553** (1993) 59c–72c. 7

[27] G. E. Brown and Monnque Rho. *Chiral Restoration in Hot and/or Dense Matter*. Phys. Report, **269** (1996) 333–380. 7, 18

[28] G. F. Chapline, M. H. Johnson, E. Teller, and M. S. Weiss. *Highly Excited Nuclear Matter*. Phys. Rev., **D8** (1973) 4302–4308. 8

[29] J. D. Bjorken. *Highly relativistic nucleus-nucleus collisions: The central rapidity region*. Phys. Rev., **D27** (1982) 140–151. 8

[30] Berndt Muller. *Physics and Signatures of the Quark-Gluon Plasma*. Rept. Prog. Phys., **58** (1995) 611–636. 9

[31] John W. Harris and Berndt Muller. *The search for the Quark-Gluon Plasma*. Ann. Rev. Nucl. Part. Sci., **46** (1996) 71–107. 9

[32] R. Rapp and J. Wambach. *Chiral symmetry restoration and dileptons in relativistic heavy-ion collisions*. Advances in Physics of Particles and Nuclei, **25** (2000) 1–205. 9

[33] T. Hatsuda and S. Lee. *QCD sum rules for vector mesons in the nuclear medium*. Phys. Rev., **C46** (1992) R34–R38. 9, 10, 18

[34] Y. Nambu and G. Jona-Lasinio. *Dynamical Model of Elementary Particles Based on an Analogy with Superconductivity. I.* Phys. Rev., **122** (1961) 345–358. 9

[35] C. M. Ko, V. Koch, and G. Q. Li. Annu. Rev. Nucl. Part Sci, **47** (1997) 505. 9

[36] G. E. Brown and Mannque Rho. *Scaling effective lagrangians in a dense medium*. Phys. Rev. Lett., **66** (1991) 2720–2723. 9, 10

[37] T. Weidmann *et.al.* e^+e^- *pairs from* π^-A *reactions*. Phys. Rev., **C59** (1999) 919–927. 10

[38] Saito K., K. Tsushima, and A. W. Thomas. *Variation of hadron masses in finite nuclei*. Phys. Rev., **C55** (1997) 2637–2648. 10

[39] Felix R. and J. Knoll. *Selfconsistent description of vector-mesons in matter*. Nucl. Phys., **A740** (2004) 287–308. 10

[40] E. Oset and A. Ramos. ϕ *decay in nuclei*. Nucl. Phys., **A679** (2001) 616–628. 10

[41] D. Cabrera and M. J. Vicente Vacas. *ϕ meson mass and decay width in nuclear matter*. Phys. Rev., **C67** (2003) 045203. 10

[42] F. Klingl, Waas T., and W. Weise. *Modification of the ϕ meson spectrum in nuclear matter*. Phys. Lett., **B431** (1998) 254–262. 10

[43] Subrata Pal, C. M. Ko, and Zi-wei Lin. *ϕ meson production in relativistic heavy ion collisions*. Nucl. Phys., **A707** (2002) 525–539. 10

[44] D. Lissauer and Edward V. Shuryak. *K meson modification in hot hadronic matter may be detected via ϕ meson decays*. Phys. Lett., **B253** (1991) 15–18. 10

[45] E. Santini, G. Burau, Amand Faessler, and C. Fuchs. *Medium effects on phi decays to dilepton and kaon antikaon pairs in relativistic heavy ion reactions*. Eur. Phys. J., **A28** (2006) 187–192. 10

[46] G. *et.al* Agakichiev. *Enhanced production of low-mass electron pairs in 200 gev/nucleon s-au collisions at the cern super proton synchrotron*. Phys. Rev. Lett., **75** (1975) 1272–1275. 10

[47] D. Adamova *et.al.* *Enhanced production of low-mass electron-positron pairs in 40-agev pb-au collisions at the cern sps*. Phys. Rev. Lett., **91** (2003) 042301. 10, 11

[48] G. Chanfray, R. Rapp, and J. Wambach. *Medium Modifications of the Rho Meson at CERN Super Proton Synchrotron Energies (200 GeV/nucleon)*. Phys. Rev. Lett, **76** (1996) 368–371. 10

[49] Itzhak Tserrya. *Electromagnetic probes*. arxiv:., **0903.0415v3** (2010) nucl–ex. 10

[50] R. Arnaldi. *First Measurement of the ρ Spectral Function in High-Energy Nuclear Collisions*. Phys. Rev. Lett., **96** (2006) 162302. 10

[51] D. Adamova. *Modification of the ρ meson detected by low-mass electron-positron pairs in central Pb-Au collisions at 158A GeV/c*. Phys. Lett., **B666** (2008) 425–429. 10

[52] A. Adare *et.al.* *Detailed measurement of the e^+e^- pair continuum in $p+p$ and $Au+Au$ collisions at $\sqrt{S_{NN}} = 200$ GeV and implications for direct photon production*. Phys. Rev., **C81** (2010) 034911. 11, 114

[53] S. V. Afanasiev *et.al.* *Production of* ϕ*-mesons in* $p+p$ *,* $p+Pb$ *and central* $Pb+Pb$ *collisions at* E_{beam}*=158 A GeV*. Phys. Lett, **B491** (2000) 59–66. 11

[54] B. Alessandro *et.al.* ϕ *production* $Pb-Pb$ *collisions at 158 GeV/c per nucleon incident momentum*. Phys. Lett, **B555** (2003) 147–155. 11

[55] D. Jouan for the NA50 collaboration. ϕ *production and* $\omega-\rho$ *production in* $d-C$*,* $d-U$*,* $S-U$ *and* $Pb-Pb$ *at SPS energies*. J. Phys., **G35** (2008) 104163. 11

[56] A. De Falco for the NA60 collaboration. *NA60 results on* ϕ *production in the hadronic and leptonic channels in* $In-In$ *at 158 GeV*. Nucl. Phys., **A830** (2009) 753c–756c. 11

[57] S. Damjanovic for the NA60 Collaboration. *First results from NA60 on low mass muon pair production in* $In-IN$ *collisions at 158 GeV/nucleon,* . J. Phys., **G31** (2005) S903–S910. 11

[58] R. Rapp. *Thermal lepton production in heavy-ion collisions*. arXiv:, (2002). 11, 12

[59] R. Rapp. *Signatures of thermal dilepton radiation at ultrarelativistic energies*. Phys. Rev., **C63** (2001) 054907. 11, 12

[60] B. Abelev *et.al.* *Measurements of* ϕ *meson production in relativistic heavy-ion collisions at RHIC*. arxiv:, **0809.4737** (2008) nucl–ex. 12

[61] S. S. Adler *et al.* *Production of* ϕ *mesons at midrapidity in* $\sqrt{s_{NN}}$ *=200 GeV* $Au+Au$ *collisions at relativistic energies*. Phys. Rev., **C72** (2005) 014903. 12, 78

[62] A. Kozlov for the PHENIX collaboration. *Low mass dielectrons from the PHENIX-experiment at RHIC*. Eur. Phys. J. A, **31 4** (2007) 836–841. 12

[63] K. Ozawa *et al.* *Observation of* ρ/ω *Meson Modification in Nuclear Matter*. Phys. Rev. Lett., **86** (2001) 5019–5022. 18

[64] M. Naruki *et al.* *Experimental Signature of Medium Modifications for* ρ *and* ω *Mesons in the 12 GeV* $p+A$ *Reactions*. Phys. Rev. Lett., **96** (2006) 092301. 18

[65] R. Muto *et al.* *Evidence for In-Medium Modification of the* ϕ *Meson at Normal Nuclear Density*. Phys. Rev. Lett., **98** (2001) 042501. 18

[66] D. Trnka *et al.* *Observation of In-Medium Modifications of the* ω *Meson*. Phys. Rev. Lett., **94** (2005) 192303. 18

[67] M. Kotulla *et al.* *Modification of the ω-Meson Lifetime in Nuclear Matter*. Phys. Rev. Lett., **100** (2008) 192302. 18

[68] M. Nanova. *In-medium modifications of the ω meson*. AIP Conf. Proc., **1257** (2010) 705–709. 18

[69] R. Nasseripour *et al.* *Search for Medium Modifications of the ρ Meson*. Phys. Rev. Lett., **99** (2007) 262302. 18

[70] R. Rapp and J. Wambach. *Low-mas dileptons at the CERN-SPS: evidence for chiral restoration?* Eur. Phys. J., **A6** (1999) 415–420. 18

[71] M. Post and U. Mosel. *Vector mesons and baryon resonances in nuclear matter*. Nucl. Phys., **A699** (2002) 169–172. 18

[72] D. Carbera, E. Oset, and Vacas Vicente. *Chiral approach to the rho meson in nuclear matter*. Nucl. Phys., **A705** (2002) 90–118. 18

[73] G. J. Lolos *et al.* *Evidence for* ρ^0 *Mass Modification in the* $^3He\ (\gamma,\rho^0)\ ppn$ *Reaction*. Phys. Rev. Lett, **80** (1998) 241–244. 19

[74] G. M. Huber, G. J. Lolos, and Z. Papandreu. *Probing the* ρ^0 *Mass Modification in the Subthreshold Region on* ^3He. Phys. Rev. Lett., **80** (1998) 5285–5288. 19

[75] G. M. Huber *et al.* *In-medium* ρ^0 *spectral function study via the* ^2H, ^3He, ^{12}C $(\gamma,\pi^+\pi^-)$ *reaction*. Phys. Rev., **C68** (2003) 065202. 19

[76] R. Rapp, G. Chanfray, and J. Wambach. *Rho meson propagation and dilepton enhancement in hot hadronic matter*. Nucl. Phys., **A617** (1997) 472–495. 19

[77] M. Post, S. Leupold, and U. Mosel. *The ρ spectral function in a relativistic resonance model*. Nucl. Phys., **A689** (2001) 753–783. 19

[78] J. L. Nagle. *PHENIX Run-08 d-Au @ 200 GeV Centrality Categorization*. PHENIX Internal Analysis Note., **an900** (2009). 13

[79] K. Adcox *et. al.* *Suppression of Hadrons with Large Transverse Momentum in Central* $Au+Au$ *Collisions at* $\sqrt{s_{NN}}$ *=130 GeV*. Phys. Rev. Lett, **88** (2002) 022301. 13, 110

[80] K. Adcox *et. al.* *Centrality Dependence of the high* p_T *Charged Hadron Suppression in* $Au+Au$ *collisions at* $\sqrt{s_{NN}}$ *=130 GeV*. Phys. Lett., **B561** (2003) 82–92. 13, 110

[81] S. S. Adler *et. al.* *High* p_T *Charged Hadron Suppression in* $Au+Au$ *collisions at* $\sqrt{s_{NN}}$ *=200 GeV*. Phys. Rev., **C69** (2004) 034910. 13, 14, 110

[82] S. S. Adler *et. al.* *Suppressed* π^0 *Production at Large Transverse Momentum in Central* $Au+Au$ *collisions at* $\sqrt{s_{NN}}$ *=200 GeV*. Phys. Rev. Lett., **91** (2003) 072301. 13, 14, 110

[83] J. Adams *et. al.* *Transverse-Momentum and Collision-Energy Dependence of High* p_T *Hadron Suppression in* $Au+Au$ *collisions at Ultrarelativistic Energies*. Phys. Rev. Lett., **91** (2003) 172302. 13, 14, 110

[84] A. Adare *et.al.* *Nuclear modification factors of* ϕ *meson in* $d+Au$ *,* $Cu+Cu$ *and* $Au+Au$ *collisions at* $\sqrt{s_{NN}}$ *=200 GeV.* Submitted to Phys. Lett. B, **arXiv:1004.3532** (2010). 14, 15, 93, 102, 108, 109, 112, 113

[85] S. S. Adler *et.al.* *Nuclear Effects on Hadron Production in* $d+Au$ *and* $p+p$ *Collisions at* $\sqrt{s_{NN}}$*=200 GeV*. Phys. Rev., **C74** (2006) 024904. 14, 15, 17, 93, 112, 113

[86] A. Adare *et.al.* *Suppression pattern of neutral pions at high transverse momentum in* $Au+Au$ *collisions at* $\sqrt{s_{NN}}$ *=200 GeV and constraints on medium transport coefficients*. Phys. Rev. Lett., **101** (2008) 232301. 14, 15

[87] Klaus Reygers. *Characteristics of Parton Energy Loss Studied with High-*p_T *Particle Spectra from PHENIX*. J. Phys., **G35** (2008) 104045. 14, 15

[88] M. Gyulassy *et. al.* *JET QUENCHING AND RADIATIVE ENERGY LOSS IN DENSE NUCLEAR MATTER*. arxiv:, **nucl-th/0302077** (2003). 14

[89] Xin-Nian Wang. *Systematic study of high* p_t *hadron spectra in pp, pa, and aa collisions at ultrarelativistic energies*. Phys. Rev. C, **61** (2000) 064910. 14, 16, 17, 110

[90] D. Kharzeev, E. Levin, and L. McLerran. *Parton saturation and* N_{part} *scaling of semi-hard processes in QCD*. Phys. Lett., **B561** (2003) 93–101. 14, 17, 110

[91] K. Gallmeister, C. Greiner, and Z. Xu. *Quenching of high* $p_\perp$ *hadron spectra by hadronic interactions in heavy ion collisions at relativistic energies*. Phys. Rev. C, **67** (2003) 044905. 14

[92] J. W. Cronin, H. J. Frisch, and M. J. Shochet. *Production of hadrons at large transverse momentum at 200, 300, and 400 gev*. Phys. Rev., **D11** (1974) 3105–3123. 16

[93] D. Antreasyan, J. W. Cronin, H. J. Frisch, and M. J. Shochet. *Production of hadrons at large transverse momentum in 200-, 300-, and 400-gev* $p+p$ *and p-nucleus collisions*. Phys. Rev., **D19** (1978) 764–778. 16

[94] M. Lev and Petersson B. *Nuclear effects at large transverse momentum in a qcd parton model*. Z. Phys. C Particles and Fields, **21** (1983) 155–161. 16, 17

[95] A. Accardi. *Cronin effect in proton-nucleus collisions: A survey of theoretical models*. hep-ph/0212148, (2000). 16, 17, 110

[96] A.L.S. Angelis *et. al.* *Large transverse momentum* π^0 *production in* $\alpha\alpha$*, dd and pp collisions at the CERN ISR*. Phys. Lett., **B185** (1987) 213–217. 16

[97] E. Wang and X. N. Wang. *Interplay of soft and hard processes and hadron* p_T *spectra in pA and AA collisions*. Phys. Rev., **C64** (2001) 034901. 16

[98] T. Alexopoulos. *The role of double parton collisions in soft hadron interactions*. Phys. Lett. B, **435** (1998) 453–457. 16

[99] S. S. Adler *et al.* *Centrality Dependence of* π^0 *and* η *Production at Large Transverse Momentum in* $\sqrt{s_{NN}}$ *=200 GeV* $d+Au$ *Collisions*. Phys. Rev. Lett., **98** (2007) 172302. 17, 111, 112, 113

[100] Toshio Ochiai, Schin Date, and Hiroyuki Sumiyoshi. *EMC Effect and Hadron Production off Nuclei at Large TransverseMomentum*. Progress of Theoretical Physics, **75** (1986) 288–300. 17

[101] Ivan. Vitev. *Initial state parton broadening and energy loss probed in* $d+Au$ *at rhic*. Phys. Lett. B, **562** (2003) 36. 17

[102] Dmitri. Kharzeev. *Cronin effect and high-*p_t *suppression in pa collisions*. Phys. Rev. D, **68** (2003) 094013. 17, 110

[103] M. Harrison, T. Ludlam, and S. Ozaki. *RHIC project overview*. Nucl. Instr. and Meth., **A499** (2003) 235–244. 21

[104] M. Adamczyk *et al.* *The BRAHMS experiment at RHIC*. Nucl. Instr. and Meth., **A499** (2003) 437–468. 23

[105] B.B. Back *et al.* *The PHOBOS detector at RHIC*. Nucl. Instr. and Meth., **A499** (2003) 603–623. 23

[106] K. Adcox *et.al.* *PHENIX detector overview*. Nucl. Instr. and Meth., **A499** (2003) 469–479. 23

[107] K.H. Ackerman *et al.* *STAR detector overview*. Nucl. Instr. and Meth., **A499** (2003) 624–632. 23

[108] H. Akikawa *et.al.* *PHENIX Muon Arms*. Nucl. Instr. and Methods, **A499** (2003) 537–548. 23

[109] M. Allen *et.al.* *PHENIX inner detectors*. Nucl. Instr. and Meth., **A499** (2003) 549–559. 28

[110] K. Ikematsu *et.al.* *A start-timing detector for the collider experiment PHENIX at RHIC-BNL*. Nucl. Instr. and Meth., **A411** (1998) 238–559. 28

[111] T. Ludlam. *Overview of experiments and detectors at rhic*. Nucl. Instr. and Meth., **A499** (2003) 428–432. 28

[112] C. Adler. *The RHIC zero degree calorimeters*. Nucl. Instr. and Meth., **A470** (2001) 488–499. 28

[113] S.H. Aronson *et.al.* *PHENIX magnet system*. Nucl. Instr. and Methods, **A499** (2003) 480–488. 29

[114] K. Adcox *et.al.* *PHENIX central arm tracking detectors*. Nucl. Instr. and Meth., **A499** (2003) 489–507. 30

[115] J.T. Mitchell *et.al.* *Event reconstruction in the PHENIX central arm spectrometers*. Nucl. Instr. and Methods, **A482** (2002) 491–512. 31, 32, 34, 49, 78

[116] K. Adcox *et al.* *Construction and performance of the PHENIX pad chambers*. Nucl. Instr. and Meth., **A497** (2003) 263–293. 32

[117] S. C. Johnson. *Three dimensional track finding in the phenix drift chamber by a combinatorial hough transform method*. In *Proc. of Intl. Conf. on Computing in High Energy Physics (CHEP 98), Chicago IL*, 1998. 33

[118] A. Chikanian *et.al.* *A momentum reconstruction algorithm for the PHENIX spectrometer at Brookhaven*. Nucl. Instr. and Methods, **A371** (1996) 480–488. 36

[119] Y. Akiba *et al. Ring imaging cherenkov detector of PHENIX experiment at RHIC*. Nucl. Instr. and Meth., **A453** (2000) 279–283. 37

[120] T. Sakaguchi *et al. Development of front end electronics for PHENIX RHIC*. Nucl. Instr. and Meth., **A453** (2000) 382–385. 37

[121] W. M. Yao *et.al. Review of particle physics*. J. Phys., **G33** (2006) 1–1232. 37

[122] L. Aphecetche *et al. PHENIX calorimeter*. Nucl. Instr. and Meth., **A499** (2003) 521–536. 37

[123] H. Fessler *et al. A tower structured scintillator-lead photon calorimeter using a novel fiber optics readout system*. Nucl. Instr. and Meth., **A228** (1985) 303–308. 37

[124] S. S. Adler *et.al. PHENIX on-line systems*. Nucl. Instr. and Meth., **A499** (2003) 560–592. 39

[125] A. Drees and Xu. Zhangbu. *Results from Luminosity Scans during the RHIC 2000*. In *Proc. of the 2001 Particle Accelerator Conference, Chicago IL*, 2001. 41

[126] S.N. White. *Diffraction dissociation - 50 years later*. In *Proc. of the AIP Conference., 792*, 527–531, 2005. 41

[127] S. R. Klein and R. Vogt. *Nuclear shadowing and high pt hadron spectra in relativistic heavy ion collisions*. Phys. Rev., **C67** (2003) 047901. 41

[128] R. J. GLauber and G. Matthiae. *High energy scattering of protons by nuclei*. Nuclear Physics B, **21** (1970) 135–157. 43

[129] L. Hulthen and M. Sagawara. *Handbuch der physik*. Springer-Verlag, Berlin, **39** (1957). 43

[130] A. Toia, A. Averbeck, T. Dahms, A. Drees, and A. Hemmick. *Analysis of dielectron continuum in $Au+Au$ at 200 GeV (RUN4)*. PHENIX Internal Analysis Note, **407** (2005). 66

[131] G. I. Kopylov. *Like particle correlations as a tool to study the multiple production mechanism*. Phys. Lett., **B50** (1974) 472–474. 72

[132] D. Drijard, H. G. Fischer, and T. Nakada. *Study of event mixing and its application to the extraction of resonance signals*. Nucl. Instr. and Meth., **A225** (1984) 367. 72

[133] D. L'Hote. *About resonance signal extraction from multiparticle data: combinatorics and event mixing methods*. Nucl. Instr. and Meth., **A337** (1994) 544–556. 72

[134] W.M. Yao *et.al. Review of Particle Physics*. J. Phys., **G33** (2006) 1–1232. 76

[135] K. Hagiwara *et.al. Review of particle physics data group*. Phys. Rev.D, **6 010001** (2002). 77

[136] R. Barlow *et.al. Sluo lectures on stats. and numerical methods in hep. lecture5: Systematic errors*. http://www-group.slac.stanford.edu/sluo/Lectures/stat lecture files/sluolec5.pdf, 2000. 77

[137] L. Lyons, D Gibaut, and D. Clifford. *How to combine correlated estimates of as single physical quantity*. Nucl. Instr. and Meth., **A270** (1988) 110. 77

[138] GEANT. *manual, v.3.2.1, cern program library w5013*, 1994. 77

[139] G.J. Gounaris and J.J. Sakurai. *Finite width corrections to the vector meson dominance prediction for* $\rho \rightarrow e^{+}e^{-}$. Phys. Rev. Lett, **21** (1968) 244–247. 78

[140] M. J. Tannenbaum. *Smearing and Binning of Falling Spectra*. PHENIX Internal Analysis Note, **62** (2001). 86

[141] G. Wilk and Z. Wlodarczyk. *On the Interpretation of Non-extensive Parameter q is Tsallis Statistics and Levy Distributions*. Phys. Rev. Lett, **84** (2000) 2770–2773. 86, 93

[142] C. Amsler *et.al. Review of Particle Physics*. Phys. Lett., **B667** (2008) 583–1058. 89

[143] S. S. Adler *et.al. Absence of suppression in particle production at large transverse momentum in* $\sqrt{s_{NN}} = 200$ *gev* $d+Au$ *collisions*. Phys. Rev. Lett., **91** (2003) 072303. 93

[144] A. Adare *et.al. Inclusive cross section and double helicity asymmetry for* π^0 *production in* $p+p$ *collisions at* $\sqrt{s_{NN}}$ *=200 GeV: implications for the polarized gluon distribution in the proton*. Phys. Rev., **D76** (2007) 051106. 93

[145] S. S. Adler *et.al. Production of* ω *meson at Large Transverse Momenta in* $p+p$ *and* $d+Au$ *Collisions at* $\sqrt{s_{NN}}$*=200 GeV*. Phys. Rev., **C75** (2007) 051902. 93, 102, 108, 109, 112, 113

[146] A. Adare *et.al.* *J/ψ production versus transverse momentum and rapidity in $p+p$ collisions at $\sqrt{s_{NN}}$ =200 GeV*. Phys. Rev. Lett, **98** (2007) 232002. 93

[147] John. Adams *et.al.* *K^*(892) Resonance Production in $Au+Au$ and $p+p$ collisions at $\sqrt{s_{NN}}$ = 200-GeV at STAR*. Phys. Rev., **C71** (2005) 064902. 93

[148] Maxim Naglis. *ϕ meson production in $p+p$, $d+Au$ and $Au+Au$ collisions at RHIC using the PHENIX detector*. PhD thesis, Weizmann Institute of Science, Israel. http://www.phenix.bnl.gov/phenix/WWW/publish/naglis/thesis.pdf, 2009. 108

[149] F. Karsch. *Lecture notes phys. 583, 209*. hep-lat/0106019, 2002. 114

[150] Z. Fraenkel, B. Khachaturov, A. Kozlov, A. Milov, D. Mukhopadhyay, D. Pal, I. Ravinovich, I. Tserruya, and S Zhou. *The PHENIX Collaboration. Technical Note* 391. http://www.phenix.bnl.gov/phenix/WWW/publish/tserruya/1-06-HBD-proposal.ps, 2001. 114, 115, 117

[151] C. Aidala *et.al.* *A Hadron Blind Detector for PHENIX*. Nucl. Inst. and Methods, **A502** (2003) 200–204. 114

[152] B. Azmoun *et.al.* *The PHENIX Collaboration. Technical Note* 415. http://www.phenix.bnl.gov/phenix/WWW/publish/tserruya/5-08-HBD-CDR/HBD-CDR.pdf, 2005. 114

[153] F. Sauli. *GEM: A new concept for electron amplification in gas detectors*. Nucl. Instr. and Meth., **A386** (1997) 531–534. 116

[154] A. Kozlov *et.al.* *Development of a triple gem uv-photon detector operated in pure cf_4 for the phenix experiment*. Nucl. Instr. and Meth., **A523** (2004) 345–354. 117, 118, 120, 129

[155] Z. Fraenkel *et.al.* *A hadron blind detector for the PHENIX experiment at RHIC*. Nucl. Instr. and Meth., **A546** (2005) 466–480. 117, 118, 120, 124

[156] J. A. Kamin. *A Hadron Blind Detector for the PHENIX Experiment at RHIC*. Eur. Phys. J., **C49** (2007) 177–180. 124

[157] C. Y. Chi, W. Anderson, B. Azmoun, C. Citron, A. Dubey, J. M. Durham, Z. Fraenkel, T. Hemmick, A. Kozlov, Milov. M, M. Naglis, P. O' Connor, R. Pisani, V. Radeka, I. Ravinovich, T. Sakaguchi, D. Sharma, A. Sickles, S. Sippach, F. W.

ans Stoll, I. Tserruya, C. Woody, and B. Yu. *A faster digitizer system for the hadron blind detector in phenix*. In IEEE Nuclear Science Symposium Conference Record, NSS'07, **Volume 3** (2007) 1997–2000. 124

[158] W. Anderson, B. Azmoun, C. Y. Chi, C. Citron, A. Dubey, J. M. Durham, Z. Fraenkel, T. Hemmick, A. Kozlov, Milov. M, M. Naglis, R. Pisani, I. Ravinovich, T. Sakaguchi, D. Sharma, A. Sickles, I. Tserruya, and C. Woody. *Understanding the gain characteristics of gems inside the hadron blind detector in phenix*. In IEEE Nuclear Science Symposium Conference Record, NSS'07, **Volume 6** (2007) 4662–4665. 125

[159] B. Azmoun *et.al.* *Collection of photoelectrons and operating parameters of csi photocathode gem detectors*. In IEEE Nuclear Science Transaction, NS-56, **Volume 3** (2009) 1554–1549. 133